FEDERAL UNIVERSITY OF SÃO CARLOS
CENTER OF EXACT SCIENCES AND TECHNOLOGY
PROGRAM OF POST-GRADUATION IN PHYSICS

Properties of coupled semiconductor quantum dot systems and their optical response

Luís Antônio Cabral

UFSCar - São Carlos
Março/2018

FEDERAL UNIVERSITY OF SÃO CARLOS
CENTER OF EXACT SCIENCES AND TECHNOLOGY
PROGRAM OF POST-GRADUATION IN PHYSICS

Properties of coupled semiconductor quantum dot systems and their optical response

Luís Antônio Cabral

Thesis presented to physics department of Federal University of São Carlos - DF/UFSCar as part of the requirements for the PhD title in Physics.

Advisor: Prof. Dr. Victor Lopez Richard
Co-Advisor: Prof. Dr. Juarez Lopez Ferreira da Silva

UFSCar - São Carlos
Março/2018

UNIVERSIDADE FEDERAL DE SÃO CARLOS

Centro de Ciências Exatas e de Tecnologia
Programa de Pós-Graduação em Física

Folha de Aprovação

Assinaturas dos membros da comissão examinadora que avaliou e aprovou a Defesa de Tese de Doutorado do candidato Luis Antonio Cabral, realizada em 31/10/2017:

Lopez Richard

Prof. Dr. Victor Lopez Richard
UFSCar

Juarez L. F. da Silva

Prof. Dr. Juarez Lopes Ferreira da Silva
USP

Vivaldo Leiria Campo Júnior

Prof. Dr. Vivaldo Leiria Campo Junior
UFSCar

Prof. Dr. Jose Pedro Rino
UFSCar

Alex Antonelli

Prof. Dr. Alex Antonelli
UNICAMP

Cedric Rocha Leão

Prof. Dr. Cedric Rocha Leão
UFABC

Acknowledgements

During the period of development of this Thesis, I had the opportunity to interact with many people who contributed to this work. Thus, I will provide my special thanks.

Thanks to my advisor, Professor PhD Victor Lopez Richard, and co-advisor, Professor PhD Juarez Lopes Ferreira da Silva, for the trust, availability and attention. There were several shared knowledges, solidifying and establishing the physical concepts in a simple and a productive way. All the support and infrastructure provided were fundamental for the results presented in this Thesis. Professors PhD Victor and Juarez had been present in every step, indicating the best way to obtain the results. In addition, they showed me the science in a elegant way.

In the same way, I'm grateful to Professor PhD Gilmar Eugenio Marques for the attention and encouragement, providing a productive environment for the development of the topics covered by this Thesis. To Professor PhD Matheus Paes Lima, whose teachings greatly contributed to the my scientific growth. To Professors PhD Leonardo Villegas Lelovsky and Anibal Thiago Bezerra for the valuable discussions in several physical systems that certainly favored my learning. To Professors PhD Adalberto Picinin and Luís Vicente Garcia for the motivation.

A special thanks to all members of *Quantum Theory of Nanomaterials*, and *Semiconductors Nanostructures* groups. In particular, to PhD Fernando Pereira Sabino, Professor PhD Vivaldo Lopes de Oliveira Neto and PhD Diego Guedes Sobrinho for the opportunity to work and collaborate. To PhD Diana Mercedes Meneses Gustin, Msc Carlos Mário Rivera Ruiz, Msc Carlos Maciel de Oliveira Bastos, Msc Rafael Costa Amaral and Felipe Antunes Calvi for friendship and companionship.

To my mother, Maria Antônia Cabral, for all teachings and support. And also, to my sister, Júlia Cabral Cardoso. They support and understand me in all the moments. To Professor PhD James Alves de Souza and Daniela Milani, whose solid friendship and reciprocity started as soon as we met at university and his daughter, Clara, whose sweet way rejoices our days filling with so much love and happiness. In the same way, to Ana, Danilo and their sons. To Patrícia Silveira Pinto, Patrícia Amanda Vieira, Janaína Martins Alves and Angélica Gasparotto for the solid friendship and for understand my absence along this research.

To all Professors and collaborators of Physics Department of UFSCar (Federal University of São Carlos) and CAPES (Coordenação de Aperfeiçoamento de Pessoal de Nível Superior) by the financial support, which allowed the development of this research.

Abstract

The study of doped semiconductor quantum dots with magnetic impurities has been a challenging task when adding spin-orbit coupling and exchange interaction with asymmetry effects. The combination of all these factors within a single theoretical model, simultaneously analyzed with external fields, reveals interesting properties. Within this framework, the adjustment of the effective Zeeman splitting due to the asymmetry and the character of the ground state are determined. The effective mass model of the electronic structure, that allows combining different confinement profiles with reduction of controllable symmetry, spin-orbit interaction effects and external fields under a variety of configurations, in a systematic way has been complemented with atomistic simulations. The connection between the effective mass model and such atomistic approaches was done through a characterization of the main trends for the manganese positioning (Mn) in cells containing cadmium selenide (CdSe) quantum dots covered by zinc selenide (ZnSe), as well as the exchange interaction terms, which is calculated with a fully *ab initio* technique.

Imperfections in nanostructures are also within the scope of this Thesis. Defects can induce magnetism in low-dimensional systems, wherein the challenge is to identify the source of this nano-magnetism in non-magnetic semiconductors, such as CdSe. In this Thesis, we present an optical evidence of this nano-magnetism due to the presence of vacancies. The formation energy analysis and the effects of the stress fields for the charged and uncharged defects under various geometries provided a better understanding of the experimental results. In addition, a study of the local deformations was performed using the molybdenum disulfide (MoS_2). Within the density functional theory, an organic molecule, called azobenzene, was placed on the MoS_2 layer in order to investigate the adsorption properties of the system.

Key-words: $\mathbf{k}\cdot\mathbf{p}$ effective mass approximation, density functional theory, spin-orbit coupling, asymmetry effects, quantum dots.

Resumo

O estudo de pontos quânticos semicondutores dopados com impurezas magnéticas é uma tarefa desafiadora ao adicionar o acoplamento spin-órbita e a interação de troca com efeitos de assimetria. A combinação de todos esses fatores dentro de um único modelo teórico, analisado concomitantemente com campos externos, revelam propriedades interessantes. Dentro desta estrutura, o ajuste do efeito Zeeman devido a assimetria e o caráter do estado fundamental são determinados. O modelo de massa efetiva da estrutura eletrônica, que permite combinar diferentes perfis de confinamento com redução de simetria controlável, efeitos da interação spin-órbita e campos externos sob uma variedade de configurações, de forma sistemática foram complementadas com simulações atomísticas. A conexão entre o modelo de massa efetiva e tais abordagens atomísticas foi realizada através da caracterização das principais tendências para o posicionamento do manganês (Mn) em células contendo pontos quânticos de seleneto de cádmio (CdSe) recobertos por seleneto de zinco (ZnSe), bem como os termos de troca, os quais são calculados com uma técnica completamente *ab initio*.

Imperfeições em nanoestruturas estão igualmente no escopo desta Tese. Defeitos podem induzir magnetismo em sistemas de baixa dimensão, em que o desafio consiste em identificar a fonte desse nano-magnetismo em semicondutores não-magnéticos, como o CdSe. Nesta Tese, apresentamos uma evidência óptica desse nano-magnetismo devido a presença de vacâncias. A análise das energias de formação e efeitos de campos de tensão para os defeitos carregados e não carregados em várias geometrias proporcionaram uma melhor compreensão dos resultados experimentais. Adicionalmente, um estudo de deformações locais no perfil de confinamento foi realizado utilizando o dissulfeto de molibdênio (MoS_2). Dentro da teoria funcional da densidade, uma molécula orgânica, chamada azobenzeno, foi disposta sobre uma camada de MoS_2 para verificar as propriedades de adsorção do sistema.

Palavras-chave: aproximação $\mathbf{k}\cdot\mathbf{p}$ da massa efetiva, teoria funcional da densidade, acoplamento spin-órbita, efeitos de assimetria, pontos quânticos.

List of Figures

List of Tables

List of abbreviations

QW	Quantum Well
QD	Quantum Dot
QR	Quantum Ring
HH	Heavy Hole
LH	Light Hole
DFT	Density Functional Theory
ZB	Zinc Blend
WT	Wurtzite
RS	Rock Salt
SOC	Spin-Orbit Coupling
FD	Fock-Darwin
DMS	Diluted Magnetic Semiconductors
DOS	Density of States
LDOS	Local Density of States
VASP	Viena *ab initio* Simulation Package
FM	Ferromagnetic
AFM	Anti-Ferromagnetic
ECN	Effective Coordination Number
VBM	Valence Band Maximum
CBM	Conduction Band Minimum
MBE	Molecular Beam Epitaxy
TMD	Transition Metal Dichalcogenides
BOAP	Born-Oppenheimer Approximation
HK	Hohenberg-Kohn
KS	Kohn-Sham
MBP	Many Body Problem
LDA	Local Density Approximation
LSDA	Local Spin Density Approximation
GGA	Generalized Gradient Approximation
XC	Exchange and Correlation

vdW	van der Waals
BJ	Becke Johnson
PBC	Periodic Boundary Conditions
AE	All Electron
PAW	Projector Augmentation Waves
OPW	Orthogonalized Plane Waves
APW	Augmented Plane Waves
PS	Pseudopotential
QCSE	Quantum Confined Stark Effect
PL	Photoluminescence
TEM	Transmission Electron Microscopy Images
FOE	Formation Energy

Contents

Chapter 1

Introduction and motivation

Several problems in semiconductors physics are analyzed within the framework of quantum mechanics. A better understanding of the confinement profile is crucial to determine the electronic properties of the system. In turn, solid state physics gained notoriety with the extension of bulk crystals theories for the investigation of thin films and multi-layered systems. Advances in Molecular Beam Epitaxy (MBE) [1] allowed the growth of individual atomic monolayers, [2] whose properties are mainly determined during the synthesis process. The orientation of the substrate where the nanostructures will be grown and the anisotropic effects that favor certain directions are responsible for the determination of the electronic structure of these semiconductor systems. This experimental control of heterostructures growth also provides fundamental technological advances. [3] Modern techniques allow the manipulation and creation of notable confined systems. Thus, in the last 20 years, a breakthrough in the studies of nanostructured materials has taken place.

Advances have been made in the study and applications of electrons confined in two dimensions, in particular, the quantum wells (QWs). The QWs are nanostructures that can be formed by stacking semiconductor layers. Thus, the simulation of their electronic structure reveals quantization effects as described by quantum mechanics. After the discovery of two-dimensional systems, there was an intense quest for the study of their properties and applications. The result, for instance, was the emergence of pioneering theories such as the Quantum Hall Effect [4] by Klaus von Klitzing's, winning work of the Nobel Prize in 1985, followed by the Fractional Quantum Hall Effect [5] by H. L. Tsui *et al*. and the theoretical works of Laughlin. [6–8]

In the early 1980's, the progress in growth and lithographic techniques allowed the study of the electronic confinement of almost-one dimensional structures, called quantum wires. [9] Subsequently, the quantization of the electrons in quasi-zero dimensional structures provided the emergence of quantum dots (QDs), firstly synthesized by scientists from Texas Instruments Incorporated. Reed *et at* reports the quantum dot growth by lithography techniques. [10] Afterward, research centers such as AT & AT Bell Laboratories [11, 12] and Bell Communication [13] reported the creation of quantum dots with diameters between 30-45 nm.

Quantum dots [14] are semiconductor nanostructures of dimensions as small as 10^{-8} and 10^{-6} m [15] whose controllable properties allow several theoretical studies and experimental manipulations. The description of quantum mechanics is used to analyze the properties of electrons and holes confined in the three spatial dimensions within the quantum dots. Due to this characteristic, quantum dots are usually known as almost-zero dimensional structures. This three dimensional confinement provides the quantization of the quantum dots states in discrete energy levels similar to an atom. [16] Optical transitions are thus allowed between these levels according to the selection rules for photon emission and absorption. Thus, the optical and electronic properties are directly and indirectly detectable from the light interaction. [2, 17]

Although the quantum dots are called as artificial atoms, there are considerable differences between an artificial and a natural atom. Concerning the electronic structure of quantum dots, the separation between energy levels can be in the order of meV and the external control of the confinement potential can be attained, while in natural atoms, the separation of energy levels is in the order of eV.

The possibility to modify the geometry of confinement and the carrier dynamics through the application of external electromagnetic fields opens a wide range of studies. It is possible, for instance, to analyze the behavior of one or more particles bound in a parabolic potential induced by a magnetic field, the quantization of Landau levels, the radiative recombination of carriers, and so on. Among several theoretical frameworks, the $\mathbf{k}\cdot\mathbf{p}$ Fock-Darwin description of confined carriers in quantum dots under the influence of an external magnetic field is notorious for its simplicity. Also, the relative small number of electrons favor the study of these systems by using first principle simulations, or *ab initio* methods. Both treatments, **k·p** and *ab initio* simulations are combined within this Thesis.

In addition, it is interesting to note that QDs can be structurally coupled, as in the case of self-organized systems or optically coupled via light interaction. The flexibility of manipulating the energy levels through the incidence of electromagnetic fields makes the QDs attractive to the scientific community, providing advances in the segments of optical detectors, transport, Rabi oscillations, decoherence, and quantum computing. An interesting study of the QDs dynamics as *qubits* was done by Loss and Divicenzo. [18]

Currently, several QDs growth processes are available that control their shape and radius. The control of the QDs geometry depends on the pressure and temperature during the growth process: chemical techniques, [19] lithographic, and MBE or MOCVD (Metal-Organic Chemical Vapor Deposition). Self-assembled QDs, grown by MBE and MOCVD, attracted the attention of the scientific community for applications in electronic semiconductor devices, such as the buildup of high temperature lasers and quantum computing schemes, wherein different lattice parameters of deposited materials lead to unavoidable strain fields and the possibility to form electron traps.

With the advent of the spintronics, the efforts for the manipulation of spins in semiconductor nanostructures became evident in several areas including Condensed Matter and Quantum Information. The first proposal for spin manipulation in nanostructures was introduced by Datta-Das, [20] wherein the authors explore the effects of the spin-orbit interaction in a 2D gas in order to manipulate and detect the polarized spins. In this way, spin and charge carry information. The spin control is particularly interesting for the construction of quantum computing devices because its operation is based in a coherent superposition of quantum states of two-electronic levels. [18] The understanding of the mechanisms that destroy the states superposition becomes crucial for modeling this systems. [21] The spin-orbit coupling is a potential source of spins relaxation, allowing the mixing of spins states. [22, 23] Thus, the combination of spin-effects, geometry, and strain is a topic of interest and one of the motivations of this Thesis. Within this search, the introduction of spin-orbit coupling effects is unavoidable.

1.1 Manganese, cadmium selenide and indium arsenide

Cadmium selenide (CdSe) is a II-VI semiconductor material. The most stable phases are zinc blend (ZB), wurtzite (WT), and rock salt (RS). [24] The experimental lattice parameter in zinc blend phase assumes 6.05 Å and the bulk modulus 53.0 GPa. CdSe shows a direct band gap in the gamma point, namely, 1.90 eV. [25] By growing the CdSe QD on another substrate material, an unavoidable strain occurs due to the lattice parameters difference. In this Thesis, we analyzed the CdSe QDs grown on zinc selenide (ZnSe) substrates. Zinc selenide crystallizes in zinc blend phase with 5.67 Å and 2.82 eV of lattice constant and gap energy, [24, 26, 27] respectively. In turn, indium arsenide (InAs) is a III-V semiconductor widely employed in nanoelectronic devices based on quantum well structures. [28] The stable phase of the bulk InAs is the zinc blend, having a cubic lattice parameter of 6.06 Å length and a narrow band gap of 0.42 eV, [29] with a strong non-parabolicity of the conduction band. In this work, we studied the InAs QDs within gallium arsenide doped with antimony (GaAs:Sb).

The formation of semiconductor QDs inside the host materials induces strain, compressing the bond lengths and introducing some perturbations in the chemical environment of the solid. Setting the CdSe QDs diameter between 2.0-7.0 nm leads to the emission between 450-650 nm. [30] Changing the composition to $CdSe_{1-x}Te_{1-x}$ and radius 5.0 nm, the emission appears between 610-800 nm. Thus, the notoriety for the particular case of CdSe QDs is the photo-stability, wherein the composition plays a key role. Usually, CdSe QDs passivated with zinc sulfide (ZnS) [31] have been used in medical [32] and biological [33] applications, preserving the core from oxidation and also promoting an increase in the photoluminescence. Usually, the InAs QDs are grown on gallium arsenide. [34] The characterization of the atom-like energy levels of InAs QDs are presented, for instance, in Ref. [35]. Within the effective mass theory, strain effects in InAs QDs were studied in Ref. [36]. These properties have an intrinsic dependence on the QD diameter and composition, determining the confinement profile, and have become one of the problems tackled and discussed here.

1.2 Transition metal dichalcogenides

The transition metal dichalcogenides (TMD) are composed by a transition metal and a chalcogen atom, such as molybdenum and sulfur, respectively. The transition atoms in the layer are strongly bonded while the atoms between the layers are linked by van der Waals (vdW) forces. [37] Due to layers formation, it is possible to exfoliate the bulk in thin layers and study them individually. Commonly, each layer is composed by three atomic planes with thickness around 6.0-7.0 Å. Furthermore, the structure of the TMD is composed by hexagonal layers. In general, the TMD material crystallizes in the hexagonal (2H) ($P6_3/mmc$), trigonal (1T) ($P\bar{3}m1$) [38] and rhombohedric (3R) ($R3m$) forms[1], [39] wherein the most of TMDs prefer 2H geometry.

The TMD are intensely studied due to the wide range of applications and the possibility to constitute layered materials, used in several areas. [40–43] In addition, TMD attracts the attention due to its applications in 2D nano-devices. [44] First-principles calculations based on the density functional theory can foresee new materials and their electronic and chemical properties. The pioneer 2D material obtained was graphene, attracting attention of the solid-state community due to the interesting electronic, optical, thermal, and mechanical properties. [45] Moreover, graphene is still explored in several studies. [46] The intensive study of graphene increased the interest in others two-dimensional materials. From that point, new 2D materials have been exfoliated from their bulk structures.

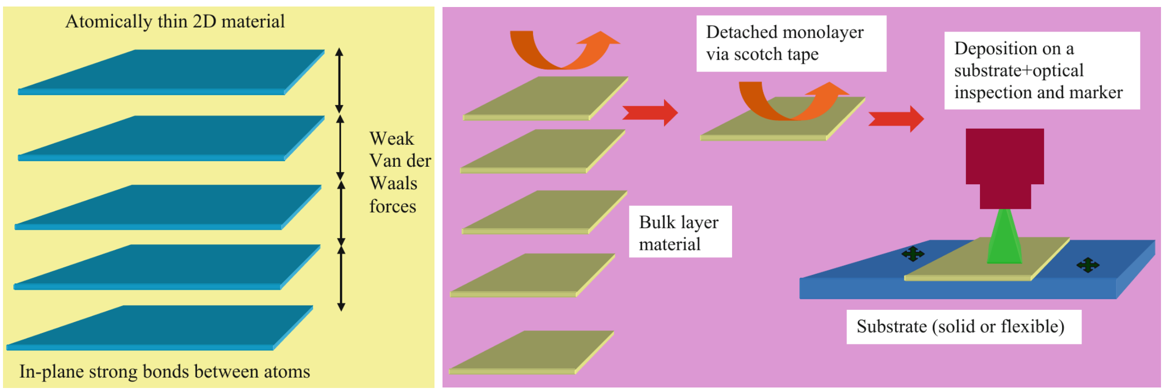

Figure 1.1: 2D materials. On the left, a bulk material composed by several 2D monolayers. The in-plane bonds are covalent and the growth direction are related to the weak van der Waals forces. On the right, we represent the mechanical exfoliation technique. The 2D monolayer has been removed from the bulk material followed by the optical characterization, determining where the material will be deposited on the layer.

[1]The 2H and 1T are also called Octahedral and Trigonal Prismatic structures.

In Fig. 1.1, taken from Ref. [47], we represent a bulk formed by several monolayers in the left and the mechanical exfoliation process in the right. The exfoliation is performed together with the optical characterization to determine where the material will be deposited on the substrate. However, the time used to produce the new layers is the major disadvantage. As mentioned above, the gap values of the TMD semiconductors can be tuned according to the experiment. By applying external voltages, by inserting or removing the number of layers, it is possible adjust the gap, which changes the confinement profile and, consequently, modifies the optical and electronic properties of these solids. Moreover, some 2D materials, such as $HFSe_2$ and HF_2, have considerable mobilities of carriers and electron masses along Γ-M direction. [47] However, several band structures parameters, such as effective masses and carrier mobility, are not available in the literature. Thus, the density functional theory is used in order to determine these values with high accuracy. The spin-orbit coupling in TMD is strong due to d-orbitals of metal ions. The inversion symmetry in bilayer of MoS_2 can be controlled by applying an electric field perpendicular to the layer. [38]

Molybdenum disulfide (MoS_2) has been widely used in several areas of research, such as photoelectrochemistry [48] and photovoltaics [49], due to its electronic, optical [50] and catalyst properties. Single MoS_2 layers have been explored due to their potential applications in electronics and nano-devices. [51] MoS_2 bulk semiconductor shows an indirect gap of 1.2 eV, however the monolayer presents a direct forbidden region of 1.8 eV. [38] Molybdenum disulfide belongs to the $P6_3/mmc$ space group. [47] The hexagonal lattices constants are a=3.16 and c=12.58 Å. [38, 52] The gap modulation by the number of layers allows foreseen their use for phototransistor architectures. [53]

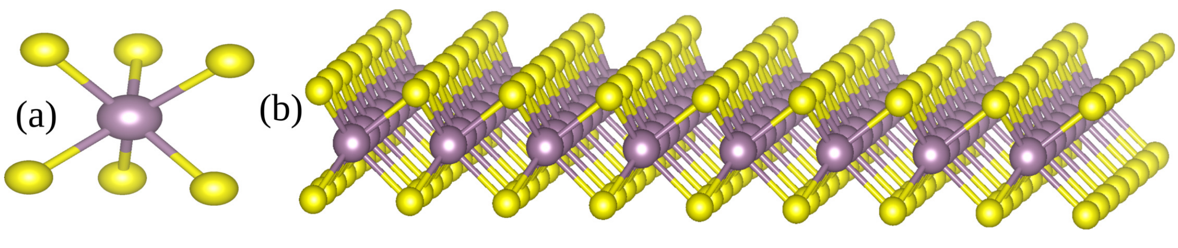

Figure 1.2: A layer of molybdenum disulfide (MoS_2). Panel (a) indicates the single MoS_2 layer and panel (b) the monolayer multiplied by eight in the lateral direction.

The emergence of new technological devices has been the topics of research of several groups. [46] Dolui group shows that the MoS_2 conductivity depends on the charge polarity trapped at the interface. [54] However, p- and n-types conductivities are observed when the MoS_2 is deposited on the SiO_2 substrates. [55, 56] The effect of substrates on the electronic properties of these 2D systems is a current investigation trend. A wide range of possibilities can be opened by varying the chemical environment and by the potential functionalization of the surfaces, as discussed in this Thesis.

1.3 Thesis scope

The main object of this Thesis is to tackled problems related to the properties of confined semiconductors systems. For this, in chapter 2, we present the methodological backgrounds of the electronic structure characterization that provide the bases for the theoretical investigations. In particular, the general aspects of the crystal symmetry and properties of solids are presented in chapter 2. After that, the $\mathbf{k}\cdot\mathbf{p}$ method is discussed to describe the electronic structure of semiconductors. The atomistic effects are analyzed within the density functional theory. Here, the Projector Augmentation Waves (PAW) method was used, as implemented in the Viena *ab initio* Simulation Package (VASP).

One of the questions to be answered in this Thesis concerns the spin modulation with geometry, strain, and impurities, all combined within the same framework. In general, these effects are tackled separately so that their relative importance can seldom be weighted. We are able to describe how they impact the spin ground state under the influence of a magnetic field. The results of the electronic structure calculations for CdSe quantum dots and InAs rings are shown in chapter 3. The shape and the quantum confinement are emulated through a variable potential. A more realistic implementation of the theoretical model is given by the external asymmetries and the spin-orbit coupling. In addition, the introduction of magnetic impurities allows to study the exchange interaction coupling between the *s*-*p* states of the host material and *d* levels of the impurity. The exchange interaction coupling was also investigated at atomistic scales using first principles calculations within the density functional theory framework, wherein a manganese (Mn) atom enters replacing the cadmium and zinc atoms in cadmium selenide (CdSe) quantum dots embedded in a zinc selenide (ZnSe) host material. Interstitial manganese atoms inside the crystal were also implemented to contrast various configurations. The interplay between the results of the $\mathbf{k}\cdot\mathbf{p}$ method and density functional theory is characterized through the effective Lande-factor.

Several imperfections can also occur in the growth process of the semiconductor nanostructures. In general, the presence of the imperfections in the crystalline structure distorts the electronic structure of the materials, providing new effects. The defects can be reproduced by the introduction of magnetic impurities, interstitial atoms and, the most common, vacancies. Thus, taking advantage of the first-principles calculations, the aim of chapter 4 is to provide the theoretical bases to explain the magnetism induced by vacancies in CdSe quantum dots embedded in ZnSe host material observed in the experiments. For this, several vacancies positions of Cd, Se and Zn atoms were created for the analysis of the magnetic moment and formation energy.

Based on experimental motivations, in chapter 5 we show the results of the adsorption of organic azobenzene molecules on the surface of molybdenum disulfide (MoS_2). Using the density functional theory, the azobenzene molecule was studied in its cis and trans isomers in gas phase. Concomitantly, the electronic properties of MoS_2 were also explored, showing the band gap transition from indirect (bulk) to direct (layer). The understanding of the quantum confinement within MoS_2 plays a key role to study the electronic states of the azobenzene on the layer. Thus, various configurations of the azobenzene molecule were placed on the MoS_2 layer, where the adsorption properties, the work function, the charge transfer, and the stability of the configurations were analyzed and contrasted to determine the most stable and energetically favorable structure.

A brief summary of the results and the future perspectives are presented in chapter 6. In the appendices, we show the details of the calculations performed in the chapters. In appendix A, we present the calculations of the spin-orbit coupling, including the asymmetric perturbative potentials for conduction and valence bands. The bump size in the potential profile is verified in the appendix B and the Luttinger calculations are demonstrated in the appendix C. The appendix D shows the details of the exchange interaction calculations. In the appendix E, we present the theoretical approach and the computational details used to obtain the results of this Thesis.

Chapter 2

Backgrounds for the electronic structure simulations

The three-dimensional periodic arrangement of crystals simplifies the theoretical description of the materials, allowing to link the real experiment and data analysis. There is a wide range of structures formed by different combinations of atomic species, wherein the introduction of the external forces, pressure and fields can result in distortions in the crystal. The intense search for the construction of electronic nano-devices, has promoted the evolution of techniques to study and simulate solids. In our case, the $\mathbf{k}\cdot\mathbf{p}$ method and density functional theory (DFT), or the interplay between them, were used to describe the electronic systems analyzed in this Thesis.

Both methods, $\mathbf{k}\cdot\mathbf{p}$ and DFT, are within the scope of many-particle physics. The $\mathbf{k}\cdot\mathbf{p}$ method is used to determine the details of the band structure in the neighborhood of an arbitrary k_0 point. The consistency and flexibility allow to emulate the optical and electronic properties of solids. The parameters used in the $\mathbf{k}\cdot\mathbf{p}$ theory are obtained from experimental techniques or *ab initio* calculations. [57] On the other hand, the density functional theory is used for investigations at atomistic scales using first principles methods. Here, mechanisms to address the electronic structure of systems of interest were introduced by complementing methodologies. So, when necessary, both DFT and $\mathbf{k}\cdot\mathbf{p}$, will be used for modeling the problems tackled in this work. These tools are essential to understand the matters discussed in this Thesis. Thus, in the following subsections we present the theoretical foundations that support the obtained results, discussed in the following chapters of this Thesis.

2.1 Crystal symmetry and properties of solids

The periodic arrangement of atoms in the lattice defines a crystal. Due to the technological applications, [3] the crystalline materials are widely studied. The crystals are described by their symmetry operations. The translations group and point operations, such as rotations, reflections and inversions, define the space group of the crystal. The non-crystalline materials receive a separate treatment because their atoms are randomly distributed. Unavoidable imperfections during the crystal growth, such as vacancies, impurities, and extra interstitial atoms can determine new effects in the optical and electronic properties of the crystal. In the next sections, we present the crystal properties and this theory will permeate all this Thesis.

2.1.1 Lattice and unit cells of crystal structure

The advancement of the theoretical descriptions allows to emulate the electronic structure of real experiments and foresee new optical and electronic properties of bulk crystals. The periodic arrangement in crystalline solids are described by the *Lattice Bravais* concept, wherein the position $\mathbf{R}$ is specified as a function of the primitive lattice vectors $\mathbf{a}_i$, $i = 1, 2, 3$, given by the relation $\mathbf{R} = n_1\mathbf{a}_1 + n_2\mathbf{a}_2 + n_3\mathbf{a}_3$, wherein n_1, n_2 and n_3 are integers. Therefore, the crystal lattice is described by the primitive vectors. The *primitive cell* is a cell with a minimum volume and, when translated by the *Bravais* vectors, occupies the whole space and its vectors are called *primitive basis vectors*. A unit cell is larger than the primitive one, which can be translated and fill the space region, reproducing a similar region of the crystal. [2] The lattice parameters are the vectors which describes the unit cell. The periodic arrangement of the crystal defines the reciprocal lattice.

Due to the diversity of crystal lattices, it is appropriate to analyze the symmetry of the unit cell. The point symmetry determines fourteen different lattices and the cells are organized in seven groups: triclinic, monoclinic, orthorhombic, tetragonal, cubic, trigonal, and hexagonal. [58] The geometry of the cubic systems can be separated into simple cubic, body-centered cubic and face-centered cubic. In addition, it is convenient to specify a orientation for the lattice planes using the reciprocal lattice. Thus, the Miller's indices are introduced as the weight of the components of the smallest vector of the reciprocal lattice normal to that plane.

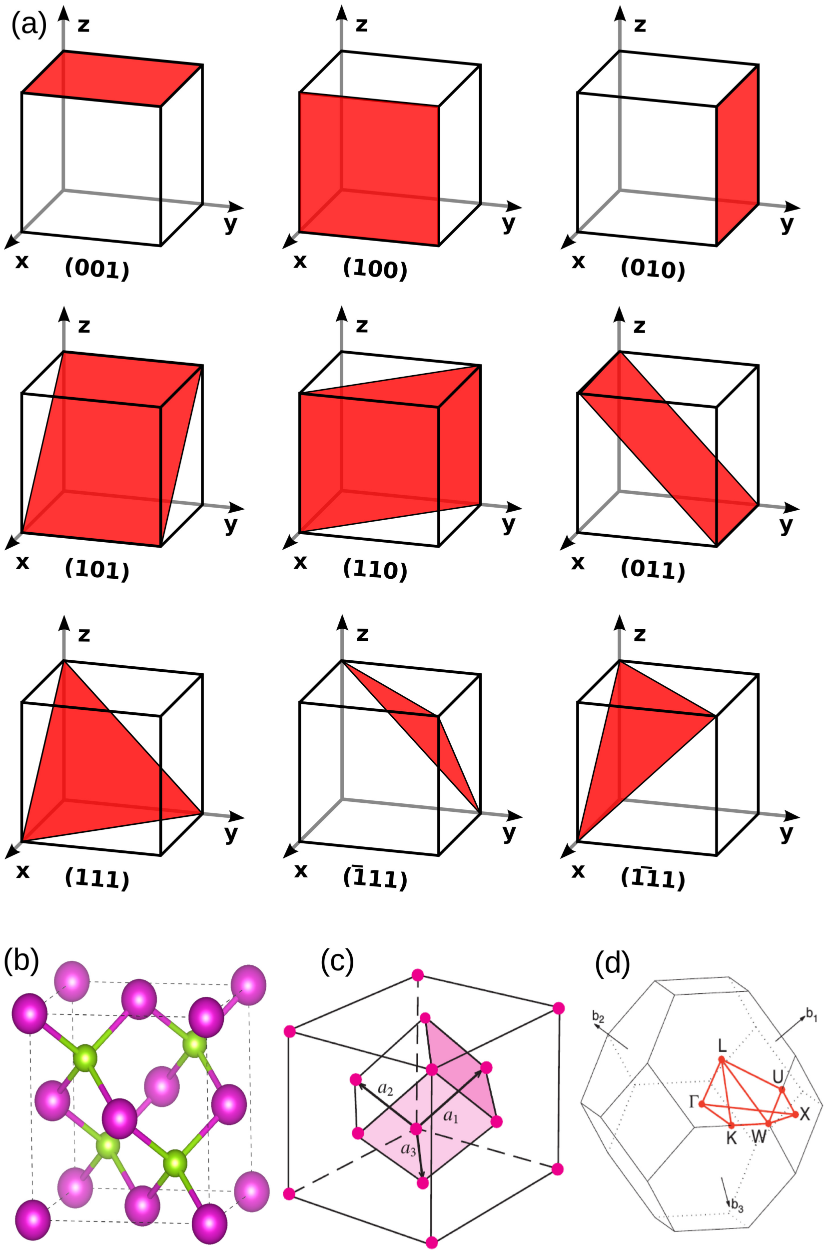

Figure 2.1: Crystal symmetry of solids. In panel (a) are depicted the Miller indexes and their respective planes. Panel (b) represents the cubic face centered unit cell for cadmium selenide bulk structure. Parts (c) and (d) show the primitive cell and the first Brillouin zone for the face centered cubic unit cell, respectively.

The III-V nanoscopic systems crystallize in zinc blend (ZB) structure. The ZB phase consists in two interpenetrating face centered cubic lattices placed at $\frac{a}{4}$ along the main diagonal of the cube, wherein a is the lattice vector. The ZB is not a Bravais lattice due to its atomic composition. The first Brillouin zone of the reciprocal lattice is a truncated octahedron, wherein the top of the valence band occurs at the Γ-point. [59] The crystallization of the ZB differs from wurtzite (WT) only by the spatial arrangement of atoms in the lattice.

The space lattice of the WT is composed by a hexagonal structure in four interpenetrating lattices, [60] wherein the basis a_1 and a_2 are two identical atoms associated to each point of the lattice and the a_3 axis is perpendicular to them. [58]

2.2 k·p method

Within the many body problem, a consistent analysis of the electronic and optical properties of solids can be performed using the **k·p** method. [61–68] Taking advantage of the lattice periodicity, the method allows to determine an effective Hamiltonian of the system within the mean field approach. The wavefunction is expanded in terms of the **k** vectors. Thus, the **k·p** approach is a consistent mathematical tool for the investigation of the electronic structure in a neighborhood of an arbitrary point, and the validity of the method is restricted to this neighborhood. In fact, the **k·p** approach is based in the determination of the Hamiltonian in a representation which couples the energy states in the $\mathbf{k}=\mathbf{k}_0$ point in order to solve the eigenvalue equation, introducing the appropriate approximations. In this Thesis, we used the parabolic approximation for the conduction band and the Luttinger model for the valence band. Due to the versatility and relatively simple mathematical manipulation, the **k·p** method is widely used in the study of the band structure of materials. In addition, the Brillouin zone is fully described by increasing the number of wavefunctions. The diagonalization of the effective Hamiltonian chosen at **k** point must provide the energy states. A complete description of solids is conditioned by a previous determination of material parameters, which is given by experimental data or first principles calculations.

2.2.1 k·p Hamiltonian

The mathematical modeling of a solid must include all the interactions between electrons and nuclei. Each carrier is subjected to the interaction with other carriers in the lattice under an effective potential. Thus, the strategy adopted is to assume a charged carrier moving in a crystal lattice under the influence of the mean field due to the periodic potential $U(\mathbf{r} + \mathbf{R}) = U(\mathbf{R})$, wherein $\mathbf{r}$ is a vector of the *Bravais* lattice. The eigenvalues is obtained by solving the Schroedinger Eq. (2.1):

$$H_0\Psi_k(\mathbf{r}) = \varepsilon\Psi_k(\mathbf{r}), \tag{2.1}$$

where $H_0 = \frac{\mathbf{p}^2}{2m_0} + U(\mathbf{r})$, with $\mathbf{p}{=}{-}i\hbar\nabla$ is the linear momentum operator and m_0 is the free electron mass. Due to the crystal periodicity, the eigenstates of the wavefunction can be expanded according to the Bloch theorem: [2]

$$\Psi_{n\mathbf{k}} = e^{i\mathbf{k}\cdot\mathbf{r}}u_{n\mathbf{k}}(\mathbf{r}), \tag{2.2}$$

where $u_{n\mathbf{k}}(\mathbf{r})$ is the Bloch wavefunction, $\mathbf{k}$ the wave vector and n the band index. Expanding the operator $H(\mathbf{k}) = e^{-i\mathbf{k}\cdot\mathbf{r}}H_0e^{i\mathbf{k}\cdot\mathbf{r}}$ in Taylor series,

$$H(\mathbf{k}) = H_0 - i\mathbf{k}\cdot[\mathbf{r}, H_0] - \frac{1}{2}\sum_{ij}\mathbf{k}_i\mathbf{k}_j[r_i, [r_j, H_0]] + \ldots, \tag{2.3}$$

where the commutators are $[\mathbf{r}, H_0]{=}i\frac{\hbar}{m_0}\mathbf{p}$ and $[\mathbf{r}_i, [\mathbf{r}_j, H_0]]{=}{-}i\frac{\hbar^2}{m_0}\delta_{ij}$, neglecting the higher order terms. Replacing the anti-commutators in Eq. (2.3), the result is:

$$H(\mathbf{k}) = \frac{\mathbf{p}^2}{2m_0} + U(\mathbf{r}) + \frac{\hbar\mathbf{k}^2}{2m_0} + \frac{\hbar}{m_0}\mathbf{k}\cdot\mathbf{p}. \tag{2.4}$$

By using the Bloch theorem, it is interesting to rewrite (2.4) in the following way:

$$\left[H(\mathbf{k_0}) + \frac{\hbar\mathbf{k}^2}{2m_0} + \frac{\hbar}{m_0}\mathbf{k}\cdot\mathbf{p}\right]u_{n\mathbf{k}}(\mathbf{r}) = \varepsilon(\mathbf{k})u_{n\mathbf{k}}(\mathbf{r}). \tag{2.5}$$

Expanding the Bloch functions $u_{n\mathbf{k}}$ in terms of the $u_{n'\mathbf{k}_0}$ in the $\mathbf{k} = \mathbf{k}_0$,

$$u_{n\mathbf{k}}(\mathbf{r}) = \sum_{n'} c_{nn'}(\mathbf{k})u_{n'\mathbf{k}_0}(\mathbf{r}). \tag{2.6}$$

After some algebraic manipulations,

$$\sum_{n'}\left\{\left[\varepsilon_n(\mathbf{k}_0) + \frac{\hbar^2}{2m_0}(\mathbf{k})\right]\delta_{n'n} + \frac{\hbar}{m_0}(\mathbf{k})\mathbf{p}_{n'n}(\mathbf{k}_0)\right\}c_{n'n} = \varepsilon_n(\mathbf{k})c_{n'n}, \tag{2.7}$$

where $\mathbf{p}_{nn'}=\int_\Omega u_{n\mathbf{k}_0}(\mathbf{r})\left(\frac{\hbar}{i}\nabla\right)u_{n'\mathbf{k}_0}(\mathbf{r})d\mathbf{r}$, Ω are the unit cell volume in a real space and $H(\mathbf{k}_0)u_{n\mathbf{k}_0}(\mathbf{r})=\varepsilon_n(\mathbf{k}_0)u_{n\mathbf{k}_0}(\mathbf{r}_0)$. [69, 70]

Until here, the discussion does not include the spin-orbit (SO) interaction. The spin-orbit coupling is the interaction of the spins with the orbital angular momentum and determines how the orbital motion of electrons are affected. The lifting of the valence band degeneracy due to the SO interaction in $\mathbf{k}$=0 originates the light (LH), heavy holes (HH) states and the split-off band separated by the gap energy Δ. In the absence of the spin-orbit interaction, the Γ-point in the valence band is triply degenerate. Thereby, the spin-orbit Hamiltonian (H_{SO}) should be added in the $\mathbf{k}\cdot\mathbf{p}$ Hamiltonian (2.7), [71]

$$H_{SO} = \frac{\hbar}{4m_0^2c^2}\left(\nabla U(\mathbf{r}\times\mathbf{p})\right)\cdot\sigma, \tag{2.8}$$

where c is the speed of light in the vacuum, $\nabla U(\mathbf{r})$ the crystalline potential gradient $U(\mathbf{r})$, $\mathbf{p}$ the electronic momentum and σ the spin Pauli matrices,

$$\sigma_x = \begin{pmatrix} 0 & 1 \\ 1 & 0 \end{pmatrix}; \qquad \sigma_y = \begin{pmatrix} 0 & -i \\ i & 0 \end{pmatrix}; \qquad \sigma_z = \begin{pmatrix} 1 & 0 \\ 0 & -1 \end{pmatrix}. \tag{2.9}$$

Eq. (2.8) describes the spin-orbit coupling in the presence of a crystalline potential, $U(\mathbf{r})$. Adopting the same procedure as used in the case without spin-orbit coupling (2.7),

$$\left[\frac{\mathbf{p}^2}{2m_0} + U(\mathbf{r}) + \frac{\hbar^2 mk^2}{2m_0} + \frac{\hbar}{m_0}\mathbf{k}\cdot\pi + \frac{\hbar}{4m_0^2c^2}(\mathbf{p}\cdot\sigma\times U(\mathbf{r}))\right]u_{n,\mathbf{k}} = \varepsilon_n(\mathbf{k})u_{n,\mathbf{k}}, \tag{2.10}$$

where, $\pi = \mathbf{p} + \frac{\hbar}{4m_0c^2}\sigma\times U(\mathbf{r})$. [27] Therefore,

$$\left[H_0 + H_{SO} + \frac{\hbar^2k^2}{2m_0} + \frac{\hbar}{m_0}\mathbf{k}\cdot\pi\right]. \tag{2.11}$$

However, within the SO approach, the spin σ is not a good quantum number. As shown in Eq. (2.11), the band index n is common for the orbital motion and the spin degree of freedom.

2.2.2 Effective mass approximation

Several interactions affect a particle moving in a crystalline lattice, which would be an obstacle to the description of the physical systems of interest. Assuming that the band structure does not show degeneracy in the expansion point $\mathbf{k}_0$ and has an extreme at this point, all lattice interactions can be included in an effective mass equation. By using quantum mechanics techniques, the eigenfunctions u_{nk} and eigenvalues ε_{nk} can be expanded until second order in $\mathbf{k}$ at the neighborhood of the $\mathbf{k}_0$ point for the unperturbed wavefunctions u_{nk} and eigenvalues ε_{nk} using perturbation approaches, [27, 58–60, 71]

$$u_{n\mathbf{k}} = u_{n\mathbf{k}_0} + \frac{\hbar}{m} \sum_{n' \neq n} \frac{\langle u_{n\mathbf{k}_0} | \mathbf{k} \cdot \mathbf{p} | u_{n'0} \rangle}{\varepsilon_{n\mathbf{k}_0} - \varepsilon_{n'\mathbf{k}_0}} u_{n'\mathbf{k}_0} \tag{2.12}$$

and

$$\varepsilon_{n\mathbf{k}} = \varepsilon_{n\mathbf{k}_0} + \frac{\hbar^2 k^2}{2m} + \frac{\hbar^2}{m^2} \sum_{n' \neq n} \frac{|\langle u_{n\mathbf{k}_0} | \mathbf{k} \cdot \mathbf{p} | u_{n'\mathbf{k}_0} \rangle|^2}{\varepsilon_{n\mathbf{k}_0} - \varepsilon_{n'\mathbf{k}_0}}, \tag{2.13}$$

where the linear terms in $\mathbf{k}$ vanish since $\varepsilon_{n\mathbf{k}_0}$ was assumed to be an extreme. Therefore, Eq. (2.13) is rewritten as follow:

$$\varepsilon_{n\mathbf{k}} = \varepsilon_{n\mathbf{k}_0} + \frac{\hbar^2 \mathbf{k}^2}{2m^*}, \tag{2.14}$$

where m^* is the effective mass of a carrier subject to a mean field approach. After some algebraic manipulations, Eqs. (2.13) and (2.14) become

$$\frac{1}{m^*} = \frac{1}{m} + \frac{2}{m^2 k^2} \sum_{n' \neq n} \frac{|\langle u_{n\mathbf{k}_0} | \mathbf{k} \cdot \mathbf{p} | u_{n'\mathbf{k}_0} \rangle|^2}{\varepsilon_{n\mathbf{k}_0} - \varepsilon_{n'\mathbf{k}_0}}. \tag{2.15}$$

Eq. (2.15) determines the effective mass of a carrier in a non-degenerate band, describing the coupling between the electronic states via $\mathbf{k}\cdot\mathbf{p}$ approach. By using group theory, it is possible to determine the $u_{n',\mathbf{k}_0}$ symmetries and analyze the coupling between the bands. Note that $m^* = m_0$ for an empty lattice U($\mathbf{r}$) = 0. [59]

2.2.3 Envelope function approach

The **k·p** method discussed until here takes advantage of the crystal periodicity. However, the introduction of defects, impurities, external electric and magnetic fields remove the crystal symmetry and, consequently, the nanostructure becomes non-periodic. Thus, the Bloch theorem loses its validity. This issue is addressed by the envelope function approach. [59, 72–74] In order to demonstrate the envelope function approach, it is assumed a hetero-junction composed by two crystal materials, A and B, disregarding the lattice parameter mismatch from the different materials. Supposing that the periodic part of the Bloch wave-function is the same in the materials at the $\mathbf{k}_0$ point ($u^{A}_{n\mathbf{k}_0}(\mathbf{r}) = u^{B}_{n\mathbf{k}_0}(\mathbf{r}) = u_{n\mathbf{k}_0}(\mathbf{r})$) and the solutions match across the boundaries, the wavefunction can be expanded in the following way: [75]

$$\Psi^{(A,B)}_{n,\mathbf{k}}(\mathbf{r}) = \sum_{n} \mathcal{F}^{(A,B)}_{n}(\mathbf{r}) u^{(A,B)}_{n\mathbf{k}_0}(\mathbf{r}), \tag{2.16}$$

where $u^{(A,B)}_{n\mathbf{k}_0}(\mathbf{r})$ are the periodic Bloch functions expanded for both A and B materials, $\mathcal{F}^{(A,B)}_{n}(\mathbf{r})$ are the envelope functions to be determined and n are the states considered in the calculation. In addition, the envelope functions are assumed to be smooth and the potential in the materials varies in a scale larger than the lattice parameter of the materials. Therefore, the envelope functions vary slower than the Bloch functions. [27, 76] A visual representation of the envelope function approach is given in Fig. 2.2, taken from Ref. [27]:

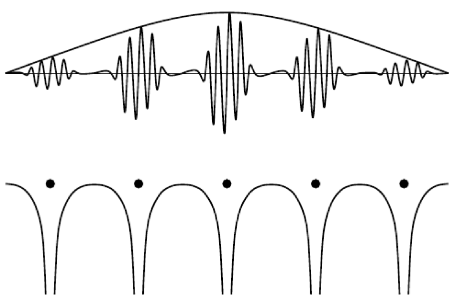

Figure 2.2: At the upper part of the Fig. the wavefunction expansion is depicted, where the slow and faster oscillation correspond to the envelope and the Bloch functions, respectively. At the bottom of the Fig. the potential that models the wavefunction is shown.

By assuming that the wavefunction is continuous at the intersection region, the envelope functions has the same shape $\mathcal{F}^{(A)}_{n}(\mathbf{r}, \mathbf{z}_0) = \mathcal{F}^{(B)}_{n}(\mathbf{r}, \mathbf{z}_0)$, where $\mathbf{z} = z_0\hat{\mathbf{z}}$ is the separation between the materials. Thus, the envelope functions are given by:

$$\mathcal{F}_n^{(A,B)}(\mathbf{r},\mathbf{z}) = \frac{1}{\sqrt{S}} e^{i\mathbf{k}\cdot\mathbf{r}} \chi_n^{(A,B)}(\mathbf{z}), \tag{2.17}$$

where $\mathbf{r}$ is the position vector, S the area in the same plane and $\chi_n^{(A,B)}(\mathbf{z})$ a function of the A and B materials. Therefore, the wavefunction for A and B materials is obtained by replacing Eq. (2.17) in (2.16). [59, 75]

2.2.4 The Kane Approximation and Luttinger Hamiltonian

The optical absorption and the band structure calculations can provide interesting analysis about the electronic states occupation. The mixing of hole states, non-parabolicity and spin effects determines essential information about the material. The **k·p** model can study these effects, wherein the band structure parameters must be previously known. Using the **k·p** perturbation theory developed by Löwdin, [77] Kane [61] solved the Schroedinger Eq. exactly within a restricted basis set at $\mathbf{k} = 0$ point. [78–80] In this model, all **k·p** interactions are taken exactly in the calculation of the bands Γ_8^c, Γ_7^c, Γ_6^c, Γ_8^v and Γ_7^v, while the other bands are treated using second order perturbation theory. [27]

The Kane basis can be given as a function of the angular momentum, [81] J_x, J_y and J_z, and a convenient representation of **k·p** model is introduced by a 8×8 matrix, which describes the valence and conduction bands. The 8×8 Kane Hamiltonian is used to describe narrow gap semiconductors, where the coupling between the conduction and valence bands must be taken into account. However, for large gap energy semiconductors, the inter-band energy coupling can be neglected. In such cases, the 6×6 Luttinger-Kohn Hamiltonian describes the behavior of heavy holes, light holes and split-off states. [63] In turn, the 4×4 Luttinger Hamiltonian details the four hole states and the split-off band is considered uncoupled from the hole states. [65]

Concerning the total angular momentum $|\mathbf{J}, m_j\rangle$, an analysis of the high symmetry points indicates that the conduction band has angular momentum $\mathbf{L}$=0 and spin $\mathbf{S}=\frac{1}{2}$. Thus, the point Γ_6 has total angular momentum $|1/2, \pm 1/2\rangle$. In the valence band, the angular momentum assumes $\mathbf{L}$=1 and spin $\mathbf{S}=\frac{1}{2}$, wherein $|3/2, \pm 3/2\rangle$, $|3/2, \pm 1/2\rangle$ correspond to HH and LH states in the Γ_8 point. In the same way, Γ_7 has $|1/2, \pm 1/2\rangle$ for the split-off states. For all the problems tackled in this Thesis, the quantization axis for the angular momentum is assumed along the crystallographic direction [001] and the basis ordering is given by: [27, 72, 75]

$$\left|\frac{1}{2},+\frac{1}{2}\right\rangle = \frac{1}{\sqrt{3}}\left|(X+iY)\downarrow\right\rangle + \frac{1}{\sqrt{3}}\left|Z\uparrow\right\rangle; \tag{2.18}$$

$$\left|\frac{1}{2},-\frac{1}{2}\right\rangle = -\frac{1}{\sqrt{3}}\left|(X-iY)\uparrow\right\rangle + \frac{1}{\sqrt{3}}\left|Z\downarrow\right\rangle; \tag{2.19}$$

$$\left|\frac{3}{2},+\frac{3}{2}\right\rangle = \frac{1}{\sqrt{2}}\left|(X+iY)\uparrow\right\rangle; \tag{2.20}$$

$$\left|\frac{3}{2},-\frac{3}{2}\right\rangle = \frac{1}{\sqrt{2}}\left|(X-iY)\downarrow\right\rangle; \tag{2.21}$$

$$\left|\frac{3}{2},+\frac{1}{2}\right\rangle = \frac{1}{\sqrt{6}}\left|(X+iY)\downarrow\right\rangle - \sqrt{\frac{2}{3}}\left|Z\uparrow\right\rangle; \tag{2.22}$$

$$\left|\frac{3}{2},-\frac{1}{2}\right\rangle = -\frac{1}{\sqrt{6}}\left|(X-iY)\uparrow\right\rangle - \sqrt{\frac{2}{3}}\left|Z\downarrow\right\rangle; \tag{2.23}$$

$$\left|\frac{1}{2},\frac{1}{2}\right\rangle = \frac{1}{\sqrt{3}}\left|(X+iY)\downarrow\right\rangle + \sqrt{\frac{1}{3}}\left|Z\uparrow\right\rangle; \tag{2.24}$$

$$\left|\frac{1}{2},-\frac{1}{2}\right\rangle = -\frac{1}{\sqrt{3}}\left|(X-iY)\uparrow\right\rangle + \sqrt{\frac{1}{3}}\left|Z\downarrow\right\rangle. \tag{2.25}$$

The Luttinger matrix and the hole states are presented in the appendix C. The Luttinger parameters can be obtained by first principles calculations or through experiments.

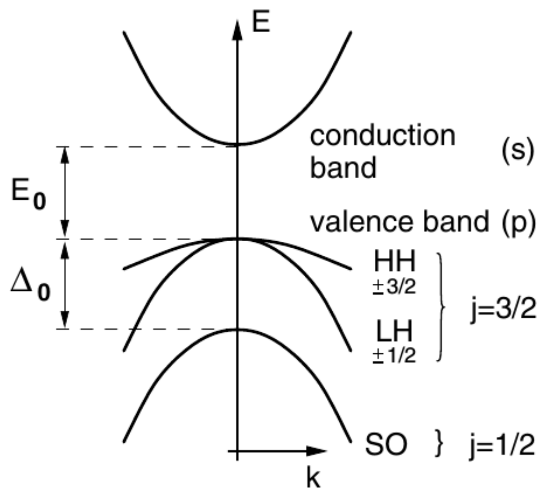

Figure 2.3: A schematic representation of the band structure for III-V semiconductors in the presence of spin-orbit interaction. The forbidden region E_0, between the conduction and valence bands, is also represented . The spin-orbit coupling introduces the energy gap, Δ_0, lifting the spin degeneracy between the heavy, light holes, and the split-off subbands.

In the Fig. 2.3, taken from Ref. [27], the band structure is represented for III-V semiconductors in the presence of the spin-orbit interaction. The spin-orbit lifts the spin degeneracy between the heavy, light holes, and the split-off subbands by including the energy gap, Δ_0, in the valence band.

2.3 Density functional theory

The exact diagonalization of the Schroedinger Eq. occurs only for simple systems, such as one particle under an external potential. However, for problems where the atomistic description is relevant, the many body effects must be included in the calculation in order to compute all interactions of the lattice. Furthermore, by increasing the number of atoms, the number of local minimums in the surface potential energy becomes higher. In this way, to determine the global minimum, all local minimums must be analyzed, increasing the computational efforts to model these systems. Thus, in the next section 2.3.1, we present the many body problem (MPB) and the computational treatment within the density functional theory (DFT).

2.3.1 The many body problem

In many cases, the interaction between charged particles in a solid can not be simplified to a single particle solution. A detailed study of interacting systems at a microscopic level needs a quantum mechanics description. The presence of many charged carriers in a solid characterizes the MBP, whose Hamiltonian is given by:

$$\begin{aligned} H(\mathbf{r},\mathbf{R}) &= \sum_{i=1}^{N}\left(-\frac{\hbar^2}{2m_e}\nabla_i^2\right) + \sum_{\alpha=1}^{M}\left(-\frac{\hbar^2}{2m_\alpha}\nabla_\alpha^2\right) + \frac{1}{8\pi\epsilon_0}\sum_{i=1}^{N}\sum_{\substack{j=1\\ i\neq j}}^{N}\frac{e^2}{|\mathbf{r}_i-\mathbf{r}_j|} \\ &+ \frac{1}{8\pi\epsilon_0}\sum_{\alpha=1}^{M}\sum_{\substack{\beta=1\\ \beta\neq\alpha}}^{M}\frac{Z_\alpha Z_\beta e^2}{|\mathbf{R}_\alpha-\mathbf{R}_\beta|} - \frac{1}{4\pi\epsilon_0}\sum_{\alpha=1}^{M}\sum_{i=1}^{N}\frac{Z_\alpha e^2}{|\mathbf{r}_i-\mathbf{R}_\alpha|}, \end{aligned} \tag{2.26}$$

where the first term corresponds to the electron kinetic energy, m_e is the electron mass, ∇_i the Laplacian acting on the electronic coordinates. The second term defines the kinetic energy of the nuclear motion, wherein m_α indicates the nuclei mass and ∇_α the Laplacian operating on the nuclear coordinates. The third term determines the interaction between the electrons i and j, wherein e is the fundamental charge and ϵ_0 is the vacuum permeability. The fourth term indicates the interactions between α and β nuclei, where Z_α and Z_β represent the nuclear atomic numbers, respectively. Finally, the last term denotes the interaction between electrons and nuclei. The difficulty in solving this Eq. is due to the large number of variables, because the MBP must consider the wavefunction of multielectronic atoms. In this way, it is interesting to adopt techniques and approaches for the most skillful resolution of the MBP, which allow to reduce the computational costs.

2.3.1.1 Born-Oppenheimer approximation

The mass of the nuclei is much larger than the mass of the electrons in a solid. Consequently, the speed of the electrons reaction to perturbations is greater than the nuclei. Therefore, the electronic movement becomes practically instantaneous in relation to the nuclear movement. For each nuclear position, the electrons are able rearrange themselves fast. Thus, the Born-Oppenheimer or Adiabatic Approximation (BOAP) considers the electronic and nuclear motion decoupled, [82]

$$\Psi_{el,k}(\mathbf{r}_i, \mathbf{R}_\alpha) = \Psi_{el}(\mathbf{r}_i, \mathbf{R}_\alpha)\Psi_k(\mathbf{R}_\alpha), \tag{2.27}$$

where $\mathbf{r}_i$ and $\mathbf{R}_\alpha$ are the electronic and nuclei coordinates, respectively, indicating different electronic positions for each nuclei configuration. Therefore, the electronic energy depends on the electrons and nuclei positions. Moreover, the total Hamiltonian is composed by the electronic and nuclei parts: $H(\mathbf{r}_i, \mathbf{R}_\alpha)= H_{el}(\mathbf{r}_i, \mathbf{R}_\alpha)+H_k(\mathbf{R}_\alpha)$. Thus,

$$H_{el}(\mathbf{r}, \mathbf{R}) = \sum_{i=1}^{N}\left(-\frac{\hbar^2}{2m_e}\nabla_i^2\right) + \frac{1}{8\pi\epsilon_0}\sum_{i=1}^{N}\sum_{\substack{j=1\\ i\neq j}}^{N}\frac{e^2}{|\mathbf{r}_i - \mathbf{r}_j|} - \frac{1}{4\pi\epsilon_0}\sum_{\alpha=1}^{M}\sum_{i=1}^{N}\frac{Z_\alpha e^2}{|\mathbf{r}_i - \mathbf{R}_\alpha|}, \tag{2.28}$$

is the electronic Hamiltonian. The nuclei is under the mean field originated by the electrons, wherein the electronic energy is the potential energy for the nuclei. The nuclei Hamiltonian is written as:

$$H_k(\mathbf{R}_\alpha) = \sum_{\alpha=1}^{M}\left(-\frac{\hbar^2}{2m_\alpha}\nabla_\alpha^2\right) + \frac{1}{8\pi\epsilon_0}\sum_{\alpha=1}^{M}\sum_{\substack{\beta=1\\ \beta\neq\alpha}}^{M}\frac{Z_\alpha Z_\beta e^2}{|\mathbf{R}_\alpha - \mathbf{R}_\beta|}. \tag{2.29}$$

In addition, the solution of the nuclei part includes the vibrational, translational, and rotational motions. Thus, when the electronic and vibrational states are strongly coupled, the BOAP loses its validity. [83, 84] However, the many electrons treatment prevents its analytical solution. In this context, some approximations were proposed to overcome the many electrons problem, such as the wavefunction methods of Hartree and Hartree-Fock. [85, 86] The Hartree method consists in a tentative multielectronic wavefunction written as function of the monoelectronic orbitals, neglecting the electronic and correlation effects, overestimating the energy of the system due to the Hartree potential. Fock and Slater proposed an antisymmetric wavefunction written as function of the atomic orbitals in the Slater determinant, satisfying the Pauli Principle and including the electronic exchange. However, in the Hartree-Fock self-consistent method, the Coulomb integral cancels exactly the exchange term for the same orbital. In order to improve the Hartree-Fock method, new wavefunctions methods were proposed, [87] although the high computational efforts become an obstacle to perform larger calculations.

2.3.2 Density functional theory

The density functional theory (DFT) is an alternative approach to the wavefunction methods. [88, 89] DFT uses the electronic density of the system to emulate the electronic structure of the materials. DFT is widely used because of the smaller computational cost compared to the wavefunction methods. Thus, it is feasible to treat larger systems using DFT. The first proposal was introduced by Thomas-Fermi (TF) model, [90, 91] where the total energy of the system is given by the electronic density functional of non-interacting homogeneous electron gas, leading to inaccuracies in the description of the electronic distribution. In TF model, the space is divided into small 3D cubes containing a fixed number of fermions with independent behaviors. For small volumes, the TF model introduces a kinetic energy functional, wherein an important advance in the density functional theory was given: the local density approximation (LDA).

2.3.2.1 Hohenberg-Kohn theory

The modern *ab initio* theories began with the Hohenberg-Kohn (HK) [88] theory describing the non-homogeneous electrons gas, being the basis of the density functional theory. The purpose of the HK theory is to determine the ground state properties as functionals of the electronic density. The main idea of the HK approach is to show that any property of a system of many interacting particles can be determined as a functional of the ground state density. Thus, the two theorems of Hohenberg-Kohn consider N electrons under an external potential. Essentially, the Hohenberg-Kohn theorems allow to use the electronic density to find the state and the energy functional to describe exactly the ground state of the system. The theorems are described as follows: [88]

1. *The external potential V_{ext} is determined in a unique way, except by one constant, through the electronic density $\rho_0(\boldsymbol{r})$.*

    - Corollary: The many body wavefunctions for all states are determined by the obtained Hamiltonian of the system, except for a constant shift. In addition, all properties of the particle system are determined by knowing only the ground state density.

2. *For a given external potential, a universal functional for the total energy of the many body system, written in terms of the electronic density, can be determined. For any particular V_{ext}, the ground state of the particle system is obtained through the minimum value of the energy functional and the density that minimizes the functional is the exact density of the ground state.*

    - Corollary: Only the energy functional is enough to determine the exact density of the ground state. However, excited states must be obtained by another method.

Concerning the first theorem, two particle system under different external potentials can not lead to the same ground state of the electronic density. The possibility to determine the ground state of the system through the minimization of the energy functional given as a function of the electronic density allows to obtain the solution of the many particle system. However, the HK theorems do not specify how to obtain the electronic density or the basis for the constrution of the functionals. The implementation of the HK approach is given by the Kohn-Sham (KS) scheme, presented in the next section, wherein the original many body problem is replaced by an auxiliary independent particle system.

2.3.2.2 Kohn-Sham theory

In the Kohn-Sham (KS) strategy, [89] the MBP is replaced by an auxiliary system, assuming that the ground state density of the original system is equal to a chosen non-interacting system. In this context, it is interesting to map the fermionic interactions through a non-interacting system by adding a correction term to accurately determine the ground state energy. This leads to independent particle Eqs. for the non-interacting system with exact solution. The ground state energy of many particles can be obtained through the minimum energy functional:

$$E[\rho(\mathbf{r})] = \int \rho(\mathbf{r})V(\mathbf{r})d^3\mathbf{r} + F[\rho(\mathbf{r})], \tag{2.30}$$

where $F[\rho(\mathbf{r})] = T[\rho(\mathbf{r})] + V_{ee}[\rho(\mathbf{r})]$ represents the kinetic energy and the electronic potential, respectively. The introduction of the kinetic energy functional of the non-interacting system ($T_n[\rho(\mathbf{r})]$) in the Kohn-Sham scheme leads to the addition of the exchange and correlation ($E_{xc}[\rho(\mathbf{r})]$) and the Hartree ($V_H[\rho(\mathbf{r})]$) terms in the functional $F[\rho(\mathbf{r})]$. Thus,

$$F[\rho(\mathbf{r})] = T_n[\rho(\mathbf{r})] + V_H[\rho(\mathbf{r})] + E_{xc}[\rho(\mathbf{r})]. \tag{2.31}$$

The functional (2.31) can be considered universal because it is independent of the system. The Hartree potential describes the classical interactions between the electrons. The exchange and correlation energy is defined by:

$$E_{xc}[\rho(\mathbf{r})] = T[\rho(\mathbf{r})] - T_n[\rho(\mathbf{r})] + V_{ee}[\rho(\mathbf{r})] - V_H[\rho(\mathbf{r})]. \tag{2.32}$$

In the KS scheme, the Euler Eq. $\mu = v(\mathbf{r}) + \frac{\delta F}{\delta \rho \mathbf{r}}$, where μ is the Lagrange multiplier, becomes $\mu = v_{eff} + \frac{\delta T_s}{\delta \rho(\mathbf{r})}$. The KS effective potential (v_{eff}) and exchange-correlation potential $\left(v_{xc} = \frac{\delta E_{xc}}{\delta \rho(\mathbf{r})}\right)$ are written as follows:

$$v_{eff}(\mathbf{r}) = v(\mathbf{r}) + \int \frac{\rho(\mathbf{r}')}{|\mathbf{r}-\mathbf{r}'|} d^3\mathbf{r}' + v_{xc}. \tag{2.33}$$

Thus,

$$E[\rho(\mathbf{r})] = T_n[\rho(\mathbf{r})] + \int \rho(\mathbf{r})V(\mathbf{r})d^3\mathbf{r} + E_{xc}[\rho(\mathbf{r})] + \frac{1}{2}\int\int \frac{\rho(\mathbf{r}')\rho(\mathbf{r})d^3\mathbf{r}d^3\mathbf{r}'}{|\mathbf{r}-\mathbf{r}'|} \tag{2.34}$$

and the electronic density $\rho(\mathbf{r}) = \sum_i^N \sum_s |\Psi_i(\mathbf{r}, s)|^2$. In this way, the energy is expressed in terms of N orbitals. Therefore, the ground state of an auxiliary system of non-interacting particles represents the ground state of the real system, correlating the many interaction particles and non-interaction particles by adding an exchange and correlation term defined in Eq. (2.32). In addition, the orthonormality of the wavefunctions $\left(\int \Psi_i^*(\mathbf{r})\Psi_j(\mathbf{r})d\mathbf{r} = \delta_{ij}\right)$ ensures that the orbitals occupations are given by:

$$N = \int \rho(\mathbf{r})d^3(\mathbf{r}). \tag{2.35}$$

The functional $\Omega[\Psi_i(\mathbf{r})]$ is defined for N orbitals in a non-interacting KS system,

$$\Omega[\Psi_i(\mathbf{r})] = E[\rho(\mathbf{r})] - \sum_i^N \sum_j^N \epsilon_{ij} \int \Psi_i^*(\mathbf{r})\Psi_j(\mathbf{r})d^3\mathbf{r}, \tag{2.36}$$

where $E[\rho]$ is the energy functional, Ψ_i are the KS orbitals and ϵ_{ij} are the Lagrange multipliers. Performing $\delta\Omega[\{\Psi_i(\mathbf{r})\}] = 0$ in Eq. (2.36) in order to obtain the minimum energy leads to the resolution of the Schroedinger Eq. under an effective potential:

$$h_{eff}(\mathbf{r})\Psi_i(\mathbf{r}) = \left[-\frac{1}{2}\nabla^2(\mathbf{r}) + v_{eff}(\mathbf{r})\right]\Psi_i(\mathbf{r}) = \sum_j^N \varepsilon_{ij}\Psi_j(\mathbf{r}), \tag{2.37}$$

where $h_{eff}(\mathbf{r})$ is the one electron Hamiltonian under an effective potential $v_{eff}(\mathbf{r})$ determined from the charge density, mapping the non-interacting system and leading to the addition of the exchange and correlation (v_{xc}) term. The wavefunction of the many interacting particles can be written according to the formalism of the Slater determinant, $\Psi_s(\mathbf{r}) = \frac{1}{\sqrt{N!}} det[\Psi_1\Psi_2\Psi_3 \ldots \Psi_N]$. Thus, the diagonalization of the Hermitian matrix (2.37) allows to obtain the KS orbitals:

$$\left[-\frac{1}{2}\nabla^2(\mathbf{r}) + v_{eff}(\mathbf{r})\right]\Psi_i(\mathbf{r}) = \epsilon_i\Psi_i(\mathbf{r}); \tag{2.38}$$

$$v_{eff}(\mathbf{r}) = v(\mathbf{r}) + \int \frac{\rho(\mathbf{r}')}{|\mathbf{r}-\mathbf{r}'|}d^3\mathbf{r}' + v_{xc}(\mathbf{r}); \tag{2.39}$$

$$\rho(\mathbf{r}) = \sum_i^N \sum_s^N |\Psi_i(\mathbf{r}, s)|^2. \tag{2.40}$$

The KS Eqs. must be solved self-consistently, e.g., by a interactive method, wherein the total energy of the system is obtained from the KS scheme:

$$E = \sum_i^N \varepsilon_i - \frac{1}{2}\int \frac{\rho(\mathbf{r})\rho(\mathbf{r})}{|\mathbf{r}'-\mathbf{r}'|}d(\mathbf{r})d(\mathbf{r}') + E_{xc}[\rho] - \int v_{xc}(\mathbf{r})\rho(\mathbf{r})d(\mathbf{r}), \tag{2.41}$$

where $\sum_i^N \varepsilon = T_s[\rho(\mathbf{r})] + \int v_{eff}(\mathbf{r})\rho(\mathbf{r})d\mathbf{r}$. Thus, if the exchange and correlation functional is determined, the exact ground state energy for an interacting particle system can be obtained by solving the KS Eqs. for non-interacting particles. Introducing N orbitals in the KS scheme implies in the solution of N Eqs. iteratively instead of only one Eq. for charge density in the TF model. Note that the KS Eqs. are open for improvements through better proposals of the exchange and correlation term E_{xc}.

2.3.2.3 Khon-Sham self-consistent cycle

As previously mentioned, the HK theorems ensure that minimizing the functional of the electronic density, the exact energy of the ground state is determined, defining the effective potential in a unique form. The KS scheme allows to obtain the properties of the real system treating the independent particle system. The Schroedinger-like independent particles Eqs. must be solved considering the effective potential and the charge density. [92] Thus, to obtain an effective potential, the charge density must be determined. Therefore, the KS Eqs. must be solved self-consistently, as follows:

1. Proposition of an initial charge density ($\rho\uparrow(\mathbf{r}), \rho\downarrow(\mathbf{r})$) for the ground state;

2. Determination of the KS effective potential (2.39) for the charge density proposed previously;

3. In order to determine the KS orbitals, the Schroedinger Eq. under the effective potential is solved and the new wavefunctions are obtained;

4. Determination of the new charge density ($\rho\uparrow(\mathbf{r}), \rho\downarrow(\mathbf{r})$) using the KS orbitals obtained in the previous step;

5. The new charge density is compared with the initial proposal by schematic convergence tests. If the new charge density satisfies the convergence criterion, the self-consistent cycle stop. Otherwise, the cycle returns to the first the step.

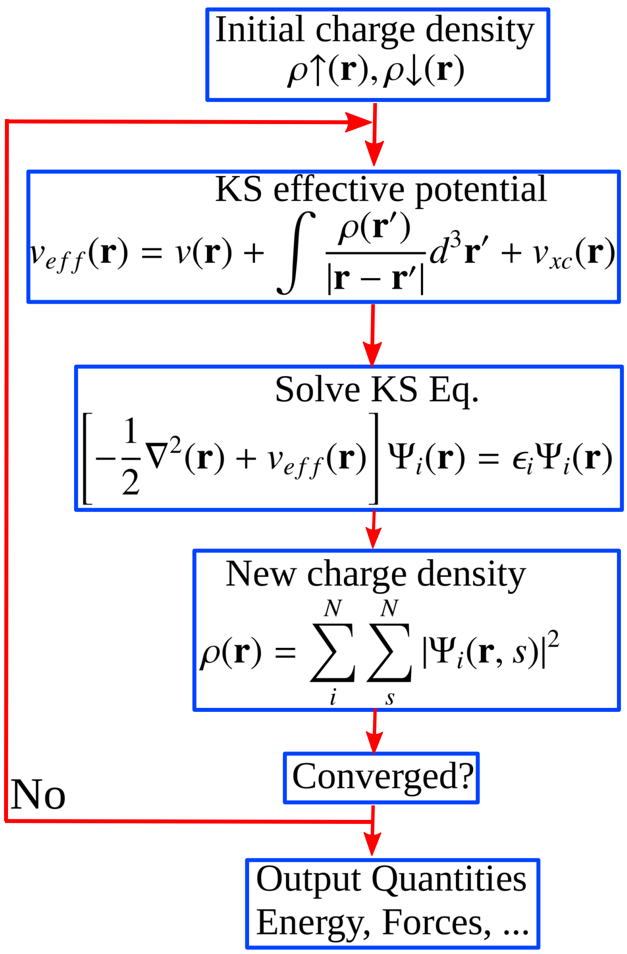

Figure 2.4: Visual representation of the KS self-consistent cycle. An initial charge density is proposed. The effective potential is obtained to solve the Kohn-Sham Eq. in order to determine the new wavefunctions and charge density. The cycle runs until the convergence of the charge density.

A visual representation of the KS self-consistent cycle is given in the Fig. 2.4, adapted from the Ref. [92]. At the end of the KS self-consistent process, [93] the KS orbitals, eigenvalues, and the ground state properties are determined.

2.3.3 Exchange and correlation functionals

The main challenge in the KS scheme is to improve the precision of the exchange and correlation functionals (XC), since there is no technique for its determination. The XC functionals includes the electronic exchange and correlation, difference between the kinetic energies of the non-interacting and real system, the correction of the self-interaction due to the classical Coulomb potential expressed in the Hartree term. Intensive efforts have been made in order to find the more precise functional. [94] In this context, the Jacob's ladder, proposed by Perdew, [95] is a biblical analogy to determine a *divine* exchange and correlation functional. The ladder comes from the wavefunction methods, such as the Hartree-Fock approach, till the heaven, an exact exchange and correlation functional which reaches the higher chemical accuracy.

The Hartree-Fock method is the first step in the Jacob's ladder because neglects the dynamic or static electronic correlation effect. [96] The next step of the Jacob's ladder represents the first proposal of the exchange and correlation functionals within the density functional theory framework, the local density approximation (LDA), studied in the next section. In addition, several works have proposed XC functionals, however the computational cost and the implementation are barriers to overcome. The semi-empirical functionals are based on the parametrization of the experimental results associated with *ab initio* calculations with high precision. The non-empirical functionals are based on the theoretical ideas to improve the accuracy of calculations of the XC functionals. [96–98]

2.3.3.1 Local density approximation

The local density approximation (LDA) was introduced by Kohn-Sham in his important paper, [89] in the same article where the self-consistent Eqs. were proposed. In the LDA approach, the electron density is described in the limit of the homogeneous electron gas, where the exchange and correlation effects are locally applied. The electronic density varies smoothly in the vicinity of a point $\mathbf{r}$, wherein the exchange and correlation energy is a simple integral in whole space. Each point of the electron density is assumed to be the same as in the homogeneous electron density. A more generalized approach than the LDA is the local spin density approximation (LSDA). The LSDA includes the spin-polarized systems in the calculation. The LSDA describes the electronic density in terms of spin character[1] wherein the total density is given by $\rho(\mathbf{r}) = \rho(\mathbf{r})\uparrow + \rho(\mathbf{r})\downarrow$. The LDA depends only on local density,

$$E_{\mathrm{xc}}^{\mathrm{LDA}}[\rho(\mathbf{r})] = \int \rho(\mathbf{r})\varepsilon_{\mathrm{xc}}[\rho(\mathbf{r})]d^3\mathbf{r}, \tag{2.42}$$

where $\varepsilon_{\mathrm{xc}}[\rho(\mathbf{r})]$ is the exchange and correlation energy. Due to the uniform local density of the electron gas in the LDA approach, the exchange energy can be determined analytically while the correlation energy must be defined by interpolation or Monte Carlo calculations. Thus,

$$E_{\mathrm{xc}}^{\mathrm{LDA}}[\rho(\mathbf{r})] = E_{\mathrm{x}}^{\mathrm{LDA}}[\rho(\mathbf{r})] + E_{\mathrm{c}}^{\mathrm{LDA}}[\rho(\mathbf{r})], \tag{2.43}$$

with $E_{\mathrm{x}}^{\mathrm{LDA}}[\rho(\mathbf{r})] = -\frac{3}{4}\left[\frac{3\rho(\mathbf{r})}{\pi}\right]^{\frac{1}{3}}$. Thus, if the exchange[2] and correlation is a universal functional and are completely determined in the limit of the homogeneous electron gas, the ground state properties can be determined using the LSDA[3] approach. However, the difficulty to determine the correlation energy provides interesting works. Ceperly and Alder [99] verified the correlation energy by interpolating the Green's functions. In the same way, Vosko [100] and Perdew [101] analyze the correlation term improving the calculations in the local spin density approximation. Concerning the accuracy of the description, the LDA functionals underestimate the exchange and overestimate the correlation energy, canceling the errors. A more precise description is given by the generalized gradient approximation (GGA), studied in the next section.

2.3.3.2 Generalized gradient approximation

The improvements in the description of the systems wherein the electronic density is non-homogeneous are given by the generalized gradient approximation (GGA). In the

[1] For unpolarized spins calculations, the system is describe by $\rho\uparrow(\mathbf{r}) = \rho\downarrow(\mathbf{r}) = \frac{\rho(\mathbf{r})}{2}$.
[2] The exchange functional is the same of the Thomas-Fermi model.
[3] Due to the homogeneous properties of the electron gas, the exchange and correlation of the LDA are considered a short range interaction.

GGA, the electronic density gradient is included. The electronic density can vary and the exchange-correlation is not only dependent on the LDA, but also of its local gradient. The GGA corrects the errors of the non-homogeneity of the electronic system. Therefore, in this method, the electronic density and its derivatives are included in the formulation of the exchange and correlation energy, which is given by:

$$E_{\mathrm{xc}}^{\mathrm{GGA}}[\rho(\mathbf{r})] = \int f(\rho(\mathbf{r}), |\nabla\rho(\mathbf{r})|)d\mathbf{r} = \int \rho(\mathbf{r})E_{xc}^{GGA}[\rho(\mathbf{r}), |\nabla\rho(\mathbf{r})|]d\mathbf{r}, \tag{2.44}$$

where E_{xc}^{GGA} is composed by the exchange E_{x}^{GGA} and correlation E_{c}^{GGA} energy in the GGA approach. The GGA formulation used in this Thesis was proposed by Perdew, Burke and Ernzerhof (PBE). [102] The exchange energy is given by:

$$E_{x}^{PBE}[\rho(\mathbf{r})] = \int \rho(\mathbf{r})E_{x}^{LDA}(\rho(\mathbf{r}))F_{x}(s)d\mathbf{r}, \tag{2.45}$$

where $F(\rho(\mathbf{r}))$ is an intensification factor related to the semi-locality of the PBE functional, as follows:

$$F_{x}(s) = 1 + \kappa - \frac{\kappa}{1 + \frac{\mu}{\kappa}s(\mathbf{r})^{2}}, \tag{2.46}$$

with $\mu = \frac{\beta\pi^2}{3}$ the effective coefficient for the exchange functional, $\beta = 0.066725$, $\kappa = 0.804$ and $s(\mathbf{r}) = \frac{|\nabla\rho(\mathbf{r})|}{2k_F\rho(\mathbf{r})}$ the density gradient, where $k_F = [3\pi^2\rho(\mathbf{r})]^{1/3}$ is the Fermi wave vector. The correlation energy is given by:

$$E_{c}[\rho(\mathbf{r})]^{PBE} = \int \rho(\mathbf{r})[\varepsilon_{c}^{LDA}(\rho(\mathbf{r})) + H_{c}^{PBE}(r_s, t)]d\mathbf{r}, \tag{2.47}$$

where

$$H(r_s, t) = \gamma ln\left[1 + \frac{\beta}{\gamma}t^2\frac{1 + At^2}{1 + At^2 + A^2t^4}\right] \tag{2.48}$$

with $\gamma = \frac{1-ln2}{\pi^2}$, $A(r_s) = \frac{\beta}{\gamma}(\gamma e^{-E_c^{LDA}/\gamma} - 1)^{-1}$, $t(\mathbf{r}) = \frac{|\nabla\rho(\mathbf{r})|}{2k_s\rho(\mathbf{r})}$ the density gradient and $k_s = \sqrt{4k_F/\pi}$

the Thomas-Fermi wave number. [103] The PBE functionals are based on the Perdew-Wang functional of 1991 (PW91), [101, 104] presenting improvements in the description of the linear response of the uniform electron gas. In the GGA formulation, some mathematical parameters are adjusted for the reproduction of the experimental data. A new proposal for the PBE functional was introduced by Zhang e Yang, [105] originating the new functional *revised-Perdew Burke e Ernzerhof* (revPBE). Another suggestion proposes a new form for chemical energy, the RPBE functional. [106] The idea of the functional *Perdew-Burke-Ernzerhof revised for solids* (PBEsol or PS) is to correct some deviations of the gradient approximation for solids, [107] having a higher accuracy in the determination of the exchange energy due to the more efficient description of some mathematical expansions. The functional initially proposed by Armiento and Mattsson in 2005 (AM05) is related to the parametrization of the Airy electron gas with appropriate gradient expansion. [108, 109]

In order to increase the accuracy of the DFT calculations, a new class of exchange and correlation functionals was proposed: the hybrid functionals. [110–113] These functionals combine the Hartree exact exchange functional with an exchange and correlation functional within the DFT approach[4]. The improvement in these functionals determines a better accuracy in the description of the properties of solids, such as the bonding energies, lattice parameters and semiconductor band gap energy. However, the computational cost of the hybrid functionals is higher than the GGA and LDA formulations. Becke proposed a new mixing of the Hartree exact exchange, improving the accuracy of thermochemical calculations. [110, 112] The B3LYP hybrid functional considers the Becke B88 exchange, Perdew Wang (PW91) correlation and the Hartree exchange functional. [114, 115] The hybrid PBE0 functional have the full correlation energy of Perdew-Burke-Ernzerhof (PBE) and the exchange functional is a fraction of the PBE and HF functionals, [116, 117]

$$E_{xc}^{PBE0} = \frac{1}{4}E_x^{HF} + \frac{3}{4}E_x^{PBE} + E_c^{PBE}, \tag{2.49}$$

where E_x^{HF} is the Hartree exchange energy, E_x^{PBE} and E_c^{PBE} are the exchange and correlation energies of the PBE functional, defined by Eqs. (2.45) and (2.47), respectively. By improving the PBE0 functional, Heyd-Scuseria-Ernzerhof proposed the HSE06 functional, [118–120] where the exchange term is separated in a short and long range through the expression:

[4]For this reason they are called hybrids.

$$\frac{1}{r} = \frac{erfc(\omega r)}{r} + \frac{erf(\omega r)}{r}, \tag{2.50}$$

where $erf(\omega r)$ is the error function, with $erfc(\omega r) = 1 - erf(\omega r)$. The first and second terms in the Eq. (2.50) are related with the short and long range, respectively. Thus, ω is an adjustable parameter, allowing to treat the exchange energy in the HSE06 functional,

$$E_{xc}^{HSE} = aE_x^{HF,SR}(\omega) + (1-a)E_x^{PBE,SR}(\omega) + E_x^{PBE,LR}(\omega) + E_c^{PBE}, \tag{2.51}$$

where $E_x^{HF,SR}(\omega)$ is the Hartree short range exchange energy, $E_x^{PBE,SR}(\omega)$ and $E_x^{PBE,LR}(\omega)$ are the short and long range components of the PBE exchange functional. The standard value of $a = 1/4$. As ω is adjustable, defining $\omega = 0$ we obtain the PBE0 functional and $\omega \to \infty$ the PBE functional. [118–120]

2.3.3.3 On site Coulomb interaction: L(S)DA+U

In previous sections, we described the exchange and correlation term within the KS approach, wherein the LDA and GGA formulations can present inaccuracies in the description of some properties of solids, such as the lattice parameter and the energy gap of the semiconductor materials. Alternatively to the high computational cost of the hybrid calculations, the Hubbard model is introduced in DFT calculations in order to correct the imperfections of the functionals. Hubbard's approach was introduced by John-Hubbard to study the electronic correlations in narrow energy bands within the many-particle interacting system. [121–126] The one-dimensional Hamiltonian of the Hubbard model is given by: [127, 128]

$$H_H = -t\sum_{j,\sigma}^{L}(c_{j+1,\sigma}^{\dagger}c_{j,\sigma} + h.c.) + U\sum_{j=1}^{L} n_{j,\uparrow}n_{j,\downarrow}, \tag{2.52}$$

where j is the atomic orbital of one-dimensional lattice, $c_{j,\sigma}^{\dagger}$, $c_{j,\sigma}$ and $n_{j,\sigma}$ are the electronic creation, annihilation and number of electrons of spin σ on site j, respectively. U and t are real numbers, representing the local Coulomb repulsion between electrons of the same orbital and the hopping amplitude between the j and $j+1$ sites, respectively. In addition, there is a probability for the hopping occurrence between a given site and its second neighbor. [129, 130] For a particular case $t << U$, the electrons can not jump around because their energy is insufficient to overcome the repulsion of other electrons in neighboring positions, corresponding to the insulator system. Otherwise, $t >> U$, the system becomes metallic.

As mentioned above, the limitations of the exchange and correlation functionals to describe the long-range interactions in non-homogeneous systems and delocalization of the electronic states, usually the d and f orbitals which are strongly correlated, lead to inclusion of a correction in the functionals. The LDA+U and GGA+U are the local density approximation and the generalized gradient approximation with U correction within the Hubbard model. The basic idea of the LDA+U and GGA+U correction is to use the Hubbard model to describe the strongly correlated electron states, where the other electronic states are calculated without any correction. [131–138] The U indicates the correction applied in the studied state to increase the accuracy of the calculation, being an adjustable parameter during the *ab initio* calculation. The Hubbard U potential represents the energy to introduce two electrons at same site, written as follows:

$$U = E(d^{n+1}) + E(d^{n-1}) - 2E(d^{n}), \tag{2.53}$$

where $n \leq 9$ are the number of d orbitals. Anderson proposed an independent study of electrons in d and f orbitals. [139] Thus, in 1998 Dudarev presented the following correction within the LDA approach to compute the total energy: [140]

$$\begin{aligned} E^{L(S)DA+U}[\rho^{\sigma}(\mathbf{r}), \{n^{\sigma}\}] &= E^{L(S)DA}[\rho^{\sigma}(\mathbf{r})] + \frac{(U-J)}{2}\sum_{\sigma}\left[\left(\sum_{m_1} \nu^{\sigma}_{m_1,m_1}\right)\right. \\ &- \left.\left(\sum_{m_1,m_2} \nu^{\sigma}_{m_1,m_2}\nu^{\sigma}_{m_2,m_1}\right)\right]. \end{aligned} \tag{2.54}$$

The exchange, J, and Coulomb, U, parameters must be adjusted in agreement with the experiment to describe the localized orbitals. The orbitals can be expressed in terms of the Slater integrals within the Hubbard correction, as implemented in the VASP package[5], given by:

[5]The Vienna *ab initio* Simulation Package - VASP. [141]

- p-electrons: $F^0 = U$; $F^2 = 5$J;
- d-electrons: $F^0 = U$; $F^2 = \frac{14}{1+0.625}J$; $F^4 = 0.625F^2$;
- f-electrons: $F^0 = U$; $F^2 = \frac{6435}{286+195\cdot 0.668+250\cdot 0.494}$; $F^4 = 0.668F^2$; $F^6 = 0.49F^2$.

Therefore, the L(S)DA+U method is determined by the choice of correction applied in the analyzed orbital.

2.3.3.4 van der Waals corrections

The van der Waals[6] (vdW) forces are the long-range cohesive attractions[7] between the atoms along the intermolecular separations. A deep investigation of the vdW corrections is crucial to investigate of the adsorption properties of the metal atoms. [143–145] The vdW forces have a quantum nature and are originated from the fluctuations of the electronic charge density due to the formation of the instantaneous dipole between the atoms. [146] London considers that electronic oscillations lead to deformations in the density. The instantaneous dipole moment can change the electronic density around other atoms. London determined the interaction between two spherically symmetric atoms at large distances (R) as follows: [147]

$$V^{disp} = \frac{C}{R^6}, \tag{2.55}$$

where C contains the physical constants of the system. The density functional theory does not include the dispersion forces in the formulation of the exchange and correlation functionals. Long-range interactions are not enough described by the *ab initio* calculations due to the short-range and semi-local nature of the GGA exchange and correlation functionals, [148] failing in the description of the dispersion forces. [149] Thus, several works proposed to include the vdW forces within the *ab initio* calculations. [150, 151] In order to include the vdW corrections in DFT functionals, the strategy is to add the dispersion-like (E_{disp}) contribution in the DFT energy (E_{DFT}) for each pair of atoms:

[6] The vdW forces are also called dispersion interactions or London forces.
[7] In 1930, London study the relation between the electronic correlation and long range forces. [142]

$$E_{tot} = E_{DFT} + E_{disp}, \tag{2.56}$$

where E_{tot} is the DFT total energy calculation. The dispersion energy is defined by the expansion:

$$E_{disp} = -S \sum_{A,B}^{N_{atom}} \sum_{L} \frac{C_{6AB}}{RAB^6} f_{damp}(R_{AB}), \tag{2.57}$$

where S is a scaling factor[8] applied uniformly to every pair of atoms, which depends on the functional used in the calculation. In turn, R_{AB} is the distance between the A and B atoms, C_{6AB} are the dispersion coefficients, which follows the relation $C_{6AB} = \sqrt{C_{6A}C_{6B}}$ and $f_{damp}(R_{6AB})$ is the damping function used to avoid unphysical solutions at short distances, [152–155]

$$f_{damp} = (R_{AB}, R^0_{AB}) = \frac{1}{1 + e^{-d\left(\frac{R_{AB}}{s_R R^0_{AB}} - 1\right)}}, \tag{2.58}$$

where R^0_{AB}=$R^0_A + R^0_B$. The parameter d adjusts the damping function and s_R is an empirical parameter that determines the magnitude of the vdW correction for a functional used in the calculation. The van der Waals radius is defined as half of the distance between two atoms. Therefore, the challenge is to determine the dispersion constants in Eq. (2.55) in order to choose the best method for the vdW correction for each system. The coefficient C_{6AB} is defined as follows: [153]

$$C_{8AB} = \frac{2C_{6AA}C_{6BB}}{\frac{\alpha^B_0}{\alpha^A_0} C_{6AA} + \frac{\alpha^A_0}{\alpha^B_0} C_{6BB}}, \tag{2.59}$$

where α^A_0 and α^B_0 are the polarizabilities for A and B free-atoms, respectively. The dispersion coefficients C_{6AA} and C_{6BB} are given by:

$$C_{6AA} = \left[\frac{V^A_{eff}}{V^A_{free}}\right]^2 (C_{6AA})^{free}. \tag{2.60}$$

[8]The scaling factor usually used is $\frac{1}{2}$.

In Eq. (2.60), the fraction represents the ratio between the effective volume, V^A_{eff}, and the volume of the free-atom, V^A_{free}, obtained by the Hirshfeld partitioning of the electronic density. The total energy of the system can be found by replacing Eq. (2.57) in (2.56). Eqs. (2.57)-(2.58) are related to the DFT-D2 correction proposed by Grimme. [155] Improvements were presented in the DFT-D3 method, [154] where the coefficients are geometry dependent. Within DFT-D3 method, the dispersion energy (2.57) is written as follow:

$$E_{disp} = -S \sum_{A,B}^{N_{atom}} \sum_{L} \frac{C_{6AB}}{R^6_{AB}} f_{damp,6}(R_{AB}) + \frac{C_{8AB}}{R^8_{AB}} f_{damp,8}(R_{AB}). \tag{2.61}$$

The damping function in DFT-D3 method is given by:

$$f_{d,n}(R_{AB}) = \frac{s_n}{1 + 6\left(\frac{R_{AB}}{s_{R,n} R_{0AB}}\right)^{-\alpha_n}}, \tag{2.62}$$

where $R_{0AB} = \sqrt{\frac{C_{8AB}}{C_{6AB}}}$, α_6, α_8, $s_{R,8}$, are fixed values and s_6, s_8 and $s_{R,6}$ are adjustable parameters dependent on the choice of the exchange and correlation functional. Becke and Johnson (BJ)[9] proposed an alternative approach to the damping function, [156]

$$f_{d,n}(R_{AB}) = \frac{s_n R^n_{AB}}{R^n_{AB} + (a_1 R_{0AB} + a_2)^n}, \tag{2.63}$$

where a_1, a_2, s_6, s_8 are adjustable parameters.

2.3.4 Monopole, dipole and quadrupole correction in solids

Within the density functional theory framework, the convergence of total energy depends, among other factors, on the size of the periodic cell, the number of atoms, monopole, dipole and quadrupole formations. The periodic boundary conditions (PBC) are compatible with the plane wave expansion. Non-periodic calculations provide divergences in the results between finite sized and infinitely large supercells due to spurious interactions of the structure with its images in neighboring supercells. For large supercells, $L \to \infty$, where L is the linear dimension of the cell, the convergence is determined by long-range forces, which

[9] This method is called BJ-damping.

includes the electrostatic forces. Therefore, the understanding of electrostatic properties in PBC's plays a key role in the convergence of defective solids in the limit of infinitely large supercells. Thus, the computational efforts increase proportionally to the volume of the cell. Therefore, the corrections of the electrostatic forces used in the supercell during the *ab initio* calculation provides a more precise DFT investigation and a faster energy convergence. [157, 158] The electrostatic potential using PBC is written as a function of all N cells:

$$\phi(\mathbf{r}) = \int_{sample} d^3\mathbf{r}' \frac{\rho(\mathbf{r}')}{|\mathbf{r} - \mathbf{r}'|} = \sum_{l} \int_{cell} d^3\mathbf{r}' \frac{\rho(\mathbf{r}')}{|\mathbf{r} - \mathbf{r}' + l|}, \tag{2.64}$$

where $\mathbf{r}$ is an arbitrary point in the sample. Setting $\mathbf{r}$ at the origin of the lattice and extending the sum of Eq. (2.64) to infinity, the convergence is obtained by the contributions of distant spherical shells. In this limit, the asymptotic form of Eq. (2.64) is written as $q_n P_n(cos\theta)|l|^{-(n+1)}$, where q is the charge and P_n are the Legendre functions. [158]

Concerning the aperiodic calculations in solids, such as the point defects, the charge density, $\rho(\mathbf{r})$, is given by the sum of periodic ($\rho_p(\mathbf{r})$) and aperiodic ($\rho_{ap}(\mathbf{r})$) charge density, where $\rho_p(\mathbf{r} + \mathbf{l}) = \rho_p(\mathbf{r})$. The aperiodic density and its multipole expansion depends on the dimensions of the cell, introducing inaccuracies in the calculation due to the interaction between the cell and its neighbors. In order to avoid this imprecision, the authors in Ref. [158] showed the correction for the charged aperiodic cells:

$$E = E_0 - \frac{q^2\alpha}{2L\varepsilon} - \frac{2\pi qQ}{3L^3\varepsilon} + O(L^{-5}), \tag{2.65}$$

where α is the Madelung constant, q the charge, ε the dielectric constant and Q the second radial moment.

2.3.5 Computational approach

In a solid, the electrons nearest to the nuclei are called core electrons and the farthest electrons from the nuclei are known as valence electrons. Core electrons have the strongest interaction with the nuclei than the valence electrons. Usually, the core electrons do not participate in chemical bonds, contrasting with the valence electrons, wherein the chemical bonds introduce perturbations in their states. Thus, the optical and electronic properties of solids depend on the valence electrons. The wavefunctions vary and oscillate faster near the nuclei due to the strongest electron-nuclei interaction. Therefore, the low computational cost obtained with the plane waves within the Bloch theorem can not be applied to the core region due to the high number of waves required. In order to overcome this barrier, the fast oscillations of the wavefunctions in the core region are studied in the Projector Augmentation Waves (PAW) approach.

2.3.5.1 Planes waves

The choice of the basis for the expansion of wavefunctions plays a key role to model the many body system. Several basis for the wavefunctions were proposed, such as the combination of the atomic orbitals. [159] In this Thesis we employed the plane waves, [160] wherein the description of periodicity of crystal follows the Bloch's theorem, [2, 58]

$$\psi_{\mathbf{k}}(\mathbf{r} + \mathbf{R}_L) = e^{i\mathbf{k}\cdot\mathbf{R}_L} u_{\mathbf{k}}(\mathbf{r}), \tag{2.66}$$

where $\mathbf{k}$, $\mathbf{R}_L$ and $u_{\mathbf{k}}(\mathbf{r})$ are the crystal momentum, the direct lattice vector and the function with the same periodicity of the crystal, [161]

$$u_{\mathbf{k}}(\mathbf{r}) = u_{\mathbf{k}}(\mathbf{r} + \mathbf{R}_L). \tag{2.67}$$

Eqs. (2.66)-(2.67) emphasize the possibility of changing the infinite number of the wavefunctions by a finite number of periodic wavefunctions. Due to the irreducible representation of the Brillouin zone, the $\mathbf{k}$-points can be studied independently. During the *ab initio* calculation, the $\mathbf{k}$-points can be given separately. The $\mathbf{k}$ vectors are defined within the first Brillouin zone, where the direct lattice vectors can be expressed by the reciprocal lattice:

$$\mathbf{b}_i \cdot \mathbf{u}_j = 2\pi\delta_{ij}, \qquad i, j = 1, 2, 3. \tag{2.68}$$

The planes waves are naturally eigenfunctions of the kinetic energy operator. Introducing a small perturbation $V(\mathbf{r})$ in the system, the wavefunctions will be a mixture of plane waves. Therefore, the higher accuracy of calculation is achieved by increasing the number of plane waves. Replacing Eq. (2.67) in Eq. (2.38), the result is:

$$\left[\frac{\hbar^2}{2m_e}\left(\nabla^2 + \mathbf{k}\right) + V^{KS}(\mathbf{r})\right] u_k(\mathbf{r}) = \varepsilon_{\mathbf{k}} u_k(\mathbf{r}), \tag{2.69}$$

where m_e is the electron mass and $u_k(\mathbf{r})$ expanded in plane waves as function of the reciprocal vectors $u_k(\mathbf{r})=\frac{1}{\Omega}\sum_G e^{i\mathbf{G}\cdot\mathbf{r}c_{\mathbf{k}}}$, being Ω the volume of the primitive cell. The secular equation is obtained by integrating in $\mathbf{r}$: [160, 162]

$$\sum_{G'}\left[\frac{\hbar}{2m}|\mathbf{k}+\mathbf{G}|^2\delta_{\mathbf{GG'}} + V^{KS}(\mathbf{G}-\mathbf{G'})\right] c_{\mathbf{k}}(G') = \varepsilon_{\mathbf{k}} c_{\mathbf{k}}(\mathbf{G}). \tag{2.70}$$

Eq. (2.70) describes several potentials in terms of their Fourier transforms. The size of the matrix is related to the cutoff energy, which in turn, is proportional to the plane waves expansion. Therefore, the infinite sum of the plane waves must be truncated and the adopted criterion is:

$$\frac{\hbar^2}{2m}|\mathbf{k}+\mathbf{G}|^2 \leq E_{cut}, \tag{2.71}$$

where $E_{cut} = \frac{\hbar^2}{2m}\mathbf{G}^2_{cut}$ is the cutoff energy. Respecting (2.71) criterion, high values of the cutoff energy provide a better wavefunction convergence. In contrast, insufficient cutoff energy leads to an imprecision in the calculation due to the exclusion of states in the expansion of the wavefunction in the reciprocal space. However, increasing the E_{cut}, the computational cost becomes higher. Therefore, the determination of sufficient cutoff energy is crucial to obtain an accurate calculation. In this Thesis, the convergence tests concerning the cutoff energies, $\mathbf{k}$-points and total energies are shown in the appendix E. Several works have proposed theoretical approaches to generate the sampling to integrate the Brillouin zone, [163, 164] such as Monkhorst Pack [165, 166] and the tetrahedron method. [167]

The advantage of the wavefunction expansion in plane waves is based in the low computational cost, however the high number of the plane wavefunctions to describe the strongly oscillating regions near the nuclei boosted the pseudo-potential method, [168, 169] wherein the core region is expanded in smooth pseudo-wavefunctions. The pseudo-potential method is the theoretical improvement of the Orthogonalized Plane Waves (OPW) approach proposed by Herring. [170] To improve the implementation of the pseudo-wavefunctions, Vanderbilt and collaborators introduced the *Ultrasoft* pseudo-potentials. [171–173] In this method, the pseudo-wavefunctions are assumed to be equal to the AE wavefunctions outside the cutoff radius. Inside the r_c, the pseudo-potentials are described as soft as possible. In this way, several works have proposed improvements in the implementation of the pseudo-potentials. [174–176]

2.3.5.2 The projector augmentation waves method

The Projector Augmentation Waves (PAW) method, [177, 178] proposed by Blöchl [179] originated from the Pseudo-potential method, studied in last section, and the Augmented Plane Waves (APW) approach. Introduced by Slater, [180] the wavefunctions in the APW approach are expanded in independent particle Equations, where the space is separated in two regions: atomic and interstitial. The atomic region is determined by the space around each atom, described by spheres centered in the atom, called augmentation spheres. The atom-like partial waves are expanded in spherical harmonics multiplied by radial Schroedinger wavefunctions. In the interstitial region between the atoms, outside the augmentation spheres, the potential is smooth and the wavefunction used is the envelope function expanded in plane waves. In the interstitial region, the atomic bonds and the chemical environment contribute to the shape of wavefunctions. Partial-waves and envelope functions are connected in the cutoff radius. Similarly to Pseudo-potential method, the PAW approach presents projectors and localized auxiliary functions.

In order to decrease the computational cost, the wavefunctions in the PAW method are smooth in the core region. The transformations are performed by a linear operation, where this Hilbert space includes all orthogonal wavefunctions to the core states. The wavefunctions of this Hilbert space is transformed into a new wavefunctions through an operator $\mathcal{T}$. This new space is called pseudo (PS) or fictitious Hilbert space. Thus, $\mathcal{T}$ is an operator which provides a linear transformation of the smooth PS wavefunctions $\tilde{\Psi}_n$ to *all electron* Kohn-Sham wavefunction Ψ_n, Ψ_n=$\mathcal{T}\tilde{\Psi}_n$. The total energy of the ground state are obtained by solving the Eq. below in the Kohn-Sham scheme:

$$\mathcal{T}^{\dagger} H \mathcal{T} |\tilde{\Psi}_n\rangle = \varepsilon_n \mathcal{T}^{\dagger}\mathcal{T}|\tilde{\Psi}_n\rangle. \tag{2.72}$$

Considering that the wavefunctions for valence electrons are already smooth, the challenge is to choose a correct linear transformation $\mathcal{T}$ to smooth the wavefunctions in the core region. Thus, an appropriate transformation is:

$$\mathcal{T} = 1 + \sum_{R} \hat{\mathcal{T}}_R, \tag{2.73}$$

where R is the atomic index, $\hat{\mathcal{T}}_R$ are the local contributions and acts only within augmentation region Ω_R close to the nuclei. Within the augmentation spheres Ω_r, the true AE wavefunction is expanded in partial waves $|\phi_i\rangle$, where each partial functions is expanded in auxiliary smooth waves $|\tilde{\phi}_i\rangle$:

$$|\phi_i\rangle = (1 + \hat{\mathcal{T}}_R)|\tilde{\phi}_i\rangle. \tag{2.74}$$

The auxiliary smooth functions represent the AE functions and are natural solutions of Schroedinger's radial Eq. for an isolated atom. Eq. (2.74) defines the linear operator $\hat{\mathcal{T}}_R|\tilde{\phi}_i\rangle$=$|\phi_i\rangle - |\tilde{\phi}_i\rangle$. Outside of the augmentation region $|r > r_c|$, $\hat{\mathcal{T}}_R$ has no effect, where the partial waves and the AE functions must be identical. Within the augmentation sphere, the PS wavefunctions can be expanded in terms of partial PS waves:

$$|\tilde{\Psi}\rangle = \sum_{i} P_i|\tilde{\phi}_i\rangle; \qquad |\mathbf{r} - R| < r_c, \tag{2.75}$$

where P_i are the coefficients of the expansion. Considering that $\hat{\mathcal{T}}_R|\tilde{\phi}_i\rangle$=$|\phi_i\rangle$, the AE wavefunction can be obtained by the following expansion:

$$|\Psi_i\rangle = \hat{\mathcal{T}}_R|\tilde{\Psi}_i\rangle = \sum_{i} P_i|\phi_i\rangle; \qquad |\mathbf{r} - R| < r_c. \tag{2.76}$$

In Eq. (2.76), the AE is transformed in smooth functions. Thus, the coefficients must be written as function of the projection for each sphere P_i=$\langle\tilde{p}_R^i|\tilde{\phi}_i\rangle$. Assuming that there is no overlap between the wavefunctions, the smooth projector can be chosen in order to satisfy the completeness and the orthogonality within the augmentation region:

$$\begin{aligned} \langle \tilde{p}_i | \phi_j \rangle &= \delta_{ij}, \\ \sum_i |\tilde{\phi}_i\rangle\langle \tilde{p}_i| &= 1. \end{aligned} \tag{2.77}$$

A convenient choice for the projector of smooth functions is given by: [92, 179]

$$\hat{\mathfrak{T}}_R = 1 + \sum_i (|\phi_i\rangle - |\tilde{\phi}_i\rangle)\langle \tilde{p}_i|. \tag{2.78}$$

The linear transformation $\hat{\mathfrak{T}}_R$ establishes the connection between valence and PS fictitious wavefunctions. Therefore, this transformations allow to obtain the KS AE wavefunction from the PS wavefunction:

$$|\Psi\rangle = |\tilde{\Psi}\rangle + \sum_i (|\phi_i\rangle - |\tilde{\phi}_i\rangle)\langle \tilde{p}_i|\tilde{\Psi}\rangle. \tag{2.79}$$

The transformation in Eq. (2.79) is given by: (a) the atomic Schroedinger-like AE partial waves ϕ_i, which are orthogonal to the core states; (b) PS partial waves $|\tilde{\phi}_i\rangle$, which coincide with the AE partial waves outside augmentation region for each partial wave; and (c) the smooth projector function $|\tilde{p}_i\rangle$ for each PS partial wave within the augmentation region.

Chapter 3

Quantum wells, rings and dots

The geometry of the semiconductor nanostructures determines the anisotropic quantum confinement (QC) of electronic states. In the analysis of three dimensional structures, the confinement can be separated in lateral and growth direction. Although disorder and defects are considered to be detrimental to the thorough control of the expected functionalities of the nanoscopic systems, they can be unavoidable in the growth process, at least up the limits determined by the current synthesis technologies. [181] Imperfections can change the shape of quantum dots. Lately, the quantum control of defects in QDs architectures has attracted the attention of the scientific community due to the tuning of its optical blinking, [182] charge transport, [183] or even implementing spin memories. [184] Due to the size and geometric shape of the QDs, their surfaces can lead to defects and diffusion of impurities. [185] These properties can be studied with intentional doping, diluted or with solitary dopants. [186]

However, a more complex framework is considered when taking into account externally applied electromagnetic fields. In addition, the challenge is the modeling of the semiconductor QDs doped with magnetic impurities that demands the emulation of the interplay of confinement asymmetries, exchange interaction, and spin-orbit coupling. [187, 188] The theoretical approach based on the effective mass model can be used, [189, 190] allowing to obtain analytical solutions under certain approximations. In this context, the most available results in the literature assume the symmetric QD structure. Its important to note that there are several challenges to overcome. The effective mass model allows to simulate the confinement profiles together with symmetry lowering, spin-orbit interaction effects, and external fields under a variety of configurations, in a systematic way and has been complemented with atomistic simulations. Density functional theory calculations provide the atomistic analysis that allows to create disorder, such as impurity localization, structural defects, and perturbations generated by localized magnetic moments, elucidating the origin and the profile of the asymmetries.

For a better understanding of the QC and how much the morphology, magnetic fields and impurities concentration can affect the electronic properties, we take advantage of the **k·p** and DFT models and explain the details of the electronic structure. The aim is to obtain a comprehensive description of the confinement, deformation strength and impurity position in defective QDs. The obtained results help to explain and contrast how each of these contributions affects the magnetic response. In this study, the asymmetry tuning of the effective Zeeman splitting was characterized along with the ground state character in the conduction band. In addition, the results provide exacts solutions in the low fields limits that allow the correlation of all effects, including the impurity positioning in plausible sites for incorporating in the system. The connection between the effective mass model and *ab initio* DFT calculations was done through the analysis of the non-equivalent sites of the impurity positioning within the QD frame, as well as an estimation for the exchange interaction term between the manganese (Mn) impurity and the cadmium selenide (CdSe) host material, topic of this chapter. In particular, DFT calculations are used for assessing the exchange interaction term and its response to the confinement effects. The results are summarized in Ref. [191]. The incidence of electric field changes the shape of the nanostructures, modulating the holes wavefunctions within the quantum confined Stark effect (QCSE). In this context, the relation between indium arsenide (InAs) QD in gallium arsenide doped by antimony (GaAsSb), was fully emulated using **k·p** model according to the experimental results.

3.1 Quantum well

The confinement along the growth direction of rings and dots is described through the quantization of the electronic states in a quantum well, given by:

$$V(z) = \begin{cases} 0, & 0<z<L; \\ \infty, & \text{otherwise}, \end{cases} \tag{3.1}$$

where L is the length of the well. By applying the boundary conditions above and by using the wavefunction $\Psi(z) = \sqrt{\frac{2}{L}} \sin\left(\frac{l\pi z}{L} + \frac{l\pi}{2}\right)$, with $l = 1, 2, 3, \ldots$, the quantized energies are:

$$E_n = \left(\frac{l^2\pi^2\hbar^2}{2\mu^* L^2}\right), \tag{3.2}$$

where n is the energy level corresponding to each eigenvalue.

3.2 Quantum dot and ring confinement

As mentioned above, the semiconductor quantum dots are almost zero dimensional structures whose carriers are confined in the three spatial directions. The effective mass model is used to describe the movement of the carriers under an external potential introduced by the atoms in the lattice. Within this framework, the diagonalization of the Hamiltonian in a Hilbert space provides the characterization of the eigenvectors of the system. Thus, the QC plays a key role to understand the behavior of the electronic properties. In order to emulate the QC, the following expression determines the lateral potential, $V(\rho, \theta)$, in cylindrical coordinates for QDs and QRs: [192, 193]

$$V(\rho, \theta) = \frac{a_1}{\rho^2} + a_2\rho^2 - 2\sqrt{a_1 a_2}, \tag{3.3}$$

where ρ is the radius of the considered structure. The parameters a_1 and a_2 control the structure shape, varying the length of the confinement. For a better understanding, fixing a_1=0 in Eq. (3.3) defines a QD, otherwise, a QR is obtained. Moreover, the radius of the QR and QD at null magnetic field can be given as $R_{QR} = (a_1/a_2)^{1/4}$ and $R^2_{QD} = h/(2\pi\sqrt{2a_2\mu^*})$, respectively. These properties are depicted in the Fig. 3.1, where the confinement potentials of QD and QR are represented in panels (a) and (b), respectively.

3.3 Spin-orbit interaction in quantum dots

In 1990, Datta-Das [20] propelled the spintronics with an experiment that aimed to manipulate the spins according to their momentum through the spin-orbit coupling. The

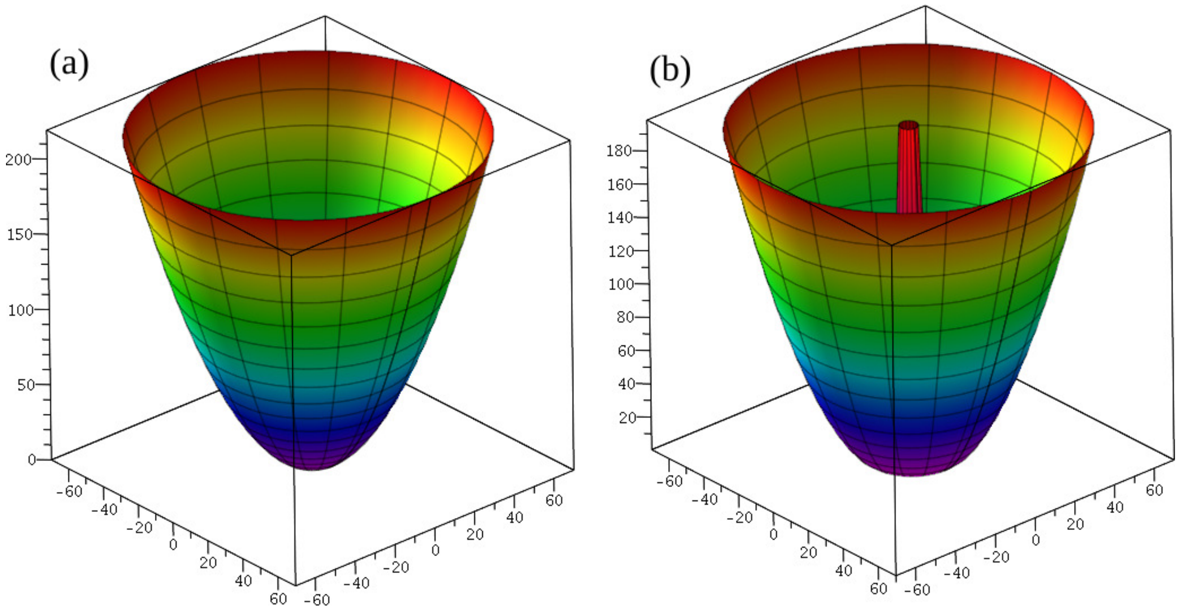

Figure 3.1: Quantum confinement profile. Panels (a) and (b) represent the confinement of quantum dot and ring, respectively.

spin coupled with its orbit encourages scientists to the preparation of spin states for logic operations. [194]

A negatively charged carrier in a solid receives the influence of the atoms in the lattice. The intensity of the electric field depends on the symmetry of the nanostructure. The breaking of the inversion symmetry, introduced by the these electric fields, defines the structural inversion asymmetry (SIA), known as spin-orbit coupling, Rashba type. [22] In zinc blend materials, wherein the crystals exhibit bulk inversion asymmetry (BIA), [195] the electric field is non-zero over crystalline directions, characterizing the spin-orbit coupling of Dresselhaus type. [23] The presence of a magnetic field, applied in the growth direction of the QD, lifts the spin degeneracy. In this case, analytic solutions for the electronic structure can be provided for the cylindrical symmetry, as described by the Fock-Darwin spectrum, studied in the next section. In addition, the effects of the spin-orbit interaction and the perturbative potentials change the symmetry character of the electronic states, introducing new crossings and anti-crossings between the energy levels.

3.3.1 Fock-Darwin spectrum

In this Thesis, the behavior of the QD carriers are modeled by a parabolic potential, e.g., a_1=0 in Eq. (3.3). Assuming that the parabolic potential is enough to confine the electronic states in the first subband of the system, the 3D effective mass Hamiltonian in the presence of magnetic field $\mathbf{B}$=$B\hat{z}$ is written as follows:

$$H_0 = \frac{\hbar}{2m}\mathbf{k} + \frac{1}{2}m\omega_0\rho^2 + \frac{g\mu_B}{2}\mathbf{B}\cdot\sigma, \tag{3.4}$$

where $\mathbf{k} = -i\nabla + e\frac{\mathbf{A}}{\hbar c}$, $\mu_B = \frac{e\hbar}{2m_0 c}$ the Bohr magnetron, m_0 the free electron mass, g the Lande-factor of the bulk and σ represents the Pauli spin matrices. The eigenvalues and eigenvectors of the Hamiltonian (3.4) were described by Fock and Darwin [196, 197] in their work before the appearance of the nanostructures. [15] Introducing the complex variables,

$$Z = x + iy, \qquad Z^* = x - iy, \tag{3.5}$$

and their derivatives

$$\partial_Z = \frac{\partial_x - i\partial_y}{2}, \qquad \partial_Z^* = \frac{\partial_x + i\partial_y}{2}. \tag{3.6}$$

The creation and annihilation operators can be defined as follows:

$$\begin{aligned} a &= \frac{Z^*/(2l_0) + 2l_0\partial_Z}{\sqrt{2}}; \qquad a^+ = \frac{Z^*/(2l_0) - 2l_0\partial_Z^*}{\sqrt{2}}; \\ b &= \frac{Z/(2l_0) + 2l_0\partial_Z^*}{\sqrt{2}}; \qquad b^+ = \frac{Z^*/(2l_0) - 2l_0\partial_Z^*}{\sqrt{2}}, \end{aligned} \tag{3.7}$$

with $l_0 = \frac{l_B}{\sqrt[4]{1+4\omega_0^2/\omega_c^2}}$ and $l_B = \sqrt{\frac{\hbar c}{eB}}$. Thus[1], the Hamiltonian (3.4) can be written in a following way:

$$H = h\omega_+\left(a^\dagger a + \frac{1}{2}\right) + h\omega_-\left(b^\dagger b + \frac{1}{2}\right), \tag{3.8}$$

as a pair of independent harmonic oscillators, with frequencies $\omega_\pm = \sqrt{\omega_0^2 + \frac{1}{4}\omega_c^2} \pm \frac{1}{2}\omega_c$. The lateral wavefunction is written as function of the radial ($R_{nl}(x)$) and angular (Θ =

[1]The operators defined in Eq. (3.7) follow the commutations relations: $[a, a^\dagger] = [b, b^\dagger] = 1$, $[a, b] = [a, b^\dagger] = 0$.

$\frac{1}{\sqrt{2\Pi}}e^{im\theta}$) parts. The radial part is given by Laguerre polynomials ($L_n^{|l|}(y)$). Introducing the wavefunction in the growth direction ($F_\kappa(z)$) in the total wavefunction,

$$\Psi_{nl\sigma_z}(x,\phi,\sigma_z) = \frac{1}{\sqrt{2\pi}}R_{nl}(x)e^{il\phi}\mathbb{X}_{\sigma_z}F_\kappa(z), \tag{3.9}$$

where

$$R_{nl}(x) = \sqrt{\frac{2n!}{\lambda^2(n+|l|)!}}x^{|l|}e^{-\frac{x}{2}}L_n^{|l|}(x^2) \tag{3.10}$$

and

$$F_\kappa(z) = \sqrt{\frac{2}{L_z}}\sin\left(\frac{\pi\kappa z}{L_z}\right), \tag{3.11}$$

with $x = \frac{\rho}{\lambda}$ and $\mathbb{X}_{\sigma_z}$ the spin eigenfunctions. The energy levels can be written as function of the quantum numbers:

$$\varepsilon(n,m) = \frac{\hbar^2\pi^2\kappa^2}{2m^*L_z^2} + \hbar\Omega(N+1) - \frac{1}{2}\hbar\omega_c m, \tag{3.12}$$

where $\kappa = 1,2,\ldots$, $n = 0,1,2,\ldots$, $l = 0,\pm1,\pm2,\ldots$, and $\Omega^2 = \omega_0^2 + \frac{1}{4}\omega_c^2$. The lateral confinement strength does not depend on the mass, however, the confined states depend[2]. The solution for the Hamiltonian (3.4) provides the Fock-Darwin spectrum:

$$\varepsilon_{nl\sigma_z} = (2n+|l|+1)\hbar\Omega - \frac{l}{2}\hbar\omega_c + \frac{g}{2}\mu_B B_0\sigma_z, \tag{3.13}$$

where $\sigma_z = \pm1$, $n = 0,1,2,3,\ldots$ and $l = 0,\pm1,\pm2,\ldots$ are the radial and azimuthal quantum numbers, $\omega_c = \frac{eB_0}{mc}$ and $\Omega = \sqrt{\omega_0^2 + \frac{\omega_c^2}{4}}$ are the cyclotron and effective frequencies of the system, respectively. In the following, the limiting cases, $\omega_0 >> \omega_c$ and $\omega_c >> \omega_0$ will be studied.

[2]In the valence band, the effective mass tensor is not isotropic. In first order approach, the effective mass can be separated into two values: one along z-direction, $m_z = m_0/(\gamma_1 - 2\gamma_2)$, and another in-plane, $m_{xy} = m_0/(\gamma_1+\gamma_2)$, being, γ_1 and γ_2, the Luttinger parameters.

3.3.1.1 Case: $\omega_0 >> \omega_c$

Setting $\omega_c = 0$, Eq. (3.13) becomes: [198]

$$\varepsilon_{nl\sigma_z} = \hbar\omega_0(N+1), \tag{3.14}$$

where $N = 2n + |l| + 1$, defines the energy levels of a two-dimensional harmonic oscillator. For a given N, n must vary from zero to $N/2$ and the values of $|l|$ have the same parity as N. For example, $N = 6$ implies that $n = 0, 1, 2, 3$ and $l = 0, \pm 2, \pm 4, \pm 6$, while $N = 5$ determines $n = 0, 1, 2$ and $l = \pm 1, \pm 3, \pm 5$.

3.3.1.2 Case: $\omega_c >> \omega_0$

Providing $\omega_0 = 0$, Eq. (3.13) transforms in: [198]

$$\varepsilon_{nl\sigma_z} = \hbar\omega_c\left(M + \frac{1}{2}\right) + \frac{1}{2}g^*\mu_0 B\sigma, \tag{3.15}$$

where $M = n + \frac{1}{2}(|l| - l)$ are the Landau levels. Thus, $M = 0, 1, 2, \ldots$ for l-degenerated levels.

3.3.2 Asymmetry effects in quantum dots

The growth process of the semiconductor nanostructures is subject to several external agents that contribute to the origin of imperfections. These irregularities in the crystalline potential affect the carriers confinement. Thus, the approximate parabolic potential of the conduction band must now include structural changes. The addition of a perturbation modifies the geometric shape of the nanostructure, changing the optical and electronic properties of the system.

Asymmetric solid state systems exhibit interesting effects, such as the modification of the dielectric properties of material. Moreover, electron-electron and electron-phonon type interactions will show a modified dynamics compared to an undisturbed lattice. The asymmetry changes the energy spectrum of the nanostructure. As consequence, the periodic oscillations of the carriers change, allowing to emerge new theories and experiments concerning the coherence times of the system.

As mentioned above, the confinement potential models the shape of the nanostructure. Decreasing a_1 in Eq. (3.3), the potential varies from QR to QD. Therefore, this flexible potential profile allows to include the effects of external electromagnetic fields and constrains of symmetry. Within this framework, the possibility to manipulate the confinement profile, and consequently, the morphology, opens a path to study and understand several nanoscopic systems. Assuming the QD case in Eq. (3.3) and z axis as the growth direction, the in-plane confinement profile in polar coordinates is given by:

$$V(\rho) = a_2\rho^2 + \delta_1\rho^2\cos^2\varphi + \delta_2\rho^2 e^{-\frac{(\varphi-\pi)^2}{2\sigma^2}}\ , \tag{3.16}$$

where $\delta_1\rho^2\cos^2\varphi$ and $\delta_2\rho^2 e^{-\frac{(\varphi-\pi)^2}{2\sigma^2}}$ are the perturbative potentials introduced in the total potential of the QD. This proposal is an extension of the confinement profile of the QD proposed in Ref. [193]. The first perturbative potential in Eq. (3.16) describes the eccentricity asymmetry of the QD and are controlled by the δ_1 parameter. After some algebraic manipulations, positives values of $\delta_1 > 0$ determine $e = \sqrt{1-(a_2+\delta_1)/a_2}$, and negative values imply in $e = \sqrt{1-(a_2+\delta_1)/a_2}$. Note that $\delta_1 > 0$ corresponds to an elliptical shrinking, while $\delta_1 < 0$ leads to an elliptical stretching. The additional third term in Eq. (3.16) represents the Gaussian perturbation, which depends on the δ_2 sign, managing the intensity of this perturbative potential and simulating a local defect positioned at $\varphi = \pi$ with an angular amplitude given by σ. This asymmetry can also be extended to a finite array of N_d defects as $v(\varphi,\rho) = \sum_{i=1}^{N_d}\delta_2^i\rho^2 e^{-\frac{(\varphi-\theta_i)^2}{2\sigma_i^2}}$ that must fulfill the symmetry constraint $v(\varphi,\rho) = v(2\pi-\varphi,\rho)$. At the top of the Fig. 3.2, we show a visual representation of the confinement profile including the asymmetric potentials and, at the bottom, the respective ground state surface:

In the upper part of Fig. 3.2 the Gaussian (a) and eccentricity (b) perturbations are shown. In the lower part, the ground state solution with negative (c) and positive (d) values of δ_2. All the calculations were performed for the quantum dot case, a_1=0 and fixing a_2=4.47 meV/100nm^2. In (a) and (b) panels we used $\delta_1 = 0$ and $\delta_2 = 0$, respectively, and varied the remain perturbation parameters in the potential.

As discussed above, the sign of δ_i, $i = 1, 2$, modulates the perturbations. Concerning the Gaussian perturbation, the sign of δ_2 defines the intensity of the dip or the bump in the

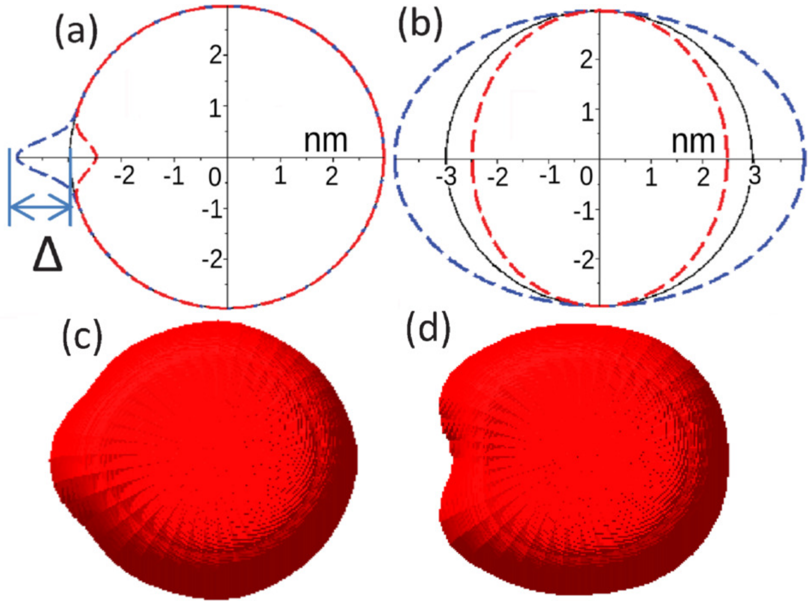

Figure 3.2: Confinement potential profile in lateral direction for a_2=4.47 meV/100nm^2 and (a) $\delta_1 = 0$ and several δ_2 values; (b) $\delta_2 = 0$ and various δ_1 values. In (c) and (d) panels are shown the ground state surface, where $\delta_2 = -4$ meV/100nm^2 and $\delta_2 = 12$ meV/100nm^2, repectively.

potential, modulating the wavefunction of the system. The ground state energy of lateral confinement in the absence of the magnetic field is written as $\epsilon_0 = \hbar^2/(m^* l_0^2)$ and the effective length of the perturbative potential can be characterized by the distance $\Delta = R_1 - R_0$, as depicted in Fig. 3.2. In the QD case, this result is obtained by the algebraic manipulation of ground state energies:

$$\epsilon_0 = (a_2 + \delta_2)R_1^2 \qquad \text{and} \qquad \epsilon_0 = a_2 R_0^2. \tag{3.17}$$

Combining the Eqs. (3.17),

$$\Delta = \sqrt{2} l_0 \left(\sqrt{\frac{a_2}{a_2 + \delta_2}} - 1 \right), \tag{3.18}$$

which modulates the dip or bump size (Δ) in the potential, depending of the δ_2 sign. The demonstration of the Eq. (3.18) is presented in appendix B.

3.3.3 Rashba spin-orbit in CdSe quantum dots

The electron motion introduces a correction term in the effective Hamiltonian of the system, [199] indicating the coupling between the spin and its orbit. The analytical description is given by Dirac's theory due to its relativistic nature. The unavoidable spin-orbit effects are emulated by the introduction of the Structrure Induced Asymmetry (SIA) term, known as Rashba contribution, [27] in the total Hamiltonian (3.4),

$$H_{SIA} = \frac{\alpha_s}{\hbar}\sigma \cdot \left[\nabla V \times (\mathbf{p} - e\mathbf{A})\right]. \tag{3.19}$$

where α parameter defines the Rashba coupling, which varies according to the material, and $V(\mathbf{r}) = V(\rho) + V(\mathbf{z})$ is the confinement potential in the lateral $V(\rho)$ and growth $V(\mathbf{z})$ direction. After some algebraic manipulations, Eq. (3.19) can be divided into $H_{SO} = H_k + H_R + H^D_{SIA}$, with

$$H^D_{SIA} = \frac{\alpha}{l_0^2}\frac{\omega_0}{\Omega}\sigma_z\left[L_z + \frac{\omega_c}{2\Omega}x^2\right]; \tag{3.20}$$

$$H_R = -\frac{1}{\hbar\Omega}\frac{\alpha}{\lambda}\frac{dV}{dz}\left[\sigma_+ L\_A\_ + \sigma\_L_+ A_+\right], \tag{3.21}$$

where H^D_{SIA} is the diagonal contribution of Rashba in the Fock-Darwin basis due to the lateral confinement and H_R is the non-diagonal Rashba elements due to the perpendicular confinement. The term $H_k = i\frac{\alpha}{l_0^2}\frac{\omega_0}{\Omega}\lambda_x\langle k_z\rangle(\sigma_+ L\_ - \sigma\_L_+)$ is canceled because $\langle k_z\rangle = 0$. In Eq. (3.21) we used $L_\pm = e^{\pm i\theta}$, $\sigma_\pm = \frac{\sigma_x \pm i\sigma_y}{2}$ and $A_\pm = \mp\frac{\partial}{\partial x} + \frac{L_z}{x} + \frac{\omega_c}{2\Omega}x$, where the terms are written in cylindrical coordinates. The Rashba coupling parameter α_s is calculated using the third order perturbation theory in the extended Kane model, [27] given by:

$$\begin{aligned}\alpha_s &= \frac{P^2}{3}\left[\frac{1}{E_0^2} - \frac{1}{(E_0+\Delta_0)^2}\right] \\ &- \frac{P'^2}{3}\left[\frac{1}{(E_0-E_0')^2} - \frac{1}{(E_0-E_0'-\Delta_0')^2}\right],\end{aligned} \tag{3.22}$$

where the band parameters in Eq. above are E_0=1.85 eV, [200] E_0'=7.39 eV, [201] Δ_0=0.42 eV, [201] $\Delta_0' = 0.64$ eV, $\Delta_0 = 0.27$ eV, [201] $P = 10.63$ eVÅ, [202] and $P' = 9.16$ eVÅ. [202] Using these values in Eq. (3.22), the obtained Rashba parameter is 3.61 Å^2. Comparing with another materials, the Rashba parameter for GaAs, InAs and InSb are 5.21 Å^2, 117.10 Å^2

and 523.0 Å^2, respectively. [27]

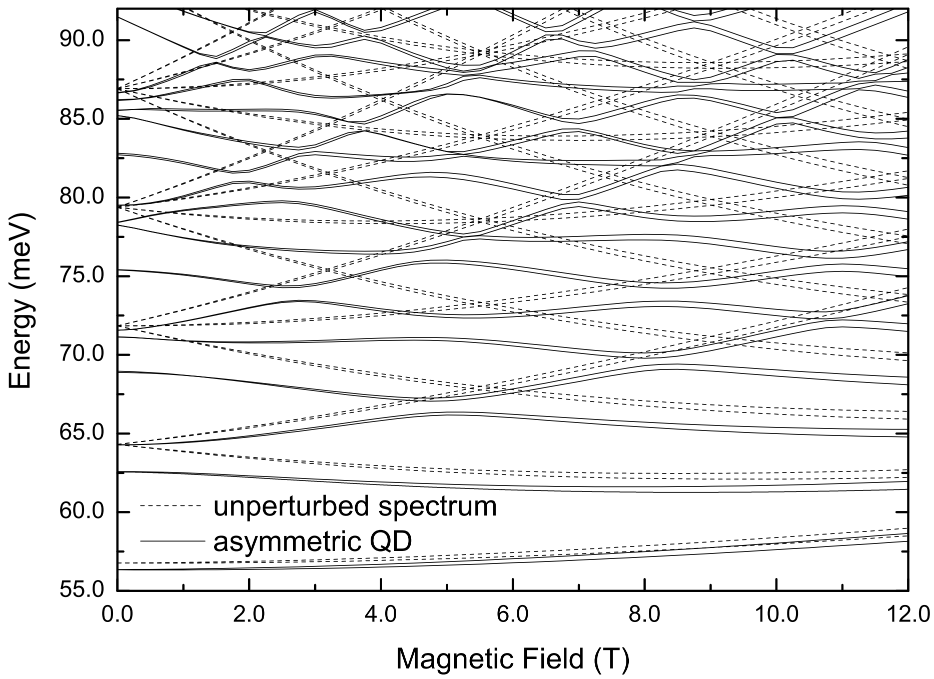

Figure 3.3: Fock-Darwin spectrum for CdSe QD under an applied magnetic field. The symmetric dispersion is represented by the dashed lines. The perturbative potential considers the eccentricity, $\delta_1 = -1$ meV/100nm^2, and Gaussian perturbation, $\delta_2 = -4$ meV/100nm^2. In all calculations were fixed $a_1 = 0$ and $a_2 = -4$ meV/100nm^2.

The SO interaction in CdSe QDs is weak. The anti-crossings in the Fock-Darwin spectrum can be intensified using perturbative potentials. In Fig. 3.3 we show a contrast between the unperturbed and perturbed spectrum with eccentricity and Gaussian asymmetries for CdSe QDs under an applied magnetic field, both combined with the spin-orbit interaction. For null magnetic field, the radial quantum number are separated for asymmetric QDs, contrasting with the unperturbed potential. For non-zero magnetic fields, Fig. 3.3 show an energy shift and several anti-crossings, indicating the inversion of the spin polarization in the perturbed case.

3.4 Quantum dot and ring under electric field

As mentioned previously, the understanding of the properties of semiconductor quantum dots is crucial for technological applications, such as nanodevices. The modulation of the QDs geometry through perturbative potentials and the incidence of external electric field allows to manipulate the electronic and optical properties, such as the control of the carrier excitations for particular desired application. [203, 204] The manipulation of the band gap of QDs and QRs via an externally applied electric field provides advances in quantum technologies. [205–207] In order to explore the properties of the confined carriers behavior in QDs, [208] the **k·p** Hamiltonian was used to describe the experimental evidence of indium arsenide (InAs) QD on the layer of gallium arsenide doped with antimony (GaAsSb) under an electric field, leading to the quantum confined Stark effect and the intertwining between the holes wavefunctions, studied in sections 3.4.1 and 3.4.2, respectively.

3.4.1 Stark effect and quantum confined Stark effect

The Stark effect is defined by the incidence of an electric field on a carrier moving in a periodic potential lattice. In 1960, Wannier studied the effective Hamiltonian and wavefunctions for Bloch electrons in an applied electric field. [209] In addition, the non-periodic potential V_F due to an electric field incidence has the following form:

$$V_F = -\varepsilon \cdot \mathbf{r}, \tag{3.23}$$

where ε and $\mathbf{r}$ are the electric field and the orbital distance of the carrier, respectively. The optical absorption and emission changes according to the electric field intensity. The non-periodic potential causes an instability in the ground state of the system, where the Bloch theorem loses its validity. Thus, the formulations of the exchange and correlation functionals within density functional theory exhibit difficulties. [210, 211] In this way, the analyzed results presented in the next section were performed within the **k·p** approach.

Quantum confined Stark effect (QCSE) is the consequence of the incidence of an external electric field in the quantized systems. In the presence of an electric field, QCSE gives a spectral shift in the energy spectrum. In addition, the incidence of an external electric fields provides an increase in the exciton recombination lifetime due to the decrease of the electron-hole wavefunction overlap. [212–215]

3.4.2 Electric and magnetic field in valence band states

In these results, the theoretical and experimental framework is focused in the heavy and light holes states, wherein the split-off states are assumed as a remote band. A visual representation of the QD wavefunction under electric field is given in the Fig. 3.4. In panel (a) we represent the indium arsenide (InAs) QD covered by gallium arsenide doped with antimony (GaAs:Sb) and, in part (b), we show the probability density distribution of the fundamental states of holes. [208]

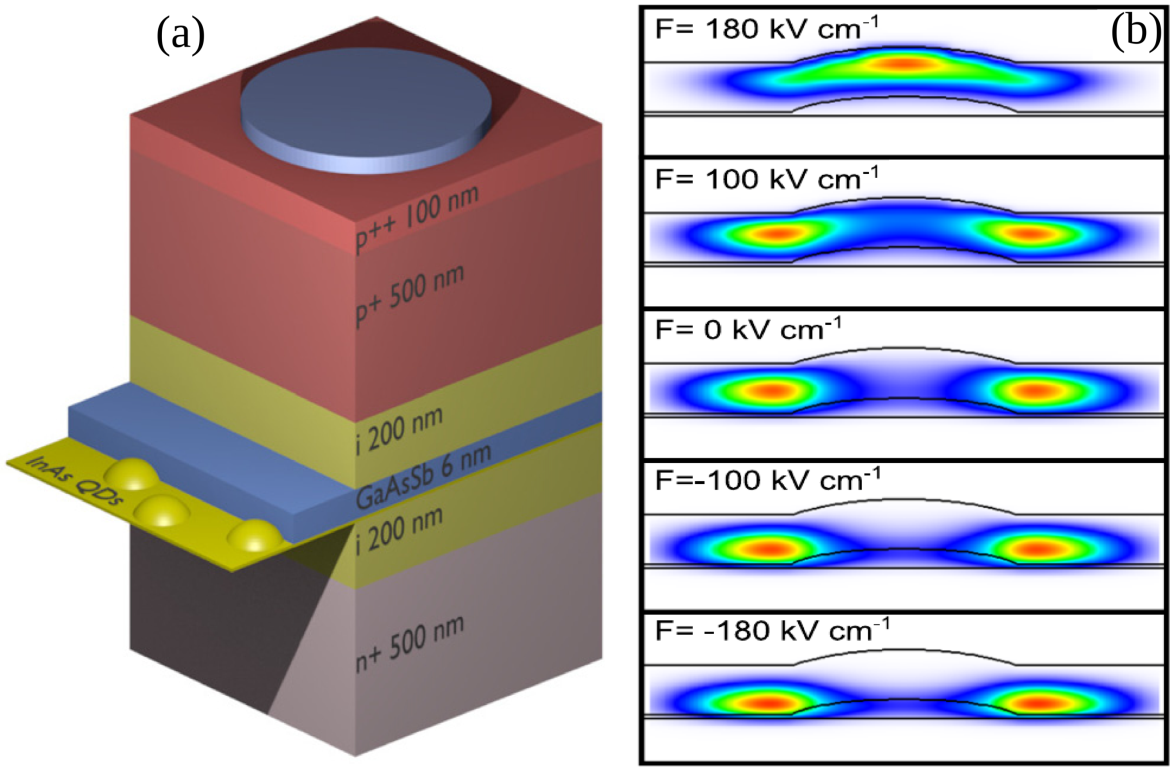

Figure 3.4: Interplay between wavefunctions in the indium arsenide (InAs) QD covered by gallium arsenide doped with antimony (GaAs:Sb). In panel (a) a schematic representation of the experimental structure is shown. In panel (b) the distribution of the probability density of the holes ground state in the (110) and $(1\bar{1}0)$ planes is represented. In each panel the electric field intensity is indicated.

In the Fig. 3.4, taken from the Ref. [208], the electric field is shown modulating the QD and QR wavefunction. Note the overlap of the wavefunction for QDs. Increasing the intensity of the electric field the QD wavefunction is obtained, otherwise the QR wavefunction prevails. However, when the magnetic field is introduced in the system, a relation between electric and magnetic fields was observed. The diamagnetic energy difference between the hole states decreases for smaller electric fields. Moreover, an inversion in the Zeeman splitting was observed, shown in the first frame of the second line of Fig. 3.5.

The management of the confinement provides a strong hybridization between the spins holes states, becoming sensitive to the incidence of the magnetic field, allowing the manipulation of the spin character. [216] To study the magnetic response of the holes states tuning the Zeeman splitting combined with an externally applied electric field, the Luttinger

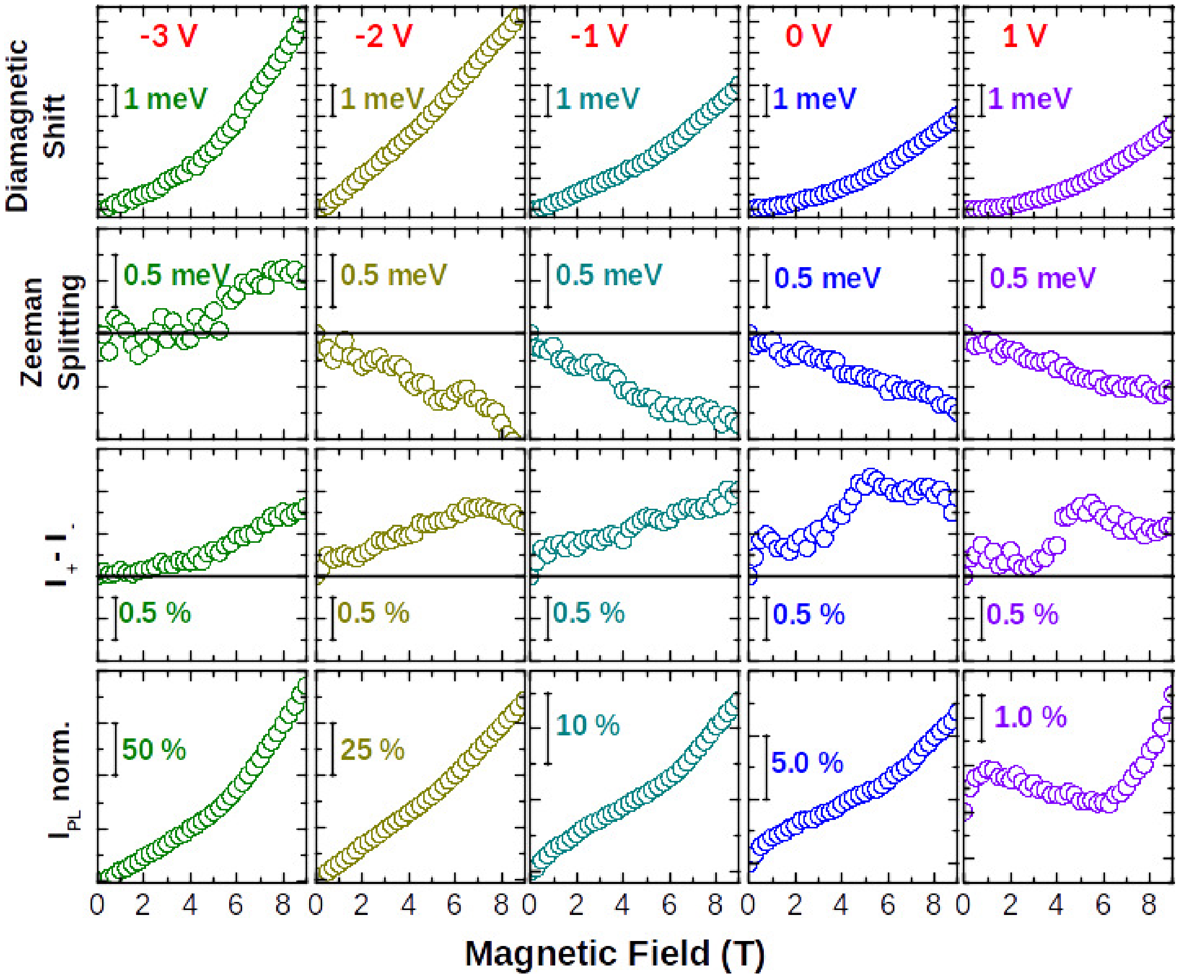

Figure 3.5: Zeeman splitting and diamagnetic shift for valence band states. Smaller values of the electric field decrease the diamagnetic shift. On the other hand, higher electric field strength increases the diamagnetic shift. An inversion in the Zeeman splitting can be observed.

model within the **k·p** method was used. In order to simulate the intertwining between the QD and QR wavefunctions, the flexible confinement potential between the QD and QR in the lateral direction, defined in Eq. 3.3, was used. The confinement along the growth direction is given by a rigid wall. The QCSE was included by adding the potential given in Eq. (3.23). In these calculations, the magnetic and electric fields were applied along the growth direction, according to the experimental results. The magnetic response of the HH is stronger than the LH in the presence of an electric field, providing the displacement of the HH states along the edge of the gallium arsenide doped with antimony (GaAs:Sb). Therefore, the electronic structure was emulated assuming the LH inside the InAs QD and the HH in the edge of the QD constituted by $GaAs_{0.83}Sb_{0.17}$, where the parameters were obtained by a linear interpolation between the GaAs and GaSb values.

The manipulation of the quantum confinement and the Zeeman splitting is depicted

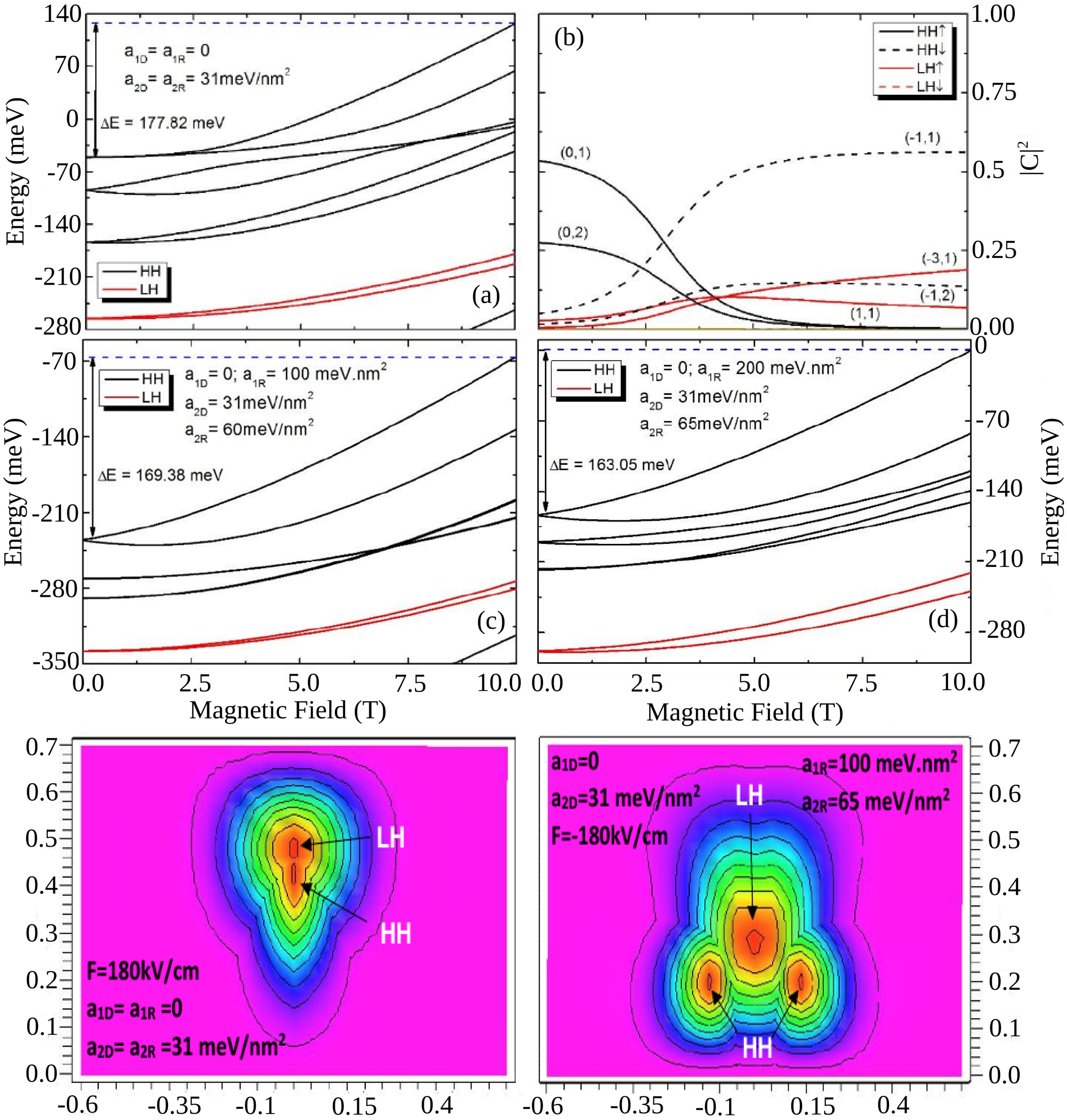

Figure 3.6: Hybridization between heavy and light holes states in the presence of a magnetic and electric field for a given confinement profile. In the panel (a) the effects of the confinement profile are indicated tuning the Zeeman splitting and opening the possibility to control the spin character. The hybridization between the spin states is given in panel (b). By decreasing the electric field, the diamagnetic shift decreases, as indicated in panels (c) and (d). At the bottom of the Fig. the migration of the heavy holes states is depicted from the center to the edge of the QD due to the decrease of the electric field.

in Fig. 3.6, where the strong hybridization between the spins character at 0 magnetic field and the diamagnetic shift of 177.82 meV is presented in panel (a), where the **k·p** parameters used were a_{1R}=a_{1D}=0, a_{2D}=a_{2R}=31.0 meV nm^{-2}, L_D=L_R=7.0 nm, F=180 kV cm^{-1}, being a_{1D} and a_{2D} the in-plane confinement for the LH and a_{1R} and a_{2R} the in-plane confinement for the HH, L_D and L_R define the height of the QD used in the LH and HH confinement, respectively. In addition, in the same panel the anti-crossing between the second and third levels is shown at 3.0 T due to the non-diagonal Luttinger parameters, indicating the inversion of the spin character due to the introduction of the magnetic field. This hybridization is confirmed in panel (b), where the coefficients of the ground state are indicated and also the inversion of the sign of the Zeeman splitting. The HH$\uparrow$ is predominant for B $\leq$ 2.9 T, otherwise HH$\downarrow$ is obtained, where the $\uparrow$ and $\downarrow$ indicates the spins up and down, respectively. This conclusion agrees with the experimental results presented in Fig. 3.5. Although spin-orbit coupling was included in this calculations, its small intensity does not produce significant effects. In panel (c) we used a_{1D}=0, a_{1R}=100 meV nm^2, a_{2D}=31 meV nm^{-2}, a_{2R}=60 meV nm^{-2}, L_D=L_R=7 nm and F=0. In the same way, panel (d) used a_{1D}=0, a_{1R}=200 meV nm^2, a_{2D}=31 meV nm^{-2}, a_{2R}=65 meV nm^{-2}, L_D=L_R=7 nm and F=$-$180 kV cm^{-1}. The diagmetic shift in panels(c) and (d) are 169.38 meV and 163.05 meV, respectively. The diamagnetic shift becomes smaller as the electric field is decreased. In addition, at the bottom of Fig. 3.6 the behavior of the wavefunction is depicted for F= $\pm$180 kV cm^{-1}, where the HH moves from the center to the edge of the QD by decreasing the electric field.

3.4.3 Effective Lande-factor and exchange interaction in CdSe quantum dots

The magnetic impurity incorporation in a non-magnetic material provides the exchange interaction between the magnetic impurity and the host material, leading to the *Giant Zeeman* splitting. Thus, the Lande-factor of the material must include the effect of the magnetic impurity. The exchange Hamiltonian due to the effect of magnetic impurity is written as follows: [27]

$$H_{ex} = -\sum_m J(\mathbf{r} - \mathbf{R}_m)\mathbf{S}_m \cdot \sigma. \tag{3.24}$$

where the sum runs over all m magnetic impurities and σ is the electron spin operator. The exchange interaction term $J(\mathbf{R}_i - \mathbf{r})$ has a range of one lattice constant and is related to the spin operator ($\mathbf{S}_m$) and the position ($\mathbf{R}_m$) of the magnetic impurity. [189] Using the mean field approximation and introducing the contribution of the N_t impurity ions trapped in localized defects, the exchange Hamiltonian (3.24) is given by:

$$H_{ex} = -J_0 x \langle \mathbf{S}_{\mathrm{Mn}} \rangle \cdot \langle \mathbf{s} \rangle - \sum_{m=1}^{N_t} J_0 \Omega_0 \left| \Phi(\mathbf{R}_m) \right|^2 \langle \mathbf{S}_m \rangle \cdot \langle \mathbf{s} \rangle \ , \tag{3.25}$$

where $|\Phi(\mathbf{R}_m)|^2$ is the mean value of the envelope function in a unit cell containing the impurity atom, x is the molar impurity fraction. The exchange interaction term is written as $J_0 = 1/\Omega_0 \int_{\Omega_0} J(\mathbf{R}_i - \mathbf{r})\, u_j^* u_j d\mathbf{r}$, with $\Omega_0 = a_0^3/4$ the unit cell volume, a_0 the lattice constant and u_j the periodic part of the Bloch function. The experimental observation of J_0 for CdMnSe and InMnAs in bulk phase is 0.26 eV and 0.5 eV, respectively. [217, 218]

For a better understanding of the Zeeman splitting, the first order correction analysis was performed for the effective Lande-factor in order to study the correlation between the confinement, asymmetry, spin character and the impurity effects. Firstly, to investigate the Zeeman splitting of the ground state without the contribution of impurity, which is diagonal in the proposed basis, combined with the spin-orbit interaction, Eqs. (3.19) and (3.25) are manipulated,

$$\Delta E_Z^{(1)} = \left(g^* + 2\frac{m^* \alpha_s}{\hbar^2} \left\langle \frac{\partial V}{\partial \rho} \rho \right\rangle \right) \cdot \mu_B B \, , \tag{3.26}$$

where g^* is the Lande-factor, V describes the lateral confinement profile in Eq. (3.16), m^* the effective mass, α_s the Rashba parameter and ρ the QD radius in cylindrical coordinates, reported previously in Refs [219, 220]. Using the perturbative potential introduced in section 3.3.2 and taking advantage of the error function $erf(x)$, the renormalized Lande-factor is

$$g_{eff}^{(1)} = g^* + 2\frac{m^* \alpha_s}{\hbar^2} \left[a_2 + \frac{\delta_1}{2} + \delta_2 \frac{\sigma}{\sqrt{2\pi}} erf\left(\frac{\pi}{\sqrt{2}\sigma} \right) \right] \lambda^2 \, . \tag{3.27}$$

Within the low field limit approach, e.g., for $\lambda \to l_0$, Eq. (3.27) can be expressed in terms of the local defects and asymmetries:

$$
\begin{aligned}
g_{eff}^{(1)} &= g^* + 2\frac{\alpha_s}{l_0^2}\Bigg\{1 + sign(\delta_1)\frac{e^2}{2 - [1 + sign(\delta_1)]e^2} \\
&+ \left[\frac{1}{\left(\frac{\Delta}{\sqrt{2}l_0} + 1\right)^2} - 1\right]\frac{\sigma}{\sqrt{2\pi}}erf\left(\frac{\pi}{\sqrt{2}\sigma}\right)\Bigg\}.
\end{aligned}
\tag{3.28}
$$

In Fig. 3.7, we present the effective Lande-factor with the spin-orbit coupling and asymmetric effects, given in Eq. (3.28). In part 3.7(a), the effective Lande-factor using the first order correction gives the calculated values of Δ/l_0 as a function of the angular amplitude of the local defect σ without eccentricity perturbation. The intensity of the local defect (Δ) and the sign of δ_2 defines the behavior of the effective Lande-factor, which is modulated by the angular amplitude (σ) due to its stronger contribution in the renormalization. In the same way, the sign of δ_1 induces changes in the QD eccentricity, as indicated in panel (b), where $\delta_1 > 0$ and $\delta_1 < 0$ provides the shrinking and enlarging of the QD, respectively. In addition, Eq. (3.28) shows that the first order spin-orbit correction of the Lande-factor increase for smaller QD radius. Therefore, the relative Lande-factor increases as the QD size is reduced, independent of the direction of the local defect shrinking. Moreover, Eq. (3.28) defines the response in spin splitting energy levels through the introduction of the asymmetries in the presence of the spin-orbit coupling, where its description is given in universal units $2\alpha_s/l_0^2$ determined by the material parameters and the strength of the spin-orbit coupling.

Until here, the analysis has been made without including the magnetic impurity. The tuning of the Lande-factor is associated with the exchange interaction parameter (J_0). The study can be performed in low field limits, where the mean field approximation can be obtained by taking the $\lim_{x\to 0}\mathcal{B}_J(x) = (J+1)/J \cdot x/3$ in Eq. (3.27). After some algebraic manipulations, the addition of the exchange interaction parameter in Eq. (3.28) is written in a following way:

$$
g_{eff}^{(2)} = g_{eff}^{(1)} - \frac{7J_0 g_{\mathrm{Mn}}}{6k(T+T_0)}\left(x + \sum_{m=1}^{N_t}\Omega_0\,|\Phi(\mathbf{R}_m)|^2\right). \tag{3.29}
$$

Assuming that the exchange interaction parameter includes only the effects of the

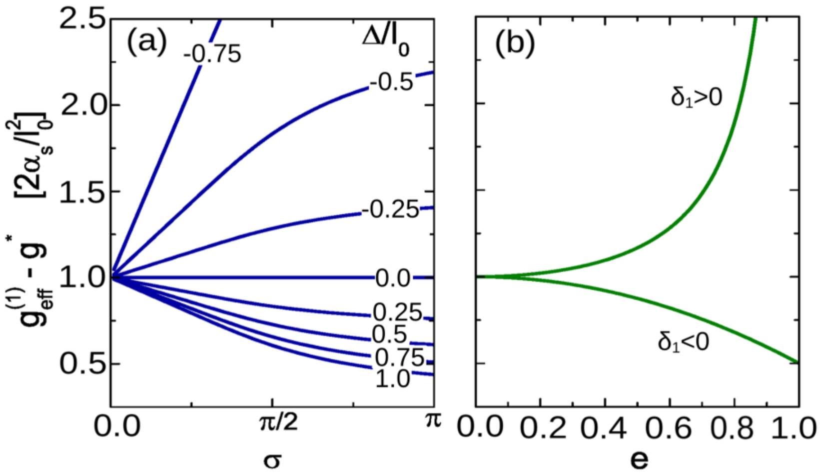

Figure 3.7: Effective Lande-factor including spin-orbit and asymmetry contributions in units $2\alpha/l_0^2$, described in Eq. (3.28). Panel (a) represent several values of Δ/l_0 without eccentricity perturbative potential for $g_{eff}^{(1)} - g^*[2\alpha_s/l_0^2]$ as function of the angular amplitude of the defect, σ. In panel (b) are shown the calculated values of the $g_{eff}^{(1)} - g^*[2\alpha_s/l_0^2]$ as function of the eccentricity with $\sigma = \Delta = 0$.

impurity and manipulating Eq. (3.29) in order to incorporate the structural parameters and temperature, the effect of the the dopant ions position in the Lande-factor renormalization is given by:

$$g_{eff}^{(2)} - g_{eff}^{(1)} = -\frac{7J_0 g_{\mathrm{Mn}}}{12k(T+T_0)} \frac{a_0^3}{\pi l_0^2 L_z} \exp\left(-\rho_{\mathrm{Mn}}^2/l_0^2\right) . \tag{3.30}$$

The impurity positioning of the magnetic atoms (ρ_{Mn}) in Eq. (3.30) affects the ground state spin splitting, being inversely proportional to the QD volume $\frac{a_0^3}{\pi l_0^2 L_z}$. The Lande-factor correction including the spin-orbit interaction and magnetic impurities positioning as function of the asymmetries is expressed in Fig. 3.8.

The description of the impurity positioning within the asymmetric QD is given at the top of the Fig. 3.8 by setting the angular dependence in $\varphi = \pi$, $x = 0$ and $N_t = 1$ in Eq. (3.30). In the lower part of the Fig. 3.8, the Lande-factor modulation is represented as a function of the eccentricity (a) and Gaussian (b) asymmetries for different impurity positions ρ_{Mn}. The dependence of the asymmetry strength, for both cases δ_1 and δ_2, changes the monotonicity depending on the Mn localization. This dependence allows to study the magnetic field responses according to the impurity drift during the growth process or thermal annealing. Evidently, in a real experiment, the impurity position can enter in several QD positions, even on the growth substrate. The atomistic analysis was performed within the density functional theory framework, detailed in the next section, comparing the non-equivalent sites

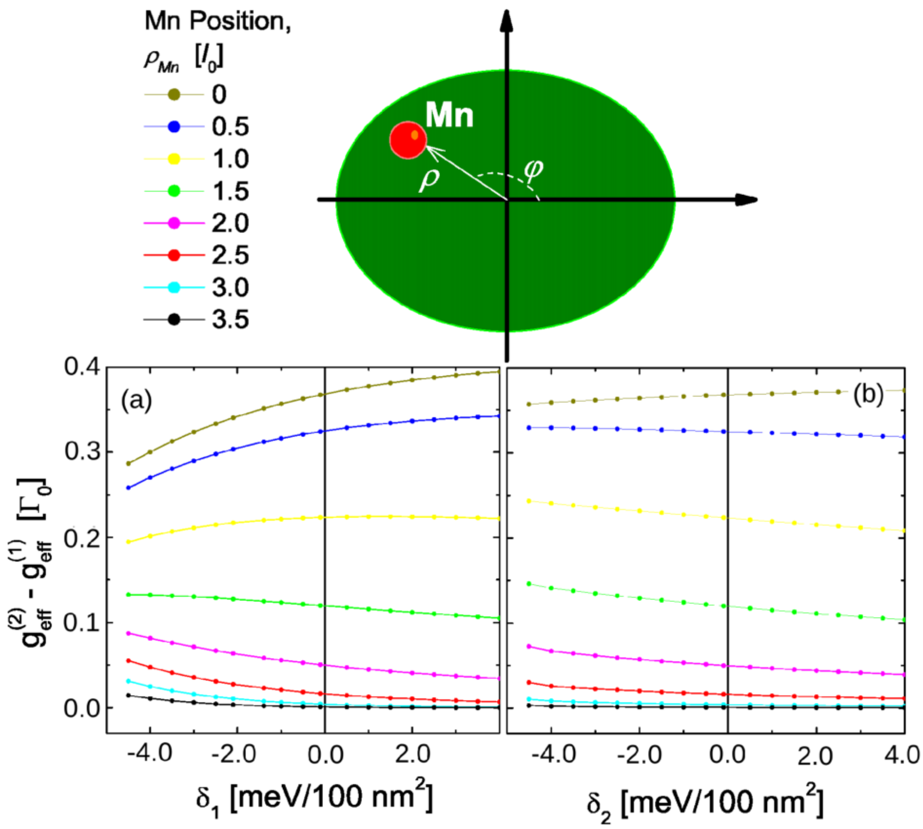

Figure 3.8: Effective Lande-factor correction, in units of $\Gamma_0 = -\frac{7J_0 g_{\mathrm{Mn}}}{12k(T+T_0)}\frac{a_0^3}{l_0^2 L_z}$, as function of the asymmetric terms and magnetic impurity localized at $\varphi = \pi$. In panel (a) the effect of eccentricity is depicted, while in panel (b) the contribution of a localized defect is represented.

of the impurity incorporation as well as the effects of the exchange interaction between the magnetic ions and non-magnetic QD host material.

3.5 Quantum dots, diluted magnetic semiconductors and density functional theory

The understanding of the Lande-factor is crucial to describe the electronic properties of the semiconductor systems. The Lande-factor has been used in this Thesis including the spin-orbit, asymmetry and impurity effects within the **k**·**p** approach. Taking advantage of the density functional theory, the main objective of this section is to elucidate the effects of impurities incorporation in a non-magnetic material, estimated by the exchange interaction parameter (J_0), which is fully emulated by the *ab initio* method. Thus, in this section we study the properties of the cadmium selenide (CdSe) and zinc selenide (ZnSe) semiconductors, as well as the CdSe QDs embedded in ZnSe host material, undoped and doped with manganese (Mn).

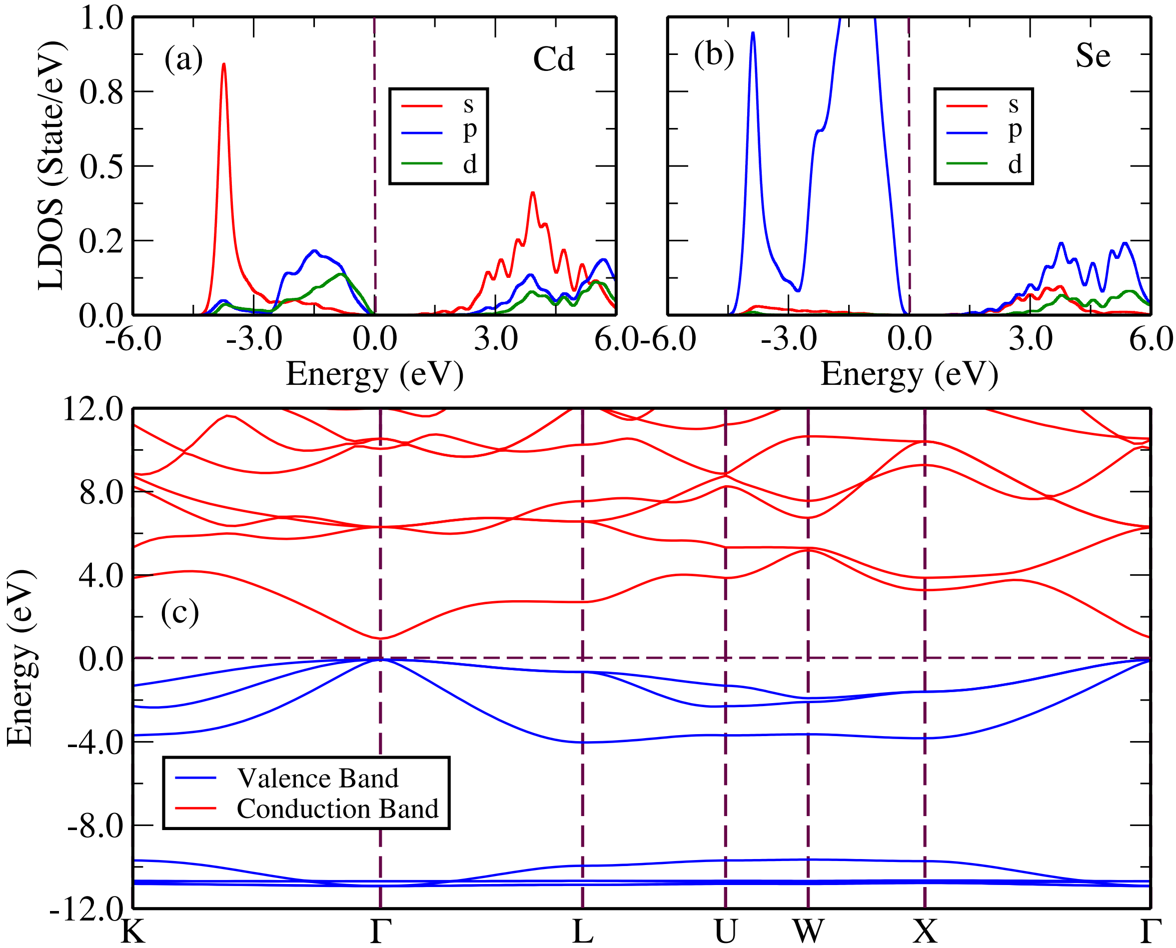

Figure 3.9: Local density of states (LDOS) and band structure of the pristine cadmium selenide (CdSe) bulk system. In panels (a) and (b) the LDOS of the cadmium (Cd) and the selenium (Se) atoms are shown, respectively. Part (c) depicts the band structure of the CdSe, where the direct gap is indicated by the Γ line.

The introduction of the magnetic doping atoms in non-magnetic materials, such as cadmium selenide doped with manganese [221–223] and cobalt [224] impurities, allows to study the exchange interaction between the *s*-*p* levels of the host material and *d* states of the impurity. [225] In this section, it is assumed that the manganese (Mn) is the doping atom in the CdSe and ZnSe materials. The magnetic moment of Mn varies with the lattice parameter. The stable phase of the Mn at room temperature is a complex bcc structure with 29 atoms per unit cell, showing an anti-ferromagnetic structure. [226]

On the left side of Fig. 3.10 the total density of states of the manganese atom is shown, for face centered cubic, body centered cubic and hexagonal centered packing structures, and CdMnSe QD in ZnSe substrate. On the right part, the local density of states is presented for zinc (Zn), cadmium (Cd), selenium (Se) and manganese (Mn) atoms. The

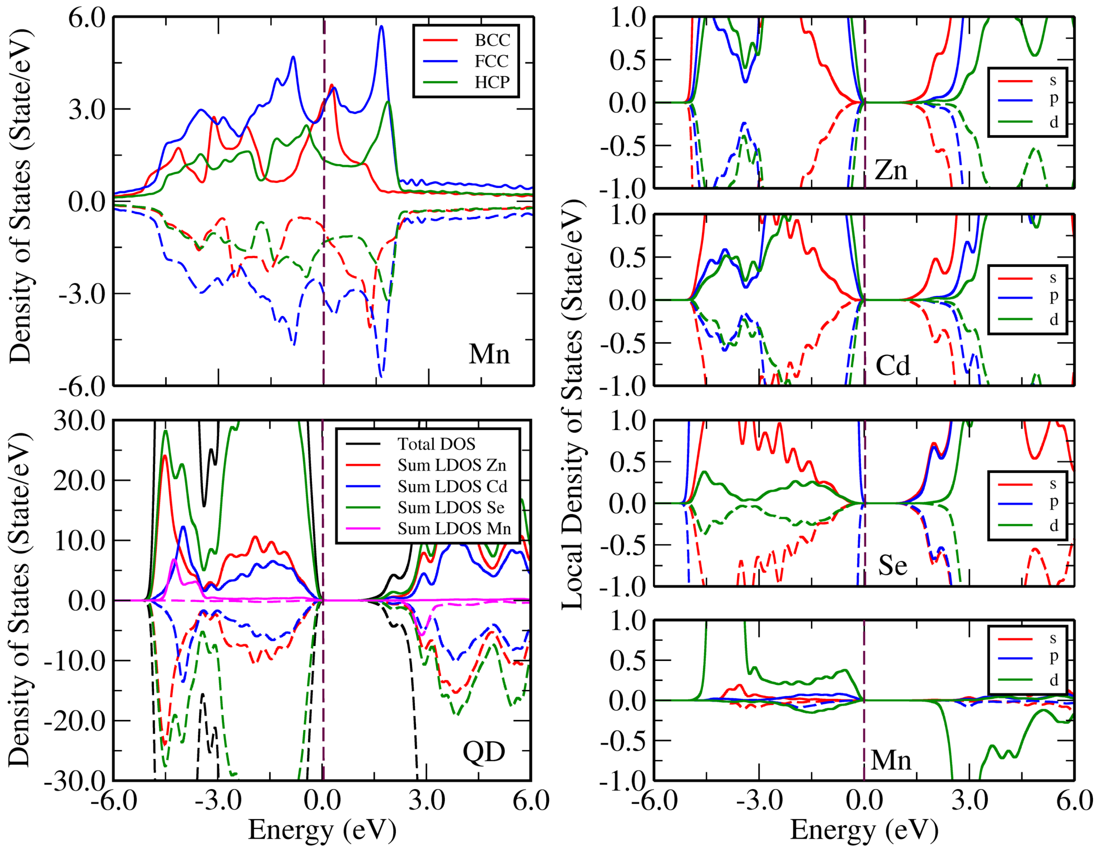

Figure 3.10: Cadmium selenide (CdSe) quantum dot in zinc selenide (ZnSe) substrate doped with manganese (Mn). On the left, the density of states of Mn and CdMnSe/ZnSe QD are presented. On the right, the local density of states of zinc (Zn), cadmium (Cd), selenium (Se) and manganese (Mn) atoms are shown.

vertical line indicates the Fermi energy, showing the forbidden region of the CdSe and ZnSe semiconductors.

3.6 Exchange interaction estimated by density functional theory

The understanding of the band structure of doped materials is crucial to design new spintronic devices. [227] Thus, the exchange interaction parameter (J_0), described in section 3.4.3, plays a key role for the analysis of the incorporation of impurities in nanoscopic systems. The density functional theory allows us to study the magnetic effects of the impurities at atomistic scales.

To simulate the doped QD within the DFT framework, a supercell of CdSe QD embedded in the ZnSe host material was provided formed by 38, 108 and 70 atoms of

Cd, Se and Zn, respectively. The manganese atom was incorporated in several places, assuming the substitutional, replacing the Cd and Zn atoms, and interstitial doping sites. Due to the periodic representation of the bulk model, we assumed in these calculations only the non-equivalent impurity sites, where the panel Fig. 3.11(a) represents the undoped QD and the circle indicates the QD region. In panel (b), the black atom depicts the Mn replacing the Zn atom in the matrix that surrounds the QD. For the interstitial configurations, panels (c), (d) and (e) emulate the Mn entering in the center, in the matrix and in the edge of the QD, respectively. For substitutional doped structures, the Mn replaces the Cd in the positions represented by the panels (f-i). Above the interstitial and substitutional configurations we displayed the energy difference between the smallest configuration energy for each type of doping and the considered structure. For example, for interstitial doping, the Mn impurity placed at the matrix of the bulk has the smallest energy comparing to the other interstitial doping sites, where the energy difference between this structure and the interstitial Mn impurity placed at the center and at the edge is 157 meV and 19 meV, respectively. In the same way, the structure QD-004 has the smallest energy considering other substitutional doping sites. The energy difference between the QD-004 and other substitutional configurations QD-001, QD-002 and QD-003 is 1 meV, 34 meV, 18 meV, respectively. Therefore, as indicate in Fig. 3.11, the Mn ion placed in the matrix and near to the center of the QD are the preferential interstitial and substitutional structures, respectively, indicating the most probable configurations to occur in the growth process. From this point of the analysis, the focus will only be on the lowest energy in the substitutional configuration QD-004, described in Fig. 3.11 (i).

The Lande-factor for DMS systems was defined previously in this Thesis within the **k·p** approach in Eq. (3.30), studying the Mn positioning (ρ) and the exchange interaction parameter (J_0). The exchange interaction can be studied at atomistic scale taking advantage of the density functional theory[3], where the J_0 can be obtained from the energy difference (ΔE_{tot}) between the anti-ferromagnetic (AF) and ferromagnetic (FM) states, as shown in Eq. below:

$$\Delta E_{tot} = E_{AF} - E_{FM}. \tag{3.31}$$

[3]These calculations were performed using the Viena *ab initio* Simulation Package (VASP), wherein the details are found in the appendix D.

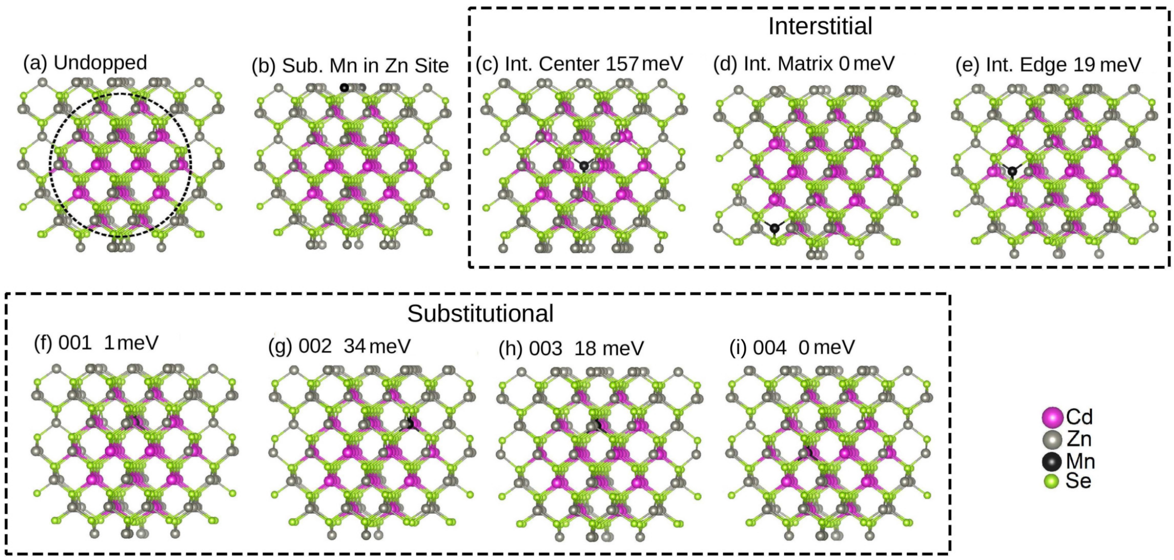

Figure 3.11: CdSe QD embedded in a ZnSe matrix undoped and doped by a Mn impurity. Panel (a) represents the undoped QD, where the QD region is indicated by a circle. In panel (b) the Mn atom is shown replacing the zinc atom in the matrix surrounding the QD. The interstitial Mn doping sites are (c) in the center, (d) in the matrix and (e) in the edge of the QD. The substitutional Mn atom replaces the Cd atom in the configurations represented in (f-i) panels.

The spins alignment for the FM and AF states induced by the manganese spin ordering is calculated by the total energy difference given in Eq. (3.31). The spins of the host material interact with the Mn spin impurity. In order to perform AF calculations, the total spin was assumed at 2, wherein a delocalized spin density of $-1/2$ with opposite spin is created. Similarly for the FM state, the total spin is fixed at 3 and the electrons spin around the impurity was observed at $-5/2$. In both cases, the Mn spin was preserved at $5/2$ and only the magnetic exchange is considered. Therefore, for AF calculations, the spin density around the impurity is aligned and, for FM, is co-aligned. In this context, the solution of the Schroedinger Eq. for the impurity contribution is given by: [225, 228–230]

$$E_G = x_{eff} N_0 \alpha \langle S_z(x_{eff}, B, T)\rangle \, , \tag{3.32}$$

where $N_0\alpha$ is the intensity of the exchange interaction between the electronic levels of the host material and impurities, $\langle S_z(x_{eff}, B, T)\rangle = S_0 B_j(x)\left[S_G g_G \mu_B \frac{B}{T+T_0}\right]$ with $B_j(x)$ the Brillouin function, S_0 the material parameter, S_G the spin impurity, g_G the Lande-factor of impurity, T_0 and T are the Curie-Weiss parameter and the temperature, respectively. Therefore, in these calculations, the initial magnetic moment for manganese atom was specified and fixed its spins for ferromagnetic and anti-ferromagnetic calculations with spin average

$\langle S_z \rangle_{total} = 6$ and 4. It was noted that the manganese preserves its local electronic distribution and there is a difference in the total magnetization in each calculation. The electrons of the impurity provides an alignment around it. The consequence is the hybridization between the *p* states of the selenium and *d* states of the manganese. The Brillouin function describes the magnetic behavior of the material as function of the spin impurity,

$$B_j(x) = \frac{2S_G + 1}{2S_G} \coth\left(\frac{2S_G + 1}{2S_G} x\right) - \frac{1}{2S_G} \coth\left(\frac{1}{2S_G} x\right), \tag{3.33}$$

where $x = \frac{g\mu_B S_G B}{K_B T}$. Note that $\langle S_z(x_{eff}, B, T) \rangle$ represents the thermal average of the spin operator S_z. In Fig. 3.11(i), the ratio of the substitutional Mn atom is $x_{eff} = 1\,\%$ and the thermal average of impurity spin is $\langle S_{\text{Mn}} \rangle = 5/2$. In this way, Eq. (3.33) becomes:

$$N_0\alpha = J_0 = -\Delta E_{tot}/x_{eff}\langle S_{\text{Mn}} \rangle\ . \tag{3.34}$$

In order to describe the CdSe:Mn using density functional theory, we employed the Hubbard DFT+U correction proposed by Dudarev *et al.* [140] The adjustment used was 7.0 eV in Cd and Zn d-states and no correction was used in p-Se levels. The choice of these values improves the description of the lattice parameters of ZnSe and CdSe in comparison with the experimental data. The details concerning the DFT+U correction in d-Cd and d-Zn shells and the obtained exchange interaction parameter (J_0) can be found in appendix D. In order to increase the accuracy in the description of the impurity, the Hubbard U_{eff} in Mn-d orbitals was varied. A visual illustration of J_0 is shown in Fig. 3.12. It is worth noting the strong dependence between the U_{eff} correction in d-Mn states and J_0, where the J_0 may vary two orders of magnitude when the U_{eff} increases from 0.0 to 7.0 eV, as depicted in the panel (a). This strong dependence is elucidated by the local density of states (LDOS), given in Fig. 3.12(b) for U_{eff}= 0.0, 3.0 and 7.0 eV. For the curves without correction in d-Mn, the unrealistic value of $J_0 \simeq 1.77$ eV defines the strong hybridization between the p-Se and d-Mn shells. Panel (b) indicates that the d-Mn peaks is shifted to lower energies due to increased correction, becoming more localized and decreasing its dispersion in the valence band. By decreasing the hybridization due to the U_{eff} correction, the value of the J_0 decreases and the exchange interaction between the impurity and host material becomes smaller. This lower hybridization is indicated by the U_{eff}= 7.0 eV in d-Mn shells in the same panel (b), where a smaller energy is required to separate the d-Mn and p-Se shells, leading to a very low value of J_0.

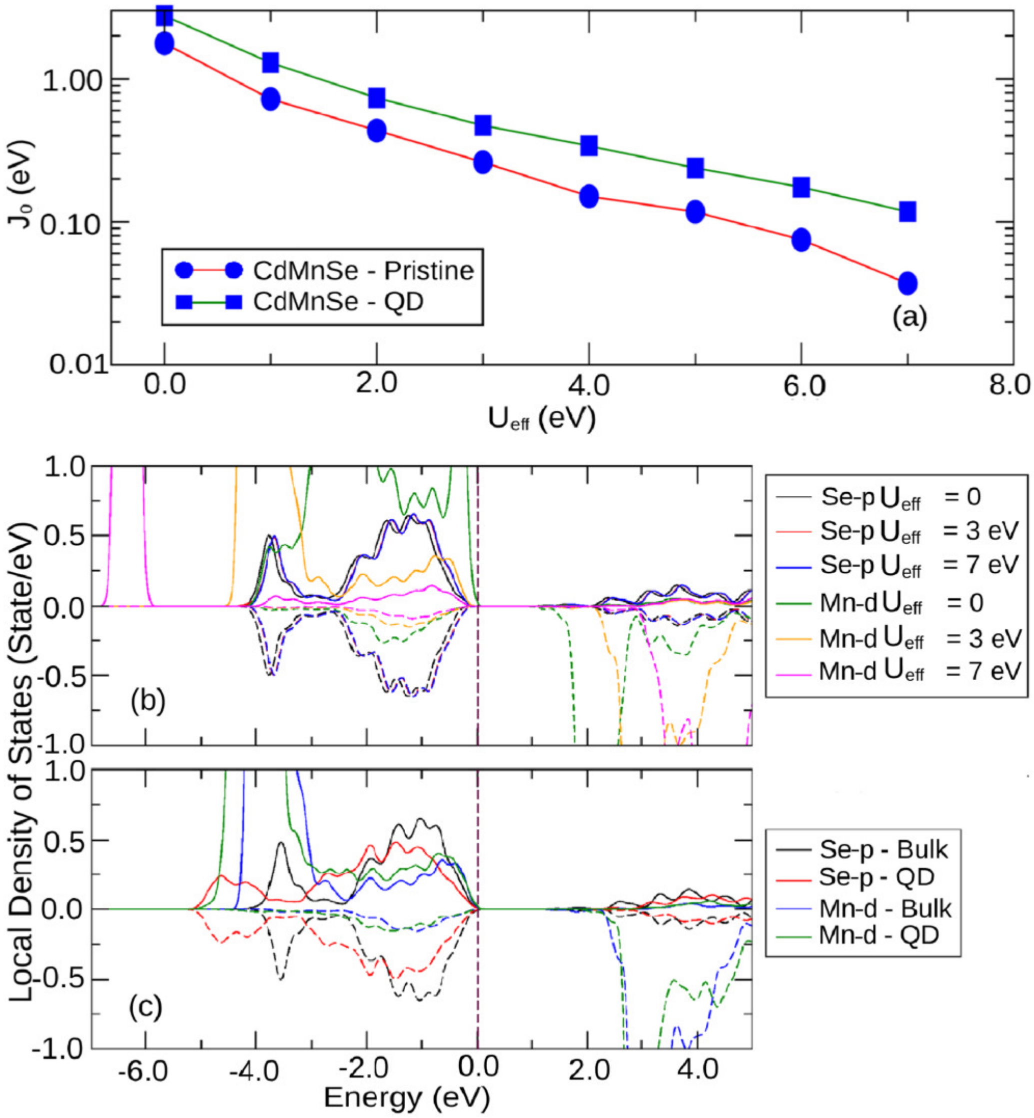

Figure 3.12: Exchange interaction term (J_0) and local density of states for bulk without and with cadmium selenide QD doped by manganese. The CdSe QD is surrounded by ZnSe atoms. In panel (a) the calculated J_0 term is shown with Hubbard correction for the bulk with and without QD. In panel (b) the local density of states is presented for CdMnSe bulk without QD using $U_{eff} = 0$, 3 and 7 eV in p-Se and d-Mn states. In part (c) the local density of states is shown for CdMnSe bulk with QD in comparison to the bulk without QD using $U_{eff} = 3$ eV in d-Mn states.

The experimental observation of the exchange interaction due to the incorporation of Mn impurities in CdSe pristine bulk material, namely, J_0=0.26 eV, [217] is reproduced with U_{eff}=3.0 eV. However, the values available in the literature correspond only for the pristine cases. Thus, the proposal of this investigation is to obtain the exchange interaction parameter for QDs. The presence of the QD inside the bulk provides changes in the quantum confinement, stress in the atoms, and new chemical potential. Consequently, the J_0 value will change. In panel (c) of Fig. 3.12, the calculated values of the J_0 are depicted for CdSe QDs in ZnSe substrate doped with substitutional Mn, replacing the Cd inside the QD. The J_0 for the doped QD is almost twice the pristine case. Thus, the U_{eff}= 3.0 eV corresponds to J_0=0.47 eV, indicating a higher magnetic coupling due to the lattice mismatch of the 7.31 % between the CdSe and ZnSe structures, which cause a compression of CdSe.

3.6.1 Stress tensor effects

The lattice parameter of cadmium selenide is higher than the zinc selenide. Thus, the CdSe atoms are strained in the ZnSe host material, which leads to a compression of the atomic bonds and changes the confinement profile. In consequence, new optical and electronic properties appear in the heterostructure. The theoretical effects of the stress tensor can be simulated through atomistic investigations performing *ab initio* techniques. Point defects[4] and the incorporation of impurities in the growth moment practically does not change the lattice parameter of the cell. In order to study the stress in the electronic properties, the total density of states of the CdSe bulk model is presented in Fig. 3.13, depicting the stress of 7.31 %, compressing and enlarging the lattice parameter. Taking as reference the structure in absence of the stress effects, as indicated by the black curve in Fig. 3.13, the variation of the lattice parameters changes the confinement profile and provides the displacement of quantum states of the stressed structures.

3.6.2 Effective coordination number concept

Here, the structural properties of the CdMnSe QD in ZnSe host material were studied within effective coordination number (ECN) concept using the coordination number (CN) studies. In CN theory, all bonds lengths between the atom i and its surrounding j with a smaller cutoff parameter (d_{cutt}) receives a unique weight ($w_{ij} = 1.0$). Thus, CN is applied for symmetrical configurations by counting the number of the bond lengths smaller than d_{cutt}, including the nearest neigbohrs. However, for non-symmetrical systems, the CN concept needs improvements in the description of different bonds lengths and the weights must follows these bonds variations ($w_{ij} \neq 0$). In ECN concept the different weights are

[4]In the chapter 4 the consequence of point defects is studied in cadmium selenide QDs grown on zinc selenide substrate.

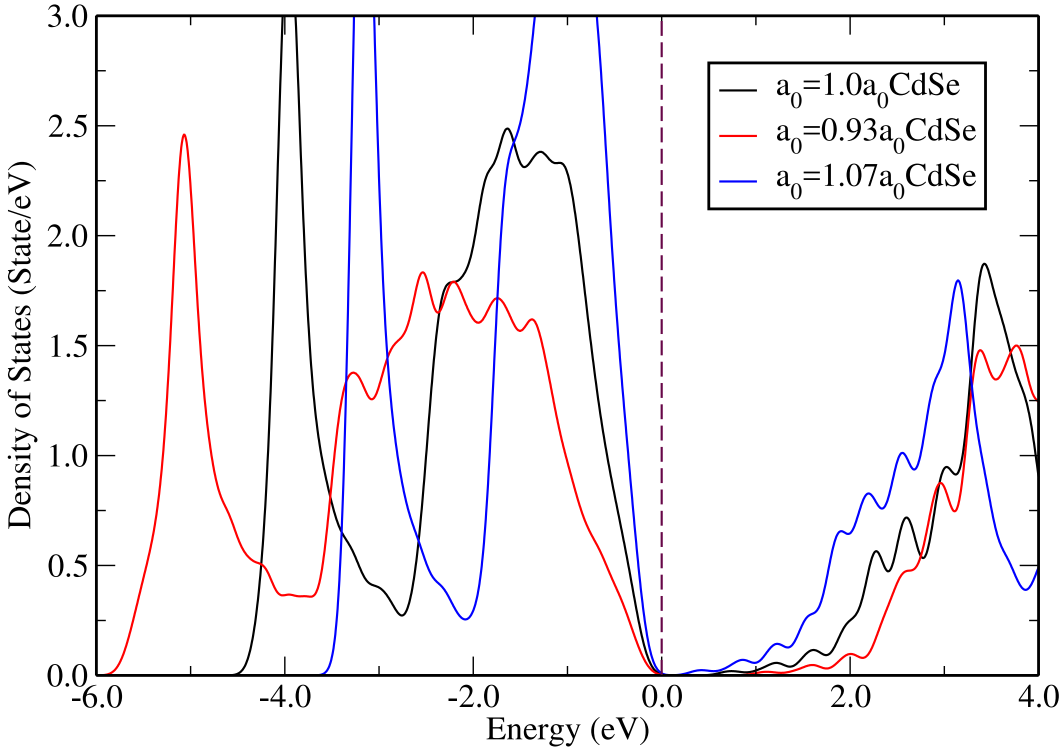

Figure 3.13: Total density of states (DOS) of cadmium selenide bulk tensioned by 7.31 %. The stress is equally introduced in the cartesian directions, compressing or enlarging the bulk. The DOS of the stressed structures is compared with the DOS of the same geometry without pressure.

included, assigned for each bond length (d_{ij}). Usually, the ECN concept is calculated to study a particular i atom strongly linked with the closer j atom. Thus, small changes in the environment and distortions in the lattice must be taken into account, where the weight is calculated considering the weighted bond lengh. The ECN$_i$ is obtained through the self-consistently cycle: [231]

$$ECN_i = \sum_j exp\left[1 - \left(\frac{d_{ij}}{d^i_{av}}\right)^6\right], \tag{3.35}$$

where d_{ij} is the distance between the i and j atoms and the average weighted bond length (d^i_{av}) is given as follows:

$$d^i_{av} = \frac{\sum_j d_{ij} exp\left[1 - \left(\frac{d_{ij}}{d^i_{av}}\right)^6\right]}{\sum_j exp\left[1 - \left(\frac{d_{ij}}{d^i_{av}}\right)^6\right]}. \tag{3.36}$$

For N number of atoms, the ECN average is written as:

$$ECN = \frac{1}{N}\sum_{i=1}^{N} ECN_i. \tag{3.37}$$

The stop criterion used to obtain the results presented in the appendix D is $|d^i_{av}(new) - d^i_{av}(old)| < 0.00010$, where the smallest bond length distance between the i and j atoms is used as the initial value for the average weighted bond length, given in Eq. 3.36. The positioning of the manganese atom in the cadmium selenide QD or in the zinc selenide substrate provides changes in the bond lengths of the system compared to the undoped QD bulk. These changes in the bonds are higher in interstitially configurations than in substitutionally geometries due to the presence of the Mn atom in the non-crystalline position. In appendix D, Table D.3, the ECN and d^i_{av} are presented for the doped and undoped QD structures, where a comparison between PBE functional with and without the Hubbard correction was performed.

Chapter 4

Calculations for vacancies in solids

Imperfections in solids are unavoidable in the growth phase, providing changes in the structural, optical, and electronic properties of these solids due to the deviation of the lattice periodicity. Some interesting properties of the crystals are related to the concentration of defects, such as the electric conductivity and luminescence phenomena. [232] Imperfections caused by external agents will disturb the equilibrium of the nanostructure, whose dynamics is described in terms of the thermodynamic variables. In the asymptotic regime, the nanostructure tends to reach the charge neutrality.

The imperfections in the crystalline structure can be classified according to their dimensionality, such as zero-dimensional or point-defects, one- and two-dimensional defects. [97] The point defects are characterized by single atomic sites. Examples of point defects are the vacancies, defined by the removal of one atom from the crystal lattice. Point defects can be studied in two groups, intrinsic and extrinsic defects. Intrinsic imperfections are, usually, vacancies. The presence of the vacancies in the periodic cell originates a strain in the lattice. Vacancies and interstitial defects can move in the crystal, where the migration energy must be overcome. [97] Substitutional magnetic impurities are considered extrinsic defects. The substitutional and interstitial magnetic impurities were studied in chapter 3 of this Thesis.

As mentioned, the properties of the semiconductor devices can be affected by the introduction of the structural asymmetries, magnetic atoms, and vacancies. Thus, in the next subsections we will study the effect of the vacancies in the electronic properties of cadmium selenide quantum dots within zinc selenide host material. The investigations were performed within the density functional theory.

4.1 Energy of formation

The analysis of the formation energy (FOE) is crucial for the investigation of the imperfections in solids. FOE allows to predict the optical and electronic properties of the defective material. Using the formation energy, it is possible to analyze the charged defects. For vacancies, the FOE is defined by the required energy to remove one atom from the crystal. In the supercell approximation, the formation energy ($E_F(\alpha, q)$) of a vacancy constituted by different atomic species (α) with a charged[1] state (q) is given by:

$$E_F(\alpha, q) = E_d(\alpha) - E_p(bulk) - \sum_{i=1} n_i \mu_i + q(\mu_e + E_{VBM}), \tag{4.1}$$

where $E_d(\alpha)$ and $E_p(bulk)$ are the total energies of the supercell with a defect (α) and the pristine material, respectively. The number (n_i) of atoms inserted ($n_i > 0$) or removed ($n_i < 0$) is related to the chemical potential (μ_i) for each atomic specie (i). The Fermi energy (μ_e) is related to the top of the valence band (E_{VBM}) of the pristine material. [233, 234] In addition, E_{VBM} can be understood as the required energy to remove one electron from the VBM to a reservoir. In the formulation of Eq. (4.1), we can study one or several defects with different chemical potentials. The energy variations in the supercell due to the presence of defects are represented by the difference $E_d(\alpha) - E_p(bulk)$. For charged vacancies ($q \neq 0$), the formation energy varies with the Fermi level of the pristine material. For finite systems, such as supercells, the top of the valence band must be corrected for charged states. The correction is based on the difference between the average potential in a region of the supercell far from the defect and the same average potential in a region without the defect. [235, 236] In semiconductor systems, the chemical potential depends on the growth conditions and the stoichiometry proportion. If the system has an excess or a deficiency of certain atomic specie, the system is called *rich* or *poor* in this element, respectively. [237–239]

[1]The charge can be positive or negative.

4.2 Defect induced magnetism in CdSe QDs

The study of the origin of the magnetism in non-magnetic materials due to external agents is a challenging topic in low-dimensional systems. It has attracted the attention of the scientific community for this area, becoming a paramount task and an active research field. Ferromagnetic ZnO thin films grown by polymer-assisted deposition increases its magnetization due to the introduction of zinc vacancies, for instance. [240] The control of magnetism in graphene by applied bias voltage becomes desirable for spintronic nanodevices. [241] The origin of magnetism in inorganic CdSe quantum dots has been previously studied. [242–246] Meulenberg, [244] Sundaresan [245] and Seehra [247] studied the emergence of the paramagnetism in CdSe QDs as a source of magnetism due to their control of their surface chemistry. Singh presented the evidence of magnetism in copper-doped cadmium selenide nanoparticles. [243] The exchange interaction in these types of nanoparticles must be considered to be a crucial factor for the magnetic ordering. [246] However the results of appearance of the magnetism is still profusely discussed in the literature. For this reason, the purpose of this section is to explore the experimental details from our collaborators, which indicate that the magnetism arises from defects in self-assembled CdSe QDs grown within a ZnSe host lattice, where the experimental investigations are corroborated by the theoretical descriptions.

Performed in 2006 and grown under the same conditions, a single layer of the QDs does not presented magnetic moments, unlike the two QD layer system. Therefore, these results seemed paradoxical. In this study, the optical evidence of the nanomagnetism in non-magnetic CdSe QDs was detected in its micro-photoluminescence (PL) and the spin-dynamics is characterized by its time resolved polarized emission.

As reported in Ref. [248], the QDs were grown through a self-assembling process. Fig. 4.1 (a), taken from Ref. [249], displays the cross section of the transmission electron microscopy images (TEM), where the arrows indicate the QDs formations. The layers of CdSe QDs are separated by ZnSe atoms around 3 nm, allowing an effective vertical electronic coupling. The characterization of the optical response was performed by exciting the sample with an argon ion laser and the micro-photoluminescence was detected in a cryostat with the temperature ranging between 2-5 K. The modulation of the magnetic field strength allows to study the polarized QD emission. Thus, Figs 4.1 (b)-(c) represent the emission from single

QDs, labeled QD1, QD2 and QD3. It is important to note that the peak splitting is verified at B=0 even for unpolarized detection, where the lifting of the spins degeneracy under the magnetic field is linked to the Zeeman effect. Fig 4.1 (d) shows the peak positions for the emission lines of the QD2 and in the panel (e) is depicted its respective energy splitting. For the case B=0, an energy splitting is noted in the experiment with hysteresis, indicating a possible magnetic ordering. In contrast, these results are not verified in the micro-PL of the single QD layer. [249]

Fig. 4.2 show the transients of the time-resolved PL with the linear excitation, for two circularly polarized detection and measured at B=0. Due to the magnetic field effects acting on the spin regime, the spin-dynamics leading to the Rabi-like flopping can be studied by the following model:

$$i\hbar\frac{d}{dt}\begin{pmatrix} s_+ \\ s_- \end{pmatrix} = \begin{pmatrix} \hbar\omega_z + i\gamma & \alpha_1 \\ \alpha_2 & -\hbar\omega_z + i\gamma \end{pmatrix}\begin{pmatrix} s_+ \\ s_- \end{pmatrix}, \tag{4.2}$$

where we considered an anisotropic spin-decoherence mechanism through the parameters $\alpha_{1,2}$ and a lifetime broadening γ of the Zeeman splitting term, $\hbar\omega_z = 1/2g^*\mu_B B$, inducing the wavefunction decay. The solutions of the system are given by:

$$s_{+(-)}(t) = e^{-\gamma t}\left[\cos(\Omega t) - (+)\, i\frac{\omega_z - (+)\,\alpha_{1(2)}}{\Omega}\sin(\Omega t)\right], \tag{4.3}$$

with $\Omega = \sqrt{\omega_z^2 + \alpha_1\alpha_2}$, where $s_+(0) = s_-(t)$. In Fig. 4.2 (a) we show the spin oscillations given by $|s_{+(-)}|^2$ with $\omega_z = 0.09\text{ps}^{-1}$, $\gamma_z = 0.0015\text{ps}^{-1}$, $\alpha_1 = 0.008\text{ps}^{-1}$, and $\alpha_2 = 0.003\text{ps}^{-1}$. In panel of Fig. 4.2 (b) is depicted the periodicity of the spin-oscillation, where the degree of the circular polarization $(|s_+|^2 - |s_-|^2)/(|s_+|^2 + |s_-|^2)$ has been displayed. The period $T = \pi/\Omega$ is related to the spin-splitting originated by the internal field B^{in} and the effective g-factor (g^*), which varies according to the confinement profile and asymmetries, as described in Ref. [191]. Note that the annulment of the Zeeman splitting leads to a certain ambiguity in Fig. 4.1 (e).

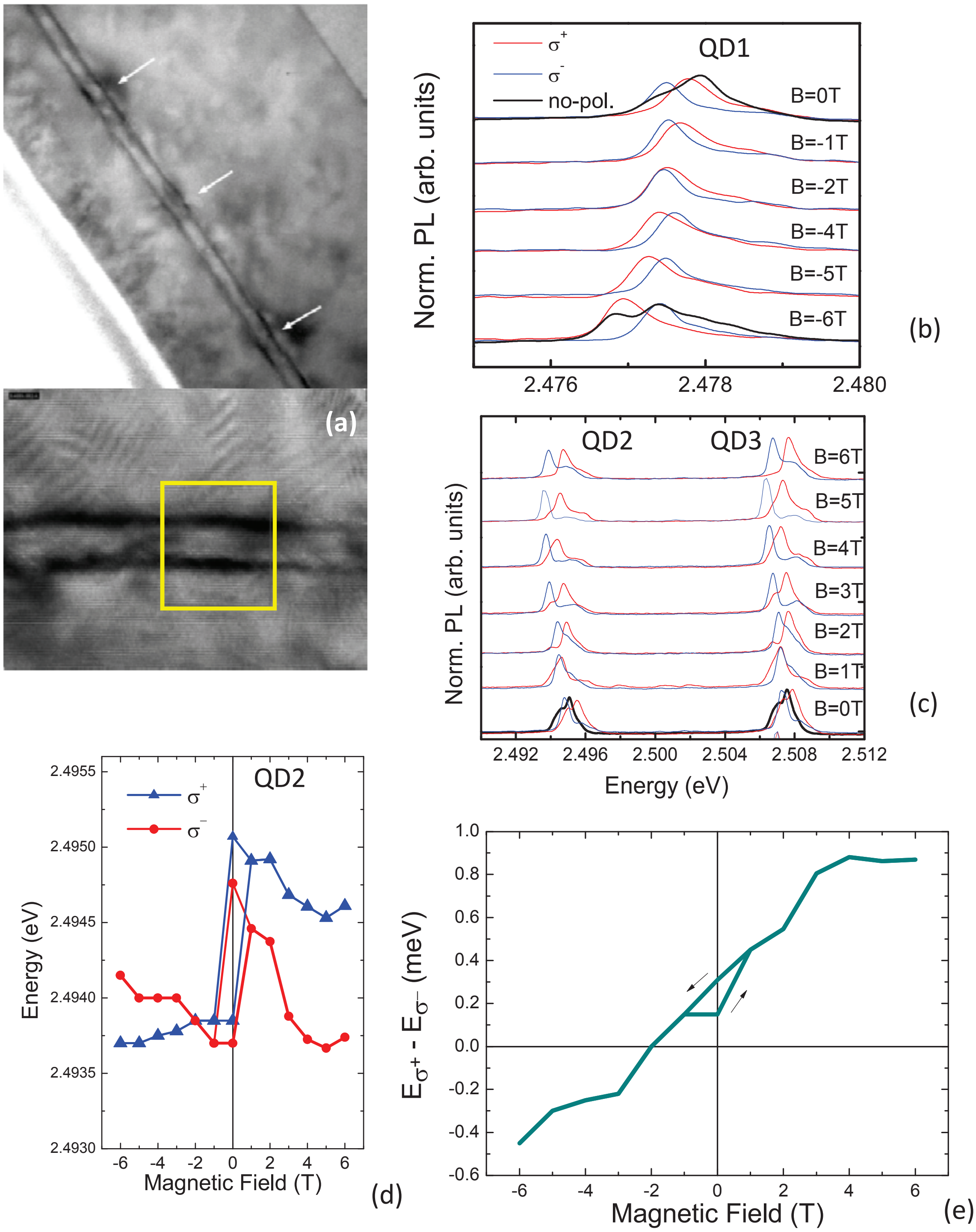

Figure 4.1: (a) Transmission electron microscopy images (TEM) of two monolayers of the CdSe quantum dots. In panels (b) and (c) the micro-photoluminescence spectra is represented for three different quantum dots for several fields and circular polarized detection. The unpolarized emission spectra were also added for certain fields values. Panel (d) depicts the peak emission positions of the quantum dot 2 (QD2) as function of the magnetic field strength for σ^+ and σ^- circular polarized emissions and part (e) details the Zeeman splitting as function of the magnetic field.

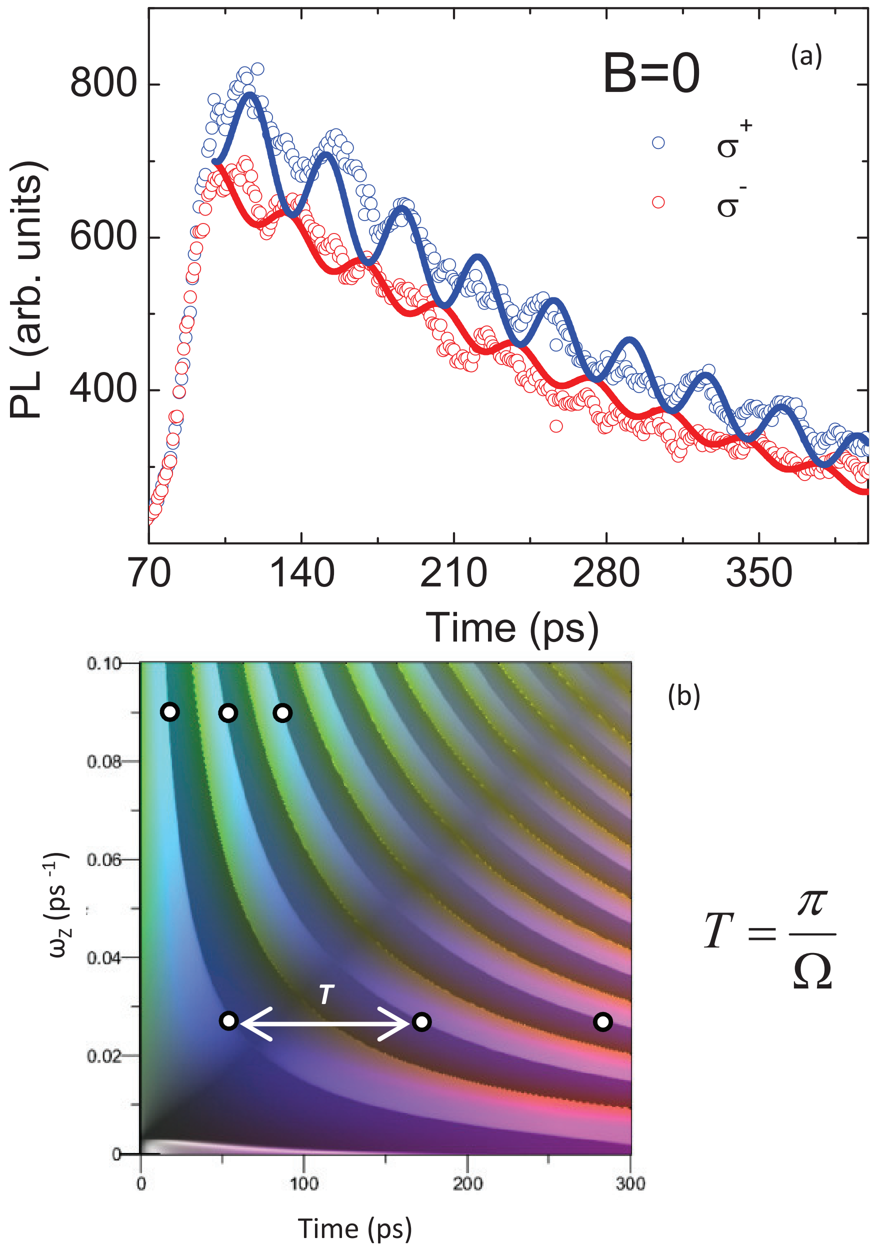

Figure 4.2: (a) Time resolved integrated intensity measured at zero external field, B=0, for a circular polarized emissions σ^+ and σ^-, indicated by open circles. In solid curves we show the spin-density evolution for each polarization. Panel (b) represents the degree of circular polarization as function of time and frequency ω_Z.

4.2.1 Cadmium selenide in zinc selenide host material: a density functional theory investigation

Several approaches have been presented in the literature to investigate the point defects in order to obtain a better understanding of the nature of the intrinsic magnetism that emerges in a variety of seemingly non-magnetic QDs systems. [250, 251] Here, the origin of the vacancies in the growth process and the local magnetic moment attributed to them are related with the paramagnetic centers.

The appearance of the nano-magnetism in cadmium selenide (CdSe) QDs in zinc selenide (ZnSe) substrate is described by emulating the electronic structure at atomistic level. The theoretical investigations using *ab initio* calculations based on density functional theory were performed. [88, 89] The spin-polarized generalized gradient approximation (GGA) and the semi-local Perdew-Burke-Erzenhof (PBE) exchange and correlation functional were used. [102] The self-consistent Kohn–Sham Eq. were solved using the Projector Augmented Wave (PAW) method [177, 179] as implemented in the Vienna *ab initio* Simulation Package-VASP. [252, 253] The details of the calculations and the theoretical approach are shown in the appendix E. Aiming to describe the experimental results, we extensively performed simulations of mono-vacancies of Cd, Zn and Se in several positions searching for spatially localized paramagnetic centers. Fig. 4.3 depicts the most relevant neutral point defects ($q = 0$), as well as the isosurfaces of the local magnetic moments. However, placing the Se vacancies inside, at the edge, or outside of the QD, does not provide the emergence of localized magnetic moment. Thus, only the geometry with the lowest energy, *Se-in*, as shown in Fig. 4.3 (d), is discussed in these results. In a comparative way, the configurations presented in Fig. 4.3 are a good sampling, denoting the main properties of the investigated defects. Taking advantage of the formation energy[2], we predict the most probable kind and position of the vacancy.

In Fig. 4.3 the structures used in the *ab initio* calculations are shown. The simulations were performed using a cubic supercell comprised by 38 atoms of Cd, 108 atoms of Se, and 70 atoms of Zn. The superlattice (L) was obtained from the zinc selenide lattice parameter of a conventional cell, where $L = 3 \times a_0^{ZnSe}$. The selenium, cadmium and zinc atoms are represented in green, magenta and gray color, repectively. The spin density isosurfaces for charged vacancies are shown in red, which values for (a) and (b) panels are $-0.012\, e\, \mathrm{\AA}^{-3}$ and $-0.014\, e\, \mathrm{\AA}^{-3}$, respectively. For panel (c), $-0.016\, e\, \mathrm{\AA}^{-3}$ was used. The selenium vacancies, depicted in the structure (d), did not show the magnetic moment in the calculations. The Cd vacancies are placed (a) inside, (b) at the edge of the QD, while Zn defect (c) is placed in the matrix of the QD and the Se vacancy is (d) inside the QD, namely, Cd-in, Cd-edge, Zn-matrix and Se-in, respectively.

[2]The formation energy was defined in section 4.1.

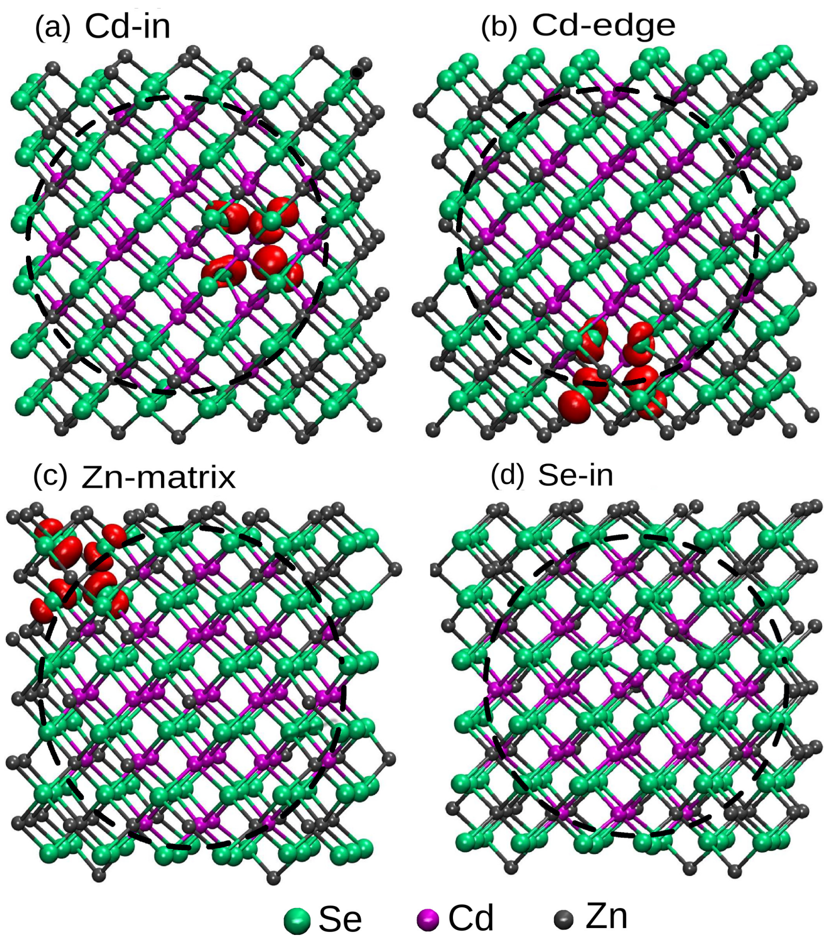

Figure 4.3: Geometries and spin density isosurfaces for uncharged cadmium selenide (CdSe) QDs embedded in a zinc selenide (ZnSe) host material with vacancies. Panel (a) the geometry *Cd-in:* Cd vacancy inside the QD and isosurface $0.012\,e\,\text{Å}^{-3}$. Panel (b) depicts the structure *Cd-edge:* Cd vacancy at the edge of QD and isosurface $0.014\,e\,\text{Å}^{-3}$. Panel (c) indicates the structure *Zn-matrix:* Zn vacancy at the host material and isosurface $0.016\,e\,\text{Å}^{-3}$. Panel (d) represents the structure *Se-in:* Se vacancy inside the QD, which does not present magnetic moment. The QD region is depicted by a circle .

Note that the electronic potential does not provide changes in the formation energy for uncharged calculations. The results indicate that the uncharged Cd-in geometry represents the smallest formation energy between the considered structures, pointing to the higher probability to occur this kind of defect. In addition, the results for neutral defects predict a d^0 magnetism induced by monovacancies created at cationic site. The obtained magnetic moment of $2\mu_B$ is due to their four Se atoms in the neighboring of the defect, as depicted in the spin density isosurfaces in panels (a-c) of Fig. 4.3. On the other hand, neutral Se-in geometry do not induce a localized magnetic moment, [254] which appears only in charged frameworks. Therefore, providing selenium uncharged vacancies does not vary the magnetic moment in relation to the pristine system. Concerning the charged vacancies, negative values of charge determines the magnetic moment $1.0\,\mu_B$, where Cd-in structure shows the smallest formation energy. Moreover, the calculated FOE for positive charged vacancies, where the structure Cd-in has the smallest intensity, shows the magnetic moment of 3.0 μ_B for Cd-in and Zn-matrix structures, and 1.0 μ_B for Cd-edge and Se-in geometries.

Table 4.1: Calculated values for the geometries presented in the Fig. 4.3. qC, Mag. Mom and E_{For} are the charge, magnetic moment and formation energy, respectively.

Struct.	qC	Mag. Mom	E_{For}
	[μ_B]	[μ_B]	[eV]
Cd-in	−1.00	1.00	2.59
Cd-in	0.00	2.00	2.45
Cd-in	1.00	3.00	4.71
Cd-edge	−1.00	1.00	2.83
Cd-edge	0.00	2.00	2.70
Cd-edge	1.00	1.00	4.97
Zn-matrix	−1.00	1.00	3.85
Zn-matrix	0.00	2.00	3.69
Zn-matrix	1.00	3.00	5.95
Se-in	−1.00	1.00	4.42
Se-in	0.00	0.00	3.19
Se-in	1.00	1.00	5.52

In Table 4.1 we show the results of the FOE simulations, where qC, Mag. Mom and E_{For} are the charge, magnetic moment and formation energy for the calculated structures. In addition, the possibility to occur charged defects was analyzed for other systems. [233] A visual representation is given in Fig. 4.4, which provides a comparison between the formation energies among all charged vacancies. [239, 255] The chemical and electronic potentials were obtained from the free-atoms and from the valence band maximum (VBM) calculations, respectively.

Note that defects can induce the appearance of local magnetic moments. For these results, the local magnetic moment varies μ_B, whereas the *Se-in* neutral vacancy is the only non-magnetized structure and Cd-in, Cd-edge and Zn-matrix uncharged geometries lead to a local magnetic moment of $2\mu_B$. Furthermore, the neutral defects have the lowest formation energy. In particular, the uncharged Cd-in vacancy has the lowest formation energy among all defects, which is lower by 250 meV in relation to the Cd-edge structure. Se-in geometry has 740 meV greater than the lowest energy configuration and Zn-matrix has the highest formation energy between all the structures. The charged vacancies have the higher FOE. Therefore, uncharged structures are preferred in the growth process.

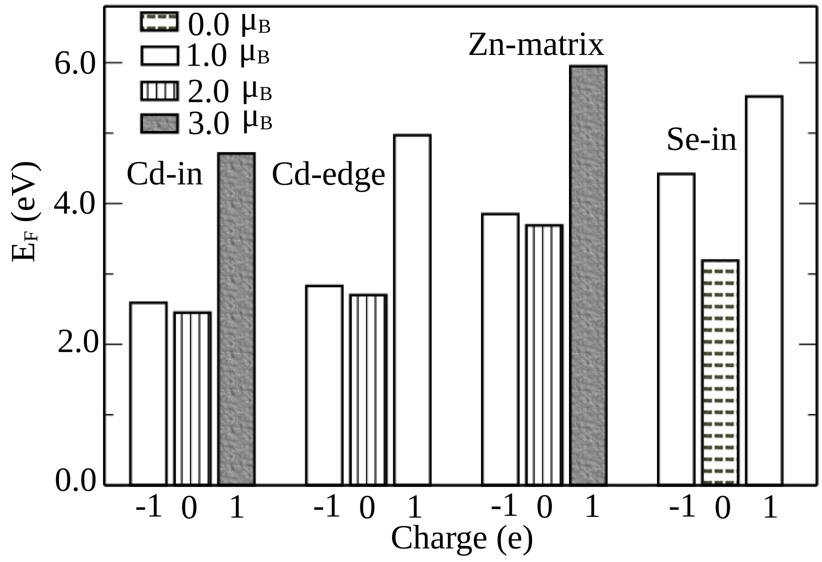

Figure 4.4: Formation energy for Cd-in, Cd-edge, Zn-matrix and Se-in structures, illustrated in Fig. 4.3. The calculations were performed for charged and uncharged states. The magnetic moment is indicated for each calculated structure.

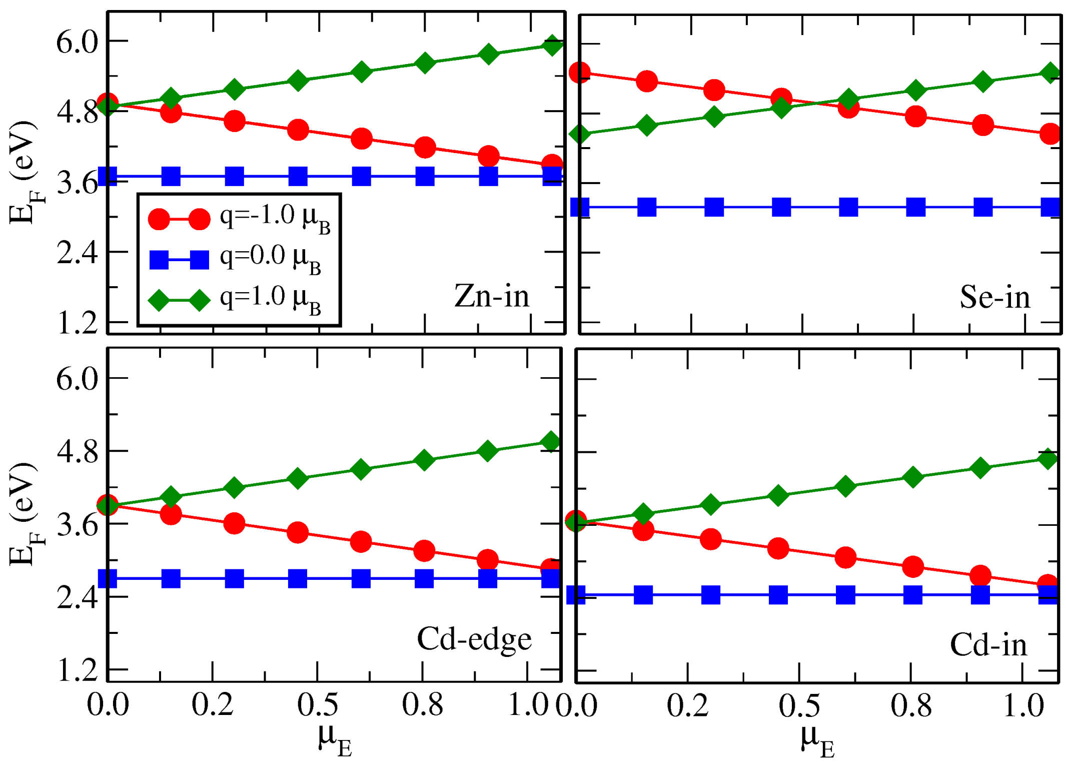

Figure 4.5: Formation energy of charged and neutral geometries presented in Fig. 4.3 as function of the electronic chemical potential, where the structures *Zn-in*, *Se-in*, *Cd-edge* and *Cd-in* denotes the Zn vacancies in the matrix, Se inside the QD, Cd at the edge and inside the QD, respectively.

In a real experiment, the electronic potential μ_E can vary from the VBM to CBM, [256] as shown in Fig. 4.5. Thus, the calculations were performed ranging μ_E from 0 to the gap energy. The obtained results show that neutral defects are the most stable. The electronic potential close to VBM favors the positive charged states, being at least 1.2 eV higher than the neutral configurations. On the other hand, μ_E close to the CBM favors the occurrence of negative charge defects. Moreover, uncharged calculations have the lowest formation energies among all calculations. In summary, the lowest formation energy is obtained when the Cd vacancies are placed inside and close to the QD center, where the local magnetic moment obtained is $2\mu_B$.

The lattice mismatch between the host material, ZnSe, and the QD structure, CdSe, provides an unavoidable strain in the system. This strain promotes a decrease in the bonds lengths, changing the semiconductor confinement. Furthermore, vacancies can also induce strain in the crystal, allowing the rearrangement of the atoms in the supercell.

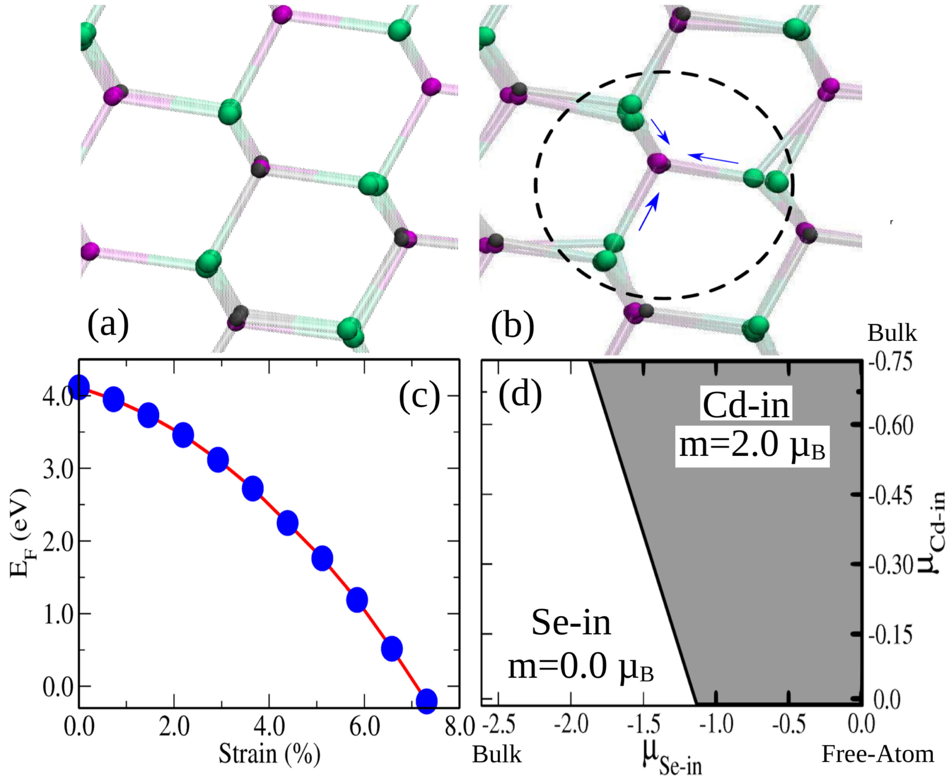

Figure 4.6: Formation energy and strain calculations. In panel (a) the QD atoms of the supercell are shown without defect and (b) the same QD region with defect, representing the *Cd-in* geometry. The atomic displacements are indicated by blue arrows. In panel (c), the strain is calculated as function of the formation energy, where strain effects are due to the lattice parameter variation. Panel (d) shows a comparison between the Cd-in and Se-in chemical potentials.

A better understanding of the formation energy is presented in Fig. 4.6, where, in panel (a), an array of QD atoms without defect and in panel (b,) an array of QD atoms with defect are represented. The atomic distortions in relation to the pristine structure are indicated in this panel by blue arrows, where the surrounding Se atoms of the defect are dislocated towards the vacancy. A relation between the strain and the formation energy is shown in panel (c) of Fig. 4.6, where the atomistic calculations were performed with 63 atoms. Note the decrease of the strain and the increase of the FOE. The absence of strain indicates that the calculation was performed using CdSe lattice parameter. Decreasing the lattice parameter of the supercell until the ZnSe lattice constant, the strain increases and the formation energy is reduced. The variation in E_F reaches 4.0 eV for strain values close to 7.0 %. Therefore, the strained CdSe QDs within ZnSe lattice facilitates the defects formation in the core region. In addition, the chemical potential of the defects can vary from the free-atom until the bulk. Thus, panel (d) represents a comparison between the Cd-in and Se-in chemical potentials for uncharged calculations, where the smaller formation energy is obtained by Cd-in geometry using the free-atom chemical potential.

Chapter 5

Adsorption properties of organic molecules on 2D semiconductor layers

Developments in semiconductors physics are results of complex theoretical and experimental endeavors. The understanding of the electronic properties of the systems based on 2D semiconductors allows to directly apply the obtained results in nanodevices, such as temperature sensors. [257] In addition, spintronics has shown promising results with technological proposals. [258, 259] In turn, light sensitive organic molecules have become interesting chemical compounds to functionalize systems, being intriguing components to engineer the electronic structure of two-dimensional layered systems. Thus, advances in nanodevices studies increase the search for light-sensitives organic molecules. [260] The modification of the optical and electronic properties induced by photoirradiation makes these organic molecules interesting to new investigations focused on applications in optical memory, [261] sensors displays, [262] and photooptic keys. [263] All of these properties can be attributed to the trans-cis optical reversibility of the isomers.

Organic molecules (OM) can be studied in two different groups: natural and artificial. The natural are called biomolecules and the artificial are produced in laboratories. In 1937, Hartley [264] noted that the incidence of ultraviolet light in azobenzene [265] can change its geometry leading to the isomerization process between the cis- and trans-geometries. [266–270] Experimentally, trans- is more stable than cis-azobenzene, [260, 271] where the cis- to trans- form can occur in the dark, however, the inverse process, trans- to cis-, is only feasible under the ultraviolet light incidence. [269, 271] Thus, the isomerization process can occur as a response of external factors, becoming the azobenzene an excellent candidate to act as a mechanical switch.

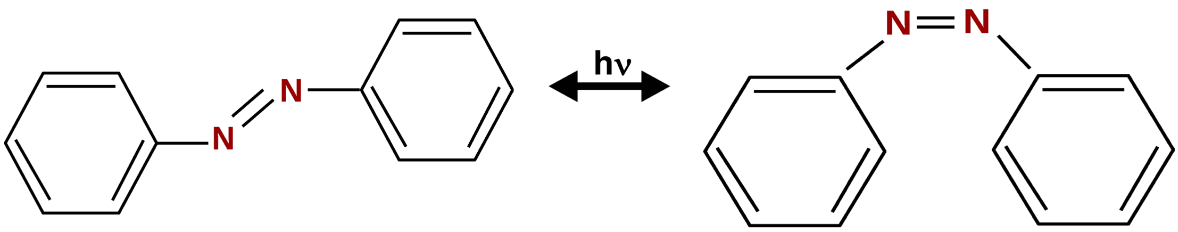

Figure 5.1: Azobenzene isomerization by light incidence with energy $\hbar\nu$. In the left (right), the trans- (cis-) configuration is depicted.

In the left part of Fig. 5.1 the trans- isomer is depicted and, in the right part, the cis-configuration, where the cis-trans isomerization is due to the allowed transitions between the electronic levels. [260, 272, 273] The isomers differ by absorption spectra, refractive index, dielectric constant, and geometric configuration. The introduction of an azobenzene fragment in biological compounds, [274] such as proteins, enzymatic activity, [275] nuclei acids, [276] allows to manipulate biological processes under light incidence.

The characterization of graphene monolayers in 2004 [277] opened the possibility to study the new area of two dimensional materials. [51, 278] Subsequently, graphene was explored in other fields, attracting the attention of the solid state community for 2D materials. [45, 46] Two-dimensional materials can also be obtained from MX_2 compounds, where M is a transition metal, such as the molybdenum (Mo) and Tungsten (W), and X is a chalcogen, such as sulfur (S), selenium (Se) and tellurium (Te). For this reason, they are called transition metal dichalcogenides (TMD). [279] The TMD are candidates for the next generation of quantum devices. [280, 281] The 2D materials have been intensively investigated due to the wide range of applications and the possibility to constitute layered materials used in several areas of knowledge. [40–43, 282–284] In particular, 2D materials have potentials applications in nanodevices. [44] The variation of the number of layers allows the manipulation of the energy gap, where atoms within a single layers are strongly bonded whereas the atoms between layers are coupled by the van der Waals interactions. The incidence of external fields changes the optical and electronic properties of the 2D materials.

Previous *ab initio* calculations investigated the energy surfaces of azobenzene isomers and their intermediate configurations. [285] Comstock, [286] Li [287] and Fu [288] studied the optical absorption of azobenzene on the Au(111), MoS_2 and graphene layers, respectively. Thus, in this chapter we present the adsorption studies of the azobenzene molecule on a molybdenum disulfide ($MoS_2(0001)$) layer. Using first-principles DFT calculations, we explore the results of the cis- and trans-azobenzene isomers placed in several positions on the molybdenum disulfide supporting layer. Taking advantage of the total energy calculations, we analyze the stability of the azobenzene in gas-phase and placed on the surface. Moreover, adsorption energies and work functions are also discussed. In addition, the mechanism of the charge flow between the molecule and the surface were studied within the effective Bader charge concept.

5.1 Atomic configurations: azobenzene

Azobenzene molecules ($C_{12}H_{10}N_2$) belong to the azo-group ($-N{=}N-$). [265] They are composed by two benzene rings linked by the $-C^b-N-N-C^b-$ chain, where the C^b are the benzene rings and the $-N{=}N-$ bonds play a key role in the azobenzene configurations. [265, 273] As discussed above, the azobenzene adopts two isomers, namely, a ground state planar structure or trans-azobenzene, which the two benzene rings and the $-C^b-N-N-C^b-$ chain are in the same plain, and the cis-azobenzene, where the two benzene rings change their orientation due to the $-C^b-N-N-C^b-$ torsion angle. Under ultraviolet light, [260] mechanical stress, or electrostatic stimulation, [263] the trans- changes to the cis-azobenzene. However, the cis- to trans- isomerization can occur spontaneously under dark conditions. [271] For a better understanding of the adsorption studies of the azobenzene molecule on the $MoS_2(0001)$ surface, in the next sections we will adopt both isomers.

5.2 Azobenzene in gas-phase

The equilibrium geometries of the azobenzene isomers were achieved performing DFT total energy calculations. The details of the calculations are reported in the appendix E. We found that the trans- configuration is 0.51 eV lower in energy than the cis-azobenzene, which is in good agreement with the experimental results obtained in the dark, namely, 0.52 eV. [260] By using the VASP package, the optimized ground state of the trans- and cis-azobenzene has an equilibrium angle of 120° between the carbons in the aromatic ring, 115° and 123° concerning the carbon and nitrogen in trans- and cis- isomers, respectively, as shown in the Fig. 5.2. The dihedral angle for $-C^b-N-N-C^b-$ are 180° (trans-) and 10.8° (cis-). The calculated distance between the farthest carbons in the aromatic ring are 9.0 Å for the trans- and 5.5 Å for the cis- configuration, according to the results presented in Ref. [260].

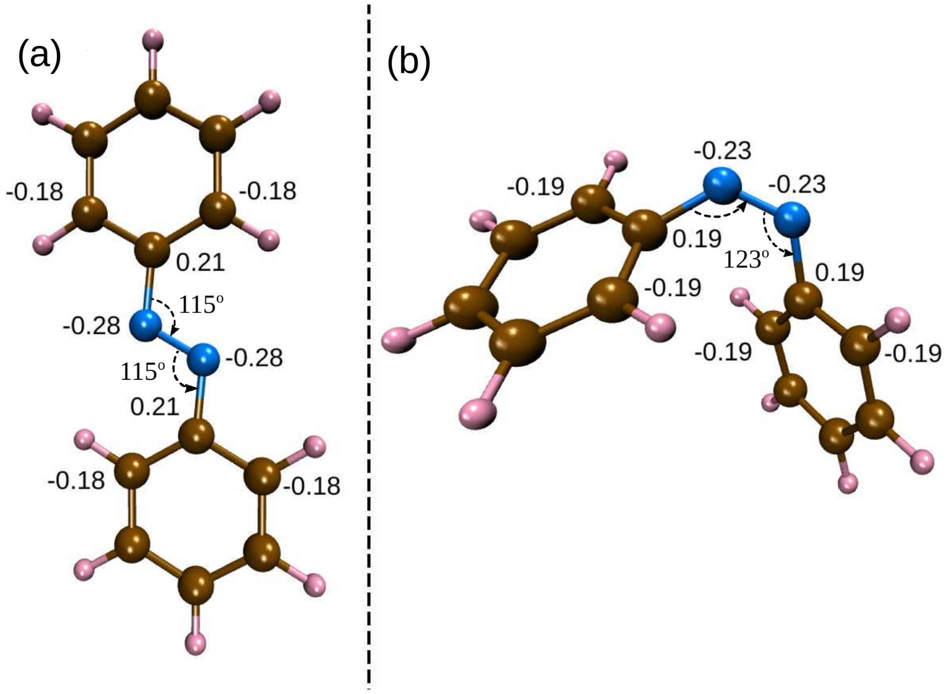

Figure 5.2: Azobenzene in gas-phase. In panels (a) and (b) the trans- and cis-configurations are depicted, respectively. The angles and Bader charge transfer between the atoms are indicated in the Figure. The angles between the carbon and nitrogen atoms for the cis- and trans- isomer are 123° and 115°, respectively. The effective Bader charge on the nitrogen atoms for the cis- and trans- isomers are $-0.28\,e$ and $-0.23\,e$, respectively.

In order to analyze the charge rearrangement between the atoms of the molecule, we calculated the effective Bader charge, as follows:

$$Q_{\text{eff}}^{\text{atom}} = Z_{\text{V}}^{\text{atom}} - Q_{\text{B}}^{\text{atom}} \tag{5.1}$$

where $Z_{\text{V}}^{\text{atom}}$ is the number of valence electrons for the hydrogen (H), carbon (C) and nitrogen (N) atoms and $Q_{\text{B}}^{\text{atom}}$ is the obtained Bader charge for the specific atom in the molecule. In Fig. 5.2, the charge rearrangement is depicted for the most important atoms in the molecule. The effective Bader charge allows to perform the electronegativity analysis, where the negative and positive values of the effective charges indicate the anionic and cationic characters of the atom in the molecule. The effective Bader charge calculation confirms that the nitrogen is the most anionic atom for both structures, namely, $-0.28\,e$ and $-0.23\,e$, in trans- and cis-configurations, respectively. Thus, we expect a larger bond length between the nitrogen atoms in the trans- than in cis-azobenzene, namely, 1.26 Å (trans-) and 1.25 Å (cis-), which is in good agreement with the results presented in Ref. [289]. The C atoms in the aromatic ring have similar effective Bader charge, $-0.18\,e$ and $-0.19\,e$, for the trans- and cis- isomers, respectively, which define approximately the same C – C bond length. The C – N bond length in cis- configuration is higher than for the trans- geometry, namely, 1.43 Å and 1.42 Å, respectively. In Fig. 5.3, we analyzed the local density of states (LDOS) per atom for each chemical specie of the molecule.

5.3 Bulk and layered MoS_2 systems

To better understand the adsorption of the azobenzene molecule on the molybdenum disulfide surface, the MoS_2 bulk and layer properties were investigated. The equilibrium lattice constants, a_0 and c_0, were found, as being 3.16 Å and 12.35 Å, respectively, in the hexagonal $P6_3/mmc$ structure. These results are in good agreement with the experimental results presented in the Ref. [290], a_0 =3.16 and c_0 =12.29 Å, corresponding to deviations of 0.0 and 0.45 %, respectively. As mentioned previously, the layers are linked by van der Waals interactions, where the vdW correction must be introduced in the DFT calculation, playing a key role in the description of the c_0 value. For example, by using the PBE exchange and correlation functional, the relative error is 9.39 %, where the lattice constant is c_0 =13.45 Å. In addition, the vdW interaction between the MoS_2 layers of the bulk does not change significantly the local chemical environment, bond length, effective coordination number, and effective Bader charge in relation to the $MoS_2(0001)$ layer. For example, using Eq. (5.1), we obtained an effective cationic charge on the Mo atoms of $0.74\,e$, and also, an anionic charge of $-0.37\,e$ on the S atoms, which changes to $-0.36\,e$ in the single $MoS_2(0001)$ layer.

Concerning the electronic properties, we calculated the local density of states and the band structure of the MoS_2 systems, depicted in Fig. 5.4. For the bulk phase, the valence band maximum (VBM) is located at the Γ-point, where the points in the same plane direction, Γ-M and Γ-K, show a wide dispersion. Out of the plane, the Γ-A point presents a smaller dispersion. The conduction band minimum (CBM) is placed between the Γ-K points. Thus,

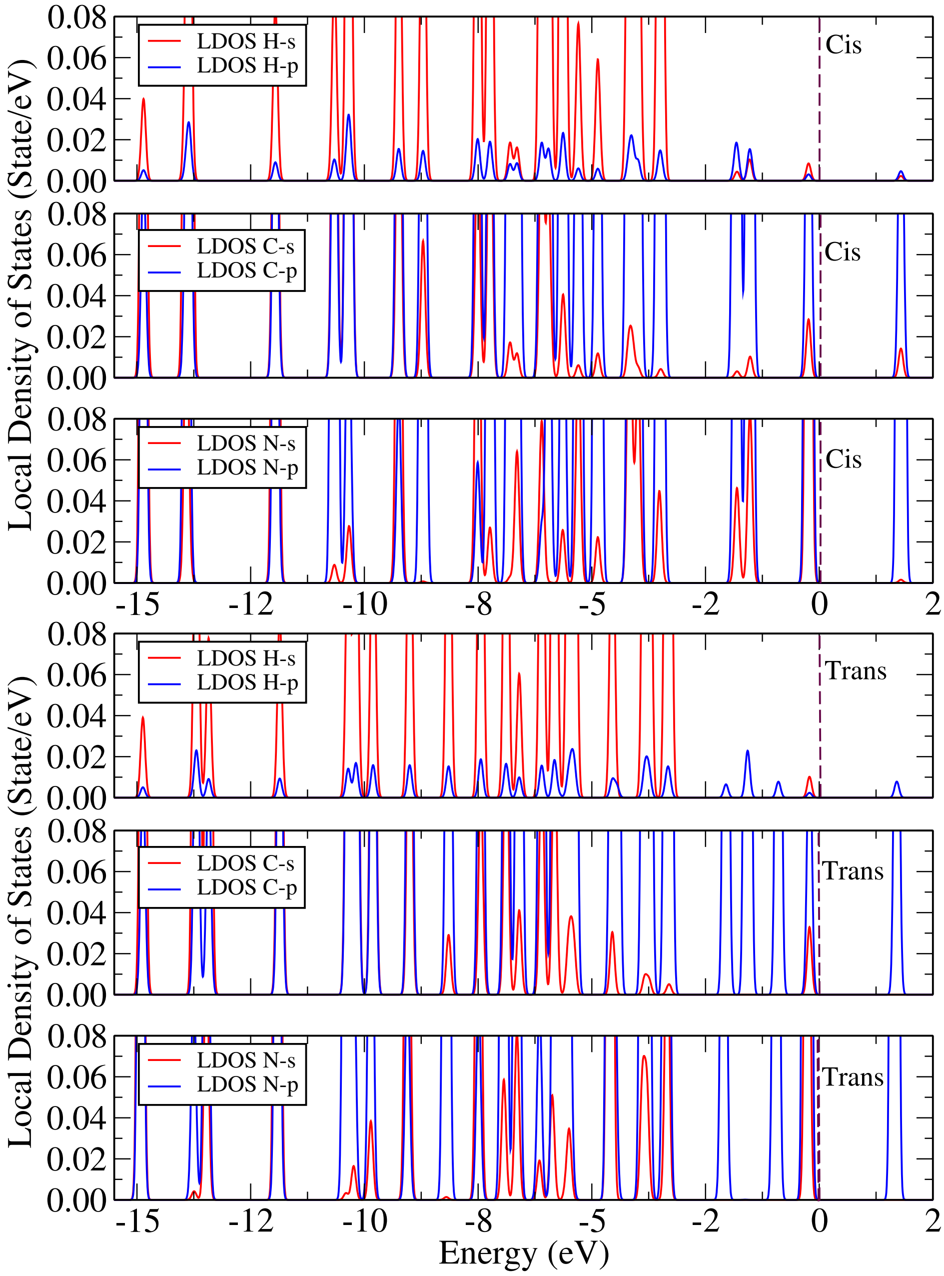

Figure 5.3: Local density of states (LDOS) per atom of the azobenzene isomers. At the top of the Fig. are shown the LDOS of the cis- isomer and, at the bottom, are presented the LDOS of the trans-azobenzene configuration.

the MoS_2 in bulk phase presents an indirect gap of 1.07 eV, underestimated in 17.05 % due to the exchange and correlation functional PBE+D3 used, where the experimental gap measured is 1.29 eV. [291] In the local density of states of the bulk and layer, the valence band is mainly composed by *d*-Mo levels. Compared with MoS_2 bulk, the single layer DOS is shifted up in energy, which is related to the confinement within the layer. In addition, the confinement profile rules the behavior of the carriers near the Fermi energy, such as the effective mass of electrons and holes.

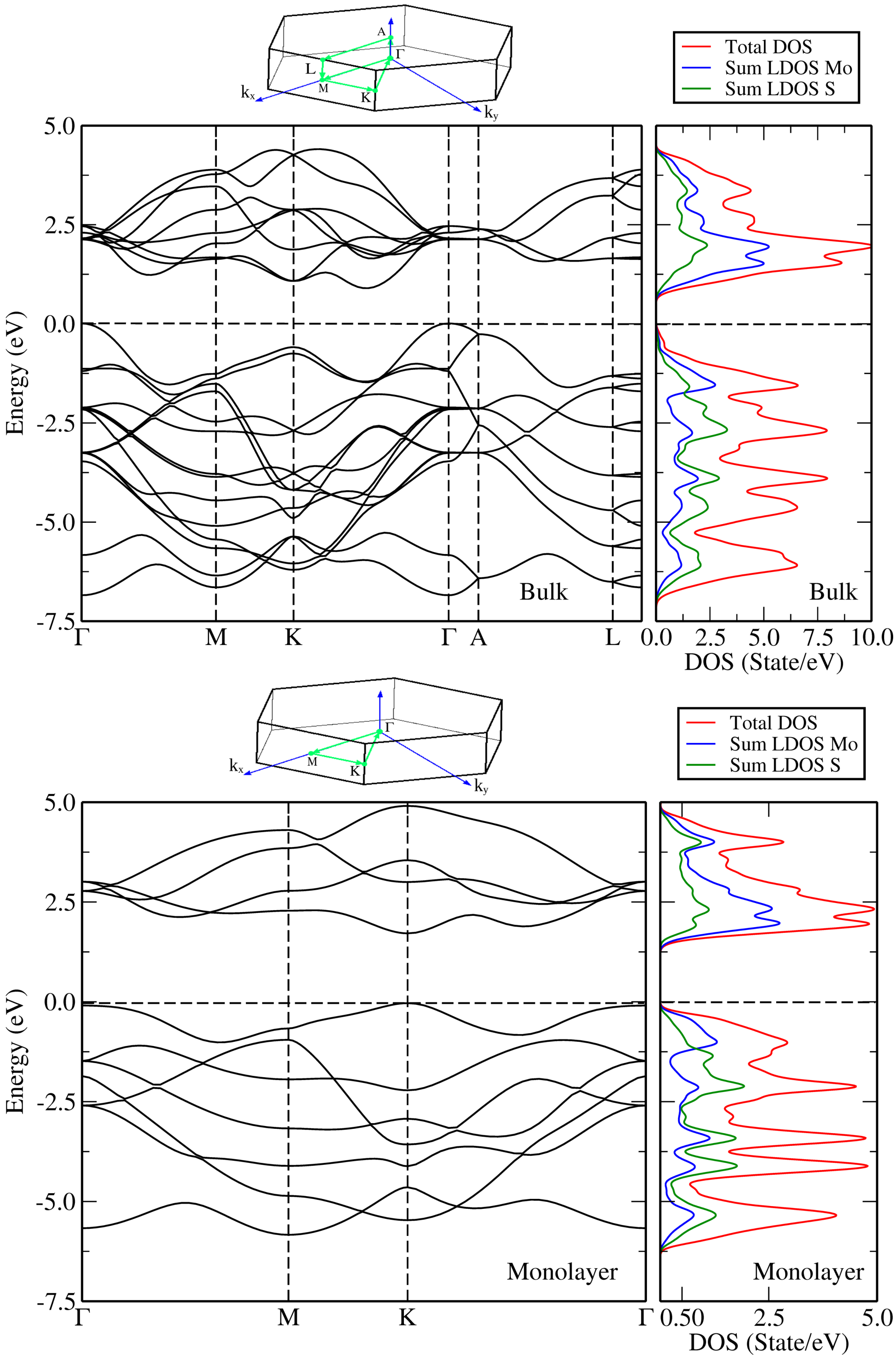

Figure 5.4: Molybdenum disulfide (MoS_2) band structure and local density of states. At the top (bottom) the bulk (layer) is represented. On the left (right) the band structure (local density of states) is depicted. At the upper part of each band structure, the points of the Brillouin zone are shown. The MoS_2 bulk (layer) presents an indirect (direct) gap energy.

5.4 Azobenzene on the MoS_2 layer

In order to analyze the adsorption site of the azobenzene on the MoS_2(0001) surface, several calculations were performed with different azobenzene geometries and positions on the MoS_2(0001) surface, as depicted in Fig. 5.5. In the CisHHex and TransHHex configurations, one azobenzene hexagonal ring is aligned with MoS_2(0001) hexagonal ring, where the C atoms are positioned at the top of the S atoms. In the CisHd and TransHd geometries, the rings of the azobenzene are not horizontally aligned with the MoS_2(0001) layer. Concerning the perpendicular orientations of the azo-molecule on the surface, the structure TransVMo has the azobenzene hexagons vertically on the Mo atom. In TransVMod and CisVMod, the azo-geometries are vertical and displaced horizontally from the Mo. In the same way, in the TransVC, TransVS and TransVS90 geometries, the molecules are perpendicularly placed at the center of the MoS_2(0001) hexagon, on the S of the MoS_2(0001) surface and rotated by 90°, respectively. In TransT geometry, the planes of the azobenzene rings are tilted in relation to the substrate. In this simulation, a single MoS_2(0001) layer was multiplied by eight in the lateral directions.

In the next sections, we show the calculations of the azobenzene on the MoS_2(0001) surface. The study was performed within DFT-PBE+D3 exchange and correlation functional focusing on the distance between the azobenzene molecule and the MoS_2(0001) layer (d_F), the adsorption energy (E_{ad}), the work function (Φ) and the total energy difference (ΔE_n) between the smallest configuration energy and the considered geometry. These results are summarized in Table 5.1. Concerning the stability of the azobenzene on the MoS_2(0001) surface, the TransHd is the preferred geometry, where the azobenzene and MoS_2(0001) rings are misaligned, followed by TransHHex and the other structures presented in the sequence of Table 5.1. Comparatively, the TransHd is 74.5 meV more stable than TranHHex, whereas CisHd geometry is 3.2 meV lower in energy than CisHHex. Therefore, the stability of the geometries increases as the benzene rings become horizontally positioned and misaligned on the MoS_2(0001) surface. When the C atoms of the azobenzene are displaced from the Mo-S, the electrostatic repulsion decreases. Similarly for the cis- configurations, the structures that have the benzene ring parallel to the layer are the most stable. Thus, there is a tendency for the cis- and trans-azobenzene to be placed parallel on the molybdenum disulfide layer. In addition, as the angle between the azo-molecules and the MoS_2(0001) surface increases, the

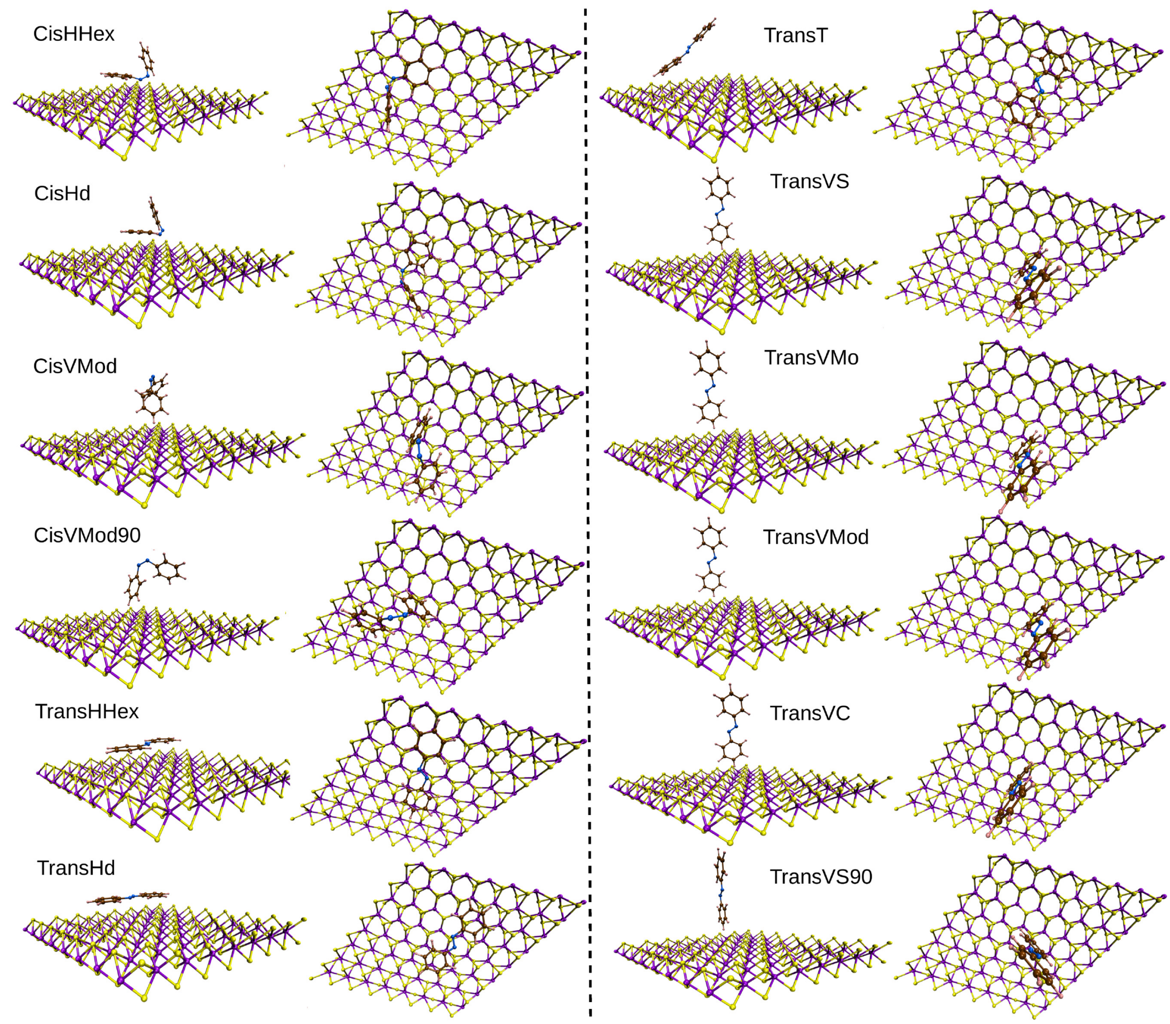

Figure 5.5: Adsorption of the azobenzene molecule on the molybdenum disulfide ($MoS_2(0001)$) layer. In the Figure are depicted the side and top views of the calculated geometries.

interaction between the azobenzene and layer decreases, as shown in Table 5.1. Moreover, when the trans- and cis-azobenezene are placed on the layer (TransHd-CisHd configurations), the energy difference between structural conformations increase, from 0.51 eV in gas-phase to 0.81 eV on the $MoS_2(0001)$ surface. In Fig. 5.6 the top and side views of the lowest energy configurations, TransHd and CisHd, are shown, where in the left (right) part depict the cis-azobenzene/$MoS_2(0001)$ (trans-azobenzene/$MoS_2(0001)$). The effective Bader charge is indicated in the top view. The vertical distance between the single $MoS_2(0001)$ layer and the closest atom of the molecule is depicted in the side view. The electron density differences due to the azobenzene on the surface are indicated at the bottom of the Figure, where the isosurfaces $\pm 0.000\,15\, e\, \text{Å}^{-3}$ were used.

Table 5.1: Adsorption of the azobenzene molecule on the single $MoS_2(0001)$ layer: distance between the azobenzene and the layer (d_F), adsorption energy (E_{ad}), work function (Φ) and the total energy difference (ΔE_n) between the smallest configuration energy and the considered geometry.

Structure	d_F	E_{ad}	Φ	ΔE_n
	[Å]	[meV]	[eV]	[meV]
TransHd	3.23	−980	5.41	**0**
TransHHex	3.36	−905	5.39	74
TransT	2.86	−295	5.22	685
TransVMo	2.68	−201	5.16	778
TransVC	2.69	−196	5.17	783
TransVMod	2.57	−178	5.17	802
TransVS	2.50	−144	5.15	836
TransVS90	2.46	−137	5.15	843
CisHd	3.26	−679	5.24	**810**
CisHHex	3.29	−676	5.23	813
CisVMod	2.81	−247	5.14	1242
CisVMod90	2.81	−247	5.15	1242

5.5 Azobenzene adsorption on $MoS_2(0001)$

The adsorption energy (E_{ad}) measures the intensity of the interaction between the azobenzene and the $MoS_2(0001)$ surface, as follows: [292]

$$E_{ad} = E_{tot}^{\mathrm{AZO/MoS_2(0001)}} - E_{tot}^{\mathrm{AZO}} - E_{tot}^{\mathrm{MoS_2(0001)}}, \tag{5.2}$$

where $E_{tot}^{\mathrm{AZO/MoS_2(0001)}}$ is the total energy of the azobenzene molecule on the $MoS_2(0001)$ surface, E_{tot}^{AZO} and $E_{tot}^{\mathrm{MoS_2(0001)}}$ are the total energies of the isolated azobenzene and layer systems, respectively. We employed the DFT total energy of the cis- and trans- isomers to obtain the E_{tot}^{AZO}. Thus, the adsorption energy takes into account only the interaction energy between the molecule and the surface. According to Eq. 5.2, negative adsorption energy favors the bonds between the azobenzene molecule and the $MoS_2(0001)$ substrate. On the other hand, positive values of E_{ad} disfavor the bonds between the organic molecule and $MoS_2(0001)$ surface. Thus, according to the Table 5.1, we obtained $E_{ad} = -0.98$ eV for the trans- and -0.68 eV for the cis- isomer on the $MoS_2(0001)$ surface, geometries TransHd and CisHd, respectively. Comparatively, the trans- binds 0.30 eV stronger than cis- isomer on the layer, which is expected due to the larger interaction of the trans- isomer with the

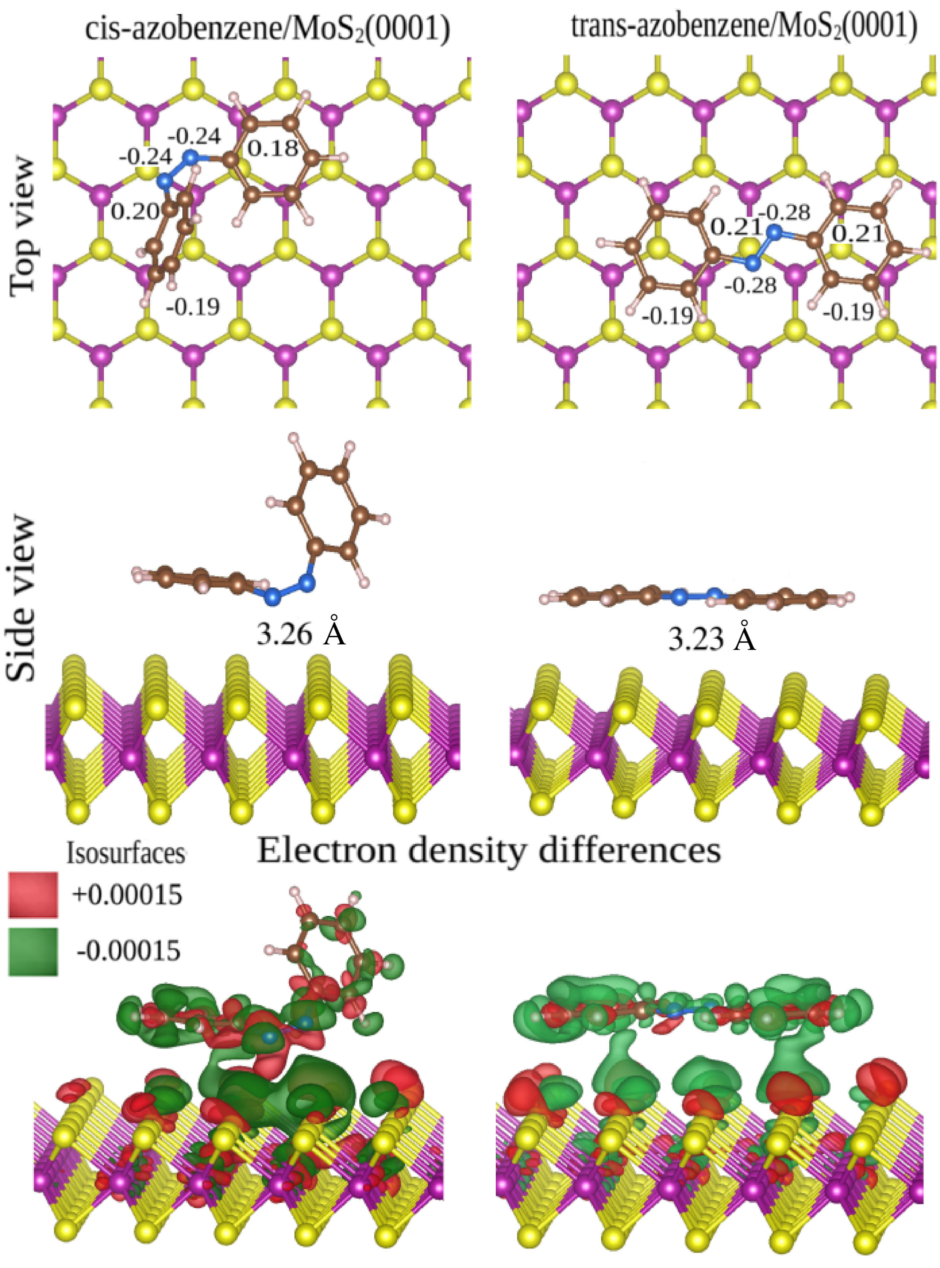

Figure 5.6: Top and side views of the lowest energy configurations, TransHd and CisHd. In the top view the effective Bader charge is indicated and, in the side view, the vertical distance between the surface and the closest atom of the molecule is shown. The electron density differences induced by the azobenzene on the surface are depicted at the bottom of the Figure.

MoS_2(0001) surface. In addition, the intensity of the adsorption energies are smaller than 1.0 eV, which is in the range of physisorption binding interactions. [293, 294]

5.6 Work function

The work function (Φ), is the energy required to remove an electron from the solid, given by:

$$\Phi = V_{es} - E_F, \tag{5.3}$$

where V_{es} is the electrostatic potential energy of the azobenzene on the $MoS_2(0001)$ and E_F is the Fermi energy of the calculated geometry. The obtained values of the work function are given in Table 5.1. Due to the conformation of the molecule on the layer, the parallel azobenzene geometries (trans-) on the single $MoS_2(0001)$ layer has the work function stronger than the cis- configurations. By increasing the angle between the molecule and surface, the work function of the structures becomes smaller. We obtained 5.41 eV for the TransHd and 5.24 eV for the CisHd configuration. Thus, the work function of the trans- isomer is 0.17 eV higher than cis- geometry. Therefore, a higher energy is required to remove an electron in the trans- than in cis- configuration on the $MoS_2(0001)$ surface.

5.7 Density of states

For a better understanding of the electronic properties of the azobenzene molecule on the $MoS_2(0001)$ surface, we increased the number of the layers of the lowest energy configuration, TransHd, as depicted in the Fig. 5.7. In addition, in the Fig. 5.8, we present the local density of states of trans-azobenzene on one (three) $MoS_2(0001)$ layers in the left (right) panel. In the LDOS of trans-azobenzene on one and three layers, the highest occupied molecular orbital of the single $MoS_2(0001)$ layer is smoothly displaced from the Fermi energy, distanced by 0.5 eV, being mostly composed by Mo-d and S-p states. In contrast, the lowest unoccupied molecular orbital (LUMO) of the surface is composed by Mo-d and S-p states. Thus, the states of the molecule enter inside the forbidden region of the molybdenum disulfide surface, changing the electronic properties of the carriers near the Fermi energy. They become interesting structures to study the electronic transport and the azobenzene switch under light incidence. In this way, any changes in the electronic properties of the geometry will be performed preferably on the molecule. In addition, as

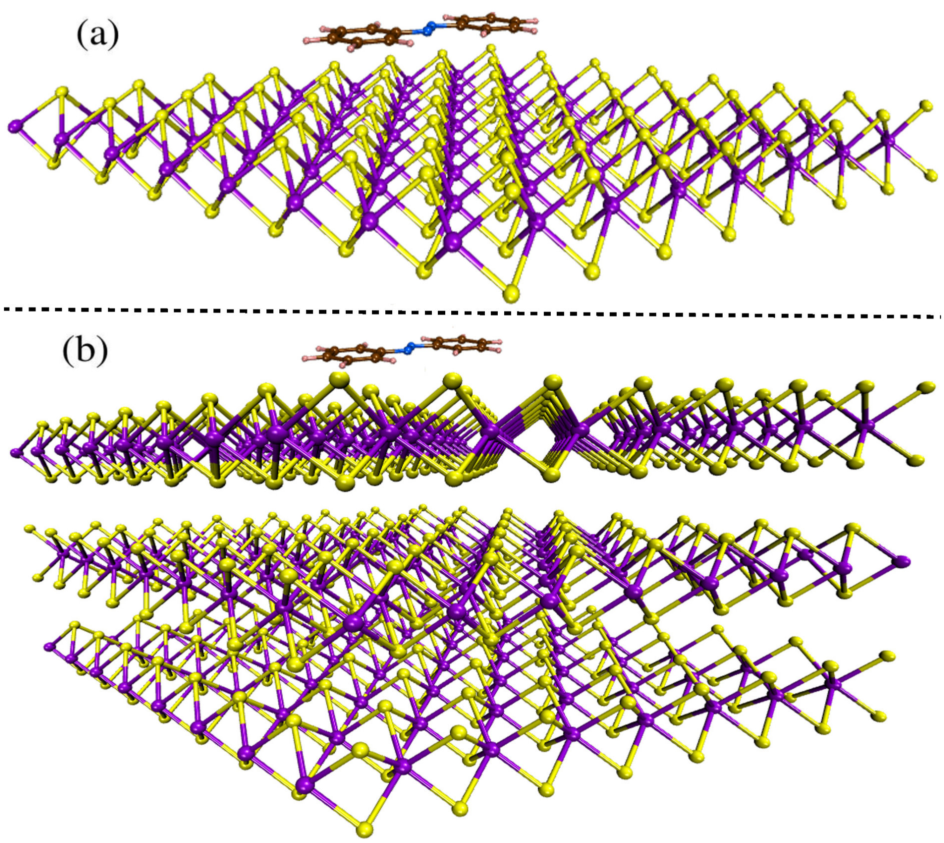

Figure 5.7: Azobenzene molecule at the top of one (a) and three (b) MoS_2(0001) layers. To understand the role of the layer in the electronic properties of the azobenzene, the number of layers was increased of the lowest energy configuration, TransHd.

the number of layers increase, the forbidden region of the MoS_2(0001) decreases. We found that the calculated gap of the one (three) MoS_2(0001) layer is 1.42 eV (1.19 eV), where the decrease of 0.23 eV in the gap of the semiconductor is obtained by the increase of the number of layers to three, tending to the bulk phase. It is worth noting that, when the molecule is placed on the MoS_2(0001) surface, the azobenzene does not change significantly the electronic properties of the semiconductor.

5.8 Charge transfer analaysis - Bader

The investigations of the charge rearrangement among the lowest energy configurations, TransHd and CisHd, and the MoS_2(0001) single and three layers were performed using the effective Bader charge calculation, Eq. (5.1), where the investigated atoms are Mo, S, H, C, N. In order to obtain a more accurate description of the charge flow, we increased

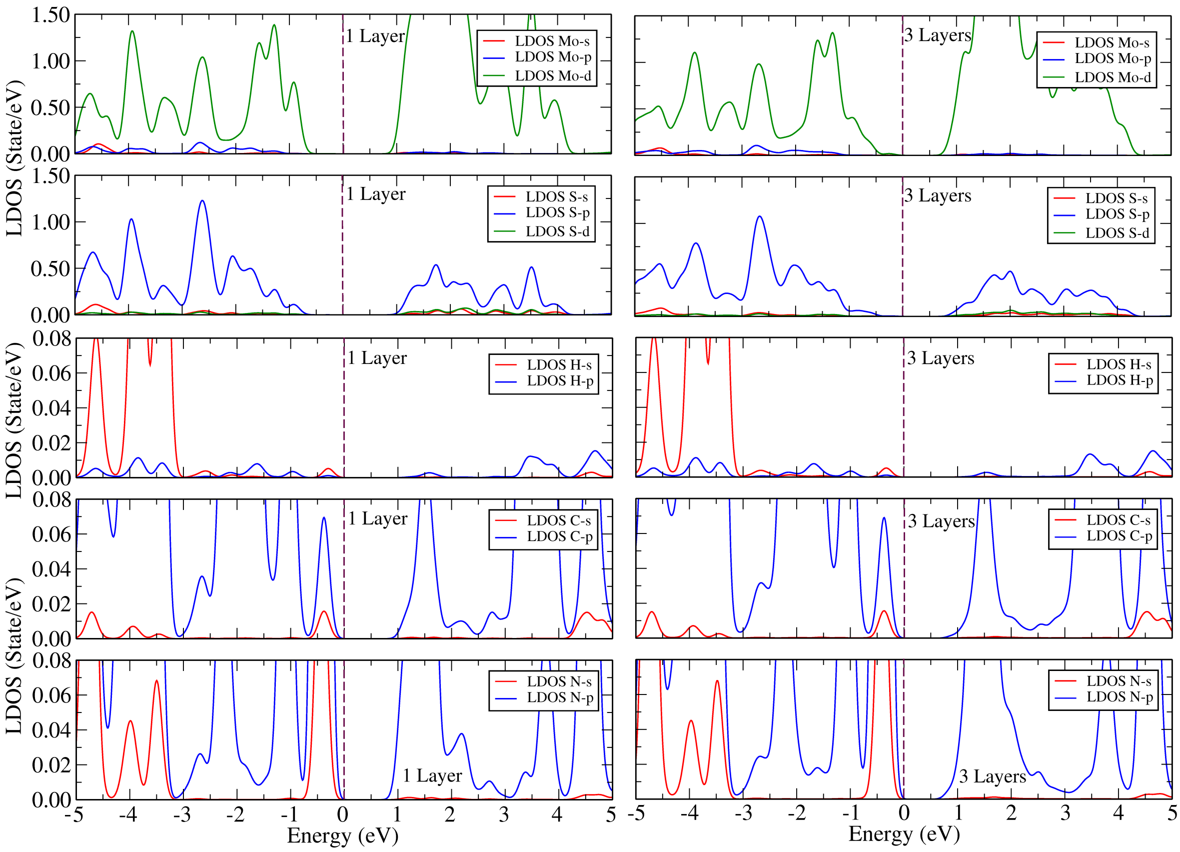

Figure 5.8: Local density of states of the trans-azobenzene on the molybdenum disulfide surface. On the left (right) the trans-azobenzene placed at the top of one (three) $MoS_2(0001)$ layers is depicted.

the grid points in the Fourier transform, multiplying by a factor of three. The results are depicted in Fig. 5.9.

On the left (right) of Fig. 5.9 the azobenzene isomers are depicted at the top of one (three) $MoS_2(0001)$ layers, where in the upper (a,c) and lower (b,d) part represent the cis- and trans- geometries, respectively. The Bader charge of the molecule on the one and three layers is similar to the azobenzene in gas-phase, which indicates that the van der Waals forces do not change significantly the charge flow in the system. By increasing the number of layers, the charge rearrangement does not change. It is important to note that, the nitrogen atom in the trans- is more anyonic than in the cis-azobenzene. We found the effective Bader charge on the nitrogen atoms $-0.28\,e$ and $-0.24\,e$ for the trans- and the cis-azobenzene, respectively. Due to this difference in the electronegativity, the nearest carbon atom from the nitrogen in the aromatic ring becomes cationic, namely, $0.21\,e$ and $0.20\,e$ for the trans- and the cis-azobenzene, respectively, and the other carbon atoms have the anyonic effective Bader charge of $-0.19\,e$.

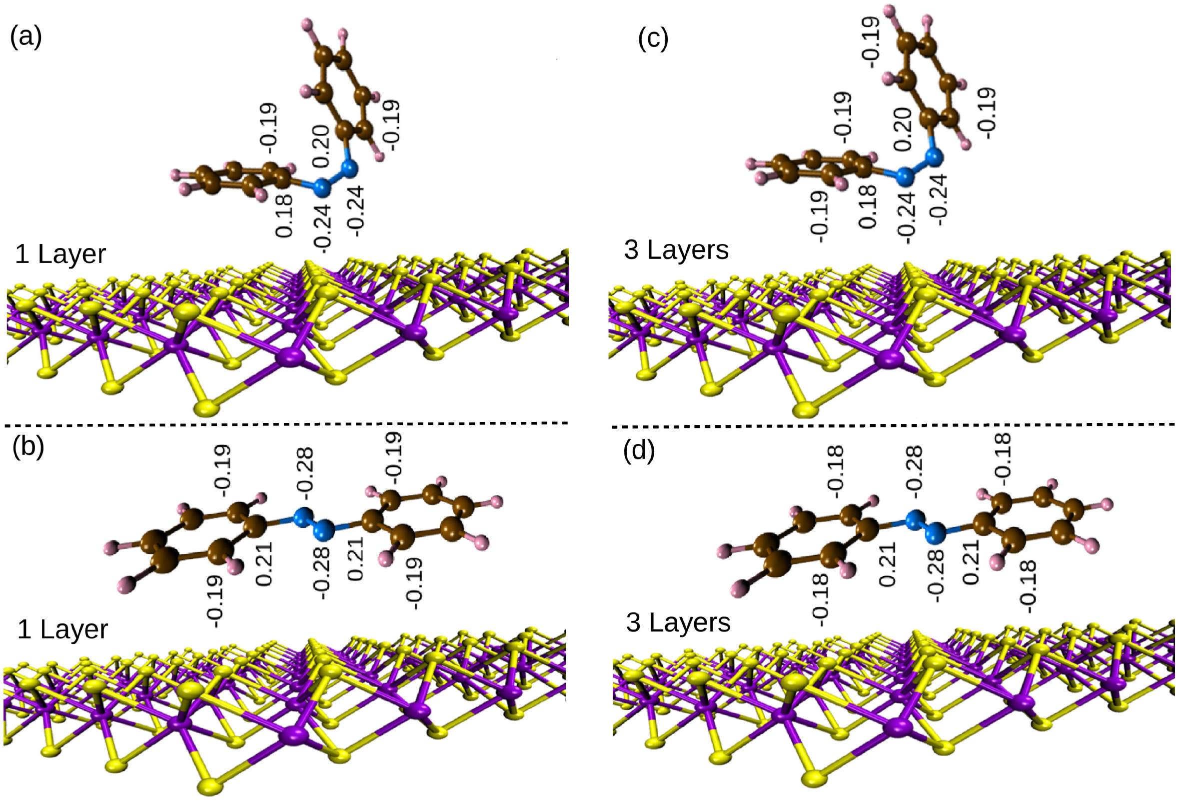

Figure 5.9: Bader charge analysis for cis- (a,c) and trans- (b,d) azobenzene isomers placed at the top of one (a,b) and three (c,d) MoS_2(0001) layers. Here we used the lowest energy configurations, TransHd and CisHd. The Bader charge for the azobenzene molecule on the surfaces is similar to the Bader charge for the molecule in the gas-phase, depicting the weak interaction of the van der Waals forces.

Chapter 6

Conclusions and future perspectives

The results presented in this Thesis tackle problems concerning quantum dots, rings, and 2D semiconductor materials. In order to understand the quantum confinement properties, vacancies and magnetic impurities were introduced in cadmium selenide (CdSe) QDs. In addition, the adsorption properties of the azobenzene molecule on 2D molybdenum disulfide ($MoS_2(0001)$) surface were analyzed. Furthermore, the local charge rearrangement induced by the azobenzene molecule on the single $MoS_2(0001)$ layer was also investigated. Thus, by moving beyond symmetric structures, the challenges proposed in this Thesis resulted in complex theoretical endeavors. Thereby, the interplay between the $\mathbf{k}\cdot\mathbf{p}$ approach and the density functional theory allowed to achieve a solid analysis of the studied systems, providing a better understanding of the results.

After a brief introduction of the investigation proposals in chapter 1, the theoretical backgrounds for the electronic structure simulations were presented in chapter 2. In chapter 3, we showed the results for cadmium selenide QDs (CdSe) in a zinc selenide (ZnSe) host material, undoped and doped with magnetic impurity of manganese (Mn). In this context, the intertwining between the structure asymmetry, defects and spin-orbit coupling was studied within a single theoretical framework. This is a more complex issue when taking into account externally applied electromagnetic fields. The effective mass model of the electronic structure allows to combine the confinement profiles with controllable symmetry lowering, spin-orbit coupling effects, and external fields under a variety of configurations. The introduction of the perturbative confinement profiles in the parabolic QD confinement allows to study the asymmetric effects, changing the shape of the QDs. In this context, the eccentricity asymmetry was introduced in the QD confinement profile, providing an elliptical shrinking or stretching, and the Gaussian asymmetry, providing a dip or bump in the QD. The introduction of Mn provides the exchange interaction between the *d*-Mn impurity states and *sp*-CdSe QD and host material levels. The combination of these effects, characterized by the effective Lande-factor, provides a better understanding of the Zeeman splitting and the modulation of the ground state character. Atomistic calculations within the density functional theory allowed to determine the plausible ways to incorporate the manganese impurity in the nanostructure. Systematic calculations were performed contrasting several Mn positions. The connection between the effective mass model and such atomistic approaches was done through a characterization of the main trends for the Mn positioning, as well as the exchange interaction term, which is calculated by a fully *ab initio* technique. The hybridization between the *p*-Se and the *d*-Mn orbitals rules the strength of the exchange interaction parameter. In the particular case of CdSe QDs embedded in a ZnSe substrate, the lattice parameter mismatch implies in a compression of the atomic bonds in the supercell, affecting the electronic states in the valence and conduction bands.

Due to unavoidable imperfections which can occur in the growth process, affecting the confinement profile, in chapter 4 we showed the results of the atomistic investigations performed within the density functional theory, studying the effects of vacancies in cadmium selenide QDs in zinc selenide host material. The presence of vacancies in the QDs provides new effects in the optical and electronic properties of the nanostructure. The defects can induce magnetism in non-magnetic QDs systems and the study of this magnetism was a paramount task for this investigations. An optical evidence of the induced magnetism in CdSe QDs was detected by their photoluminescence (PL) for circular polarized emission and traced down to the spin-dynamics, characterized by its time resolved polarized emission. Concerning the theoretical framework, the formation energy of such systems, calculated in a systematic way, reveals that the Cd vacancy position nearest to the center of the QD is the most probable to occur during the growth process. After DFT calculations, we characterized how the atoms in the defective bulk are displaced from their crystalline positions. Contrasting the uncharged and charged defective systems in the computation of the formation energy, the selenium uncharged vacancies did not show magnetic moment. However, cadmium and zinc uncharged vacancies presented $2\mu_B$ magnetic moment. Cadmium vacancies at the edge of the QD and selenium vacancies, both charged by ± 1, presented $1\mu_B$ magnetic moment.

Cadmium vacancies near to the center of the QD and zinc vacancies in the matrix of the QD showed $1\mu_B$ and $3\mu_B$ magnetic moment for charges -1 and $+1$, respectively. In addition, by applying strain in defective QD, the magnetic moment changes in contrast to the non-strained structure.

Taking advantage of atomistic calculations using the density functional theory, the adsorption properties of the organic molecules in 2D material were analyzed in chapter 5. In this context, the light sensitive cis- and trans-azobenzene isomers in gas-phase were investigated, wherein the trans-azobenzene is the preferred structure, which is in good agreement with the experimental results. In the same way, the molybdenum disulfide bulk and layer were individually calculated in order to study the adsorption properties of the azobenzene molecule on the MoS_2(0001) surface. Several configurations of cis- and trans-azobenzene molecule on top of the singe MoS_2(0001) layer were analyzed. The horizontal configurations of cis- and trans-azobenzene isomers on the surface are the most stable structures. On the other hand, the parallel structures in cis- and trans-configurations on the layer have the lowest adsorption energy and the higher work function. Furthermore, the charge flow between the molecule and surface was analyzed using the Bader charge concept, where the electronegativity of the nitrogen atoms and the torsion angles of the molecule rules the charge rearrangement at the MoS_2(0001) surface.

The understanding of the electronic structure of these semiconductors allows to link the theoretical obtained results with potential applications in nanoelectronic devices, such as photo-transistors. [295] Also, the spintronics shows promising results with technological applications. [258, 259] 2D materials have been intensively investigated due to the wide range of applications and the possibility to build layered materials, used in several areas of knowledge. [40–43] In particular, two-dimensional materials have extensive applications [44] focused on technological innovations, [51, 296, 297] such as transistors, [298, 299] sensors, [300] and optoelectronic devices. [301] Thus, taking advantage of the $\mathbf{k}\cdot\mathbf{p}$ method and the density functional theory, the optical properties and electronic transport will permeate the future investigations concerning these 2D systems. [282–284] Vacancies, substitutional and interstitial magnetic impurities in layered systems will provide new effects in the investigations of the 2D semiconductors. In order to study the electronic transport, metallic contacts will be combined with the dichalcogenides material, as shown in Fig. 6.1, taken from the Ref. [302], wherein the lattice mismatch at the interfaces must be reduced.

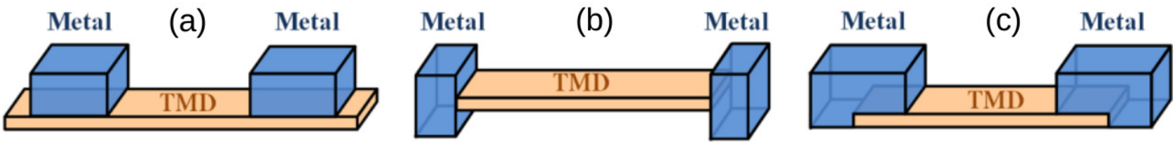

Figure 6.1: 2D material connected by contacts constituted by metallic atoms. The metallic contacts are placed (a) on the layered 2D dichalcogenide (TMD), (b) laterally linked at the edge of the TMD and (c) combined with the dichalcogen layers.

The Schottky barrier emerges at the interface between the semiconductor and metal, preventing the current flow. [302–304] Thus, the calculation of the work function of the semiconductor-metal structures becomes crucial for understanding the Schottky barrier. [305, 306] The electronic transport properties obtained by *ab initio* calculations will be concomitantly analyzed and complemented by the effective mass methods.

Appendix A

Spin-orbit interaction calculations

In this appendix, we show the details of the calculations concerning the spin-orbit interaction and the asymmetries effects used in the chapter 3.

A.1 Growth direction

The carriers confinement in a QD can be separated in the three spatial directions. In this section, the spin-orbit calculations will be assumed in the growth direction of the nanostructure.

A.1.1 Conduction band - electrons

For the conduction band, the spin-orbit interaction is given by: [27]

$$H^{r}_{6c6c} = r^{6c6c}_{41}[(k_y\varepsilon_z - k_z\varepsilon_y)\sigma_x + cp], \tag{A.1}$$

where $\mathbf{k} = k_x, k_y, k_z$ is the wave vector, $\varepsilon = \varepsilon_x, \varepsilon_y, \varepsilon_z$ the intensity of the electric field and $\sigma = \sigma_x, \sigma_y, \sigma_z$ the Pauli matrices. Eq. (A.1) is written in the three spatial directions by developing the cyclic permutation (cp),

$$H^{r}_{6c6c} = r^{6c6c}_{41}[(k_y\varepsilon_z - k_z\varepsilon_y)\sigma_x + (k_z\varepsilon_x - k_x\varepsilon_z)\sigma_y + (k_x\varepsilon_y - k_y\varepsilon_x)\sigma_z]. \tag{A.2}$$

Considering the electric field only in the z axis, Eq. (A.2) becomes:

$$H^r_{6c6c} = r^{6c6c}_{41}\varepsilon_z[k_y\sigma_x - k_x\sigma_y]. \tag{A.3}$$

Defining the operations:

$$\sigma_\pm = \frac{1}{2}(\sigma_x \pm \sigma_y) \qquad \text{and} \qquad k_\pm = k_x \pm ik_y. \tag{A.4}$$

After some algebraic manipulations,

$$H^r_{6c6c} = -i\alpha_S\frac{\partial V}{\partial z}[\sigma_+k_- - \sigma_-k_+]. \tag{A.5}$$

Here, we can use $k_\pm = \pm iL_\pm A_\pm$,

$$H_R = -i\alpha_s\frac{\partial V}{\partial z}\left(\sigma_+(-iL_-\hat{A}_-) - \sigma_-(iL_+\hat{A}_+)\right). \tag{A.6}$$

We can define $\hat{A}_\pm = A_\pm \mp \frac{1}{\rho}$,

$$H_R = -\alpha_s\frac{\partial V}{\partial z}\left(\sigma_+L_-\left(A_- + \frac{1}{\rho}\right) + \sigma_-L_+\left(A_+ - \frac{1}{\rho}\right)\right). \tag{A.7}$$

In cylindrical coordinates, the $k_\pm$ can be rewritten as follows:

$$k_\pm = \pm iL_\pm A_\pm \qquad \text{and} \qquad A_\pm = \mp\frac{\partial}{\partial\rho} - \frac{i}{\rho}\frac{\partial}{\partial\phi} + \alpha\rho, \tag{A.8}$$

where $\alpha = \frac{eB_z}{2c\hbar}$ and $L_\pm = e^{\pm i\phi}$. Therefore,

$$k_\pm = -ie^{\pm i\phi}\left[\frac{\partial}{\partial\rho} \pm \frac{i}{\rho}\frac{\partial}{\partial\phi} \mp \alpha\rho\right]. \tag{A.9}$$

Thus,

$$\begin{aligned} H_R \;=\; & -i\alpha_s\frac{\partial V}{\partial z}\left\{\sigma_+\left[-ie^{-i\phi}\left(\frac{\partial}{\partial\rho} - \frac{i}{\rho}\frac{\partial}{\partial\rho} + \frac{eB_z\rho}{2c\hbar}\right)\right]\right. \\ & -\left.\sigma_-\left[-ie^{i\phi}\left(\frac{\partial}{\partial\rho} + \frac{i}{\rho}\frac{\partial}{\partial\phi} - \frac{eB_z\rho}{2c\hbar}\right)\right] - \frac{i}{\rho}\sigma_+e^{-i\phi} + \frac{i}{\rho}\sigma_-e^{i\phi}\right\}. \end{aligned} \tag{A.10}$$

$$\begin{aligned} H_R &= -\alpha_S \frac{\partial V}{\partial z}\Bigg\{\sigma_+ \left[e^{-i\phi}\left(\frac{\partial}{\partial \rho} - \frac{i}{\rho}\frac{\partial}{\partial \phi} + \frac{eB_z}{2c\hbar}\rho + \frac{1}{\rho}\right)\right] \\ &- \sigma_- \left[e^{i\phi}\left(\frac{\partial}{\partial \rho} + \frac{i}{\rho}\frac{\partial}{\partial \phi} - \frac{eB_z}{2c\hbar}\rho + \frac{1}{\rho}\right)\right]\Bigg\}. \end{aligned} \tag{A.11}$$

To obtain the eigenvalues, we employ the appropriate selection rules and $\langle \Psi^*_{m_1}|H_R|\Psi_{m_2}\rangle = E_R$,

$$\begin{aligned} E_R &= -\alpha_S \frac{\partial V}{\partial z} 2\pi \Bigg\{\sigma_+ \left[\frac{\partial}{\partial \rho} - \frac{(m_2-1)}{\rho} + \frac{eB_z}{2c\hbar}\rho\right]\delta_{m_2,m_{1-1}} \\ &- \sigma_- \left[\frac{\partial}{\partial} + \frac{(m_2+1)}{\rho} - \frac{eB_z}{2c\hbar}\rho\right]\delta_{m_2,m_{1+1}}\Bigg\}. \end{aligned} \tag{A.12}$$

Using the following relation,

$$(\langle \Psi^*_{m_1}|H_R|\Psi_{m_2}\rangle)^\dagger = \langle \Psi^*_{-m_2}|H_R^\dagger|\Psi_{-m_1}\rangle = E'_R(m_2, m_1). \tag{A.13}$$

Thus,

$$\begin{aligned} E'_R &= -\alpha_S \frac{\partial V}{\partial z} 2\pi \Bigg\{(-\sigma_-) \left[\frac{\partial}{\partial \rho} - \frac{(-m_1-1)}{\rho} + \frac{e(-B_z)}{2c\hbar}\rho\right]\delta_{-m_2,-m_{1-1}} \\ &- (-\sigma_+) \left[\frac{\partial}{\partial \rho} + \frac{(-m_1+1)}{\rho} - \frac{e(-B_z)}{2c\hbar}\rho\right]\delta_{-m_2,-m_{1+1}}\Bigg\}. \end{aligned} \tag{A.14}$$

$$\begin{aligned} E'_R &= -\alpha_S \frac{\partial V}{\partial z} 2\pi \Bigg\{(-\sigma_-) \left[\frac{\partial}{\partial \rho} + \frac{(m_1+1)}{\rho} - \frac{eB_z}{2c\hbar}\rho\right]\delta_{m_2,m_{1+1}} \\ &+ (\sigma_+) \left[\frac{\partial}{\partial \rho} - \frac{(m_1-1)}{\rho} + \frac{eB_z}{2c\hbar}\rho\right]\delta_{m_2,m_{1-1}}\Bigg\}. \end{aligned} \tag{A.15}$$

Separating the terms,

$$E_{R_1} = -\alpha_S \frac{\partial V}{\partial z} 2\pi\sigma_+ \left[\frac{\partial}{\partial \rho} - \frac{(m_2-1)}{\rho} + \frac{eB_z}{2c\hbar}\rho\right]\delta_{m_2,m_{1-1}}; \tag{A.16}$$

$$E_{R_2} = \alpha_S \frac{\partial V}{\partial z} 2\pi\sigma_- \left[\frac{\partial}{\partial \rho} + \frac{(m_2+1)}{\rho} - \frac{eB_z}{2c\hbar}\rho\right]\delta_{m_2,m_{1+1}}; \tag{A.17}$$

$$E'_{R_1} = \alpha_S \frac{\partial V}{\partial z} 2\pi\sigma_- \left[\frac{\partial}{\partial \rho} + \frac{(m_1+1)}{\rho} - \frac{eB_z}{2c\hbar}\rho\right]\delta_{m_2,m_{1+1}}; \tag{A.18}$$

$$E'_{R_2} = -\alpha_S \frac{\partial V}{\partial z} 2\pi\sigma_+ \left[\frac{\partial}{\partial \rho} - \frac{(m_1-1)}{\rho} + \frac{eB_z}{2c\hbar}\rho\right]\delta_{m_2,m_{1-1}}. \tag{A.19}$$

Eqs. (A.16)-(A.19) are the matrix elements of the SIA spin-orbit interaction for electrons in conduction band.

A.1.2 Valence band - heavy holes

In this subsection, the light holes (LH) are assumed away from heavy holes (HH). Below we show the spin-orbit calculation for heavy holes.

$$\begin{aligned} H^r_{8v8v} &= r_{41}^{8v8v}[(k_y\varepsilon_z - k_z\varepsilon_y)J_x + cp] + r_{42}^{8v8v}[(k_y\varepsilon_z - k_z\varepsilon_y)J_x^3 + cp] \\ &+ r_{51}^{8v8v}[(\varepsilon_x\{J_y, J_z\}) + cp] + r_{52}^{8v8v}[(k_y\varepsilon_z + k_z\varepsilon_y)\{J_x, J_y^2 - J_z^2\} + cp]. \end{aligned} \tag{A.20}$$

Performing the cyclic permutations and using Eqs. (A.4),

$$\begin{aligned} H^r_{8v8v} &= r_{41}^{8v8v}\left[k_y\varepsilon_z J_x - k_x\varepsilon_z J_y\right] + r_{42}^{8v8v}\left[k_y\varepsilon_z J_x^3 - k_x\varepsilon_z J_y^3\right] \\ &+ r_{51}^{8v8v}\left[\varepsilon_z J_x J_y + \varepsilon_z J_y J_x\right] \\ &+ r_{52}^{8v8v}\Big[(k_y\varepsilon_z)(J_x J_y^2 + J_y^2 J_x - J_x J_z^2 - J_z^2 J_x) \\ &+ (k_x\varepsilon_z)(J_y J_z^2 + J_z^2 J_y - J_y J_x^2 - J_x^2 J_y)\Big]. \end{aligned} \tag{A.21}$$

$$\begin{aligned} H^r_{8v8v} &= r_{41}^{8v8v}\varepsilon_z\left[\left(\frac{k_+ - k_-}{2i}\right)J_x - \left(\frac{k_+ + k_-}{2}\right)J_y\right] \\ &+ r_{42}^{8v8v}\varepsilon_z\left[\left(\frac{k_+ - k_-}{2i}\right)J_x^3 - \left(\frac{k_+ + k_-}{2}\right)J_y^3\right] + r_{51}^{8v8v}\varepsilon_z\left[J_x J_y + J_y J_x\right] \\ &+ r_{52}^{8v8v}\varepsilon_z\Bigg[\left(\frac{k_+ - k_-}{2i}\right)\left(J_x J_y^2 + J_y^2 J_x - J_x J_z^2 - J_z^2 J_x\right) \\ &+ \left(\frac{k_+ + k_-}{2}\right)\left(J_y J_z^2 + J_z^2 J_y - J_y J_x^2 - J_x^2 J_y\right)\Bigg]. \end{aligned} \tag{A.22}$$

$$
\begin{aligned}
H^{r}_{8v8v} &= r^{8v8v}_{41}\varepsilon_z\left[\frac{k_+J_x}{2i}-\frac{k_-J_x}{2i}-\frac{k_+J_y}{2}-\frac{k_-J_y}{2}\right] \\
&+ r^{8v8v}_{42}\varepsilon_z\left[\frac{k_+J_x^3}{2i}-\frac{k_-J_x^3}{2i}-\frac{k_+J_y^3}{2}-\frac{k_-J_y^3}{2}\right]+r^{8v8v}_{51}\varepsilon_z\left[J_xJ_y+J_yJ_z\right] \\
&+ r^{8v8v}_{52}\varepsilon_z\left[\frac{k_+}{2i}(J_xJ_y^2+J_y^2J_x-J_xJ_z^2-J_z^2J_x)\right. \\
&- \frac{k_-}{2i}(J_xJ_y^2+J_y^2J_x-J_xJ_z^2-J_z^2J_x) \\
&+ \left.\frac{k_+}{2}(J_yJ_z^2+J_z^2J_x-J_yJ_x^2-J_x^2J_y)+\frac{k_-}{2}(J_yJ_z^2+J_z^2J_x-J_yJ_x^2-J_x^2J_y)\right].
\end{aligned}
\tag{A.23}
$$

For heavy holes $r^{8v8v}_{42}=r^{8v8v}_{51}=r^{8v8v}_{52}=0$. Using the relations (A.4), (A.8) and (A.9),

$$
\begin{aligned}
H^{r}_{8v8v} &= r^{8v8v}_{41}\varepsilon_z\left[\frac{J_x}{2}\left(e^{i\phi}\left(A_+-\frac{1}{\rho}\right)+e^{-i\phi}\left(A_-+\frac{1}{\rho}\right)\right)\right. \\
&+ \left. i\frac{J_y}{2}\left(-e^{i\phi}\left(A_+-\frac{1}{\rho}\right)+e^{-i\phi}\left(A_-+\frac{1}{\rho}\right)\right)\right].
\end{aligned}
\tag{A.24}
$$

$$
\begin{aligned}
H^{r}_{8v8v} &= \frac{r^{8v8v}_{41}}{2}\varepsilon_z\left[J_x\left(e^{i\phi}\left(-\frac{\partial}{\partial\rho}-\frac{i}{\rho}\frac{\partial}{\partial\phi}+\frac{eB_z\rho}{2c\hbar}-\frac{1}{\rho}\right)\right.\right. \\
&+ \left.e^{-i\phi}\left(\frac{\partial}{\partial\rho}-\frac{i}{\rho}\frac{\partial}{\partial\phi}+\frac{eB_z\rho}{2c\hbar}+\frac{1}{\rho}\right)\right)+iJ_y\left(-e^{i\phi}\left(-\frac{\partial}{\partial\rho}-\frac{i}{\rho}\frac{\partial}{\partial\phi}\right.\right. \\
&+ \left.\left.\left.\frac{eB_z\rho}{2c\hbar}-\frac{1}{\rho}\right)+e^{-i\phi}\left(\frac{\partial}{\partial\rho}-\frac{i}{\rho}\frac{\partial}{\partial\phi}+\frac{eB_z\rho}{2c\hbar}+\frac{1}{\rho}\right)\right)\right].
\end{aligned}
\tag{A.25}
$$

Here, we replace $J_\pm = J_x \pm iJ_y$,

$$
\begin{aligned}
H^{r}_{8v8v} &= \frac{r^{8v8v}_{41}}{2}\frac{\partial V}{\partial z}\left[\left(\frac{J_++J_-}{2}\right)\left(e^{i\phi}\left(-\frac{\partial}{\partial\rho}-\frac{i}{\rho}\frac{\partial}{\partial\phi}+\frac{eB_z}{2c\hbar}-\frac{1}{\rho}\right)\right.\right. \\
&+ \left.e^{-i\phi}\left(\frac{\partial}{\partial\rho}-\frac{i}{\rho}\frac{\partial}{\partial\phi}+\frac{eB_z}{2c\hbar}+\frac{1}{\rho}\right)\right) \\
&+ \left(\frac{J_+-J_-}{2}\right)\left(-e^{i\phi}\left(-\frac{\partial}{\partial\rho}-\frac{i}{\rho}\frac{\partial}{\partial\phi}+\frac{eB_z}{2c\hbar}-\frac{1}{\rho}\right)\right. \\
&+ \left.\left.e^{-i\phi}\left(\frac{\partial}{\partial\rho}-\frac{i}{\rho}\frac{\partial}{\partial\phi}+\frac{eB_z}{2c\hbar}+\frac{1}{\rho}\right)\right)\right].
\end{aligned}
\tag{A.26}
$$

After that, we apply $\langle\Psi^*_{m_1}|H_R|\Psi_{m_2}\rangle = E_R$ and use the selection rules to obtain the energy of the system, given by:

$$\begin{aligned} E_R &= \frac{2\pi}{2} r_{41}^{8v8v} \varepsilon_z \Bigg[\left(\frac{J_+ + J_-}{2}\right)\left(-\frac{\partial}{\partial\rho} + \frac{(m_2+1)}{\rho} + \frac{eB_z\rho}{2c\hbar}\right)\delta_{m_2,m_{1+1}} \\ &+ \left(\frac{\partial}{\partial\rho} + \frac{(m_2-1)}{\rho} + \frac{eB_z\rho}{2c\hbar}\right)\delta_{m_2,m_{1-1}} \\ &+ \left(\frac{J_+ - J_-}{2}\right)\left(-\left(-\frac{\partial}{\partial\rho} + \frac{(m_2+1)}{\rho} + \frac{eB_z\rho}{2c\hbar}\right)\right)\delta_{m_2,m_1+1} \\ &+ \left(\frac{\partial}{\partial\rho} + \frac{(m_2-1)}{\rho} + \frac{eB_z\rho}{2c\hbar}\right)\delta_{m_2,m_{1-1}} \Bigg]. \end{aligned} \tag{A.27}$$

Adopting the same procedure as (A.13),

$$\begin{aligned} E'_R &= \frac{2\pi}{2} r_{41}^{8v8v} \varepsilon_z \Bigg[\left(\frac{J_+ + J_-}{2}\right)\left(-\frac{\partial}{\partial\rho} + \frac{(-m_1+1)}{\rho} + \frac{e(-B_z)\rho}{2c\hbar}\right) \\ &\quad \delta_{-m_2,-m_{1+1}} + \left(\frac{\partial}{\partial\rho} + \frac{(-m_1-1)}{\rho} + \frac{e(-B_z)\rho}{2c\hbar}\right)\delta_{-m_2,-m_{1-1}} \\ &+ \left(\frac{J_+ + J_-}{2}\right)\left(-\left(-\frac{\partial}{\partial\rho} + \frac{(-m_1+1)}{\rho} + \frac{e(-B_z)\rho}{2c\hbar}\right)\right)\delta_{-m_2,-m_1+1} \\ &+ \left(\frac{\partial}{\partial\rho} + \frac{(-m_1-1)}{\rho} + \frac{e(-B_z)\rho}{2c\hbar}\right)\delta_{-m_2,-m_{1-1}} \Bigg]. \end{aligned} \tag{A.28}$$

$$\begin{aligned} E'_R &= \frac{2\pi}{2} r_{41}^{8v8v} \varepsilon_z \Bigg[\left(\frac{J_+ + J_-}{2}\right)\left(-\frac{\partial}{\partial\rho} - \frac{(m_1-1)}{\rho} - \frac{eB_z\rho}{2c\hbar}\right)\delta_{m_2,m_{1-1}} \\ &+ \left(\frac{\partial}{\partial\rho} - \frac{(m_1+1)}{\rho} - \frac{eB_z\rho}{2c\hbar}\right)\delta_{m_2,m_{1+1}} \\ &+ \left(\frac{J_+ - J_-}{2}\right)\left(\frac{\partial}{\partial\rho} + \frac{(m_1-1)}{\rho} + \frac{eB_z\rho}{2c\hbar}\right)\delta_{m_2,m_1-1} \\ &+ \left(\frac{\partial}{\partial\rho} - \frac{(m_1+1)}{\rho} - \frac{eB_z\rho}{2c\hbar}\right)\delta_{m_2,m_{1+1}} \Bigg]. \end{aligned} \tag{A.29}$$

Separating in parts,

$$E_{R_1} = \alpha_S \pi \varepsilon_z \left[\left(\frac{J_+ + J_-}{2}\right)\left(-\frac{\partial}{\partial\rho} + \frac{(m_2+1)}{\rho} + \frac{eB_z\rho}{2c\hbar}\right)\delta_{m_2,m_1+1}\right]; \tag{A.30}$$

$$E_{R_2} = \alpha_S \pi \varepsilon_z \left[\left(\frac{J_+ + J_-}{2}\right)\left(\frac{\partial}{\partial\rho} + \frac{(m_2-1)}{\rho} + \frac{eB_z\rho}{2c\hbar}\right)\delta_{m_2,m_1-1}\right]; \tag{A.31}$$

$$E_{R_3} = \alpha_S \pi \varepsilon_z \left[\left(\frac{J_+ - J_-}{2}\right)\left(\frac{\partial}{\partial\rho} - \frac{(m_2+1)}{\rho} + \frac{eB_z\rho}{2c\hbar}\right)\delta_{m_2,m_1+1}\right]; \tag{A.32}$$

$$E_{R_4} = \alpha_S \pi \varepsilon_z \left[\left(\frac{J_+ - J_-}{2} \right) \left(\frac{\partial}{\partial \rho} + \frac{(m_2 - 1)}{\rho} + \frac{eB_z\rho}{2c\hbar} \right) \delta_{m_2,m_1-1} \right]; \tag{A.33}$$

$$E'_{R_1} = \alpha_S \pi \varepsilon_z \left[\left(\frac{J_+ + J_-}{2} \right) \left(-\frac{\partial}{\partial \rho} - \frac{(m_1 - 1)}{\rho} - \frac{eB_z\rho}{2c\hbar} \right) \delta_{m_2,m_1-1} \right]; \tag{A.34}$$

$$E'_{R_2} = \alpha_S \pi \varepsilon_z \left[\left(\frac{J_+ + J_-}{2} \right) \left(\frac{\partial}{\partial \rho} - \frac{(m_1 + 1)}{\rho} - \frac{eB_z\rho}{2c\hbar} \right) \delta_{m_2,m_1+1} \right]; \tag{A.35}$$

$$E'_{R_3} = \alpha_S \pi \varepsilon_z \left[\left(\frac{J_+ - J_-}{2} \right) \left(\frac{\partial}{\partial \rho} + \frac{(m_1 - 1)}{\rho} + \frac{eB_z\rho}{2c\hbar} \right) \delta_{m_2,m_1-1} \right]; \tag{A.36}$$

$$E'_{R_4} = \alpha_S \pi \varepsilon_z \left[\left(\frac{J_+ - J_-}{2} \right) \left(\frac{\partial}{\partial \rho} - \frac{(m_1 + 1)}{\rho} - \frac{eB_z\rho}{2c\hbar} \right) \delta_{m_2,m_1+1} \right]. \tag{A.37}$$

Therefore, Eqs. (A.30)-(A.37) are the matrix elements for the SIA spin-orbit interaction for heavy holes.

A.2 Lateral direction

In this section, we introduce the SO in the lateral direction for valence and conduction bands.

A.2.1 Conduction band - electrons

The in-plane SIA Hamiltonian (A.2) can be written in a following way:

$$H_{SIA} = \alpha_S \left[\left(\sigma_x \frac{\partial V}{\partial y} - \sigma_y \frac{\partial V}{\partial x} \right) k_z + \frac{\partial V}{\partial z} \left(\sigma_y k_x - \sigma_x k_y \right) + \sigma_z \left(\frac{\partial V}{\partial x} k_y - \frac{\partial V}{\partial y} k_x \right) \right]. \tag{A.38}$$

Eq. (A.38) can be decomposed in H_{SIA}=H_R+H^D_{SIA}+H_k, where the last term vanish because $\langle k_z \rangle = 0$. Using Eqs. (A.8) and (A.4) to write (A.38) in cylindrical coordinates,

$$H_{SIA} = \alpha_S \left\{ \frac{\partial V}{\partial z} [-i(\sigma_+ - \sigma_-)k_x - (\sigma_+ + \sigma_-)k_y] + \sigma_z \left(\frac{\partial V}{\partial x} k_y - \frac{\partial V}{\partial y} k_x \right) \right\}, \tag{A.39}$$

$$H_{SIA} = \alpha_S \left\{ -\frac{\partial V}{\partial z} [i\sigma_+(k_x - ik_y) - i\sigma_-(k_x + ik_y)] + \sigma_z \left(\frac{\partial V}{\partial x} k_y - \frac{\partial V}{\partial y} k_x \right) \right\}. \tag{A.40}$$

Thus,

$$H_{SIA} = \alpha_S \left\{ -i\frac{\partial V}{\partial z}(\sigma_+ k_- - \sigma_- k_+) + \sigma_z \left[\frac{\partial V}{\partial x}\left(\frac{k_+ - k_-}{2i}\right) - \frac{\partial V}{\partial y}\left(\frac{k_+ + k_-}{2}\right)\right]\right\}, \tag{A.41}$$

$$H_{SIA} = \alpha_S \left\{ -i\frac{\partial V}{\partial z}(\sigma_+ k_- - \sigma_- k_+) - \frac{i}{2}\sigma_z \left[\left(\frac{\partial V}{\partial x} - i\frac{\partial V}{\partial y}\right)k_+ - \left(\frac{\partial V}{\partial x} + i\frac{\partial V}{\partial y}k_-\right)\right]\right\}. \tag{A.42}$$

To calculate the above Hamiltonian in cylindrical coordinates,

$$\frac{\partial}{\partial x} \mp i\frac{\partial}{\partial y} = L_{\mp}\left(\frac{\partial}{\partial \rho} \mp \frac{i}{\rho}\frac{\partial}{\partial \rho}\right), \tag{A.43}$$

where $L_{\pm} = e^{\pm i\phi}$,

$$H_{SIA} = \alpha_S \left\{ -i\frac{\partial V}{\partial z}(\sigma_+ k_- - \sigma_- k_+) - \frac{i}{2}\sigma_z \left[L_-\left(\frac{\partial V}{\partial \rho} - \frac{i}{\rho}\frac{\partial V}{\partial \phi}\right)k_-\right]\right\}. \tag{A.44}$$

Considering the electric field applied only in the lateral direction,

$$H_{SIA} = -i\frac{\alpha_S}{2}\sigma_z \left[\frac{\partial V}{\partial \rho}(L_- k_+ - L_+ k_-) - \frac{i}{\rho}\frac{\partial V}{\partial \phi}(L_- k_+ + L_+ k_-)\right]. \tag{A.45}$$

Using Eqs. (A.8),

$$\begin{aligned} H_{SIA} &= -i\frac{\alpha_S}{2}\sigma_z \left\{ \frac{\partial V}{\partial \rho}[L_-(iL_+A_+) + L_+(iL_-A_-)] - \frac{i}{\rho}\frac{\partial V}{\partial \phi}[L_-(iL_+A_+) \right. \\ &- \left. L_+(iL_-A_-)]\right\}. \end{aligned} \tag{A.46}$$

A more compact form of Eq. above is given by:

$$H_{SIA} = \frac{\alpha_S}{2}\sigma_z \left\{ \frac{\partial V}{\partial \rho}[A_+ + A_-] - \frac{i}{\rho}\frac{\partial V}{\partial \phi}[A_+ - A_-]\right\}. \tag{A.47}$$

In Eq. below we replace $A_\pm$ by $A_\pm$=$A_\pm \mp \frac{1}{\rho}$. Therefore,

$$H_{SIA} = \frac{\alpha_S}{2}\sigma_z \left\{ \frac{\partial V}{\partial \rho}\left[A_+ - \frac{1}{\rho} + A_- + \frac{1}{\rho}\right] - \frac{i}{\rho}\frac{\partial V}{\partial \phi}\left[A_+ - \frac{1}{\rho} - A_- + \frac{1}{\rho}\right]\right\}. \tag{A.48}$$

After some algebraic manipulations,

$$H^D_{SIA} = \alpha_s \sigma_z \left[\frac{\partial V}{\partial \rho}\left(-\frac{i}{\rho}\frac{\partial}{\partial \rho} + \frac{eB_z\rho}{2c\hbar}\right) + \frac{i}{\rho}\frac{\partial V}{\partial \phi}\frac{\partial}{\partial \rho} + \frac{i}{\rho^2}\frac{\partial V}{\partial \rho}\right]. \tag{A.49}$$

In the next section, the Gaussian perturbation is introduced in the confinement profile within the SIA Hamiltonian, Eq. (A.49).

A.2.1.1 Gaussian perturbative potential

The Gaussian perturbation is described by the additional potential $V_p(\rho,\theta)$=$\delta\rho^2 e^{-(\phi-\pi)^2/2\sigma^2}$ in the confinement profile. Thus, the total confinement (V_T) is given by:

$$V_T = \frac{a_1}{\rho^2} + a_2\rho^2 - \sqrt{a_1 a_2} + V_p(\rho,\theta) \qquad \text{being that} \qquad V_p(\rho,\theta) = \delta\rho^2 e^{-(\phi-\pi)^2/2\sigma^2}. \quad \text{(A.50)}$$

Deriving (A.50),

$$\begin{aligned}
\frac{\partial V_p(\rho,\theta)}{\partial\rho} &= -2\frac{a_1}{\rho^3} + 2a_2\rho + 2\delta\rho e^{-(\phi-\pi)/2\sigma^2}, \\
\frac{\partial V_p(\rho,\theta)}{\partial\phi} &= -\delta\rho^2 e^{(-\phi-\pi)^2/2\sigma^2}\frac{(\phi-\pi)}{\sigma^2}.
\end{aligned} \quad \text{(A.51)}$$

Replacing in the Hamiltonian (A.49),

$$\begin{aligned}
H^D_{SIA} &= \alpha_S\sigma_z\Bigg\{\left[-2\frac{a_1}{\rho^3} + 2a_2\rho + 2\delta\rho e^{-(\phi-\pi)^2/2\sigma^2}\right]\frac{eB_z\rho}{2c\hbar} \\
&- \frac{i}{\rho}\left[-2\frac{a_1}{\rho^3} + 2a_2\rho + 2\delta\rho e^{-(\phi-\pi)^2/2\sigma^2}\right]\frac{\partial}{\partial\phi} + \\
&+ \frac{i}{\rho}\left[-\delta\rho^2 e^{-(\phi-\pi)^2/2\sigma^2}\frac{(\phi-\pi)}{\sigma^2}\right]\frac{\partial}{\partial\rho} + \frac{i}{\rho^2}\left[-\delta\rho^2 e^{-(\phi-\pi)^2/2\sigma^2}\frac{(\phi-\pi)}{\sigma^2}\right]\Bigg\}.
\end{aligned} \quad \text{(A.52)}$$

Thus,

$$\begin{aligned}
H^D_{SIA} &= 2\alpha_S\sigma_z\Bigg\{\left[-\frac{a_1}{\rho^2} + a_2\rho^2 + \delta\rho^2 e^{-(\phi-\pi)^2/2\sigma^2}\right]\frac{eB_z}{2c\hbar} \\
&- i\left[-\frac{a_1}{\rho^4} + a_2 + \delta e^{-(\phi-\pi)^2/2\sigma^2}\right]\frac{\partial}{\partial\phi} + \\
&+ i\left[-\frac{\delta}{2}\rho e^{-(\phi-\pi)^2/2\sigma^2}\frac{(\phi-\pi)}{\sigma^2}\right]\frac{\partial}{\partial\rho} + i\left[-\frac{\delta}{2}e^{-(\phi-\pi)^2/2\sigma^2}\frac{(\phi-\pi)}{\sigma^2}\right]\Bigg\}.
\end{aligned} \quad \text{(A.53)}$$

Applying $\langle\Psi^*_{m_1}|H_R|\Psi_{m_2}\rangle = E_R$ and using the following integrals

- Int_1: $\int_0^{2\pi} e^{im_1\phi}e^{-im_2\phi}d\phi = \int_0^{2\pi} e^{i(m_1-m_2)\phi}d\phi = 2\pi\delta_{m_2,m_1} = F_1\delta_{m_2,m_1}$;

- Int_2: $\int_0^{2\pi} e^{im_1\phi} e^{-(\phi-\pi)^2/2\sigma^2} e^{-im_2\phi} d\phi = F_2 \begin{cases} \delta_{m_2,m_1} \\ \delta_{m_2,m_1\pm1,\pm2,\pm3,...} \end{cases}$;
- Int_3: $\int_0^{2\pi} e^{im_1\phi} \frac{\partial}{\partial\phi} e^{-im_2\phi} d\phi = -2\pi i m_2 \delta_{m_2,m_1} = -im_2 F_1 \delta_{m_2,m_1}$;
- Int_4: $\int_0^{2\pi} e^{im_1\phi} e^{-(\phi-\pi)^2/2\sigma^2} \frac{\partial}{\partial\phi} e^{-im_2\phi} d\phi = -im_2 F_2 \begin{cases} \delta_{m_2,m_1} \\ \delta_{m_2,m_1\pm1,\pm2,\pm3,...} \end{cases}$;
- Int_5: $\int_0^{2\pi} e^{im_1\phi} e^{-(\phi-\pi)^2/2\sigma^2} \frac{(\phi-\pi)}{\sigma^2} e^{-im_2\phi} d\phi = F_3 \begin{cases} \delta_{m_2,m_1} \\ \delta_{m_2,m_1\pm1,\pm2,\pm3,...} \end{cases}$,

the energy of the system is written in a following way:

$$\begin{aligned} E^D_{SIA} &= 2\alpha_S \sigma_z \Bigg\{ \left[-\frac{a_1}{\rho^2} + a_2\rho^2 \right] \frac{eB_z}{2c\hbar} \mathrm{Int}_1 + \delta\rho^2 \frac{eB_z}{2c\hbar} \mathrm{Int}_2 \\ &- i \left[-\frac{a_1}{\rho^4} + a_2 \right] \mathrm{Int}_3 - i\delta \mathrm{Int}_4 + i \left[-\frac{\delta}{2} \rho \mathrm{Int}_5 \right] \frac{\partial}{\partial\rho} + i \left[-\frac{\delta}{2} \mathrm{Int}_5 \right]. \end{aligned} \tag{A.54}$$

The selection rules for the Gaussian perturbation do not cancel for any value of m_1, m_2. In this way, all terms must be considered in the calculations. Therefore,

$$\begin{aligned} E^D_{SIA} &= 2\alpha_S \sigma_z \Bigg\{ \left[-\frac{a_1}{\rho^2} + a_2\rho^2 \right] \frac{eB_z}{2c\hbar} \mathrm{Int}_1 + \delta\rho^2 \frac{eB_z}{2c\hbar} \mathrm{Int}_2 \\ &- i \left[-\frac{a_1}{\rho^4} + a_2 \right] (-im_2 \mathrm{Int}_1) - i\delta(-im_2) \mathrm{Int}_2 - i\frac{\delta}{2} \left[\rho \frac{\partial}{\partial\rho} + 1 \right] \mathrm{Int}_5 \Bigg\}. \end{aligned} \tag{A.55}$$

$$\begin{aligned} E^D_{SIA} &= 2\alpha_S \sigma_z \Bigg\{ \Bigg\{ \left[-\frac{a_1}{\rho^2} + a_2\rho^2 \right] \frac{eB_z}{2c\hbar} F_1 + \delta\rho^2 \frac{eB_z}{2c\hbar} F_2 \\ &- m_2 \left[-\frac{a_1}{\rho^4} + a_2 \right] F_1 - m_2\delta F_2 - i\frac{\delta}{2} \left[\rho \frac{\partial}{\partial\rho} + 1 \right] F_3 \Bigg\} \delta_{m_2,m_1} \\ &+ \left\{ \delta\rho^2 \frac{eB_z}{2c\hbar} F_2 - m_2\delta F_2 - i\frac{\delta}{2} \left[\rho \frac{\partial}{\partial\rho} + 1 \right] F_3 \right\} \delta_{m_2,m_1\pm1,\pm2,\pm3,...} \Bigg\}. \end{aligned} \tag{A.56}$$

Performing the same procedure as (A.13),

$$\begin{aligned} E^D_{SIA} &= 2\alpha_S(-\sigma_z) \Bigg\{ \Bigg\{ \left[-\frac{a_1}{\rho^2} + a_2\rho^2 \right] \frac{e(-B_z)}{2c\hbar} F_1 + \delta\rho^2 \frac{e(-B_z)}{2c\hbar} F_2 \\ &- (-m_1) \left[-\frac{a_1}{\rho^4} + a_2 \right] F_1 - (-m_1)\delta F_2 + i\frac{\delta}{2} \left[\rho \frac{\partial}{\partial\rho} + 1 \right] F_3 \Bigg\} \delta_{m_2,m_1} \\ &+ \left\{ \delta\rho^2 \frac{e(-B_z)}{2c\hbar} F_2 - (-m_1)\delta F_2 + i\frac{\delta}{2} \left[\rho \frac{\partial}{\partial\rho} + 1 \right] F_3 \right\} \delta_{m_2,m_1\pm1,\pm2,\pm3,...} \Bigg\}. \end{aligned} \tag{A.57}$$

Thus,

$$
\begin{aligned}
E^{D}_{SIA} &= 2\alpha_S\sigma_z\Bigg\{\Bigg\{\left[-\frac{a_1}{\rho^2}+a_2\rho^2\right]\frac{eB_z}{2c\hbar}F_1+\delta\rho^2\frac{eB_z}{2c\hbar}F_2 \\
&- m_1\left[-\frac{a_1}{\rho^4}+a_2\right]F_1-m_1\delta F_2-i\frac{\delta}{2}\left[\rho\frac{\partial}{\partial\rho}+1\right]F_3\Bigg\}\delta_{m_2,m_1} \\
&+ \Bigg\{-\delta\rho^2\frac{eB_z}{2c\hbar}F_2+m_1\delta F_2+i\frac{\delta}{2}\left[\rho\frac{\partial}{\partial\rho}+1\right]F_3\Bigg\}\delta_{m_2,m_1\pm1,\pm2,\pm3,\ldots}\Bigg\}.
\end{aligned}
\tag{A.58}
$$

Rearranging the terms:

$$
\begin{aligned}
E^{D}_{SIA_1} &= 2\alpha_S\sigma_z\Bigg\{\left[-\frac{a_1}{\rho^2}+a_2\rho\right]\frac{eB_z}{2c\hbar}F_1+\delta\rho^2\frac{eB_z}{2c\hbar}F_2 \\
&- m_2\left[-\frac{a_1}{\rho^4}+a_2\right]F_1-\delta m_2F_2-i\frac{\delta}{2}\left[\rho\frac{\partial}{\partial\rho}+1\right]F_3\Bigg\}\delta_{m_2,m_1};
\end{aligned}
\tag{A.59}
$$

$$
E^{D}_{SIA_2} = 2\alpha_S\sigma_z\left\{\delta\rho^2\frac{eB_z}{2c\hbar}F_2-\delta m_2F_2-i\frac{\delta}{2}\left[\rho\frac{\partial}{\partial\rho}+1\right]F_3\right\}\delta_{m_2,m_1\pm1,\pm2,\pm3,\ldots}; \tag{A.60}
$$

$$
\begin{aligned}
E'^{D}_{SIA_1} &= 2\alpha_S\sigma_z\Bigg\{\left[-\frac{a_1}{\rho^2}+a_2\rho\right]\frac{eB_z}{2c\hbar}F_1+\delta\rho^2\frac{eB_z}{2c\hbar}F_2 \\
&- m_1\left[-\frac{a_1}{\rho^4}+a_2\right]F_1-\delta m_1F_2-i\frac{\delta}{2}\left[\rho\frac{\partial}{\partial\rho}+1\right]F_3\Bigg\}\delta_{m_2,m_1};
\end{aligned}
\tag{A.61}
$$

$$
E'^{D}_{SIA_2} = 2\alpha_S\sigma_z\left\{-\delta\rho^2\frac{eB_z}{2c\hbar}F_2+\delta m_1F_2+i\frac{\delta}{2}\left[\rho\frac{\partial}{\partial\rho}+1\right]F_3\right\}\delta_{m_2,m_1\pm1,\pm2,\pm3,\ldots}. \tag{A.62}
$$

The procedure to obtain the spin-orbit Hamiltonian for heavy holes in lateral direction is similar to presented in Eq. (A.49).

Appendix B

Bump size in the potential profile

Here, we present the relation between bump size and the perturbative potentials used in the chapter 3. In the section 3.3.2, the ground state energies and the bump size were defined as follows,

$$\Delta = R_1 - R_0; \qquad R_1 = \left(\frac{\varepsilon_0}{a_2 + \delta_2}\right)^{\frac{1}{2}}; \qquad R_0 = \left(\frac{\varepsilon_0}{a_2}\right)^{\frac{1}{2}}. \tag{B.1}$$

Replacing R_0 and R_1 in Δ,

$$\Delta = \varepsilon_0^{\frac{1}{2}}\left[\frac{1}{(a_2 + \delta_2)^{1/2}} - \frac{1}{a_2^{1/2}}\right]. \tag{B.2}$$

Multiplying by $a_2^{1/2}$,

$$\Delta = \left(\frac{\varepsilon_0}{a_2}\right)^{1/2}\left[\frac{a_2^{1/2}}{(a_2 + \delta_2)^{1/2}} - 1\right]. \tag{B.3}$$

Using relations $\varepsilon_0 = \hbar\frac{2a_2}{m}$ and ε_0=$\hbar^2\frac{1}{ml_0^2}$, where l_0=$\sqrt{\frac{\hbar}{(2a_2m)^{1/2}}}$, and inserting in Eq. (B.3), the bump size is given by:

$$\Delta = \sqrt{2}l_0\left[\frac{a_2^{1/2}}{(a_2 + \delta_2)^{1/2}} - 1\right]. \tag{B.4}$$

Thus, Eq. (B.4) becomes:

$$\delta_2 = a_2\left[\frac{1}{\left(\frac{\Delta}{\sqrt{2}l_0}\right)^2} - 1\right]. \tag{B.5}$$

The sign of δ_2 modulates the direction and intensity of the Gaussian perturbation.

Appendix C

Luttinger model

In this appendix, we show the details of the calculations within the Luttinger[1] model used to describe HH and LH coupling studied in chapter 3, section 3.4. The Luttinger elements are given by the linear combination of the total angular momentum: [59]

$$\left|\frac{3}{2},+\frac{3}{2}\right\rangle = \frac{1}{\sqrt{2}}\left|(X+iY)\uparrow\right\rangle; \tag{C.1}$$

$$\left|\frac{3}{2},-\frac{3}{2}\right\rangle = \frac{1}{\sqrt{2}}\left|(X-iY)\downarrow\right\rangle; \tag{C.2}$$

$$\left|\frac{3}{2},+\frac{1}{2}\right\rangle = \frac{1}{\sqrt{6}}\left|(X+iY)\downarrow\right\rangle - \sqrt{\frac{2}{3}}\left|Z\uparrow\right\rangle; \tag{C.3}$$

$$\left|\frac{3}{2},-\frac{1}{2}\right\rangle = -\frac{1}{\sqrt{6}}\left|(X-iY)\uparrow\right\rangle - \sqrt{\frac{2}{3}}\left|Z\downarrow\right\rangle. \tag{C.4}$$

The matrix elements are written in the following way:

$$H_K = \begin{pmatrix} a_+^{hh\uparrow} & b_- & c_- & 0 \\ b_+ & a_-^{lh\uparrow} & 0 & c_- \\ c_+ & 0 & d_-^{lh\downarrow} & b_- \\ 0 & c_+ & b_+ & d_+^{hh\downarrow} \end{pmatrix}, \tag{C.5}$$

[1]The Luttinger model was studied in the chapter 2, section 2.2.4.

where $hh\uparrow$, $hh\downarrow$, $lh\uparrow$ and $lh\downarrow$ are the heavy (hh) and light holes (lh) with spins up ($\uparrow$) and down ($\downarrow$), respectively. Thus, the matrix elements are written as follows: [27]

$$\begin{aligned} a_{\pm} &= -\frac{\hbar^2}{2m_0}(\gamma_1 \mp 2\gamma_2)k_z^2 - \frac{\hbar^2}{4m_0}(\gamma_1 \pm \gamma_2)(k_+k_- + k_-k_+) \\ &+ \frac{(2\pm1)}{2}\hbar\omega_e\left(\kappa + \frac{(5\pm4)}{4}q\right); \end{aligned} \tag{C.6}$$

$$\begin{aligned} d_{\pm} &= -\frac{\hbar^2}{2m_0}(\gamma_1 \mp 2\gamma_2)k_z^2 - \frac{\hbar^2}{4m_0}(\gamma_1 \pm \gamma_2)(k_+k_- + k_-k_+) \\ &- \frac{(2\pm1)}{2}\hbar\omega_e\left(\kappa + \frac{(5\pm4)}{4}q\right); \end{aligned} \tag{C.7}$$

$$b_{\mp} = \hbar^2\frac{\sqrt{3}}{4m_0}\gamma_3 k_z k_{\mp}; \tag{C.8}$$

$$c_{\mp} = \hbar^2\frac{\sqrt{3}}{4m_0}(\gamma_2 + \gamma_3)k_{\mp}^2, \tag{C.9}$$

where $\omega_e = \frac{eB}{m_0}$, q and κ are the Zeeman elements, γ_α, $\alpha = 1, 2, 3$, the Luttinger parameters. The q, κ and γ_α depends on the material, which are reported by experiments or *ab initio* calculations. Thus, introducing the confinement potential in the Luttinger matrix, the result is:

$$H_L = \begin{pmatrix} a_+^{hh\uparrow} + V(r) & b_- & c_- & 0 \\ b_+ & a_-^{lh\uparrow} + V(r) & 0 & c_- \\ c_+ & 0 & d_-^{lh\downarrow} + V(r) & b_- \\ 0 & c_+ & b_+ & d_+^{hh\downarrow} + V(r) \end{pmatrix}. \tag{C.10}$$

For cylindrical coordinates, the **k** vectors are transformed in the following way:

$$k_{\mp} = -ie^{\mp i\varphi}\left(\frac{\partial}{\partial\rho} \mp \frac{i}{\rho}\frac{\partial}{\partial\varphi} \pm \frac{m_0\omega_e}{2\hbar}\rho\right), \qquad k_z = -i\frac{\partial}{\partial z}. \tag{C.11}$$

Thus,

$$\begin{aligned} a_{\pm} &= \frac{\hbar^2}{2m_0}(\gamma_1 \mp 2\gamma_2)\frac{\partial^2}{\partial z^2} + \frac{\hbar^2}{2m_0}(\gamma_1 \pm \gamma_2)\left[\frac{\partial^2}{\partial\rho^2} + \frac{1}{\rho}\frac{\partial}{\partial\rho} + i\alpha\frac{\partial}{\partial\varphi} + \frac{1}{\rho^2}\frac{\partial^2}{\partial\varphi^2} - \alpha^2\rho^2\right] \\ &+ \frac{(2\pm1)}{2}\hbar\omega_e\left(\kappa + \frac{(5\pm4)}{4}q\right); \end{aligned} \tag{C.12}$$

$$d_{\pm} = \frac{\hbar^2}{2m_0}(\gamma_1 \mp 2\gamma_2)\frac{\partial^2}{\partial z^2} + \frac{\hbar^2}{2m_0}(\gamma_1 \pm \gamma_2)\left[\frac{\partial^2}{\partial \rho^2} + \frac{1}{\rho}\frac{\partial}{\partial \rho} + i\alpha\frac{\partial}{\partial \varphi} + \frac{1}{\rho^2}\frac{\partial^2}{\partial \varphi^2} - \alpha^2\rho^2\right] - \frac{(2\pm 1)}{2}\hbar\omega_e\left(\kappa + \frac{(5\pm 4)}{4}q\right); \tag{C.13}$$

$$b_{\mp} = -\frac{\sqrt{3}}{4}\frac{\hbar^2}{m_0}\gamma_3 e^{\pm i\varphi}\left(\frac{\partial^2}{\partial \rho \partial z} \pm \frac{i}{\rho}\frac{\partial^2}{\partial \varphi \partial z} \mp \alpha\rho\frac{\partial}{\partial z}\right); \tag{C.14}$$

$$c_{\mp} = -\frac{\sqrt{3}}{4}\frac{\hbar^2}{m_0}(\gamma_2 + \gamma_3)e^{\pm 2i\varphi}\left[\frac{\partial^2}{\partial \rho^2} - \left(\frac{1}{\rho} \pm \alpha\rho\right)\frac{\partial}{\partial \rho} - \frac{1}{\rho^2}\frac{\partial^2}{\partial \varphi^2} - \left(i\alpha \pm \frac{2i}{\rho^2}\right)\frac{\partial}{\partial \varphi} \pm \frac{2i}{\rho}\frac{\partial^2}{\partial \rho \partial \varphi} + \alpha^2\rho^2\right]. \tag{C.15}$$

After some algebraic manipulations,

$$a_{\pm} = \left\{\frac{\hbar^2}{m_0}(\gamma_1 \mp 2\gamma_2)\frac{\partial^2}{\partial z^2} + \frac{\hbar^2}{m_0}(\gamma_1 \pm \gamma_2)\left[\frac{\partial^2}{\partial \rho^2} + \frac{1}{\rho}\frac{\partial}{\partial \rho} + \alpha m_2 - \frac{m_2^2}{\rho^2} - \alpha^2\rho^2\right] + \frac{(2\pm 1)}{2}\hbar\omega_e\left(\kappa + \frac{(5\pm 4)}{4}q\right)\right\}\delta_{m_2,m_1}; \tag{C.16}$$

$$d_{\pm} = \left\{\frac{\hbar^2}{m_0}(\gamma_1 \mp 2\gamma_2)\frac{\partial^2}{\partial z^2} + \frac{\hbar^2}{m_0}(\gamma_1 \pm \gamma_2)\left[\frac{\partial^2}{\partial \rho^2} + \frac{1}{\rho}\frac{\partial}{\partial \rho} + \alpha m_2 - \frac{m_2^2}{\rho^2} - \alpha^2\rho^2\right] - \frac{(2\pm 1)}{2}\hbar\omega_e\left(\kappa + \frac{(5\pm 4)}{4}q\right)\right\}\delta_{m_2,m_1}; \tag{C.17}$$

$$b_{\mp} = -\frac{\sqrt{3}}{2}\frac{\hbar^2}{m_0}\gamma_3\left(\frac{\partial^2}{\partial \rho \partial z} \pm \frac{m_2}{\rho}\frac{\partial}{\partial z} \mp \alpha\rho\frac{\partial}{\partial z}\right)\delta_{m_2,m_1\pm 1}; \tag{C.18}$$

$$c_{\mp} = -\frac{\sqrt{3}}{2}\frac{\hbar^2}{m_0}(\gamma_2 + \gamma_3)\left[\frac{\partial^2}{\partial \rho^2} - \left(\frac{1}{\rho} \pm \alpha\rho\right)\frac{\partial}{\partial \rho} - \frac{1}{\rho^2}\frac{\partial^2}{\partial \varphi^2} - \left(\alpha m_2 \pm \frac{2m_2}{\rho^2}\right) \pm \frac{2m_2}{\rho}\frac{\partial}{\partial \rho} + \alpha^2\rho^2\right]\delta_{m_2,m_1\pm 2}. \tag{C.19}$$

These elements of Luttinger matrix describe the electronic structure of LH and HH including the Zeeman splitting, where the split-off states are considered as a remote band.

Appendix D

Exchange interaction parameter

The objective of this appendix is to describe the details of the calculation of the exchange interaction parameter. In the section D.1, we show the adjustment process of the Hubbard correction on *d* states of the cadmium and zinc in CdMnSe QDs, studied in the chapter 3. Using the effective coordination number (ECN) concept, in the section D.2, we present a structural analysis for the CdSe QDs undoped and doped by Mn impurity in a ZnSe host material. Section D.3 exhibits the obtained values of the exchange interaction parameter, J_0, investigated within the density functional theory framework.

D.1 Cadmium selenide and zinc selenide in bulk model - GGA+U$_{eff}$

Assuming the zinc blend phase for the cadmium selenide and zinc selenide pristine geometries, the Hubbard U$_{eff}$ correction was varied for a better gap energy and lattice parameter description. The obtained values are shown in Table D.1 and the details of the calculations are found in the appendix E, wherein the exchange and correlation functional used was proposed by Perdew-Burke-Ernzerhof (PBE). The experimental lattice parameters and gap energies of the CdSe and ZnSe pristine structures are, namely, 6.05 Å and 5.67 Å, 1.90 eV and 2.82 eV, respectively. Fig. D.1 depicts the local density of states with the Hubbard correction on *d*-Cd and *d*-Zn states:

Table D.1: Effective Hubbard correction U_{eff} on *d* states of cadmium and zinc atoms applied to obtain a better accuracy of the lattice parameter (a_0) and gap energy (E_g) of the pristine CdSe and ZnSe bulk structures.

U_{eff} [eV]	a_0^{CdSe} [Å]	a_0^{ZnSe} [Å]	E_g^{CdSe} [eV]	E_g^{ZnSe} [eV]
0	6.19	5.74	0.50	1.13
1	6.19	5.72	0.54	1.21
2	6.18	5.73	0.61	1.24
3	6.16	5.72	0.68	1.32
4	6.15	5.71	0.76	1.37
5	6.13	5.70	0.84	1.44
6	6.11	5.69	0.92	1.51
7	6.08	5.68	1.04	1.58

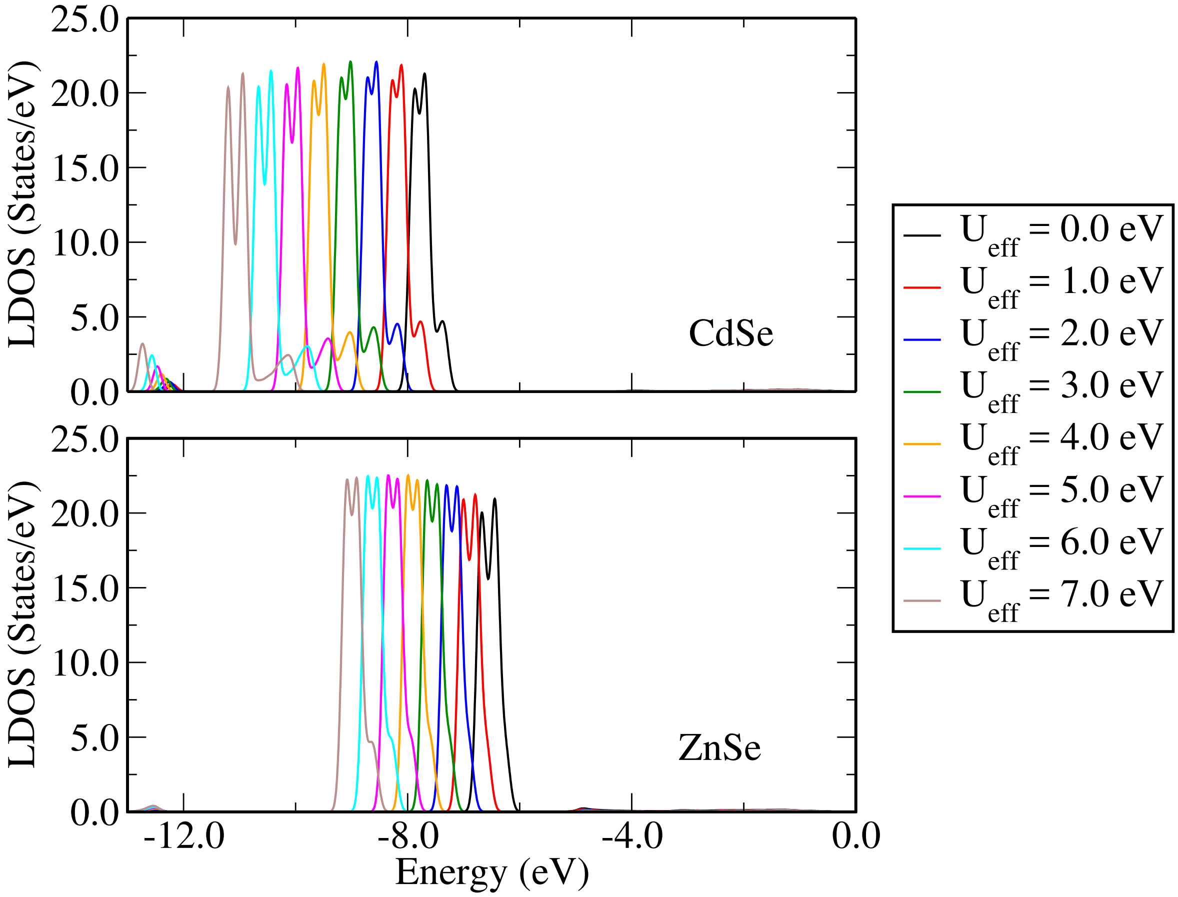

Figure D.1: Local density of states as function of the effective Hubbard U_{eff} correction on *d* cadmium and zinc states in CdSe and ZnSe pristine bulk structures.

D.2 CdSe and ZnSe quantum dots

Using the Perdew-Burke-Ernzerhof (PBE) exchange and correlation functional, in Table D.2 we present a comparison between the CdSe QDs in ZnSe substrate with and without the effective Hubbard correction of U_{eff}=7.0 eV on d-Cd and d-Zn states.

Table D.2: Calculated values of the lattice parameter (a_0) and gap energy (E_g) with and without Hubbard correction U_{eff}=7.0 eV on d-Cd and d-Zn states for CdSe QDs within ZnSe host material.

CdSe em ZnSe	a_0	E_g
	[Å]	[eV]
PBE	17.68	0.83
PBE+U_{eff}	17.49	1.30

In the next calculations, one Mn atom enters interstitially in the crystal and replacing the Cd and Zn inside and outside the QD, respectively. Fixing the lattice parameter in order to analyze the effective coordination number (ECN)[1], Table D.3 indicates the relation between ECN and average distance as function of the Hubbard[2] correction U_{eff}=7.0 eV on d-Cd and d-Zn states:

Table D.3: Effective coordination number ($\mathrm{ECN}_{\mathrm{atom}}$) and average distance ($d_{AV}^{\mathrm{atom}}$), where atom is the chemical specie (Mn, Cd, Se, Zn), with and without Hubbard correction.

Structure	ECN_{Mn}	ECN_{Cd}	ECN_{Se}	ECN_{Zn}	d_{AV}^{Mn}	d_{AV}^{Cd}	d_{AV}^{Se}	d_{AV}^{Zn}
Undoped	-	4.00	3.95	4.00	-	2.65	2.55	2.50
Undoped$^{U_{eff}}$	-	4.00	3.96	4.00	-	2.61	2.52	2.48
Mn Subst. Zn	4.00	4.00	3.95	4.00	2.53	2.65	2.55	2.50
Mn Subst. Zn$^{U_{eff}}$	4.00	4.00	3.96	4.00	2.59	2.61	2.52	2.48
QD-004	4.00	4.00	3.95	4.00	2.51	2.65	2.55	2.50
QD-004$^{U_{eff}}$	4.00	4.00	3.96	4.00	2.57	2.61	2.52	2.48
Int. Matrix	6.24	4.01	3.98	4.00	2.64	2.65	2.55	2.50
Int. Matrix$^{U_{eff}}$	6.61	4.00	4.00	4.00	2.68	2.61	2.52	2.48

The introduction of the Hubbard correction changes the atomic radius, providing a better description of the lattice parameter and gap energy of the structure. In addition, the Hubbard correction changes the magnetic moment of the geometries. In Table D.4, we show the local magnetization (Local Mag.) and the final magnetization (Final Mag.) of the CdSe QDs undoped and doped by Mn impurity in ZnSe host material. The calculations were performed with and without Hubbard correction of U_{eff} =7.0 eV on d-Cd and d-Zn states, wherein the PBE exchange and correlation functional were used.

[1]For more details, the effective coordination number concept was presented in section 3.6.2.
[2]The Hubbard correction was determined in section D.1.

Table D.4: Local magnetic moment (Local Mag.) and final magnetic moment (Final Mag.) of the CdSe QDs undoped and doped by Mn impurity in ZnSe substrate. The calculations were performed with and without Hubbard correction of U_{eff} =7.0 eV on d-Cd and d-Zn states.

Struct.	Local Mag.	Final Mag.
	$[\mu_B]$	$[\mu_B]$
Undoped	-	-
Undoped$^{U_{eff}}$	-	-
Mn Subst. Zn	4.26	5.00
Mn Subst. Zn$^{U_{eff}}$	4.97	5.00
QD-004	4.23	5.00
QD-004$^{U_{eff}}$	4.97	5.00
Int. Matrix	4.12	5.00
Int. Matrix$^{U_{eff}}$	4.95	5.00

Due to partially occupied d-Mn states, the final magnetization is 5.0 μ_B and the local magnetization varies according to the structure.

D.3 Exchange interaction calculation

In order to elucidate the exchange interaction parameter J_0, it was performed a comparison between the CdSe pristine and CdSe QD within ZnSe substrate, both structures doped by the Mn impurity, containing 216 atoms, namely 107 Cd, 108 Se and 1 Mn in the bulk without QD and 70 Zn, 37 Cd, 108 Se and 1 Mn in the bulk with QD. As mentioned in section 3.6, the experimental exchange interaction parameter observed for CdMnSe bulk is J_0=0.26 eV. [217] The concentration for one Mn impurity in the supercell is x_{eff} =1.0 %. The spin impurity average is given by $\langle S \rangle = \frac{5}{2}$. Taking Eq. (3.32) in the form $N_0\alpha = J_0 = -\frac{\Delta E_{tot}}{x_{eff}\frac{5}{2}}$ and varying the U$_{eff}$ for d manganese states, wherein the U_{eff}=7.0 eV was fixed for d-Cd and d-Zn states, the calculations for the bulk with and without QD were performed using initial magnetic moment (Mag) and fixing the spin impurity (Nel) for each calculation. The exchange and correlation functional used was proposed by Perdew-Burke-Ernzerhof (PBE) and the results are presented in the following sections.

D.3.1 Bulk without quantum dot

In Table the D.5, we present the results of the investigations for the exchange interaction parameter J_0 for the cadmium selenide bulk doped by manganese impurity.

Table D.5: Calculated values for the exchange interaction parameter for the cadmium selenide bulk doped by manganese impurity.

Exchange	U	Local Mag.	Total Mag.	Energy	ΔE_{tot}	J_0
	[eV]	[μ_B]	[μ_B]	[eV]	[eV]	[eV]
Mag4 -Nel4	0	4.211	3.861	−558.25288	−0.04427	−1.77089
Mag6 -Nel6	0	4.317	5.151	−558.20861	-	-
Mag4 -Nel4	1	4.395	3.940	−557.89439	−0.01810	−0.72406
Mag6 -Nel6	1	4.430	5.217	−557.87629	-	-
Mag4 -Nel4	2	4.513	4.003	−557.59892	−0.01087	−0.43492
Mag6 -Nel6	2	4.528	5.277	−557.58805	-	-
Mag4 -Nel4	3	4.607	4.059	−557.34883	−0.00654	−0.26158
Mag6 -Nel6	3	4.616	5.332	−557.34229	-	-
Mag4 -Nel4	4	4.689	4.111	−557.13760	−0.00378	−0.15113
Mag6 -Nel6	4	4.694	5.384	−557.13382	-	-
Mag4 -Nel4	5	4.765	4.164	−556.96340	−0.00294	−0.11772
Mag6 -Nel6	5	4.769	5.436	−556.96046	-	-
Mag4 -Nel4	6	4.839	4.218	−556.82475	−0.00187	−0.07479
Mag6 -Nel6	6	4.843	5.490	−556.82288	-	-
Mag4 -Nel4	7	4.918	4.280	−556.72293	−0.00093	−0.03715
Mag6 -Nel6	7	4.922	5.552	−556.72200	-	-

Therefore, for the bulk without QD, the J_0=0.26 eV was theoretically achieved for U_{eff}^{Cd}=7.0 eV and U_{eff}^{Mn}=3.0 eV on d cadmium and manganese states, respectively.

D.3.2 Bulk with quantum dot

In Table D.6, we show the calculations for the exchange interaction parameter for the CdSe QD doped by Mn impurity within ZnSe host material, structure (i) QD-004 in Fig. 3.11.

The QD inside the bulk changes the behavior of the exchange interaction parameter due to the strain given by the lattice parameters difference between the CdSe and ZnSe structures. As shown in Table D.6, J_0 achieves the experimental results for the Hubbard correction between U_{eff}=4.0 eV and 5.0 eV on d-Mn level, where was fixed the U_{eff}=7.0 eV for d-Cd and Zn states.

Table D.6: Exchange interaction parameter calculations for the CdSe:Mn quantum dot within ZnSe substrate.

Exchange	U	Local Mag.	Total Mag.	Energy (eV)	ΔE_{tot}(eV)	J_0 (eV)
	[eV]	[μ_B]	[μ_B]	[eV]	[eV]	[eV]
Mag4 -Nel4	0	4.135	3.837	−577.50684	−0.06890	−2.75600
Mag6 -Nel6	0	4.277	5.154	−577.43794	-	-
Mag4 -Nel4	1	4.345	3.924	−577.12152	−0.03240	−1.29600
Mag6 -Nel6	1	4.397	5.225	−577.08912	-	-
Mag4 -Nel4	2	4.484	3.995	−576.80740	−0.01842	−0.73680
Mag6 -Nel6	2	4.506	5.291	−576.78898	-	-
Mag4 -Nel4	3	4.591	4.059	−576.54642	−0.01180	−0.47200
Mag6 -Nel6	3	4.602	5.353	−576.53462	-	-
Mag4 -Nel4	4	4.683	4.119	−576.33060	−0.00849	−0.33960
Mag6 -Nel6	4	4.692	5.412	−576.32211	-	-
Mag4 -Nel4	5	4.772	4.180	−576.15650	−0.00596	−0.23840
Mag6 -Nel6	5	4.778	5.473	−576.15054	-	-
Mag4 -Nel4	6	4.861	4.248	−576.02532	−0.00438	−0.17520
Mag6 -Nel6	6	4.866	5.540	−576.02094	-	-
Mag4 -Nel4	7	4.962	4.328	−575.94106	−0.00295	−0.11800
Mag6 -Nel6	7	4.966	5.621	−575.93811	-	-

D.3.3 Comparative results

In Fig. D.2, we present a comparison between the CdSe bulk doped by Mn and the CdSe QD doped by Mn impurity within the ZnSe host material for the exchange interaction parameter as function of the DFT total energy and the effective Hubbard correction.

It is important to emphasize the distinct values of the Hubbard U_{eff} corrections for both cases, bulk with and without QD, as shown in the Fig. D.2. A more detailed comparison is depicted in the Fig. D.3.

Therefore, these analyzes proposes a new method for the J_0 calculations in Diluted Magnetic Semiconductor systems at atomistic scales using the density functional theory.

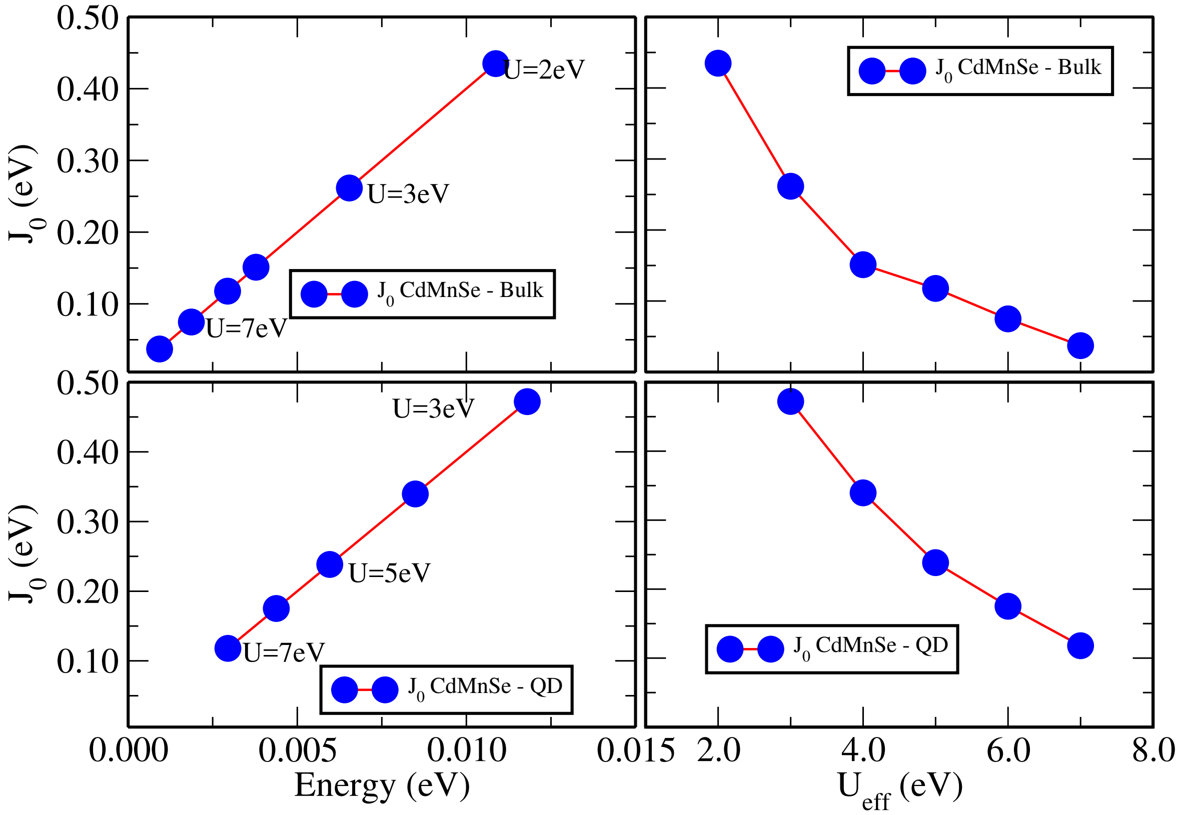

Figure D.2: Comparison between the CdSe bulk doped by Mn and the CdSe QD doped by Mn within the ZnSe substrate for the exchange interaction parameter as function of the DFT total energy and the effective Hubbard correction. At upper part of the Fig. we represent the bulk without QD and, at the bottom, the bulk with QD. In both cases, the Mn impurity replaces one Cd atom.

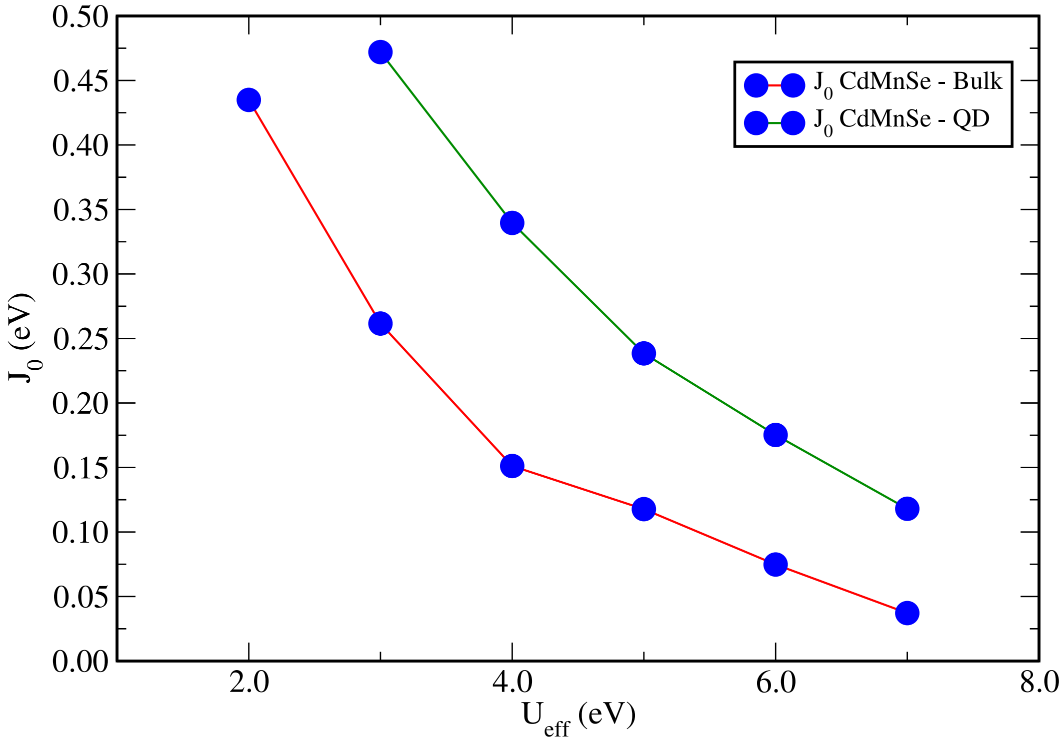

Figure D.3: Exchange interaction parameter for the geometries with and without CdSe QD. The distinct behavior of the exchange interaction is due to the QD presence in the bulk, introducing a strain and changing the local environment of the structure.

Appendix E

Theoretical approach and computational details

In this appendix, we present the details of the calculations performed to obtain the results of this Thesis. The description of the studied systems is within the many body problem, wherein the effective mass and density functional theory, as shown in the chapter 2, are the theoretical approaches used.

The full diagonalization of the Schroedinger Eq. within the $\mathbf{k}\cdot\mathbf{p}$ approach was performed using the Maplesoft package, version 18.0. The eigenvalues were ordered in a growing sequence of energy. The Fock-Darwin spectrum was used to describe the quantum states. The atomistic calculations used in this Thesis are based on the density functional theory. [88, 89] The Projector Augmented Wave (PAW) method [179] and the semilocal exchange and correlation functional proposed by Perdew, Burke, and Ernzerhof (PBE) [102] were used to solve self-consistently the all-electron Kohn-Sham Eq., as implemented in the Viena *ab initio* Simulation Package (VASP). [252, 253] The PAW projectors include in the valence the following states, namely, $4d^{10}\ 5s^2$, $3d^{10}\ 4s^2$, $3d^{10}\ 4s^2\ 4p^4$, $3d^5\ 4s^2$, $5s^1 4d^5$, $3s^2 3p^4$, $2s^2 2p^2$, $2s^2 2p^3$, and $1s^1$ for Cd, Zn, Se, Mn, Mo, S, C, N, and H, respectively. The equilibrium volume was reached by the minimization of the stress tensor and atomic forces using a plane wave expansion cutoff of 656 eV and 689 eV for cadmium selenide and molybdenum disulfide systems, respectively, while for the total energies calculations a cutoff of 369 eV and 473 eV were employed for CdSe and MoS_2 configurations, respectively, 12.5 % higher than recommended by the VASP package. For the integration of the Brillouin zone, the Γ-point was used to sample the reciprocal space of the CdMnSe QD in the ZnSe host material, as described in chapter 3. In the chemical potential calculations, performed in the chapter 4, an orthorhombic box of $24 \times 25 \times 26$ Å^3 was used to compute the free-atom using the Γ-point for integrate the Brillouin zone. In addition, the **k**-point mesh of $19 \times 19 \times 19$, $13 \times 13 \times 10$ and $22 \times 22 \times 10$ was used for the Cd, Se and Zn bulk systems, respectively. In the calculations of chapter 5, a special grids of $8 \times 8 \times 2$ and $8 \times 8 \times 1$ were employed for integrate the Brillouin zone of the MoS_2 bulk and single layer, respectively. Concerning the electronic properties calculations, such as, density of states, the **k**-mesh used was twice larger. The atoms were allowed to relax until all the forces were smaller than 0.0250 eV Å^{-1} for CdSe:Mn systems and, to provide a better description of the adsorption properties of the azobenzene molecule on MoS_2 surface, 0.010 eV Å^{-1} was adopted. The results were obtained using a Gaussian smearing of 0.01 eV.

In order to avoid self-image interactions in the charged defect calculations, [158] which can affect the total energy and the atomic forces, the monopole corrections introduced by Neugebauer *et al*. were used. [157] A quadratic electrostatic potential was added to the local potential, correcting the errors introduced by the periodic calculations. The computational efforts for the plane wave expansion using the Kohn-Sham scheme are related to the size L of the supercell. Increasing the size of the supercell, the convergence is determined by long range forces, which in general are the electrostatic forces. The convergence properties are obtained by the analysis of the electrostatic energy in the periodic calculations. The charge density of the crystalline system with a point defect is the sum of the periodic and aperiodic charge densities, where the correction in the energy is given by: [158]

$$E = E_0 - \frac{q^2\alpha}{2L\varepsilon} - \frac{2\pi Q}{3L^3\varepsilon} + O(L^{-5})\,, \tag{E.1}$$

with Q the second radial moment only for the aperiodic density that does not arise from the dielectric ε response. The total energy calculations ($E_{tot}^{\mathrm{DFT+D3}}$) concerning the azobenzene molecule and molybdenum disulfide layer were obtained using the van der Waals (E_{disp}^{D3}) corrections and DFT-PBE total energy (E_{tot}^{DFT}), namely,

$$E_{tot}^{\mathrm{DFT+D3}} = E_{tot}^{\mathrm{DFT}} + E_{disp}^{\mathrm{D3}}\,, \tag{E.2}$$

where

$$E^{\mathrm{D3}}_{disp} = -\frac{1}{2}\sum_{i=1}^{M}\sum_{j=1}^{M}\sum_{L}\left(f_{d,6}(R_{ij,L})\frac{C_6^{ij}}{R_{ij,L}^6} + f_{d,8}(R_{ij,L})\frac{C_8^{ij}}{R_{ij,L}^8}\right). \tag{E.3}$$

Eq. (E.3) determines the magnitude of the vdW interactions. The sums are made on all M atoms of the unit cell $L = (l_1, l_2, l_3)$. The parameters C_{6ij} are the dispersion coefficients of the vdW corrections from atom pair AB within the internuclear distances $R_{ij}^{6,8}$. These parameters are obtained from the self-consistent Tkatchenko-Scheffler approach. [153] To avoid singularities at interatomic scales, a damping function ($f_{d,n}$) was employed,

$$f_{d,n} = \frac{s_n}{1 + 6(R_{ij}/(s_{R,n}R_0^{ij}))^{-\alpha_n}}, \tag{E.4}$$

where $s_{R,n}$ are the scaling factors concerning the cutoff radii, $R_0^{ij} = \sqrt{\frac{C_8^{ij}}{C_6^{ij}}}$ and α_n are fixed values whose choices depend on the exchange and correlation functional. In this calculations, only one side of the surface supporting the azobenzene molecule was considered. Therefore, the dipole corrections were introduced in all calculations of chapter 5. [157, 158] The charge flow analysis were performed using the Bader charge concept, wherein the number of grid-points were increased by a three factor along the lattice parameters directions to calculate the Fast Fourier Transform (FFT), improving the accuracy of the effective Bader charge calculation for each atomic specie.

E.1 Convergence tests

In the following, we present the calculations performed in order to obtain the converged values of the lattice parameters and the **k**-mesh within the density functional theory using the VASP package. The refinement of the **k**-points and the cutoff energy provides a precise DFT calculation, performed in sufficient times and avoiding inaccuracies in results.

The lattice parameter calculation is given by the minimization of the total energy of the system using the stress tensor simulation, changing the cell volume until all the forces reach the stop criterion determined for the calculation. When the criterion of forces is attained, the equilibrium geometry is obtained. This process is performed again until the final volume of structure is determined. An enough cutoff energy must be used in the total energy calculation to achieve the converged structural parameters with a high accuracy. The electronic wavefunctions are expanded in terms of a discrete set of the planes waves for each **k**-point in the Brillouin zone. However, some divergences in the calculations can arise using a constant number of plane waves and cutoff energy, leading to incorrect components of the stress tensor. [307] These inaccuracies are called *Pulay stress*. [308]

In a solid, the strain is a deformation of the lattice. The external forces acting on the atoms cause a state of stress in the geometry. The stressed atoms increase the pressure of the cell. The Hellmann-Feynman theorem, originally derived by Ehrenfest, [309] gives the force conjugate to the atomic position. The stress tensor dynamics was formulated in terms of the *stress theorem*. [310, 311]

The number of plane waves used in the calculation is related to the computational efforts of DFT calculations, wherein the solution of the integrals in the Brillouin zone includes the **k**-point sampling. In the most of density functional theory codes, the Monkhorst and Pack method is implemented for the choice of the **k**-point sampling. [165, 166] In order to decrease the computational cost, the integrals in the reciprocal space can be solved in the reduced portion of the Brillouin zone, called irreducible Brillouin zone, which can be extended to fill the entire Brillouin zone. However, the integration of the Brillouin zone in some materials can be complex, such as the metallic systems, where the bands intercept the Fermi energy leading to discontinuities in the electronic state occupation. The solution for this particular case is obtained by increasing the **k**-mesh, which leads to an increase in the computational cost of the calculation. The *smearing* methods for the integration of the Brillouin zone contributes to overcome the discontinuity of the integrals, [147] where the step-function is replaced by a similar Fermi-Dirac function at a finite temperature: [312]

$$f\left(\frac{\varepsilon-\mu}{\sigma}\right)=\left[\frac{1}{exp(\frac{\varepsilon-\mu}{\sigma})+1}\right], \tag{E.5}$$

or a Gauss-like function:

$$f\left(\frac{\varepsilon-\mu}{\sigma}\right)=\frac{1}{2}\left[1-erf\left(\frac{\varepsilon-\mu}{\sigma}\right)\right], \tag{E.6}$$

where ε and μ are the energy for each state and the Fermi energy, respectively. The parameter $\sigma = k_B T$ is related to the artificial temperature. An alternative approach of *smearing* is the Methfessel and Paxton method. [313] The tetrahedron method [314–316] and the scheme proposed by Blöchl [167] are widely used as strategies to integrate the Brillouin zone.

Thus, below we present the convergence of the cutoff energy and **k**-points. For the pristine cadmium selenide cell, the converged lattice parameter and gap energy values, namely, 6.19 Å and 0.49 eV, respectively, were obtained by using the PBE exchange and correlation functional and k-density of 25, corresponding to a **k**-mesh of 4x4x4. The total energy also stabilizes in the same k-density value. A visual representation of the lattice parameter, gap energy and total energy are given in the Fig. E.1:

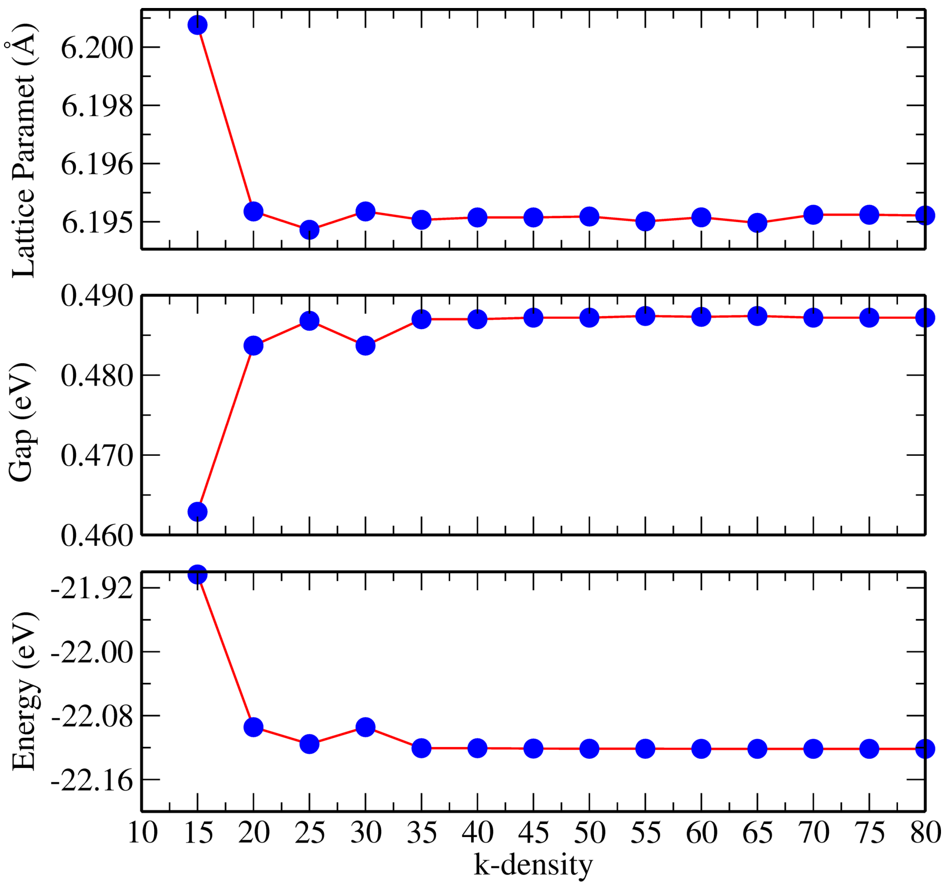

Figure E.1: Calculated values for the lattice parameter, gap energy, and total energy for several k-density values using PBE exchange and correlation functional. The special grid of 25 k-density provides a good accuracy of the obtained results, which corresponds to a **k**-mesh of 4x4x4.

Concerning the calculation of the cadmium (Cd), selenium (Se) and zinc (Zn) structures used for the determination of the chemical potential of the pristine systems in chapter 4, where the Cd and Zn bulk contains two atoms and Se three atoms in hexagonal structures, 30 k-density is enough to obtain a precise description of the lattice parameters.

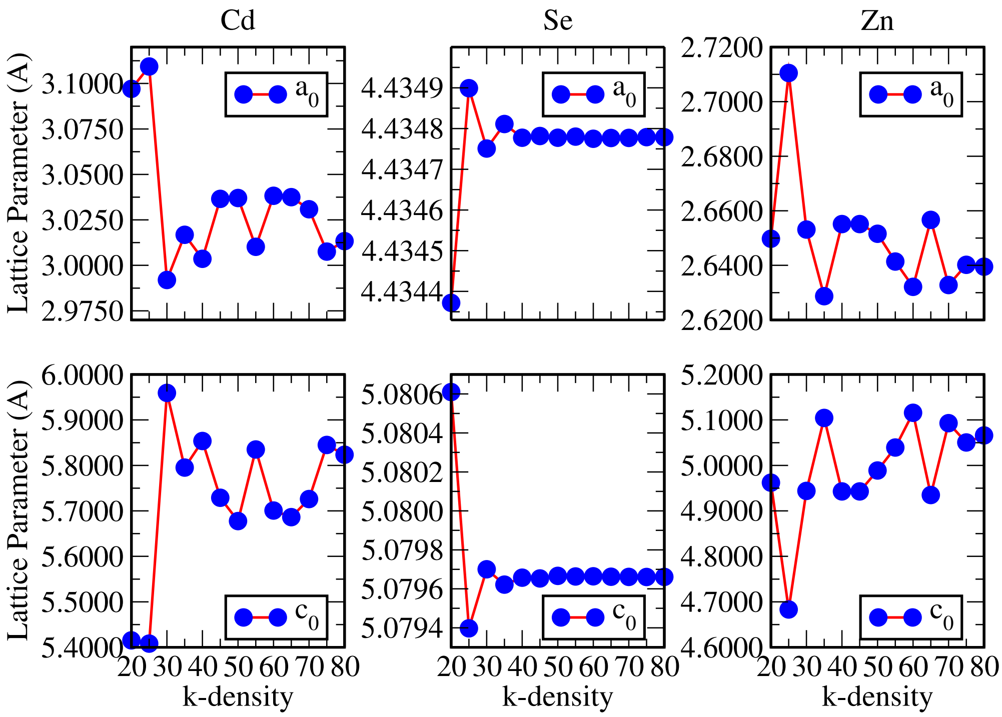

Figure E.2: Lattice parameter of cadmium, selenium, and zinc in hexagonal close packing bulk structures analyzed as function of the k-density sampling. These obtained results were used in the calculation of the chemical potential of the chapter 4. The properties achieve the accuracy for 30 k-density.

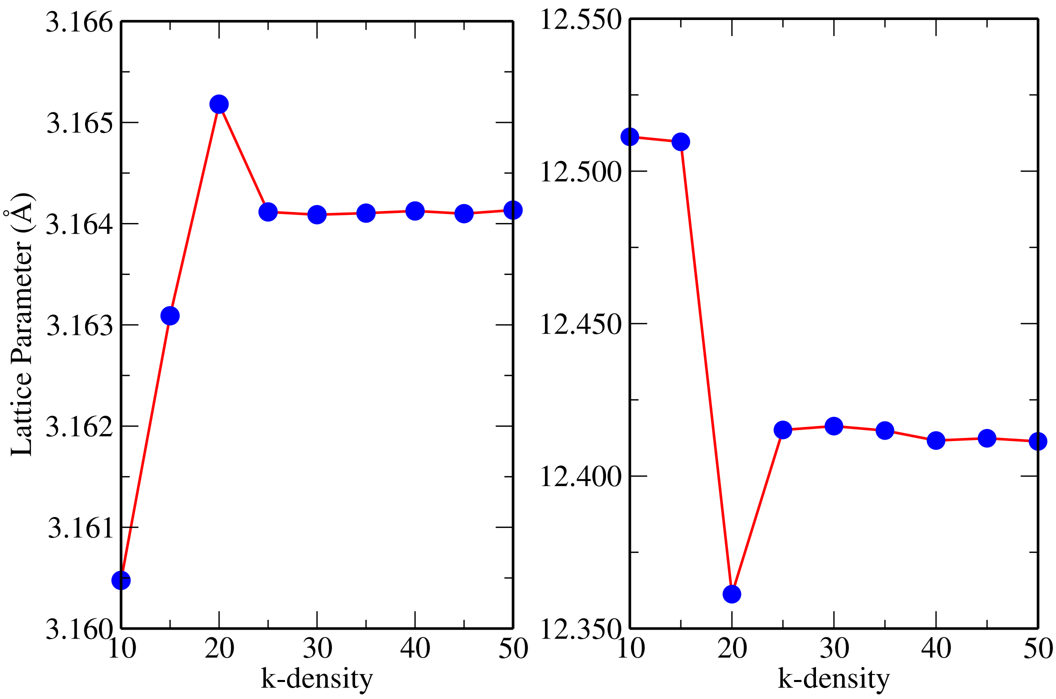

Figure E.3: Molybdenum disulfide (MoS_2) lattice parameters as function of the **k**-points. The convergence tests were performed using bulk structures in Octahedral geometry, where the 25 k-density gives the converged values for the MoS_2 lattice parameters. The calculated lattice parameters and the **k**-mesh were used in the chapter 5.

In the Fig. E.3, we present the convergence tests for the molybdenum disulfide bulk in Octahedral symmetry, studied in chapter 5. Assuming the **k**-mesh of 9x9x2 (25 k-density) for the integration of the Brillouin zone, the obtained lattice parameters are 3.16 Å and 12.37 Å, where the PBE exchange and correlation functional and the van der Waals corrections were used.

Bibliography

[1] R.F.C. Farrow. *Molecular Beam Epitaxy: Applications to Key Materials*. Materials science and process technology series: Electronic materials and process technology. Elsevier Science, 2012.

[2] N. W. Ashcroft and N. M. Mermin. *Solid State Physics*. Holt-Saunders International Editions, 1976.

[3] D J Mowbray and M S Skolnick. New physics and devices based on self-assembled semiconductor quantum dots. *Appl. Phys.*, 38(13):2059, 2005.

[4] K. v. Klitzing, G. Dorda, and M. Pepper. New method for high-accuracy determination of the fine-structure constant based on quantized hall resistance. *Phys. Rev. Lett.*, 45:494–497, Aug 1980.

[5] D. C. Tsui, H. L. Stormer, and A. C. Gossard. Two-dimensional magnetotransport in the extreme quantum limit. *Phys. Rev. Lett.*, 48:1559–1562, May 1982.

[6] R. B. Laughlin. Quantized hall conductivity in two dimensions. *Phys. Rev. B*, 23:5632–5633, May 1981.

[7] R. B. Laughlin. Quantized motion of three two-dimensional electrons in a strong magnetic field. *Phys. Rev. B*, 27:3383–3389, Mar 1983.

[8] R. B. Laughlin. Anomalous quantum hall effect: An incompressible quantum fluid with fractionally charged excitations. *Phys. Rev. Lett.*, 50:1395–1398, May 1983.

[9] P. M. Petroff, A. C. Gossard, R. A. Logan, and W. Wiegmann. Toward quantum well wires: Fabrication and optical properties. *Appl. Phys. Lett.*, 41(7):635–638, 1982.

[10] M. A. Reed, R. T. Bate, K. Bradshaw, W. M. Duncan, W. R. Frensley, J. W. Lee, and H. D. Shih. Spatial quantization in GaAs–AlGaAs multiple quantum dots. *J Vac. Science Tech. B: Microel. Proc. and Phenomena*, 4(1):358–360, 1986.

[11] J. Cibert, P. M. Petroff, G. J. Dolan, S. J. Pearton, A. C. Gossard, and J. H. English. Optically detected carrier confinement to one and zero dimension in GaAs quantum well wires and boxes. *Appl. Phys. Lett.*, 49(19):1275–1277, 1986.

[12] H. Temkin, G. J. Dolan, M. B. Panish, and S. N. G. Chu. Low–temperature photoluminescence from InGaAs/InP quantum wires and boxes. *Appl. Phys. Lett.*, 50(7):413–415, 1987.

[13] K. Kash, A. Scherer, J. M. Worlock, H. G. Craighead, and M. C. Tamargo. Optical spectroscopy of ultrasmall structures etched from quantum wells. *Appl. Phys. Lett.*, 49(16):1043–1045, 1986.

[14] Bernhard Urbaszek, Xavier Marie, Thierry Amand, Olivier Krebs, Paul Voisin, Patrick Maletinsky, Alexander Högele, and Atac Imamoglu. Nuclear spin physics in quantum dots: An optical investigation. *Rev. Mod. Phys.*, 85:79–133, Jan 2013.

[15] Lucjan Jacak, Pawel Hawrylak, and Arkadiusz Wojs. *Quantum Dots*. Springer, 1998.

[16] Marc A. Kastner. Artificial atoms. *Phys. Today*, 46(1):24–31, 1993.

[17] B. Sadigh, P. Erhart, D. Åberg, A. Trave, E. Schwegler, and J. Bude. First-principles calculations of the urbach tail in the optical absorption spectra of silica glass. *Phys. Rev. Lett.*, 106:027401, 2011.

[18] Daniel Loss and David P. DiVincenzo. Quantum computation with quantum dots. *Phys. Rev. A*, 57:120–126, Jan 1998.

[19] C. B. Murray, D. J. Norris, and M. G. Bawendi. Synthesis and characterization of nearly monodisperse CdE (E = sulfur, selenium, tellurium) semiconductor nanocrystallites. *J. Am. Chem. Soc.*, 115(19):8706–8715, 1993.

[20] Supriyo Datta and Biswajit Das. Electronic analog of the electro–optic modulator. *Appl. Phys. Lett.*, 56(7):665–667, 1990.

[21] David D. Awschalom, Lee C. Bassett, Andrew S. Dzurak, Evelyn L. Hu, and Jason R. Petta. Quantum spintronics: Engineering and manipulating atom-like spins in semiconductors. *Science*, 339(6124):1174–1179, 2013.

[22] Yu A Bychkov and E I Rashba. Oscillatory effects and the magnetic susceptibility of carriers in inversion layers. *J. Phys. C: Solid State Phys.*, 17(33):6039, 1984.

[23] G. Dresselhaus. Spin-orbit coupling effects in zinc blende structures. *Phys. Rev.*, 100:580–586, Oct 1955.

[24] Urte Hotje, Christoph Rose, and Michael Binnewies. Lattice constants and molar volume in the system ZnS, ZnSe, CdS, CdSe. *Solid State Sci.*, 5(9):1259–1262, 2003.

[25] E. Deligoz, K. Colakoglu, and Y. Ciftci. Elastic, electronic, and lattice dynamical properties of CdS, CdSe, and CdTe. *Phys. B: Cond. Matt.*, 373(1):124–130, 2006.

[26] F. Benkabou, H. Aourag, and M. Certier. Atomistic study of zinc–blende CdS, CdSe, ZnS, and ZnSe from molecular dynamics. *Mat. Chem. and Phys.*, 66(1):10–16, 2000.

[27] R. Winkler. *Spin-Orbit Coupling Effects in Two-Dimensional Electron and Hole Systems*. Springer-Verlag, Berlin, 2003.

[28] D. H. Chow, H. L. Dunlap, W. Williamson, S. Enquist, B. K. Gilbert, S. Subramaniam, P. M. Lei, and G. H. Bernstein. InAs/AlSb/GaSb resonant interband tunneling diodes and Au-on-InAs/AlSb–superlattice schottky diodes for logic circuits. *IEEE Electron Device Lett.*, 17(2):69–71, Feb 1996.

[29] I. Vurgaftman, J. R. Meyer, and L. R. Ram-Mohan. Band parameters for III–V compound semiconductors and their alloys. *J. Appl. Phys.*, 89(11):5815–5875, 2001.

[30] Smith Andrew M., Gao Xiaohu, and Nie Shuming. Quantum dot nanocrystals for in vivo molecular and cellular imaging. *Photochem. and Photobio.*, 80(3):377–385, 2004.

[31] Fanqing Chen and Daniele Gerion. Fluorescent CdSe/ZnS nanocrystal–peptide conjugates for long-term, nontoxic imaging and nuclear targeting in living cells. *Nano Lett.*, 4(10):1827–1832, 2004.

[32] X. Michalet, F. F. Pinaud, L. A. Bentolila, J. M. Tsay, S. Doose, J. J. Li, G. Sundaresan, A. M. Wu, S. S. Gambhir, and S. Weiss. Quantum dots for live cells, in vivo imaging, and diagnostics. *Science*, 307(5709):538–544, 2005.

[33] Timothy Jamieson, Raheleh Bakhshi, Daniela Petrova, Rachael Pocock, Mo Imani, and Alexander M. Seifalian. Biological applications of quantum dots. *Biomaterials*, 28(31):4717 – 4732, 2007.

[34] J. M. Moison, F. Houzay, F. Barthe, L. Leprince, E. André, and O. Vatel. Self–organized growth of regular nanometer–scale InAs dots on GaAs. *Appl. Phys. Lett.*, 64(2):196–198, 1994.

[35] Banin Uri, Cao YunWei, Katz David, and Millo Oded. Identification of atomic–like electronic states in indium arsenide nanocrystal quantum dots. *Nature*, 400(6744):542–544, aug 1999.

[36] Hongtao Jiang and Jasprit Singh. Strain distribution and electronic spectra of InAs/GaAs self–assembled dots: An eight–band study. *Phys. Rev. B*, 56:4696–4701, Aug 1997.

[37] Alexander V. Kolobov and Junji Tominaga. *Two-Dimensional Transition–Metal Dichalcogenides*. Springer International Publishing, 2016.

[38] Z. M. Wang. *MoS_2: Materials, Physics, and Devices: 21 (Lecture Notes in Nanoscale Science and Technology)*. Springer, 2013.

[39] Ronald E. Bell and Robert E. Herfert. Preparation and characterization of a new crystalline form of molybdenum disulfide. *J. Am. Chem. Soc.*, 79(13):3351–3354, 1957.

[40] P.A. Lee. *Optical and Electrical Properties*. Physics and Chemistry of Materials. Springer Netherlands, 2012.

[41] Berit Hinnemann, Poul Georg Moses, Jacob Bonde, Kristina P. Jørgensen, Jane H. Nielsen, Sebastian Horch, Ib Chorkendorff, and Jens K. Nørskov. Biomimetic hydrogen evolution: MoS_2 nanoparticles as catalyst for hydrogen evolution. *J. Am. Chem. Soc.*, 127(15):5308–5309, 2005.

[42] Thomas F. Jaramillo, Kristina P. Jørgensen, Jacob Bonde, Jane H. Nielsen, Sebastian Horch, and Ib Chorkendorff. Identification of active edge sites for electrochemical H_2 evolution from MoS_2 nanocatalysts. *Science*, 317(5834):100–102, 2007.

[43] Andrei Ionescu, Alain Allouche, Jean-Pierre Aycard, Michel Rajzmann, and Raphael Le Gall. Study of y–alumina-supported hydrotreating catalyst: I. adsorption of bare MoS_2 sheets on y–alumina surfaces. *J. Phys. Chem.*, 107(33):8490–8497, 2003.

[44] B. Radisavljevic, A. Radenovic, J. Brivio, V. Giacometti, and A. Kis. Single–layer MoS_2 transistors. *Nat. Nanotechnol.*, 6(3):147–150, mar 2011.

[45] M. Dragoman and D. Dragoman. *2D Nanoelectronics: Physics and Devices of Atomically Thin Materials*. NanoScience and Technology. Springer International Publishing, 2016.

[46] Mikael Syväjärvi (Editor) Ashutosh Tiwari (Editor), editor. *Advanced 2D Materials (Advanced Material Series)*. Wiley–Scrivener, 2016.

[47] Mircea Dragoman and Daniela Dragoman. *2D Nanoelectronics: Physics and Devices of Atomically Thin Materials*. Springer, 2017.

[48] Gary Kline, Kam Keung Kam, Ruth Ziegler, and B.A. Parkinson. Further studies of the photoelectrochemical properties of the group VI transition metal dichalcogenides. *Sol. Energy*, 6(3):337 – 350, 1982.

[49] A. Aruchamy. *Photoelectrochemistry and Photovoltaics of Layered Semiconductors*. Springer My Copy UK, 1992.

[50] J. H. Robertson. *Physics and chemistry of materials with layered structures. Vol. 4. Optical and electrical properties* by G. B. Jensen edited by P. A. Lee. *Acta Crystallogr., Sect. B: Struct. Sci.*, 35(3):794, Mar 1979.

[51] Kin Fai Mak, Changgu Lee, James Hone, Jie Shan, and Tony F. Heinz. Atomically thin MoS_2: A new direct-gap semiconductor. *Phys. Rev. Lett.*, 105:136805, Sep 2010.

[52] Intek Song, Chibeom Park, and Hee Cheul Choi. Synthesis and properties of molybdenum disulphide: from bulk to atomic layers. *RSC Adv.*, 5:7495–7514, 2015.

[53] Hee Sung Lee, Sung-Wook Min, Youn-Gyung Chang, Min Kyu Park, Taewook Nam, Hyungjun Kim, Jae Hoon Kim, Sunmin Ryu, and Seongil Im. MoS_2 nanosheet phototransistors with thickness-modulated optical energy gap. *Nano Lett.*, 12(7):3695–3700, 2012.

[54] Kapildeb Dolui, Ivan Rungger, and Stefano Sanvito. Origin of the n-type and p-type conductivity of MoS_2 monolayers on a SiO_2 substrate. *Phys. Rev. B*, 87:165402, Apr 2013.

[55] Yi-Hsien Lee, Xin-Quan Zhang, Wenjing Zhang, Mu-Tung Chang, Cheng-Te Lin, Kai-Di Chang, Ya-Chu Yu, Jacob Tse-Wei Wang, Chia-Seng Chang, Lain-Jong Li, and Tsung-Wu Lin. Synthesis of large-area MoS_2 atomic layers with chemical vapor deposition. *Adv. Mater.*, 24(17):2320–2325, 2012.

[56] Yijin Zhang, Jianting Ye, Yusuke Matsuhashi, and Yoshihiro Iwasa. Ambipolar MoS_2 thin flake transistors. *Nano Lett.*, 12(3):1136–1140, 2012.

[57] Carlos M. O. Bastos, Fernando P. Sabino, Paulo E. Faria Junior, Tiago Campos, Juarez L. F. Da Silva, and Guilherme M. Sipahi. Stability and accuracy control of $\mathbf{k}\cdot\mathbf{p}$ parameters. *Semicond. Sci. Technol.*, 31(10):105002, Sept. 2016.

[58] Charles Kittel. *Introduction to Solid State Physics, 8th Ed.* John Wiley & Sons, Inc., New York, 2004.

[59] G. Bastard. *Wave mechanics applied to semiconductor heterostructures*. Monographies de physique. Les Éditions de Physique, 1988.

[60] Rolf Enderlein. *Fundamentals of Semiconductor Physics and Devices*. World Scientific Pub Co Inc, 1997.

[61] Evan O. Kane. Band structure of indium antimonide. *J. Phys. Chem. Solids*, 1(4):249–261, Jan. 1957.

[62] Manuel Cardona and Fred H. Pollak. Energy-band structure of germanium and silicon: The k·p method. *Phys. Rev.*, 142:530–543, Feb 1966.

[63] J. M. Luttinger and W. Kohn. Motion of electrons and holes in perturbed periodic fields. *Phys. Rev.*, 97(4):869–883, Feb. 1955.

[64] W. Kohn and J. M. Luttinger. Quantum theory of cyclotron resonance in semiconductors. *Phys. Rev.*, 96:529–530, Oct 1954.

[65] J. M. Luttinger. Quantum theory of cyclotron resonance in semiconductors: General theory. *Phys. Rev.*, 102:1030–1041, May 1956.

[66] Fred H. Pollak and Manuel Cardona. Energy band structure of germanium and gallium arsenide: The k.p method. *J. Phys. Chem. Solids*, 27(2):423 – 425, 1966.

[67] Manuel Cardona. Band parameters of semiconductors with zincblende, wurtzite, and germanium structure. *J. Chem. Phys.*, 24(12):1543–1555, 1963.

[68] J. M. Luttinger. The effect of a magnetic field on electrons in a periodic potential. *Phys. Rev.*, 84:814–817, Nov 1951.

[69] Daniel Ferreira Cesar. *Efeitos Eletrônicos, Elásticos e Estruturais em Sistemas Semicondutores Nanoscópicos*. PhD thesis, Federal University of São Carlos, 2012.

[70] Fabrizio Myaki Alves. *Propriedades dos Spins de Elétrons e de Buracos em Pontos Quânticos Semicondutores*. PhD thesis, Federal University of São Carlos, 2008.

[71] P. Y. Yu and M. Cardona. *Fundamentals of Semiconductors, 2nd ed.* Spinger-Verlag, Berlin, 1999.

[72] G. Bastard. Superlattice band structure in the envelope–function approximation. *Phys. Rev. B*, 24:5693–5697, Nov 1981.

[73] G. Bastard. Theoretical investigations of superlattice band structure in the envelope–function approximation. *Phys. Rev. B*, 25:7584–7597, Jun 1982.

[74] M. Altarelli. Electronic structure and semiconductor–semimetal transition in InAs–GaSb superlattices. *Phys. Rev. B*, 28:842–845, Jul 1983.

[75] Morten Willatzen Lok C. Lew Yan Voon. *The **kp** Method*. Springer–Verlag GmbH, 2009.

[76] F. Rossi. *Theory of Semiconductor Quantum Devices: Microscopic Modeling and Simulation Strategies*. NanoScience and Technology. Springer Berlin Heidelberg, 2011.

[77] P.-O. Löwdin. A note on the quantum-mechanical perturbation theory. *J. Chem. Phys.*, 19:1396, 1951.

[78] J.H. Davies. *The Physics of Low-dimensional Semiconductors: An Introduction*. Cambridge University Press, 1998.

[79] R.K. Willardson and A.C. Beer. *Semiconductors and Semimetals*. Number V. 3 in Semiconductors and Semimetals. Elsevier Science, 1967.

[80] B. M. Askerov. *Electron Transport Phenomena in Semiconductors*. World Scientific, 1994.

[81] D.J. Griffiths. *Introduction to Quantum Mechanics*. Pearson international edition. Pearson Prentice Hall, 2005.

[82] M. Born and R. Oppenheimer. Zur quantentheorie der molekeln. *Ann. Phys. (Leipzig)*, 389(20):457–484, 1927.

[83] Nancy R. Forde, Tanya L. Myers, and Laurie J. Butler. Chemical reaction dynamics when the Born–Oppenheimer approximation fails Understanding which changes in the electronic wavefunction might be restricted. *Faraday Discuss.*, 108:221–242, 1997.

[84] Ira N. Levine. *Quantum Chemistry (5th Edition)*. Prentice Hall, 1999.

[85] D. R. Hartree. The wave mechanics of an atom with a non-Coulomb central field. Part I. Theory and methods. *Math. Proc. Cambridge Philos. Soc.*, 24(1):89–110, 1928.

[86] V. Fock. Selfconsistent field mit austausch für natrium. *Zeitschrift für Physik*, 62(11):795–805, Nov 1930.

[87] A. Szabo and N.S. Ostlund. *Modern Quantum Chemistry: Introduction to Advanced Electronic Structure Theory*. Dover Books on Chemistry. Dover Publications, 1989.

[88] P. Hohenberg and W. Kohn. Inhomogeneous electron gas. *Phys. Rev.*, 136(3B):B864–B871, Nov. 1964.

[89] W. Kohn and L. J. Sham. Self-consistent equations including exchange and correlation effects. *Phys. Rev.*, 140(4A):A1133–A1138, Nov. 1965.

[90] L. H. Thomas. The calculation of atomic fields. *Math. Proc. Cambridge Philos. Soc.*, 23(5):542–548, 1927.

[91] E. Fermi. Un Metodo Statistico per la determinazione di Alcune priorieta dell' atome. *Rend. Accad. Naz. Lincei*, 6:602, 1927.

[92] R.M. Martin. *Electronic Structure: Basic Theory and Practical Methods*. Cambridge University Press, 2004.

[93] John A. Pople, Peter M.W. Gill, and Benny G. Johnson. Kohn–sham density–functional theory within a finite basis set. *Chem. Phys. Lett.*, 199(6):557–560, 1992.

[94] Ann E. Mattsson. In pursuit of the "divine" functional. *Science*, 298(5594):759–760, 2002.

[95] John P. Perdew, Adrienn Ruzsinszky, Jianmin Tao, Viktor N. Staroverov, Gustavo E. Scuseria, and Gábor I. Csonka. Prescription for the design and selection of density functional approximations: More constraint satisfaction with fewer fits. *J. Chem. Phys.*, 123(6):062201, 2005.

[96] Anderson Silva Chaves. *Estudo Teórico das Propriedades Estruturais, Eletrônicas e Reatividade de Clusters de Metais de Transição*. PhD thesis, University of São Paulo, 2015.

[97] E. Kaxiras. *Atomic and Electronic Structure of Solids*. Cambridge University Press, 2003.

[98] E.K.U. Gross and R.M. Dreizler. *Density Functional Theory*. Nato Science Series B:. Springer US, 2013.

[99] D. M. Ceperley and B. J. Alder. Ground state of the electron gas by a stochastic method. *Phys. Rev. Lett.*, 45:566–569, Aug 1980.

[100] S. H. Vosko, L. Wilk, and M. Nusair. Accurate spin–dependent electron liquid correlation energies for local spin density calculations: a critical analysis. *Can. J. Phys.*, 58(8):1200–1211, 1980.

[101] John P. Perdew and Yue Wang. Accurate and simple analytic representation of the electron–gas correlation energy. *Phys. Rev. B*, 45:13244–13249, Jun 1992.

[102] John P. Perdew, Kieron Burke, and Matthias Ernzerhof. Generalized gradient approximation made simple. *Phys. Rev. Lett.*, 77:3865–3868, Oct 1996.

[103] Rafael Luiz Heleno Freire. *Estudo de Primeiros Princípios da Adsorço de Água e de Etanol sobre Ligas de Superfície de Metais de Transição sob Efeitos de Deformação Expansiva e Compressiva*. PhD thesis, University of São Paulo, 2016.

[104] John P. Perdew and Wang Yue. Accurate and simple density functional for the electronic exchange energy: Generalized gradient approximation. *Phys. Rev. B*, 33:8800–8802, Jun 1986.

[105] Y. Zhang and W. Yang. Comment on “generalized gradient approximation made simple”. *Phys. Rev. Lett.*, 80:890–890, Jan 1998.

[106] B. Hammer, L. B. Hansen, and J. K. Nørskov. Improved adsorption energetics within density–functional theory using revised Perdew–Burke–Ernzerhof functionals. *Phys. Rev. B*, 59:7413–7421, Mar 1999.

[107] John P. Perdew, Adrienn Ruzsinszky, Gábor I. Csonka, Oleg A. Vydrov, Gustavo E. Scuseria, Lucian A. Constantin, Xiaolan Zhou, and Kieron Burke. Restoring the density-gradient expansion for exchange in solids and surfaces. *Phys. Rev. Lett.*, 100(13):136406, Apr. 2008.

[108] Ann E. Mattsson, Rickard Armiento, Joachim Paier, Georg Kresse, John M. Wills, and Thomas R. Mattsson. The AM05 density functional applied to solids. *J. Chem. Phys.*, 128(8):084714, 2008.

[109] Ann E. Mattsson and Rickard Armiento. Implementing and testing the AM05 spin density functional. *Phys. Rev. B*, 79:155101, Apr 2009.

[110] Axel D. Becke. A new mixing of Hartree–Fock and local density–functional theories. *J. Chem. Phys.*, 98(2):1372–1377, 1993.

[111] Matthias Ernzerhof and Gustavo E. Scuseria. Assessment of the Perdew–Burke–Ernzerhof exchange-correlation functional. *J. Chem. Phys.*, 110(11):5029–5036, 1999.

[112] Axel D. Becke. Density–functional thermochemistry. III. the role of exact exchange. *J. Chem. Phys.*, 98(7):5648–5652, 1993.

[113] Miguel A. L. Marques Carlos Fiolhais, Fernando Nogueira, editor. *A Primer in Density Functional Theory (Lecture Notes in Physics) (v. 620).* Springer, 2003.

[114] Joachim Paier, Martijn Marsman, and Georg Kresse. Why does the B3LYP hybrid functional fail for metals? *J. Chem. Phys.*, 127(2):024103, 2007.

[115] A. D. Becke. Density–functional exchange-energy approximation with correct asymptotic behavior. *Phys. Rev. A*, 38:3098–3100, Sep 1988.

[116] Matthias Ernzerhof, John P. Perdew, and Kieron Burke. Coupling–constant dependence of atomization energies. *Inter. J. of Quantum Chemistry*, 64(3):285–295, 1 1997.

[117] John P. Perdew, Matthias Ernzerhof, and Kieron Burke. Rationale for mixing exact exchange with density functional approximations. *J. Chem. Phys.*, 105(22):9982–9985, 1996.

[118] Jochen Heyd, Gustavo E. Scuseria, and Matthias Ernzerhof. Hybrid functionals based on a screened Coulomb potential. *J. Chem. Phys.*, 118(18):8207–8215, 2003.

[119] Jochen Heyd and Gustavo E. Scuseria. Efficient hybrid density functional calculations in solids: Assessment of the Heyd–Scuseria–Ernzerhof screened Coulomb hybrid functional. *J. Chem. Phys.*, 121(3):1187–1192, July 2004.

[120] Jochen Heyd, Gustavo E. Scuseria, and Matthias Ernzerhof. Erratum: "Hybrid functionals based on a screened Coulomb potential" [J. Chem. Phys. 118, 8207 (2003)]. *J. Chem. Phys.*, 124(21):219906, 2006.

[121] J. Hubbard. Electron correlations in narrow energy bands. *Proc Royal Soc. London A: Math., Phys. and Eng. Sciences*, 276(1365):238–257, 1963.

[122] J. Hubbard. Electron correlations in narrow energy bands. II. The degenerate band case. *Proc Royal Soc. London A: Math., Phys. and Eng. Sciences*, 277(1369):237–259, 1964.

[123] J. Hubbard. Electron correlations in narrow energy bands. III. An improved solution. *Proc. Royal Soc. London A: Math., Phys. and Eng. Sciences*, 281(1386):401–419, 1964.

[124] J. Hubbard. Electron correlations in narrow energy bands. IV. The atomic representation. *Proc Royal Soc. London A: Math., Phys. and Eng. Sciences*, 285(1403):542–560, 1965.

[125] J. Hubbard. Electron correlations in narrow energy bands. V. A perturbation expansion about the atomic limit. *Proc Royal Soc. London A: Math., Phys. and Eng. Sciences*, 296(1444):82–99, 1967.

[126] J. Hubbard. Electron correlations in narrow energy bands. VI. The connexion with many-body perturbation theory. *Proc Royal Soc. London A: Math., Phys. and Eng. Sciences*, 296(1444):100–112, 1967.

[127] Elliott H. Lieb and F. Y. Wu. Absence of Mott transition in an exact solution of the short–range, one-band model in one dimension. *Phys. Rev. Lett.*, 20:1445–1448, Jun 1968.

[128] F.H.L. Essler, H. Frahm, F. Göhmann, A. Klümper, and V.E. Korepin. *The One-Dimensional Hubbard Model*. Cambridge University Press, 2005.

[129] Robert Peters and Thomas Pruschke. Half-filled hubbard model on a bethe lattice with next-nearest-neighbor hopping. *Phys. Rev. B*, 79:045108, Jan 2009.

[130] S. Nishimoto, T. Shirakawa, and Y. Ohta. Charge and spin excitation spectra in the one-dimensional Hubbard model with next-nearest–neighbor hopping. *Phys. Rev. B*, 77:115102, Mar 2008.

[131] O. Gunnarsson and K. Schönhammer. Density-functional treatment of an exactly solvable semiconductor model. *Phys. Rev. Lett.*, 56:1968–1971, May 1986.

[132] K Schonhammer and O Gunnarsson. Discontinuity of the exchange-correlation potential in density functional theory. *J. Phys. Chem. C*, 20(24):3675, 1987.

[133] K. Schönhammer, O. Gunnarsson, and R. M. Noack. Density-functional theory on a lattice: Comparison with exact numerical results for a model with strongly correlated electrons. *Phys. Rev. B*, 52:2504–2510, Jul 1995.

[134] Erich Runge and Gertrud Zwicknagl. Electronic structure calculations and strong correlations: A model study. *Ann. Phys. (Leipzig)*, 508(4):333–354, 1996.

[135] I. V. Solovyev, P. H. Dederichs, and V. I. Anisimov. Corrected atomic limit in the local-density approximation and the electronic structure of d impurities in Rb. *Phys. Rev. B*, 50:16861–16871, Dec 1994.

[136] V. I. Anisimov, I. V. Solovyev, M. A. Korotin, M. T. Czyżyk, and G. A. Sawatzky. Density-functional theory and NiO photoemission spectra. *Phys. Rev. B*, 48:16929–16934, Dec 1993.

[137] Vladimir I. Anisimov, Jan Zaanen, and Ole K. Andersen. Band theory and Mott insulators: Hubbard U instead of stoner I. *Phys. Rev. B*, 44:943–954, Jul 1991.

[138] V. I. Anisimov and O. Gunnarsson. Density-functional calculation of effective coulomb interactions in metals. *Phys. Rev. B*, 43:7570–7574, Apr 1991.

[139] P. W. Anderson. Localized magnetic states in metals. *Phys. Rev.*, 124:41–53, Oct 1961.

[140] S. L. Dudarev, G. A. Botton, S. Y. Savrasov, C. J. Humphreys, and A. P. Sutton. Electron-energy-loss spectra and the structural stability of nickel oxide: An LSDA+U study. *Phys. Rev. B*, 57:1505–1509, Jan 1998.

[141] Jürgen Hafner. Ab initio simulations of materials using vasp: Density–functional theory and beyond. *J. Comput. Chem.*, 29(13):2044–2078, 2008.

[142] Fritz London. Über einige eigenschaften und anwendungen der molekularkräfte. *Z. Phys. Chem*, 11:222–251, 1930.

[143] Fatah Chiter, Van Bac Nguyen, Nathalie Tarrat, Magali Benoit, Hao Tang, and Corinne Lacaze-Dufaure. Effect of van der Waals corrections on DFT–computed metallic surface properties. *Mat. Res. Exp*, 3(4):046501, 2016.

[144] Javier Carrasco, Jiří Klimeš, and Angelos Michaelides. The role of van der Waals forces in water adsorption on metals. *J. Chem. Phys.*, 138(2):024708, 2013.

[145] Polina Tereshchuk and Juarez L. F. Da Silva. Ethanol and water adsorption on close-packed 3*d*, 4*d*, and 5*d* transition-metal surfaces: A density functional theory investigation with van der Waals correction. *J. Phys. Chem. C*, 116(46):24695–24705, Nov. 2012.

[146] Deyu Lu, Yan Li, Dario Rocca, and Giulia Galli. Ab initio calculation of van der waals bonded molecular crystals. *Phys. Rev. Lett.*, 102:206411, May 2009.

[147] D. Sholl and J.A. Steckel. *Density Functional Theory: A Practical Introduction*. Wiley, 2009.

[148] Erin R. Johnson, Iain D. Mackie, and Gino A. DiLabio. Dispersion interactions in density-functional theory. *J. Phys. Org. Chem.*, 22(12):1127–1135, 2009.

[149] Yan Li, Deyu Lu, Huy-Viet Nguyen, and Giulia Galli. van der Waals interactions in molecular assemblies from first–principles calculations. *J. Phys. Chem. A*, 114(4):1944–1952, 2010.

[150] Kyuho Lee, Éamonn D. Murray, Lingzhu Kong, Bengt I. Lundqvist, and David C. Langreth. Higher-accuracy van der Waals density functional. *Phys. Rev. B*, 82:081101, Aug 2010.

[151] M. Dion, H. Rydberg, E. Schröder, D. C. Langreth, and B. I. Lundqvist. Van der Waals density functional for general geometries. *Phys. Rev. Lett.*, 92:246401, Jun 2004.

[152] Alexandre Tkatchenko, Robert A. DiStasio, Roberto Car, and Matthias Scheffler. Accurate and efficient method for many-body van der Waals interactions. *Phys. Rev. Lett.*, 108(23):236402, June 2012.

[153] Alexandre Tkatchenko and Matthias Scheffler. Accurate molecular van der Waals interactions from ground-state electron density and free-atom reference data. *Phys. Rev. Lett.*, 102(7):073005, Feb. 2009.

[154] Stefan Grimme, Jens Antony, Stephan Ehrlich, and Helge Krieg. A consistent and accurate *ab initio* parametrization of density functional dispersion correction (DFT-D) for the 94 elements H-Pu. *J. Chem. Phys.*, 132(15):154104, 2010.

[155] Stefan Grimme. Semiempirical GGA-type density functional constructed with a long-range dispersion correction. *J. Comput. Chem.*, 27(15):1787–1799, 2006.

[156] Stefan Grimme, Stephan Ehrlich, and Lars Goerigk. Effect of the damping function in dispersion corrected density functional theory. *J. Comput. Chem.*, 32(7):1456–1465, Mar. 2011.

[157] Jörg Neugebauer and Matthias Scheffler. Adsorbate-substrate and adsorbate-adsorbate interactions of Na and K adlayers on Al(111). *Phys. Rev. B*, 46(24):16067–16080, Dec. 1992.

[158] G. Makov and M. C. Payne. Periodic boundary conditions in ab initio calculations. *Phys. Rev. B*, 51:4014–4022, Feb 1995.

[159] T. Ozaki. Variationally optimized atomic orbitals for large-scale electronic structures. *Phys. Rev. B*, 67:155108, Apr 2003.

[160] M. C. Payne, M. P. Teter, D. C. Allan, T. A. Arias, and J. D. Joannopoulos. Iterative minimization techniques for ab initio total-energy calculations molecular dynamics and conjudate gradients. *Rev. Mod. Phys.*, 64:1045, 1992.

[161] D.J. Singh and L. Nordstrom. *Planewaves, Pseudopotentials, and the LAPW Method*. Springer ebook collection / Chemistry and Materials Science 2005-2008. Springer US, 2005.

[162] Giovani Manzeppi Faccin. *Estudo ab initio de Propriedades Estruturais e Magnéticas de Nanopartículas de Metais de Transição*. PhD thesis, Unicamp, 2012.

[163] A. Baldereschi. Mean-value point in the Brillouin zone. *Phys. Rev. B*, 7:5212–5215, Jun 1973.

[164] D. J. Chadi and Marvin L. Cohen. Special points in the Brillouin zone. *Phys. Rev. B*, 8:5747–5753, Dec 1973.

[165] Hendrik J. Monkhorst and James D. Pack. Special points for Brillouin-zone integrations. *Phys. Rev. B*, 13:5188–5192, Jun 1976.

[166] James D. Pack and Hendrik J. Monkhorst. "special points for Brillouin-zone integrations"–a reply. *Phys. Rev. B*, 16:1748–1749, Aug 1977.

[167] Peter E. Blöchl, O. Jepsen, and O. K. Andersen. Improved tetrahedron method for Brillouin–zone integrations. *Phys. Rev. B*, 49:16223–16233, Jun 1994.

[168] O. Krogh Andersen. Linear methods in band theory. *Phys. Rev. B*, 12:3060–3083, Oct 1975.

[169] O. K. Andersen and O. Jepsen. Explicit, first-principles tight-binding theory. *Phys. Rev. Lett.*, 53:2571–2574, Dec 1984.

[170] Conyers Herring. A new method for calculating wave functions in crystals. *Phys. Rev.*, 57:1169–1177, Jun 1940.

[171] D. Vanderbilt. Soft self–consistent pseudopotentials in a generalized eigenvalue formalism. *Phys. Rev. B*, 41:7892–7895, Apr 1990.

[172] Kari Laasonen, Roberto Car, Changyol Lee, and David Vanderbilt. Implementation of ultrasoft pseudopotentials in ab initio molecular dynamics. *Phys. Rev. B*, 43:6796–6799, Mar 1991.

[173] K. Laasonen, A. Pasquarello, R. Car, C. Lee, and D. Vanderbilt. Car–Parrinello molecular dynamics with Vanderbilt ultrasoft pseudopotentials. *Phys. Rev. B*, 47:10142–10153, Apr 1993.

[174] N. Troullier and José Luís Martins. Efficient pseudopotentials for plane-wave calculations. *Phys. Rev. B*, 43:1993–2006, Jan 1991.

[175] G. B. Bachelet, D. R. Hamann, and M. Schlüter. Pseudopotentials that work: From H to Pu. *Phys. Rev. B*, 26:4199–4228, Oct 1982.

[176] G. B. Bachelet, D. R. Hamann, and M. Schlüter. Erratum: Pseudopotentials that work: From H to Pu. *Phys. Rev. B*, 29:2309–2309, Feb 1984.

[177] G. Kresse and D. Joubert. From ultrasoft pseudopotentials to the projector augmented-wave method. *Phys. Rev. B*, 59(3):1758–1775, Jan. 1999.

[178] N. A. W. Holzwarth, G. E. Matthews, R. B. Dunning, A. R. Tackett, and Y. Zeng. Comparison of the projector augmented-wave, pseudopotential, and linearized augmented-plane-wave formalisms for density-functional calculations of solids. *Phys. Rev. B*, 55:2005–2017, Jan 1997.

[179] P. E. Blöchl. Projector augmented–wave method. *Phys. Rev. B*, 50:17953–17979, Dec 1994.

[180] J. C. Slater. Wave functions in a periodic potential. *Phys. Rev.*, 51:846–851, May 1937.

[181] N. A. Hastas, C. A. Dimitriadis, L. Dozsa, E. Gombia, and R. Mosca. Characterization of traps related to InAs quantum-dot growth-induced defects in GaAs by low-frequency noise measurements in reverse-biased schottky diodes. *J. Appl. Phys.*, 93(9):5833–5835, 2003.

[182] Hu Fengrui, Cao Zengle, Zhang Chunfeng, Wang Xiaoyong, and Xiao Min. Defect–induced photoluminescence blinking of single epitaxial InGaAs quantum dots. *Sci. Rep.*, 5:8898, mar 2015.

[183] Yingjie Zhang, Danylo Zherebetskyy, Noah D. Bronstein, Sara Barja, Leonid Lichtenstein, David Schuppisser, Lin-Wang Wang, A. Paul Alivisatos, and Miquel Salmeron. Charge percolation pathways guided by defects in quantum dot solids. *Nano Lett.*, 15(5):3249–3253, 2015.

[184] Kobak J., Smoleński T., Goryca M., Papaj M., Gietka K., Bogucki A., Koperski M., Rousset J.-G., Suffczyński J., Janik E., Nawrocki M., Golnik A., Kossacki P., and Pacuski W. Designing quantum dots for solotronics. *Nat. Commun.*, 5:3191, jan 2014.

[185] P. Möck, T. Topuria, N. D. Browning, L. Titova, M. Dobrowolska, S. Lee, and J. K. Furdyna. Self-ordered CdSe quantum dots in ZnSe and (Zn, Mn)Se matrices assessed by transmission electron microscopy and photoluminescence spectroscopy. *J. Eletron. Mater.*, 30(6):748–755, 2001.

[186] T. Smoleński, W. Pacuski, M. Goryca, M. Nawrocki, A. Golnik, and P. Kossacki. Optical spin orientation of an individual Mn^{+2} ion in a CdSe/ZnSe quantum dot. *Phys. Rev. B*, 91:045306, Jan 2015.

[187] Rémi Beaulac, Yong Feng, Joseph W. May, Ekaterina Badaeva, Daniel R. Gamelin, and Xiaosong Li. Orbital pathways for Mn^{+2}-carrier $sp - d$ exchange in diluted magnetic semiconductor quantum dots. *Phys. Rev. B*, 84:195324, Nov 2011.

[188] L. Villegas-Lelovsky, Fanyao Qu, L. O. Massa, V. Lopez-Richard, and G. E. Marques. Hole-mediated ferromagnetism in coupled semimagnetic quantum dots. *Phys. Rev. B*, 84:075319, Aug 2011.

[189] T. Jungwirth, Jairo Sinova, J. Mašek, J. Kučera, and A. H. MacDonald. Theory of ferromagnetic (III,Mn)V semiconductors. *Rev. Mod. Phys.*, 78:809–864, Aug 2006.

[190] Ranber Singh and Gabriel Bester. Effects of charged defects on the electronic and optical properties of self–assembled quantum dots. *Phys. Rev. B*, 85:205405, May 2012.

[191] L. Cabral, Fernando P. Sabino, Vivaldo Lopes-Oliveira, Juarez L. F. Da Silva, Matheus P. Lima, Gilmar E. Marques, and Victor Lopez-Richard. Interplay between structure asymmetry, defect–induced localization, and spin–orbit interaction in Mn–doped quantum dots. *Phys. Rev. B*, 95:205409, May 2017.

[192] W-C Tan and J C Inkson. Electron states in a two–dimensional ring – an exactly soluble model. *Semicond. Sci. Technol.*, 11(11):1635, 1996.

[193] Vivaldo Lopes-Oliveira, Yuriy I. Mazur, Leonardo Dias de Souza, Lucas A. Bernardes Marçal, Jiang Wu, Marcio Daldin Teodoro, Angelo Malachias, Vitaliy G. Dorogan, Mourad Benamara, Georgiy G. Tarasov, Euclydes Marega, Gilmar E. Marques, Zhiming M. Wang, Milan Orlita, Gregory J. Salamo, and Victor Lopez-Richard. Structural and magnetic confinement of holes in the spin-polarized emission of coupled quantum ring–quantum dot chains. *Phys. Rev. B*, 90:125315, Sep 2014.

[194] Nan Zhao, L. Zhong, Jia-Lin Zhu, and C. P. Sun. Spin entanglement induced by spin-orbit interactions in coupled quantum dots. *Phys. Rev. B*, 74:075307, 2006.

[195] Partoens Bart. Spin-orbit interactions: Hide and seek. *Nat. Phys.*, 10(5):333–334, may 2014.

[196] V. Fock. Bemerkung zur quantelung des harmonischen oszillators im magnetfeld. *Zeitschrift für Physik*, 47(5):446–448, 1928.

[197] C. G. Darwin. The diamagnetism of the free electron. *Math. Proc. Cambridge Philos. Soc.*, 27(1):86–90, 1931.

[198] E. Lipparini. *Modern Many-particle Physics: Atomic Gases, Quantum Dots and Quantum Fluids*. World Scientific, 2003.

[199] G.E. Marques and L.J. Sham. Theory of space–charge layers in narrow–gap semiconductors. *Surf. Sci.*, 113(1):131–136, 1982.

[200] Tristan Richard, Pierre Lefebvre, Henry Mathieu, and Jacques Allègre. Effects of finite spin-orbit splitting on optical properties of spherical semiconductor quantum dots. *Phys. Rev. B*, 53:7287–7298, Mar 1996.

[201] P. Lawaetz. Valence-band parameters in cubic semiconductors. *Phys. Rev. B*, 4:3460–3467, Nov 1971.

[202] M. Willatzen, M. Cardona, and N. E. Christensen. Spin–orbit coupling parameters and electron g factor of II–VI zinc-blende materials. *Phys. Rev. B*, 51:17992–17994, Jun 1995.

[203] Chao-Yuan Jin and Osamu Wada. Photonic switching devices based on semiconductor nano–structures. *J. Phys. D: Appl. Phys.*, 47(13):133001, 2014.

[204] O. Wada. Recent progress in semiconductor-based photonic signal–processing devices. *IEE J. Sel. Top. in Quantum Electron.*, 17(2):309–319, March 2011.

[205] Alex A. High, Ekaterina E. Novitskaya, Leonid V. Butov, Micah Hanson, and Arthur C. Gossard. Control of exciton fluxes in an excitonic integrated circuit. *Science*, 321(5886):229–231, 2008.

[206] E. A. Stinaff, M. Scheibner, A. S. Bracker, I. V. Ponomarev, V. L. Korenev, M. E. Ware, M. F. Doty, T. L. Reinecke, and D. Gammon. Optical signatures of coupled quantum dots. *Science*, 311(5761):636–639, 2006.

[207] Hubert J. Krenner, Craig E. Pryor, Jun He, and Pierre M. Petroff. A semiconductor exciton memory cell based on a single quantum nanostructure. *Nano Lett.*, 8(6):1750–1755, 2008.

[208] J. M. Llorens, L. Wewior, E. R. Cardozo de Oliveira, J. M. Ulloa, A. D. Utrilla, A. Guzmán, A. Hierro, and B. Alén. Type II InAs/GaAsSb quantum dots: Highly tunable exciton geometry and topology. *Appl. Phys. Lett.*, 107(18):183101, 2015.

[209] Gregory H. Wannier. Wave Functions and Effective Hamiltonian for Bloch Electrons in an Electric Field. *Phys. Rev.*, 117:432–439, Jan 1960.

[210] Ivo Souza, Jorge Íñiguez, and David Vanderbilt. First-principles approach to insulators in finite electric fields. *Phys. Rev. Lett.*, 89:117602, Aug 2002.

[211] Huaxiang Fu and L. Bellaiche. First–principles determination of electromechanical responses of solids under finite electric fields. *Phys. Rev. Lett.*, 91:057601, Jul 2003.

[212] G. W. Wen, J. Y. Lin, H. X. Jiang, and Z. Chen. Quantum–confined Stark effects in semiconductor quantum dots. *Phys. Rev. B*, 52:5913–5922, Aug 1995.

[213] Rafid A. Abdullah and Kamarulazizi Ibrahim. Effects of quantum confined Stark effect and well thickness on optical properties of double quantum wells violet InGaN laser diodes. *Optik - Int. J. Light and Elec. Op.*, 124(4):292 – 296, 2013.

[214] B. Szafran, T. Chwiej, F. M. Peeters, S. Bednarek, J. Adamowski, and B. Partoens. Exciton and negative trion dissociation by an external electric field in vertically coupled quantum dots. *Phys. Rev. B*, 71:205316, May 2005.

[215] J. Singh. *Electronic and Optoelectronic Properties of Semiconductor Structures*. Cambridge University Press, 2007.

[216] Leonardo K. Castelano, Daniel Ferreira Cesar, Victor Lopez-Richard, Gilmar E. Marques, Odilon D. D. Couto, Fernando Iikawa, Rudolf Hey, and Paulo V. Santos. Zeeman splitting and spin dynamics tuning by exciton charging in two-dimensional systems. *Phys. Rev. B*, 84:205332, Nov 2011.

[217] A. Twardowski, T. Dietl, and M. Demianiuk. The study of the s-d type exchange interaction in $Zn_{1-x}Mn_xSe$ mixed crystals. *Solid State Commun.*, 48(10):845 – 848, 1983.

[218] G. D. Sanders, Y. Sun, F. V. Kyrychenko, C. J. Stanton, G. A. Khodaparast, M. A. Zudov, J. Kono, Y. H. Matsuda, N. Miura, and H. Munekata. Electronic states and cyclotron resonance in n–type InMnAs. *Phys. Rev. B*, 68:165205, Oct 2003.

[219] C. F. Destefani, Sergio E. Ulloa, and G. E. Marques. Spin-orbit coupling and intrinsic spin mixing in quantum dots. *Phys. Rev. B*, 69:125302, Mar 2004.

[220] F. M. Hashimzade, A. M. Babayev, and B. H. Mehdiyev. Rashba spin-orbit coupling effects in $Cd_{1-x}Mn_xTe$ quantum dots. *Phys. Rev. B*, 73:245321, Jun 2006.

[221] G. Bacher, H. Schömig, M. K. Welsch, S. Zaitsev, V. D. Kulakovskii, A. Forchel, S. Lee, M. Dobrowolska, J. K. Furdyna, B. König, and W. Ossau. Optical spectroscopy on individual CdSe/ZnMnSe quantum dots. *Appl. Phys. Lett.*, 79(4):524–526, 2001.

[222] Rachel Fainblat, Franziska Muckel, Charles J. Barrows, Vladimir A. Vlaskin, Daniel R. Gamelin, and Gerd Bacher. Valence-band mixing effects in the upper-excited-state magneto-optical responses of colloidal Mn^{2+}-doped CdSe quantum dots. *ACS Nano*, 8(12):12669–12675, 2014.

[223] Woo-Chul Kwak, Yun-Mo Sung, Tae Geun Kim, and Won-Seok Chae. Synthesis of Mn–doped zinc blende CdSe nanocrystals. *Appl. Phys. Lett.*, 90(17):173111, 2007.

[224] Paul I. Archer, Steven A. Santangelo, and Daniel R. Gamelin. Direct observation of sp–d exchange interactions in colloidal Mn^{2+}- and Co^{2+}-doped CdSe quantum dots. *Nano Lett.*, 7(4):1037–1043, 2007.

[225] J. K. Furdyna. Diluted magnetic semiconductors. *J. Appl. Phys.*, 64(4):R29–R64, 1988.

[226] G. Fuster, N. E. Brener, J. Callaway, J. L. Fry, Y. Z. Zhao, and D. A. Papaconstantopoulos. Magnetism in bcc and fcc manganese. *Phys. Rev. B*, 38:423–432, Jul 1988.

[227] Anh Le Duc, Hai Pham Nam, and Tanaka Masaaki. Observation of spontaneous spin-splitting in the band structure of an n-type zinc-blende ferromagnetic semiconductor. *Nat. Commun.*, 7:13810, dec 2016.

[228] Kai Chang, J. B. Xia, and F. M. Peeters. Magnetic field tuning of the effective g factor in a diluted magnetic semiconductor quantum dot. *Appl. Phys. Lett.*, 82(16):2661–2663, 2003.

[229] Tomasz Dietl and Hideo Ohno. Dilute ferromagnetic semiconductors: Physics and spintronic structures. *Rev. Mod. Phys.*, 86:187–251, Mar 2014.

[230] H. Munekata, H. Ohno, S. von Molnar, Armin Segmüller, L. L. Chang, and L. Esaki. Diluted magnetic III–V semiconductors. *Phys. Rev. Lett.*, 63:1849–1852, Oct 1989.

[231] Juarez L. F. Da Silva. Effective coordination concept applied for phase change $(GeTe)_m(Sb_2Te_3)_n$ compounds. *J. Appl. Phys.*, 109(2):023502, 2011.

[232] R.A. Swalin. *Thermodynamics of solids*. Wiley series on the science and technology of materials. Wiley, 1962.

[233] Su-Huai Wei, S. B. Zhang, and Alex Zunger. First–principles calculation of band offsets, optical bowings, and defects in CdS, CdSe, CdTe, and their alloys. *J. Appl. Phys.*, 87(3):1304–1311, 2000.

[234] Su-Huai Wei and S. B. Zhang. Chemical trends of defect formation and doping limit in II-VI semiconductors: The case of CdTe. *Phys. Rev. B*, 66:155211, Oct 2002.

[235] Gustavo Martini Dalpian. *A Natureza de Defeitos em Bulk e em Superfície de Semicondutores*. PhD thesis, Univ. of Sao Paulo, 2003.

[236] Enésio Marinho da Silva Junior. *Modulação das Propriedades Eletrônicas de Óxidos Metálicos para Aplicação em Células Fotoeletroquímicas*. PhD thesis, Federal Univ. of ABC, 2016.

[237] E. Menéndez-Proupin and W. Orellana. Theoretical study of intrinsic defects in CdTe. *J. Phys. Conf. Ser.*, 720(1):012031, 2016.

[238] Clas Persson, Yu-Jun Zhao, Stephan Lany, and Alex Zunger. n-type doping of $CuInSe_2$ and $CuGaSe_2$. *Phys. Rev. B*, 72:035211, Jul 2005.

[239] Christoph Freysoldt, Blazej Grabowski, Tilmann Hickel, Jörg Neugebauer, Georg Kresse, Anderson Janotti, and Chris G. Van de Walle. First-principles calculations for point defects in solids. *Rev. Mod. Phys.*, 86:253–305, Mar 2014.

[240] Hongtao Ren, Gang Xiang, Gangxu Gu, Xi Zhang, Wenjun Wang, Peng Zhang, Baoyi Wang, and Xingzhong Cao. Zinc vacancy-induced room-temperature ferromagnetism in undoped ZnO thin films. *J. Nanomat.*, 2012:6, 2012.

[241] Nair R.R., Tsai I.-L., Sepioni M., Lehtinen O., Keinonen J., Krasheninnikov A.V., Castro Neto A.H., Katsnelson M.I., Geim A.K., and Grigorieva I.V. Dual origin of defect magnetism in graphene and its reversible switching by molecular doping. *Nat. Commun.*, 4:2010, jun 2013.

[242] S. Neeleshwar, C. L. Chen, C. B. Tsai, Y. Y. Chen, C. C. Chen, S. G. Shyu, and M. S. Seehra. Size–dependent properties of CdSe quantum dots. *Phys. Rev. B*, 71:201307, May 2005.

[243] Shashi B. Singh, Mukta V. Limaye, Sadgopal K. Date, and Sulabha K. Kulkarni. Room temperature ferromagnetism in thiol-capped CdSe and CdSe:Cu nanoparticles. *Chem. Phys. Lett.*, 464(4):208–210, 2008.

[244] Robert W. Meulenberg, Jonathan R. I. Lee, Scott K. McCall, Khalid M. Hanif, Daniel Haskel, Jonathan C. Lang, Louis J. Terminello, and Tony van Buuren. Evidence for ligand-induced paramagnetism in CdSe quantum dots. *J. Am. Chem. Soc.*, 131(20):6888–6889, 2009.

[245] A. Sundaresan and C.N.R. Rao. Ferromagnetism as a universal feature of inorganic nanoparticles. *Nano Today*, 4(1):96 – 106, 2009.

[246] Avijit Saha and Ranjani Viswanatha. Magnetism at the interface of magnetic oxide and nonmagnetic semiconductor quantum dots. *ACS Nano*, 11(3):3347–3354, 2017.

[247] Mohindar S. Seehra, Prasanta Dutta, Sonnathi Neeleshwar, Yang-Yuan Chen, Cheng Lung Chen, Shang Wei Chou, Chia Chun Chen, Chung-Li Dong, and Ching-Lin Chang. Size–controlled ex–nihilo ferromagnetism in capped CdSe quantum dots. *Adv. Mater.*, 20(9):1656–1660, 2008.

[248] S. Mahapatra, T. Kiessling, E. Margapoti, G. V. Astakhov, J. Renner, U. Bass, C. Bougerol, T. Schmidt, A. Bendounan, F. Schmitt, C. Schumacher, L. Worschech, W. Ossau, J. Geurts, L. W. Molenkamp, F. Reinert, A. Forchel, and K. Brunner. CdSe/ZnSe heteroepitaxy: aspects of growth and self organization of nanostructures. *Phys. Status Solidi C*, 4(9):3129–3149, 2007.

[249] E. Margapoti, Fabrizio M. Alves, S. Mahapatra, T. Schmidt, V. Lopez-Richard, C. Destefani, E. Menéndez-Proupin, Fanyao Qu, C. Bougerol, K. Brunner, A. Forchel, G. E. Marques, and L. Worschech. Characterization of spin-state tuning in thermally annealed semiconductor quantum dots. *Phys. Rev. B*, 82:205318, Nov 2010.

[250] Jian-Ping Tang, Ling ling Wang, Hai-Jun Luo, and Wen-Zhi Xiao. Magnetic properties in zinc-blende CdS induced by Cd vacancies. *Phys. Lett. A*, 377(7):572–576, 2013.

[251] Wen-Zhi Xiao, Ling ling Wang, Qing-Yan Rong, Gang Xiao, and Bo Meng. Magnetism in undoped ZnS studied from density functional theory. *J. Appl. Phys.*, 115(21):213905, 2014.

[252] G. Kresse and J. Hafner. *Ab initio* molecular dynamics for open-shell transition metals. *Phys. Rev. B*, 48(17):13115–13118, Nov. 1993.

[253] G. Kresse and J. Furthmüller. Efficient iterative schemes for *Ab initio* total-energy calculations using a plane-wave basis set. *Phys. Rev. B*, 54(16):11169–11186, Oct. 1996.

[254] Kesong Yang, Rongqin Wu, Lei Shen, Yuan Ping Feng, Ying Dai, and Baibiao Huang. Origin of d^0 magnetism in II–VI and III–V semiconductors by substitutional doping at anion site. *Phys. Rev. B*, 81:125211, Mar 2010.

[255] Ji-Sang Park, Ji-Hui Yang, Teresa Barnes, and Su-Huai Wei. Effect of intermixing at CdS/CdTe interface on defect properties. *Appl. Phys. Lett.*, 109(4):042105, 2016.

[256] S. B. Zhang and John E. Northrup. Chemical potential dependence of defect formation energies in GaAs: Application to Ga self-diffusion. *Phys. Rev. Lett.*, 67:2339–2342, Oct 1991.

[257] Andreas Pfenning, Fabian Hartmann, Mariama Rebello Sousa Dias, Leonardo Kleber Castelano, Christoph Submeier, Fabian Langer, Sven Hofling, Martin Kamp, Gilmar Eugenio Marques, Lukas Worschech, and Victor Lopez-Richard. Nanothermometer based on resonant tunneling diodes: from cryogenic to room temperatures. *ACS Nano*, 9(6):6271–6277, 2015.

[258] Zhongying Wang and Baoxia Mi. Environmental applications of 2d molybdenum disulfide (MoS_2) nanosheets. *Environ. Sci. Technol.*, 51(15):8229–8244, 2017.

[259] Eric Singh, Ki Seok Kim, Geun Young Yeom, and Hari Singh Nalwa. Atomically thin–layered molybdenum disulfide (MoS_2) for bulk–heterojunction solar cells. *ACS Appl. Mater. and Interfaces*, 9(4):3223–3245, 2017.

[260] Estibaliz Merino and Maria Ribagorda. Control over molecular motion using the cis trans photoisomerization of the azo group. *Beilstein J. Org. Chem.*, 8:1071–1090, 2012.

[261] Tomiki Ikeda and Osamu Tsutsumi. Optical switching and image storage by means of azobenzene liquid-crystal films. *Science*, 268(5219):1873–1875, 1995.

[262] H. Finkelmann, E. Nishikawa, G. G. Pereira, and M. Warner. A new opto-mechanical effect in solids. *Phys. Rev. Lett.*, 87:015501, Jun 2001.

[263] Jadranka Dokić, Marcel Gothe, Jonas Wirth, Maike V. Peters, Jutta Schwarz, Stefan Hecht, and Peter Saalfrank. Quantum chemical investigation of thermal cis-to-trans isomerization of azobenzene derivatives: Substituent effects, solvent effects, and comparison to experimental data. *J. Phys. Chem.*, 113(24):6763–6773, 2009.

[264] G. S. Hartley. The cis-form of azobenzene. *Nature*, 140:281, Aug. 1937.

[265] J. Griffiths. II. Photochemistry of azobenzene and its derivatives. *Chem. Soc. Rev.*, 1:481–493, 1972.

[266] Naoto Tamai and Hiroshi Miyasaka. Ultrafast dynamics of photochromic systems. *Chem. Rev.*, 100(5):1875–1890, 2000.

[267] Chih-Wei Chang, Ying-Chih Lu, Tsai-Te Wang, and Eric Wei-Guang Diau. Photoisomerization dynamics of azobenzene in solution with s_1 excitation: a femtosecond fluorescence anisotropy study. *J. Am. Chem. Soc.*, 126(32):10109–10118, 2004.

[268] Karina Morgenstern. Isomerization reactions on single adsorbed molecules. *Acc. Chem. Res.*, 42(2):213–223, 2009.

[269] Eric Wei-Guang Diau. A new trans–to–cis photoisomerization mechanism of azobenzene on the $s_1(n, \pi*)$ surface. *J. Phys. Chem. A*, 108(6):950–956, 2004.

[270] Byoung-Young Choi, Se-Jong Kahng, Seungchul Kim, Hajin Kim, Hyo Won Kim, Young Jae Song, Jisoon Ihm, and Young Kuk. Conformational molecular switch of the azobenzene molecule: A scanning tunneling microscopy study. *Phys. Rev. Lett.*, 96:156106, Apr 2006.

[271] Andrew A. Beharry and G. Andrew Woolley. Azobenzene photoswitches for biomolecules. *Chem. Soc. Rev.*, 40:4422–4437, 2011.

[272] Ellis V. Brown and G. Richard Granneman. Cis–trans isomerism in the pyridyl analogs of azobenzene. kinetic and molecular orbital analysis. *J. Am. Chem. Soc.*, 97(3):621–627, 1975.

[273] H. M. Dhammika Bandara and Shawn C. Burdette. Photoisomerization in different classes of azobenzene. *Chem. Soc. Rev.*, 41:1809–1825, 2012.

[274] Oruganti Srinivas, Nivedita Mitra, Avadhesha Surolia, and Narayanaswamy Jayaraman. Photoswitchable multivalent sugar ligands: synthesis, isomerization, and lectin binding studies of azobenzene–glycopyranoside derivatives. *J. Am. Chem. Soc.*, 124(10):2124–2125, 2002.

[275] Pamela R. Westmark, John P. Kelly, and Bradley D. Smith. Photoregulation of enzyme activity. photochromic, transition-state-analog inhibitors of cysteine and serine proteases. *J. Am. Chem. Soc.*, 115(9):3416–3419, 1993.

[276] Andreas Aemissegger, Vincent Kräutler, Wilfred F. van Gunsteren, and Donald Hilvert. A photoinducible β-hairpin. *J. Am. Chem. Soc.*, 127(9):2929–2936, 2005.

[277] K. S. Novoselov, A. K. Geim, S. V. Morozov, D. Jiang, Y. Zhang, S. V. Dubonos, I. V. Grigorieva, and A. A. Firsov. Electric field effect in atomically thin carbon films. *Science*, 306(5696):666–669, 2004.

[278] Q. H. Wang, K. Kourosh, A. Kis, J. N. Coleman, and M. S. Strano. Electronics and optoelectronics of two–dimensional transition metal dichalcogenides. *Nat. Nanotechnol.*, 7(11):699–712, nov 2012.

[279] Manish Chhowalla, Hyeon Suk Shin, Goki Eda, Lain-Jong Li, Kian Ping Loh, and Hua Zhang. The chemistry of two-dimensional layered transition metal dichalcogenide nanosheets. *Nat. Chem.*, 5(4):263–275, Mar. 2013.

[280] C. Jung, S. M. Kim, H. Moon, G. Han, J. Kwon, Y. Hong, I. Omkaram, Y. Yoon, S. Kim, and J. Park. Highly crystalline CVD-grown multilayer $MoSe_2$ thin film transistor for fast photodetector. *Sci. Rep.*, 5:15313, oct 2015.

[281] J. S. Ross, S. Wu, H. Yu, N. J. Ghimire, A. M. Jones, Grant Aivazian, J. Yan, D. G. Mandrus, Di Xiao, W. Yao, and X. Xu. Electrical control of neutral and charged excitons in a monolayer semiconductor. *Nat. Commun.*, 4:1474, feb 2013.

[282] Mak Kin Fai and Shan Jie. Photonics and optoelectronics of 2d semiconductor transition metal dichalcogenides. *Nature Photon.*, 10(4):216–226, apr 2016.

[283] Matheus Paes Lima, José Eduardo Padilha, Renato Borges Pontes, Adalberto Fazzio, and Antônio José Roque da Silva. Stacking–dependent transport properties in few–layers graphene. *Solid State Commun.*, 250:70–74, 2017.

[284] Wonbong Choi, Nitin Choudhary, Gang Hee Han, Juhong Park, Deji Akinwande, and Young Hee Lee. Recent development of two–dimensional transition metal dichalcogenides and their applications. *Mater. Today*, 20(3):116–130, 2017.

[285] S. Monti, G. Orlandi, and P. Palmieri. Features of the photochemically active state surfaces of azobenzene. *Chem. Phys.*, 71(1):87–99, 1982.

[286] Matthew J. Comstock, Niv Levy, Armen Kirakosian, Jongweon Cho, Frank Lauterwasser, Jessica H. Harvey, David A. Strubbe, Jean M. J. Fréchet, Dirk Trauner, Steven G. Louie, and Michael F. Crommie. Reversible photomechanical switching of individual engineered molecules at a metallic surface. *Phys. Rev. Lett.*, 99:038301, Jul 2007.

[287] Juan Li, Jakob Wierzbowski, Özlem Ceylan, Julian Klein, Filippo Nisic, Tuan Le Anh, Felix Meggendorfer, Carlos-Andres Palma, Claudia Dragonetti, Johannes V. Barth, Jonathan J. Finley, and Emanuela Margapoti. Tuning the optical emission of MoS_2 nanosheets using proximal photoswitchable azobenzene molecules. *Appl. Phys. Lett.*, 105(24):241116, 2014.

[288] Qiang Fu, Caterina Cocchi, Dmitrii Nabok, Andris Gulans, and Claudia Draxl. Graphene-modulated photo-absorption in adsorbed azobenzene monolayers. *Phys. Chem. Chem. Phys.*, 19:6196–6205, 2017.

[289] Hermann Rau. Spectroscopic properties of organic Azo compounds. *Angew. Chem. Int. Ed.*, 12(3):224–235, 1973.

[290] P A Young. Lattice parameter measurements on molybdenum disulphide. *J. Phys. D: Appl. Phys.*, 1(7):936, 1968.

[291] Jason K. Ellis, Melissa J. Lucero, and Gustavo E. Scuseria. The indirect to direct band gap transition in multilayered MoS_2 as predicted by screened hybrid density functional theory. *Appl. Phys. Lett.*, 99(26):261908, 2011.

[292] Yohanna Seminovski, Polina Tereshchuk, Adam Kiejna, and Juarez L. F. Da Silva. The role of the cationic Pt sites in the adsorption properties of water and ethanol on the Pt_4/Pt(111) and Pt_4/CeO_2(111) substrates: A density functional theory investigation. *J. Chem. Phys.*, 145(12):124709, Sept. 2016.

[293] M.-C. Desjonquères and D. Spanjaard. *Concepts in Surface Science*. Springer, 1995.

[294] L. W. Bruch, M. W. Cole, and E. Zaremba. *Physical Adsorption: Forces and Phenomena*. Oxford Science Publications, 1997.

[295] Wenzhong Bao, Xinghan Cai, Dohun Kim, Karthik Sridhara, and Michael S. Fuhrer. High mobility ambipolar MoS_2 field–effect transistors: Substrate and dielectric effects. *Appl. Phys. Lett.*, 102(4):042104, 2013.

[296] K. F. Mak, K. L. McGill, J. Park, and P. L. McEuen. The valley hall effect in MoS_2 transistors. *Science*, 344(6191):1489–1492, 2014.

[297] Xiaobo Yin, Ziliang Ye, Daniel A. Chenet, Yu Ye, Kevin O'Brien, James C. Hone, and Xiang Zhang. Edge nonlinear optics on a MoS_2 atomic monolayer. *Science*, 344(6183):488–490, 2014.

[298] Britton W. H. Baugher, Hugh O. H. Churchill, Yafang Yang, and Pablo Jarillo-Herrero. Intrinsic electronic transport properties of high–quality monolayer and bilayer MoS_2. *Nano Lett.*, 13(9):4212–4216, 2013.

[299] Deblina Sarkar, Wei Liu, Xuejun Xie, Aaron C. Anselmo, Samir Mitragotri, and Kaustav Banerjee. MoS_2 field–effect transistor for next-generation label–free biosensors. *ACS Nano*, 8(4):3992–4003, 2014.

[300] F. K. Perkins, A. L. Friedman, E. Cobas, P. M. Campbell, G. G. Jernigan, and B. T. Jonker. Chemical vapor sensing with monolayer MoS_2. *Nano Lett.*, 13(2):668–673, 2013.

[301] R. S. Sundaram, M. Engel, A. Lombardo, R. Krupke, A. C. Ferrari, Ph. Avouris, and M. Steiner. Electroluminescence in single layer MoS_2. *Nano Lett.*, 13(4):1416–1421, 2013.

[302] Jiahao Kang, Wei Liu, Deblina Sarkar, Debdeep Jena, and Kaustav Banerjee. Computational study of metal contacts to monolayer transition–metal dichalcogenide semiconductors. *Phys. Rev. X*, 4:031005, Jul 2014.

[303] Hongxia Zhong, Ruge Quhe, Yangyang Wang, Zeyuan Ni, Meng Ye, Zhigang Song, Yuanyuan Pan, Jinbo Yang, Li Yang, Ming Lei, Junjie Shi, and Jing Lu. Interfacial properties of monolayer and bilayer MoS_2 contacts with metals: Beyond the energy band calculations. *Sci. Rep.*, 6:21786, mar 2016.

[304] Igor Popov, Gotthard Seifert, and David Tománek. Designing electrical contacts to MoS_2 monolayers: A computational study. *Phys. Rev. Lett.*, 108:156802, Apr 2012.

[305] Li-Yong Gan, Yu-Jun Zhao, Dan Huang, and Udo Schwingenschlögl. First-principles analysis of MoS_2/Ti_2C and MoS_2/Ti_2CY (Y=F and OH) all–2d semiconductor/metal contacts. *Phys. Rev. B*, 87:245307, Jun 2013.

[306] Saptarshi Das, Hong-Yan Chen, Ashish Verma Penumatcha, and Joerg Appenzeller. High performance multilayer MoS_2 transistors with scandium contacts. *Nano Lett.*, 13(1):100–105, 2013.

[307] G P Francis and M C Payne. Finite basis set corrections to total energy pseudopotential calculations. *J. Phys.: Condens. Matter*, 2(19):4395, 1990.

[308] P. Pulay. Ab initio calculation of force constants and equilibrium geometries in polyatomic molecules. *Mol. Phys.*, 17(2):197–204, 1969.

[309] P. Ehrenfest. Bemerkung über die angenäherte gültigkeit der klassischen mechanik innerhalb der quantenmechanik. *Zeitschrift für Physik*, 45(7):455–457, Jul 1927.

[310] O. H. Nielsen and Richard M. Martin. Stresses in semiconductors: Ab *initio* calculations on Si, Ge, and GaAs. *Phys. Rev. B*, 32:3792–3805, Sep 1985.

[311] O. H. Nielsen and Richard M. Martin. Quantum–mechanical theory of stress and force. *Phys. Rev. B*, 32:3780–3791, Sep 1985.

[312] N. David Mermin. Thermal properties of the inhomogeneous electron gas. *Phys. Rev.*, 137:A1441–A1443, Mar 1965.

[313] M. Methfessel and A. T. Paxton. High–precision sampling for Brillouin–zone integration in metals. *Phys. Rev. B*, 40:3616–3621, Aug 1989.

[314] G Gilat. Analysis of methods for calculating spectral properties in solids. *J. Comput. Phys.*, 10(3):432–465, 1972.

[315] G. Gilat. Methods of Brillouin zone integration. *Meth. Comput. Phys.: Adv. in Res. and Appl.*, 15:317–370, 1976.

[316] A H MacDonald, S H Vosko, and P T Coleridge. Extensions of the tetrahedron method for evaluating spectral properties of solids. *J. Phys. C: Solid State Phys.*, 12(15):2991, 1979.